On the Formation of Elliptical Galaxies via Mergers in Galaxy Groups

by

Dan S. Taranu

A thesis submitted in conformity with the requirements
for the degree of Doctor of Philosophy
Graduate Department of Astronomy and Astrophysics
University of Toronto

Abstract

On the Formation of Elliptical Galaxies via Mergers in Galaxy Groups

Dan S. Taranu
Doctor of Philosophy
Graduate Department of Astronomy and Astrophysics
University of Toronto
2014

Elliptical galaxies comprise the majority of luminous galaxies in our universe. Ellipticals have long been thought to form through gas-rich "major" mergers of two roughly equal-mass spiral galaxies. We propose instead that ellipticals form through gas-poor, mainly minor mergers of spirals in groups. This hypothesis is tested using a novel sample of hundreds of numerical simulations of mergers in groups of three to twenty-five spiral galaxies. These simulations are accompanied by mock observations of the central remnants in each group, comparing to data on ellipticals from galaxy surveys. The simulated merger remnants have similar surface brightness profiles to observed ellipticals - if the spirals begin with concentrated bulges. The remnants follow tight size-luminosity and velocity dispersion-luminosity relations (<0.12 dex scatter), with similar slopes as observed. Stochastic merging can produce tight scaling relations if the merging galaxies follow tight scaling relations themselves. However, the remnants are too large and have too low dispersions at fixed luminosity. Some remnants show substantial ($v/\sigma >$ 0.1) rotational support, but most are slow rotators with $v/\sigma \ll 0.5$. Ellipticals also follow a tight "fundamental plane" scaling relation between size, mean surface brightness and velocity dispersion: $R \propto \sigma^a \mu^b$. This relation has tiny (< 0.05 dex) scatter and significantly different coefficients from the expected scaling (a "tilt"). The remnants lie on a similar fundamental plane, with even smaller scatter than observed and a tilt in the correct sense (albeit weaker than observed). This tilt is mainly driven by variable dark matter fractions, such that massive merger remnants have larger central dark matter fractions than their lower-mass counterparts. The origin of this mass-dependent dark matter fraction and fundamental plane tilt is examined in detail, linking with dynamical masses and the virial theorem. Contrary to previous studies, massive ellipticals can originate from multiple, mainly minor and dry mergers. However, significant gas dissipation may be needed to produce lower-mass, rapidly-rotating ellipticals.

Dedication

To Carmen and Alex, Emily and John, Marija and Dan, and last but not least, Oscar and Oscar, who will surely read this most carefully of all.

Acknowledgements

First and foremost, I would like to thank my advisors John Dubinski and Howard Yee for motivating and supporting this endeavour from start to finish. This project would not have been possible without their guidance and contributions.

Many other members of the astronomy community at the University of Toronto assisted me in various ways. In particular, Bob Abraham, Lei Bai, Ray Carlberg, Dennis Just and Shelley Wright provided helpful advice, suggestions, and consultations. Most of all, I am grateful to my (second) favourite officemate Preethi Nair for all of the above, and for her tireless work on morphological classifications of galaxies, which motivated much of the observational components of this thesis. The staff at the Department of Astronomy and Astrophysics also deserve credit for their friendly assistance, especially Marc Goodman and Angie Ho.

I am also grateful for the stimulating discussions and useful data provided by Frank van den Bosch, Michele Cappellari, Davor Krajnović, and especially Trevor Mendel.

I would also like to acknowledge the financial support from Ontario Graduate Scholarships, the Walter John Helm and Mary and Ron Martin Graduate Fellowships, and the National Science and Engineering Research Council of Canada. The computing resources provided by the Canadian Institute for Theoretical Astrophysics, SciNet and Compute Canada were also for the completion of this project.

I feel strangely compelled to acknowledge certain contributions from Brian and Jim, and possibly also Bao, Gordon and Justin. You know what you did.

Finally, I am deeply indebted to Carmen and Alex Taranu, and Marija and Oscar Stanković, for obvious reasons.

Contents

List of Tables

List of Figures

Per astra ad aspera.

Chapter 1

Introduction

1.1 Elliptical Galaxies

As gravitationally bound collections of stars, gas, dust and dark matter, galaxies are fundamental building blocks of the matter in our universe. Our own galaxy, the Milky Way, is clearly visible as a narrow band of stars across the night sky. Decades of research have proven that this milky band is, in fact, a rotating disk of stars, bespoked by numerous spiral arms and a central bar. However, until the 1920s, it was not known whether the Milky Way was the extent of our known universe, or whether other such "island universes" or galaxies existed. The Great Shapley-Curtis debate of 1920 failed to settle the question of whether some of the thousands of nebulae catalogued during the 1700s and 1800s were actually galaxies much like our own, or merely clouds of gas and stars within our Milky Way.

Hubble's seminal work, "The Realm of Nebulae" (Hubble, 1936), established without a doubt that most nebulae are in fact galaxies consisting of billions of stars. Hubble also developed and popularized the so-called Hubble sequence as a classification system for galaxies. This system includes three major, broad categories of galaxies: disk-dominated spirals; smooth, round and rather featureless ellipticals; and a somewhat mysterious intermediate class called lenticulars.

Since then, numerous studies have confirmed that ellipticals are physically distinct from spirals. Ellipticals are mainly supported against gravitational collapse by the random motions of their stars, rather than ordered rotation in a disk. Most ellipticals contain very little cold, star-forming gas. Ellipticals comprise the majority of galaxies brighter than our own galaxy, and the luminosity function of ellipticals is roughly symmetrical (e.g. de Lapparent et al., 2004) rather than dominated by faint galaxies like the spiral luminosity function (see also e.g. Madgwick et al., 2002, for luminosity functions separated by star formation rates). Dense environments like groups and clusters tend to host more ellipticals than spirals - the so-called morphology-density relation (Dressler, 1980). All of these observational facts suggest that ellipticals have substantially different formation histories from spirals.

Unlike spirals, the stellar populations of elliptical galaxies are dominated by old stars (e.g.

Bower et al., 1992; Trager et al., 2000), with little evidence for recently-formed stars. This fact, combined with the near-circular surface brightness contours of some ellipticals led early theorists to suggest that ellipticals were formed in a single, early, rapid collapse of a gas cloud (Larson, 1969), often referred to as a "monolithic collapse" (see also Eggen et al., 1962, as applied to our own galaxy). In this framework, galaxies originate from the collapse of a roughly spherical cloud of gas, forming stars in a rapid burst. Spirals are distinguished by having larger net angular momentum, which results in the remaining gas forming a disk. Ellipticals would form mainly in non-rotating halos with relatively little angular momentum (e.g. Chiosi & Carraro, 2002). The remaining gas would be inhibited from cooling and settling into a disk, perhaps being blown away by "feedback" from star formation, such as the energy and momentum released by the supernovae of massive stars.

While conceptually simple, the monolithic collapse model has difficulties explaining a number of properties of ellipticals. Most notably, recent studies have found that the a large fraction of fainter ellipticals have substantial net rotation (Emsellem et al., 2007, 2011), possibly even embedded disks. Some ellipticals are considerably younger than the age of the universe (Trager et al., 2000), suggesting that their stars did not all form in the early universe. Many have dust lanes (e.g. Sadler & Gerhard, 1985; van Dokkum & Franx, 1995) indicative of recent star formation or merger activity (Kaviraj et al., 2012), although these dust lanes are usually not prominent. Early studies found limited evidence for cold gas in ellipticals (Faber & Gallagher, 1976), but more recent studies suggest that a minority of ellipticals could host modest quantities of cold gas, likely having an external origin (e.g. Serra & Oosterloo, 2010).

The main argument against monolithic collapse owes itself to the accurate determination of cosmological parameters from microwave satellites like the Wilkinson Microwave Anisotropy Probe (WMAP Spergel et al., 2003) and from observations of supernovae (e.g. Riess et al., 1998). After cold dark matter became the widely accepted cosmological paradigm, numerical simulations like the Millennium simulation (Springel et al., 2005b) showed beyond the shadow of a doubt that massive halos assemble hierarchically (see also White & Rees, 1978), merging smaller halos and growing in mass and size. This pushed the already well-established merger theory of elliptical galaxy formation into widespread acceptance, relegating monolithic collapse to the sidelines - though it is still possible that some compact galaxies may form in a rapid burst at very high ($z > 2$) redshifts.

Mergers are now thought to be an important mechanism for growing galaxies of all kinds, integral especially for the formation of massive and luminous ellipticals. In a recent review, Kormendy et al. (2009) illustrated how many of the structural properties of ellipticals (and correlations thereof) are consistent with a merger-driven formation scenario. This warrants a more careful examination of the history and motivation behind the merger theory of elliptical formation.

1.2 Mergers of Spiral Galaxies in Groups as the Origin of Elliptical Galaxies

Merging of spiral galaxies is a promising mechanism for producing elliptical galaxies. Although it was perhaps not until Toomre (1977) that interacting spirals became widely accepted as elliptical progenitors, simulations of interacting spirals date back at least to Toomre & Toomre (1972) and arguably as far as Holmberg (1941). Much of this work has focused on major mergers (mass ratio $<$ 3:1) of pairs of spiral galaxies on parabolic orbits. While such binary major mergers certainly are observed in the local universe - and will likely be the ultimate fate of the Milky Way and M31 - they may not be as common as hierarchical minor mergers, and several problems persist with a purely major merger scenario (Naab & Ostriker, 2009).

Observational evidence (e.g. Geller & Huchra, 1983) and numerical simulations (e.g. McGee et al., 2009) suggest that most L* galaxies are found in groups, where the central galaxy is likely to have experienced multiple mergers and have several surviving satellites. Furthermore, late-type galaxies in groups follow a Schechter luminosity function (Schechter, 1976) similar to those in other environments (Croton et al., 2005; Robotham et al., 2010). However, the fraction of red galaxies in groups decreases strongly with redshift (e.g. Li et al., 2012), while red galaxies tend to build up in high-density regions like groups over time (e.g. Cooper et al., 2007). Thus, high-redshift groups are likely composed primarily of spiral galaxies - perhaps several bright spirals, and a larger number of fainter satellites - some of which are bound to merge over time. Our hypothesis is that groups of three or more spiral galaxies with luminosity distributions following a Schechter function will naturally merge to produce a luminous, central elliptical galaxy, along with some less luminous, tidally-stripped satellites.

We aim to test this hypothesis with numerical experiments. More specifically, we test whether the properties of the central galaxies formed through collisionless mergers in groups of spirals are consistent with observations of local ellipticals. We will demonstrate that these merger remnants are both qualitatively and quantitatively different from both the more prevalent studies on binary mergers and also the less abundant literature on galaxy group mergers. We present results on morphological and kinematical measures as well as two dimensional scaling relations; the three dimensional fundamental plane scaling relation will be introduced in §1.3. To further motivate this endeavour, we will outline some of the key results of the past several decades of work in this field.

Carnevali et al. (1981) and Ishizawa et al. (1983) were amongst the first to produce simulations of mergers in groups of galaxies (10-20 each), using 20 and 100 particles per galaxy, respectively. Barnes (1985) introduced separate stellar and dark matter profiles, with 30 and 270 particles for each component, respectively. Barnes (1989) added stellar disks and bulges to the galaxy models, taking advantage of the newly invented N-body tree code (Barnes & Hut, 1986) to increase resolution to 4096 luminous and dark particles each. While the arrangement of orbits was somewhat artificial (a pair of triple systems each consisting of a binary

orbiting a more massive single galaxy), the study showed that mergers of realistic galaxies in compact groups can be rapid and produce central remnants with de Vaucouleurs profiles and shell structures, similar to local ellipticals.

A problem with the collisionless merger scenario was identified by Carlberg (1986). Collisionless mergers cannot increase central phase space density, which is necessary if disks are to merge and produce ellipticals with higher central densities than their progenitors, as is often the case. Hernquist et al. (1993) directly addressed this issue with simulations of binary mergers of spirals with bulges (Hernquist, 1993), which, unlike mergers of bulgeless spirals (Hernquist, 1992), are capable of producing sufficiently centrally dense remnants.

Weil & Hernquist (1996) extended this methodology to mergers of groups of six equal-mass spirals. The resolution of these simulations was a factor of 18 higher than Barnes (1989), with almost 150,000 particles per galaxy, and included a comparison sample of pair mergers. Group mergers were shown to produce remnants with some rotation, in contrast to the non-rotating remnants typical of dry binary mergers (Cox et al., 2006). Both varieties of mergers produced early-type galaxies well-fit by de Vaucouleurs profiles. However, group mergers with bulges did not maintain centrally concentrated profiles, exhibiting the same low central phase space density as found in bulgeless pair mergers. This may be seen as once again disfavoring the group merging scenario; however, it should be noted these mergers were of equal-mass galaxies and hence of very large mass ratios, which would tend to maximize this problem. Furthermore, King & Minkowski (1972), Graham et al. (2003), Kormendy et al. (2009) and others have argued that ellipticals have lower central densities ("cores") than expected from inward extrapolation of their outer surface brightness profiles. This is consistent with the group merging scenario and essentially the opposite of the central phase space density problem, although Kormendy et al. (2009) attribute these cores to scouring of inner stars by inspiraling supermassive black holes rather than purely stellar dynamical processes.

Since Weil & Hernquist (1996), the relatively rapid pace of advancements in the field of simulations of merging in galaxy groups has slowed, with the focus shifting to studies of hydrodynamical processes in group environments. This can be partially attributed to the findings of Robertson et al. (2006) that collisionless binary mergers are unable to produce ellipticals following a tilted fundamental plane relation, although Aceves & Velázquez (2005) found an appreciable tilt by merging spirals sampled from an appropriate Schechter luminosity function. Robertson et al. (2006) also found that collisionless binary mergers could only produce very slow-rotating remnants and that dissipation was required to produce significantly rotationally-supported ellipticals. However, between Weil & Hernquist (1996) and Robertson et al. (2006), very few studies have tested whether these results apply to multiple collisionless mergers as well. Galaxy clusters (Dubinski, 1998) and starbursts in groups (Bekki, 2001) have been considered. Ciotti et al. (2007) simulated consecutive mergers of spheroidal galaxies, roughly approximating hierarchical group merging. While this approach has provided useful estimates of the growth of stellar mass and size, the use of purely spheroidal progenitors is questionable given the preva-

lence of disks at high redshift. Hopkins et al. (2009) combined the results of binary merger simulations with cosmological merger trees, using empirical halo occupation models and spiral scaling relations to predict the evolution of early-type scaling relations. However, the models only incorporated multiple mergers by allowing binary merger remnants sufficient time to relax dynamically, whereas Moster et al. (2014) find that halos undergoing multiple mergers are likely to have two mergers in quick succession. Galaxies in groups are thus likely to undergo multiple mergers within a relatively short periods rather than a steady stream of isolated mergers.

More recently, fully cosmological simulations of mergers in a group or several groups of galaxies have been performed by, for example, Khalatyan et al. (2008) and Feldmann et al. (2011). Such simulations naturally incorporate hierarchical merging, typically by using the "zoom-in" method of re-simulating a small sub-volume of a large dark matter-only cosmological simulation at higher resolution. Naab et al. (2009) and Oser et al. (2012) demonstrated that ellipticals can form in groups, with minor mergers being an important mechanism in controlling the evolution of the central galaxy size and mass. Feldmann et al. (2011) showed success in producing not only a central elliptical but also early-type satellites by simulating a single group using this method. However, such ab initio simulations encounter difficulties achieving sufficient spatial resolution to produce realistic spiral galaxies. Typical softening lengths in such simulations are between 500 to 1000 pc, which significantly alters the inner profile of ellipticals, especially at low masses. Increasing the resolution can mitigate this problem but also greatly increases computational cost and limits the possible sample size to a few groups.

It is clear that there is a gap in the literature on multiple mergers in groups, even though multiple mergers likely create brightest cluster galaxies (Dubinski, 1998). By contrast, observations of elliptical galaxies have advanced tremendously in recent years, providing public catalogs of morphologies of thousands of nearby ellipticals and spirals alike (e.g. Blanton et al., 2005; Hyde & Bernardi, 2009a; Nair & Abraham, 2010; Simard et al., 2011), mainly based on Sloan Digital Sky Survey (SDSS) images. The SAURON project (de Zeeuw et al., 2002) and its volume-limited successor survey ATLAS3D (Cappellari et al., 2011) have provided integral-field kinematics of hundreds of early type galaxies at a comparable resolution to SDSS. It is increasingly necessary to match the large samples of observations with simulations and explore the vast parameter space of conditions in galaxy groups.

To meet the requirement of a large simulation sample, it is currently necessary to focus on dry merging and gravitational dynamics alone. Hydrodynamical simulations are more computationally expensive and add numerous parameters to initial conditions: disk gas fractions, gas disk scale heights and lengths relative to the stellar disk, the presence of a gaseous halo, etc. More importantly, existing literature has yet to establish the effects of collisionless gravitational dynamics in group mergers on central remnant structure. There is observational evidence suggesting that dry merging contributes significantly to the growth of massive galaxies, particularly ellipticals (e.g. van Dokkum et al., 2010). Even if exclusively dry merging is not the most common mechanism for forming ellipticals, many ellipticals will have experienced at least

one dry merger in their lifetimes and it is instructive to ask what collisionless dynamics alone would predict before moving on to hydrodynamical processes.

Two chapters of this thesis are dedicated to answering the question of whether merger remnants formed at the centres of groups resemble ellipticals. Section 2.1 motivates and details the methods used in creating the simulations of mergers in groups, while §2.2 details the analysis methodology and pipeline, with additional tests presented in Appendix A.1. A more detailed examination of numerical convergence can be found in Appendix A.2. Key results on morphology, scaling relations and kinematics of central remnants are presented in §3.1. The implications of these results on theories of elliptical galaxy formation are detailed in §3.2, with reference to prior studies on the subject. The conclusions are summarized in §3.3. All of these results have been published in the Astrophysical Journal as Taranu et al. (2013), with minor modifications. The key, three-dimensional fundamental plane scaling relation merits its own chapter and introduction.

1.3 The Fundamental Plane of Elliptical Galaxies

Three simple but fundamental properties of galaxies are their sizes, luminosities and velocity dispersions. Elliptical galaxies show some of the strongest correlations between these properties, with small or even negligible internal scatter. Explaining the origin of these scaling relations is a long-standing challenge in elliptical formation theory.

Two of the key scaling relations of elliptical galaxies were first noted over 35 years ago. The first of these is the Faber-Jackson (FJ) relation (Faber & Jackson, 1976) between velocity dispersion σ and luminosity L, typically observed to be $L \propto \sigma^4$. Shortly afterwards, the Kormendy relation (Kormendy, 1977) connected size (more specifically the half-light or effective radius R_e) with surface brightness μ. Originally this was μ *at* R_e, but now the mean μ within R_e is used, such that $\mu = -2.5 \log (L/R_e^2) + c$.

Djorgovski & Davis (1987) coined the term "fundamental plane" (FP for short) to describe the three-dimensional scaling relation between R, σ and μ as $R \propto \sigma^a \mu^b$, effectively combining the Faber-Jackson and Kormendy relations (since μ is interchangeable with L). Dressler et al. (1987) are also credited with the independent and concurrent discovery of the FP relation, if not its name. In optical passbands, it has since consistently been found that the value of the coefficient a lies in the range 1–1.5, and b from 0.25–0.35. That same year, Faber (1987) pointed out that the virial theorem can be rewritten as $R \propto \sigma^2 \mu^{0.4}$ - a relation very similar to the FP but with larger values for the coefficients a and b. The FP's deviation from the virial scalings implies a scaling of the mass-to-light ratio with FP parameters, now commonly referred to as the "tilt" of the fundamental plane.

The tilt and small scatter of the FP are now recognized as strong constraints on models for the formation of elliptical galaxies; however, no firm consensus has yet been reached on the importance of various mechanisms (e.g. hierarchical merging, dissipation, variations in stellar

populations) on the FP and its tilt. The numerical simulations presented in Chapter 2 are an ideal tool to test the hypothesis that ellipticals form from mergers of spiral galaxies in groups. More specifically, Chapter 4 tests whether these simulated merger remnants lie on an FP with appropriate tilt and scatter. We begin with a review of the FP and its tilt (§4.1), as well as of previous results in this field. Section 4.2 summarizes the changes in methodology and data from the more detailed description in Chapter 2. Measurements of the fundamental plane (§4.3.1) and its tilt (§4.3.2) are provided next, along with a full examination of the virial FP (§4.3.3) and a re-derivation of the FP from the virial theorem (§4.3.4). We derive dynamical masses from the virial FP in §4.3.5 and verify the previous results with simple, spherical bulge plus halo models in §4.3.6. In §4.4, we introduce an alternative parameterization of the tilt, along with a novel interpretation of its origin (§4.5). Section 4.6 addresses some of the details of the implications of these findings, which are summarized in §4.7. Two appendices are provided with further data on the run of the virial ratio with radius within sample galaxies (Appendix C.1), as well as the sensitivity of the simulated fundamental plane terms to initial conditions (Appendix C.2), specifically the orbital configurations of galaxies within each group.

The results related to the fundamental plane - Chapter 4, and the accompanying appendices - have been submitted to the Astrophysical Journal as Taranu et al. (2014). They are presented here with minor modifications. We end with a summary of the conclusions, areas for improvement and possible avenues for future work (Chapter 5).

Chapter 2

Simulation and Observation Methods

Having set the stage for simulations of mergers in groups, a thorough description of the setup of the numerical experiments is in order. The basic philosophy underpinning the simulations is that each group should resemble a halo undergoing gravitational collapse at high redshift ($z = 2$), while the groups should span a wide range of plausible merger histories. The full details of these simulations are given first in §2.1. Mock observations of the central galaxies in each group (§2.2) will allow testing of how closely their properties match those of nearby ellipticals. The observational data are mainly from catalogueues of local ellipticals ($z < 0.2$), as these are the largest and best-resolved samples available today. These are described in §2.3.

2.1 Simulations

The simulations are designed to extend the methodology of binary galaxy merger simulations to groups of galaxies. This section details the parameters of the group sample (§2.1.1), as well as the two key ingredients in the initial conditions: group configuration (§2.1.2) and galaxy models (§2.1.3). Finally, the code and parameters used for the simulations are described in §2.1.4.

Our choice of initial condition parameterization is designed to evenly sample the parameter space of groups which are likely to produce a central elliptical remnants, rather than be a unbiased sampling of real, nearby galaxy groups. This approach is similar to that used in binary mergers simulations, in which the orbits are typically nearly parabolic, with some cosmologically-motivated distribution of pericentric distance and disk alignment. In our case, we model group-sized halos at the turnaround radius at z=1-2, such that the subhalos are likely to contain spiral galaxies which will eventually merge to form one central elliptical.

We use two galaxy models designed to reproduce the surface brightness profile and rotation curve of M31 and scale these models according to the Tully-Fisher relation (Tully & Fisher,

1977). The only parameter we vary between the models is the profile of the bulge, which has a substantial impact on the structure of the merger remnant (§3.1.1). While this approach does not reproduce the variety of spiral galaxies found in the local universe, let alone at high redshift, it maintains the simplicity of the initial conditions. We do not vary the bulge fraction in the progenitors, as pre-formed bulges are required to produce sufficient central densities in the merger remnant. We discuss these choices further in §3.2.

Although the simulations are nominally scale-free, as with any system of units having G=1, our simulations assume units of length in kpc, velocity in 100 kms^{-1}, time in 9.73 million years and mass in $2.325 \times 10^9 M_\odot$. The luminosity function sampling and initial group radius impose a unique, preferred scaling to each simulation, such that mergers of groups with the same number of galaxies but different luminosities are not simply re-scaled versions of each other.

2.1.1 Group Sample

We create groups with total luminosities from 0.1-10L* and masses between $2 \times 10^{11} - 2 \times 10^{13} M_\odot$. We incorporate several basic assumptions consistent with observations and cosmological simulation predictions. More massive groups contain more galaxies on average, with galaxies preferentially located closer to the centre of the group. The group as a whole is initially collapsing, with galaxies located within $r_{max} = 2 \times R_{200,z=2}$ but having insufficient orbital energy to prevent collapse (i.e. the groups are sub-virial). We simulate each group configuration twice, with each simulation containing either spiral galaxies with exponential bulges or classical bulges (but not both), referring to the former sample as B.n$_s$=1 and the latter as B.n$_s$=4 for short.

There are 3 sets of simulations, each with different random seeds for the initial conditions. Each set has 7 target luminosity (or mass) bins, ranging from 1/8 to 8 L* and increasing by factors of 2. Each bin contains 8 groups, for a total of $3 \times 7 \times 8 = 168$ simulations, of which $3 \times 7 \times 2 = 42$ are mergers of spirals with equal masses, while the remaining 126 are sampled from a realistic luminosity function. Since each simulation is run twice (with different spiral bulge profiles), there are nominally 336 simulations, but only 168 different sets of galaxy masses and orbits.

Each group has a number of galaxies between $N_{min} = 3$ and $N_{max} = 2+(5/6)\times 10 \cdot (L/L*)^{1/2}$. Within each group luminosity bin, the number of galaxies in each simulation varies linearly from the minimum (3) to the maximum, so that L* groups have between 3 and 10 galaxies and the largest groups have 25 galaxies. This range of galaxy numbers roughly covers the number of bright galaxies one would expect in poor groups. The mass range covered by the groups is $2.0 \times 10^{11} M_\odot$ to $3.0 \times 10^{13} M_\odot$.

We further subdivide the sample into groups with relatively many mergers (the Many-merger or "M" subsample) or relatively few (Few-merger or "F"). The groups in each mass bin with the three lowest initial galaxy counts are part of the F subsample, while the groups with the three largest initial galaxy counts qualify for the M subsample. Because the maximum number of

Table 2.1: Ranges of numbers of galaxies initially in each group

Group Mass (M*)	N_{min}	N_{max},F	N_{min},M	N_{max}
1/8	3	3	4	4
1/4	3	4	5	6
1/2	3	5	6	8
1	3	6	7	10
2	3	7	9	13
4	3	9	12	18
8	3	12	16	25

Each simulation sample is divided into those groups with relatively Few (F) or Many (M) galaxies for their mass, with three groups in either category per mass bin. The minimum and maximum number of galaxies in a group is listed, as well as the maximum for the F and the minimum for the M subsamples.

galaxies changes in each mass bin, the dividing line between the Many-merger and Few-merger subsamples depends on mass and is not a fixed number of galaxies or mergers. Each mass bin also contains two groups with equal-mass galaxies ("Eq"), one with three galaxies ("F-Eq") and the other with the same number of galaxies - N_{min},M - as the fourth group in the LF-sampled simulations (i.e., the group in the 'M' subsample with the fewest galaxies). The number of galaxies in a representative number of groups is listed in Tab. 2.1.

2.1.2 Group Configuration

Once the target luminosity and number of galaxies are selected, each group is initialized through the following steps:

1. Randomly select luminosities for all of the galaxies from a restricted range of the spiral galaxy luminosity function.
2. Set the maximum radius within which to spawn galaxies, $r_{max} = 2r_{200,z=2}$.
3. Place the most luminous galaxy in the centre.
4. Place all other galaxies by descending order of luminosity.
5. Compute the group's gravitational potential energy.
6. Assign random velocities to the satellite galaxies, applying an inward and radial bias and re-selecting any velocities with $v > v_{esc}$.

Galaxy luminosities are randomly sampled from the inclination- and extinction-corrected spiral luminosity (Schechter) function of Shao et al. (2007). For the r-band, the faint-end slope $\alpha = -1.26$ and $M*_r = -20.99 + 5\log(h = 0.71)$, or $M*_r = -21.73$, which is nearly identical to our standard M31 model's absolute magnitude of $M_r = -21.69$. We set a minimum luminosity of $0.01L*$ for the spirals, as we do not expect the luminosity function to continue to arbitrarily

faint magnitudes. Luminosities are drawn from a restricted range of the luminosity function with a width equal to $(N_{galaxies} + 2)/10$ dex, such that the integral under the curve is equal to the target group luminosity. This limited range produces groups with smaller magnitude differences between the brightest central galaxy and the next brightest satellite, making major mergers more likely - especially in groups with few galaxies. We avoid simulating groups with a single luminous spiral and several much fainter satellites, since these groups would only produce relatively minor mergers and would be unlikely to produce ellipticals. The 42 groups with equal-mass spirals ("Eq") are not sampled from an LF and instead have exactly the target luminosity, split evenly between three or a larger number of galaxies.

Once a luminosity is determined for each group galaxy, the galaxies are randomly assigned locations within the group in descending order of luminosity. The most luminous galaxy is placed at the centre of the halo, while subsequent galaxies are given a random radius with a likelihood inversely proportional to radius, i.e., $\rho \propto r^{-1}$, and with $r < r_{max}$, where $r_{max} = 2r_{200,z=2}$. $r_{200,z=2}$ is the radius at which a volume enclosing the total group mass has a mean density of 200 times the critical density at z=2. Next, a random polar and azimuthal angle is given. The minimum distance between galaxies is set by $0.5 \times r_{max} * (M_{galaxy}/M_{group})^{1/3}$, which allows galaxy halos to be in contact but not overlap significantly. The radial distribution of satellites is perhaps somewhat shallow. The r^{-1} density profile only partly counteracts the r^3 increase in volume with radius, and so it is likely that more satellites are initially placed within 1–$2r_{200}$ than would be found in cosmological simulations (see e.g. the satellite radial PDFs of Khandai et al., 2014). However, the group does collapse rapidly, so most satellites do not remain at such large distances from the central galaxy for very long.

Because the sampling width of the luminosity function ranges from 0.3 to 2.7 dex, depending on the number of galaxies, the mass ratio between the central galaxy and its satellites is not necessarily large, and so some of the first mergers can be classified as major rather than minor (mass ratio 3:1 or smaller). However, since galaxies are placed in descending order by mass, with the most massive galaxy in the centre, it is generally the case that the most massive galaxies are merged first, within a few billion years. Subsequent mergers of the less massive satellites typically have larger mass ratios of 10 or higher.

All of the galaxies are given preferentially inward and radial orbits. The group itself is sub-virial to ensure collapse and no satellite is given a speed $|v| > v_{escape}$. This is accomplished by giving each group a target virial ratio $Q_{target} = -2T/W = 0.5$, where W is the gravitational potential energy of the group. This is equivalent to a zero-energy parabolic orbit in a galaxy pair, where T=-W. The group velocity dispersion is determined by Q_{target}: $\sigma = (-Q \times (W/a)/M)^{0.5}$, where $a = 3s - 2\beta$ and β is an orbital anisotropy parameter. Each galaxy's radial velocity is then $\sigma * s$, where s is a number randomly selected from a unit Gaussian centred on $s = -0.5$. On average more than 70% of galaxies will have inward radial velocities. The azimuthal and polar velocities are given by $\sigma(s \times (1 - \beta)^{0.5})$, where $\beta = 0.5$ directs most of the velocity of the galaxy radially. Because groups can have as few as three galaxies, all with randomly sampled

positions and velocities, the actual group virial ratio Q can be significantly smaller or larger than the target value of 0.5.

Because radial velocities are sampled from a Gaussian distribution centred on $s = -0.5$, a significant number of satellite galaxies could have relatively small radial velocities. Thus, there is initially not as large of a radial bias as found for infalling satellites by Wetzel (2011). However, the inwards bias means that most galaxies begin falling into the group right away and picking up speed. Those satellites initially more distant than r_{200} will have larger (negative) radial velocities once they cross r_{200}. The seeding of galaxies in order of mass also promotes early, rapid consecutive mergers, as found by Moster et al. (2014). Thus, the orbits of individual galaxies are not inconsistent with those in cosmological groups.

In two of the three sets of simulations, the initial conditions in groups of similar mass (1/8 to 1/2, 1 to 4, and 8L*) are correlated, in the sense that galaxy positions are seeded in the same order (but not individual galaxy masses or orbits). This is intended to test the effect of adding additional galaxies to otherwise similar initial conditions. In the third set, all of the initial conditions are completely randomized. We note no statistically significant differences between the partially and completely random initial conditions for the relations presented in Chapter 3, but some differences are reported in Chapter 4 (specifically Appendix C.2).

Finally, each galaxy has its own massive, extended dark halo. In practice, the these individual halos overlap in their outer regions, leaving little to no "empty" space between galaxies. We have also experimented with including a separate dark matter halo for the group, not associated with any particular galaxy, but find that group galaxies then (unrealistically) merge with this invisible dark halo rather than with each other.

2.1.3 Galaxy Models

Initial spiral galaxy models are created using the GalactICS galaxy initial condition code (Widrow & Dubinski, 2005). This code generates equilibrium models of galaxies with a bulge, disk and halo through spherical harmonic expansions of analytic potentials. Although the models begin in equilibrium and do not require additional time to settle, they have been tested in isolation. All models remain (statistically) unchanged for at least a Hubble time, even at the lowest resolution (55,000 particles per galaxy), which the vast majority of galaxies exceed.

The models are similar to the "M31c" model of Widrow & Dubinski (2005), with some parameters adjusted following the approach of Widrow et al. (2008) to better reproduce the surface brightness profile and rotation curve of M31. M31 was chosen as a well-studied, nearby spiral having a sufficiently massive bulge to produce concentrated merger remnants. The models are bar-stable and contain a massive, non-rotating bulge, as well as a dark matter halo. The first variant uses a nearly exponential bulge with $n_s = 0.93$, which will be referred to as exponential for convenience. A second variant uses an $n_s = 4$ de Vaucouleurs (1948) or "classical" bulge with otherwise identical parameters.

The halo density profile is designed to match an NFW (Navarro et al., 1997) profile at

large radii and smoothly drop to zero at large radii. The halo has a 6.07 kpc scale radius, $\rho \propto r^{-1}$ inner cusp and $r^{-2.3}$ outer slope, an outer radius of 300 kpc (beyond which the density steadily drops, reaching zero at 400 kpc) and a total mass of 1185 units, or $2.75 \times 10^{12} M_{\odot}$. This profile produces a 30:1 ratio in dark:baryonic (stellar) mass, which is a factor of two larger than estimates for M31 and the Milky Way (e.g. Watkins et al., 2010), but smaller than global estimate for the universal dark:stellar mass ratio.

The disk has a 5.8 kpc scale radius and a 750 pc sech^2 scale height, equivalent to a 375 pc exponential scale height. The disk is cut off past 6 scale radii, or 35 kpc, for a total mass of 25 simulation units, or $5.8 \times 10^{10} M_{\odot}$. We adopt a disk stellar mass-to-light ratio of $(M/L_r)_D = 3.4$.

Each bulge has a 1.5 kpc effective radius. The exponential bulge and de Vaucouleurs bulge have masses of 14.75 units ($3.4 \times 10^{10} M_{\odot}$) and 15 units ($3.5 \times 10^{10} M_{\odot}$), respectively. The bulge-to-total mass ratio B/T_M is about 33% in both models, larger than the 20-30% estimate for the R-band B/T ratio B/T_R in M31 (Courteau et al., 2011). The models could compensate by using a lower $(M/L_r)_B$; however, the bulge kinematics favour a lower value of 1.9 (Widrow & Dubinski, 2005), which we adopt here. While $(M/L_r)_B$ does not affect the simulations, the resulting bulge-to-total light ratio B/T_r is 50%, and so mock images are more strongly weighted to bulge stars than disk stars.

The rotation curve for both models is shown in Fig. 2.1. The bulge dominates within the inner 4-5 kpc and the halo thereafter, with the disk contribution typically half that of the halo. The non-maximal disk is both consistent with recent observations of spiral galaxies (see van der Kruit & Freeman (2011) for a review) and also promotes bar stability. Although the exponential bulge can be torqued into a bar, the intrinsic bar stability means that any remnant properties such as rotation are a result of the merging process and not secular instabilities.

To scale our model to different masses, we multiply all masses by a factor m while retaining the same M/L_R. Velocities are scaled by $m^{0.29}$, assuring that the galaxies follow a Tully-Fisher relation $V \propto L^{0.29}$ (Courteau et al., 2007). To maintain virial equilibrium ($R \propto M/\sigma^2$, or, $\log(R) \propto \log(M) - 2\log(\sigma)$), particle distances from the centre of the galaxy are scaled by a factor of $R \propto M/\sigma^2 \propto m^{1-2\times0.29}$, or, $R \propto m^{0.42}$. As a result, surface brightness scales weakly with mass - $L/R^2 \propto m^{0.16}$ - consistent with the Tully-Fisher relation's assumption of nearly constant effective and/or central surface brightnesses. We do not incorporate scatter into the input galaxy scaling relations, so that scatter in the merger remnant scaling relations is both a lower limit and dependent on the formation process (merging) and bulge profile, rather than an additional input parameter like the Tully-Fisher relation's scatter. Similarly, we use the same bulge fraction for all galaxies. We deliberately avoid using bulgeless disks, as existing literature (e.g., Hernquist (1993)) shows that bulgeless disk mergers do not produce sufficiently high central densities. We will further discuss the implications of these choices in §3.2.

The lowest resolution model has 5,000 bulge, 10,000 disk and 40,000 halo particles, for a 1:2:8 bulge:disk:halo ratio, and 15,000 stellar particles. More massive galaxies have larger particle counts by factors of two, up to a maximum of 480,000 disk particles. Most groups have

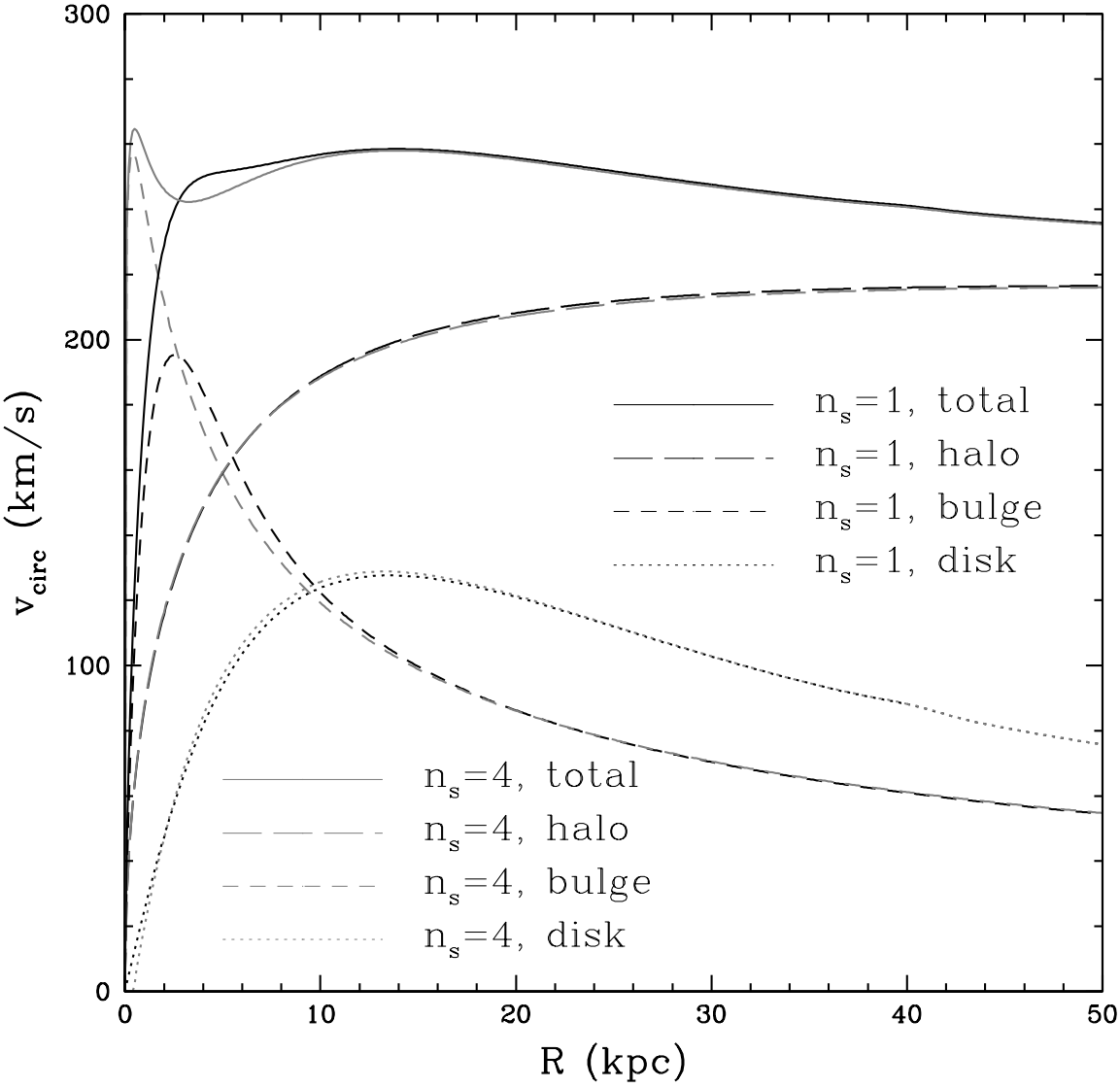

Figure 2.1: The rotation curves of the M31 models used in these simulations. The rotation curve is dominated by the bulge within the inner 5 kpc and by the halo thereafter. The more concentrated $n_s = 4$ bulge also produces a sharper, inner peak in the rotation curve at 1 kpc.

at least three galaxies with 60,000 stellar particles and only a few tens of galaxies have fewer than 30,000 stellar particles. By scaling resolution this way, stellar particles all have the same mass within a factor of three, while dark particles are not more than 10 times more massive than star particles, limiting spurious numerical artefacts. Appendix A.2 discusses the effects of numerical resolution in greater detail; in summary, this resolution is more than sufficient for the more massive galaxies and adequate for the least massive satellites.

2.1.4 Simulation Code and Parameters

Each group is simulated for 10 Gyr with the parallel N-body tree code PARTREE (Dubinski, 1996). Figures 2.2 and 2.3 show a typical evolution for one such group. The simulations use 52,000 fixed timesteps of 0.02 units - about 195,000 years - and a softening length (spatial resolution) of 100 pc. We use an opening angle of $\theta = 0.9$ with forces computed to quadrupole order. While this opening angle is somewhat larger than typical values of 0.7 to 0.8, PARTREE calculates forces between nearby particles in different trees directly, eliminating the source of the largest force errors. For $\theta = 1.0$, PARTREE has been shown to produce median force errors under 0.2%, with 90% of force errors under 0.5% (Dubinski, 1996); force errors with $\theta = 0.9$ are considerably smaller.

2.2 Analysis

The simulations are analysed at three different epochs after 5.0, 7.7 and 10.3 Gyr, which correspond to formation redshifts of about 0.5, 1, and 2, respectively, if one assumes that the group formed at t=0 Gyr. Since the only redshift-dependent parameter in the initial conditions is the maximum radius of the group, analysis of the same group at different epochs is equivalent to assuming a different age for the group. Also, since galaxies are given an initial separation sufficient to prevent their halos from overlapping significantly, it typically takes 1-2 Gyr for the first mergers to occur. Groups with fewer galaxies complete the merger process after another 2-3 Gyr and so are not sensitive to the choice of formation time, while groups with more galaxies continue slowly accreting lower-mass satellites and growing even after 10 Gyr. Although we do not introduce additional galaxies into the simulation to mimic cosmological accretion, we note that the long merging time for less massive galaxies still allows for late-time mergers in richer groups.

2.2.1 Analysis Pipeline

Once the simulations are complete, we create mock r-band photometry and kinematics of each group at the three different epochs, placing the group at a mock redshift of 0.025 (about 100 Mpc away). In brief, we create SDSS-like photometry of the central galaxy out to 8 effective radii, including a sky background and appropriate signal-to-noise ratio. We use GALFIT (Peng et al., 2002, 2010) to fit a single Sersic (1968) profile to each galaxy. We also use GALMORPH

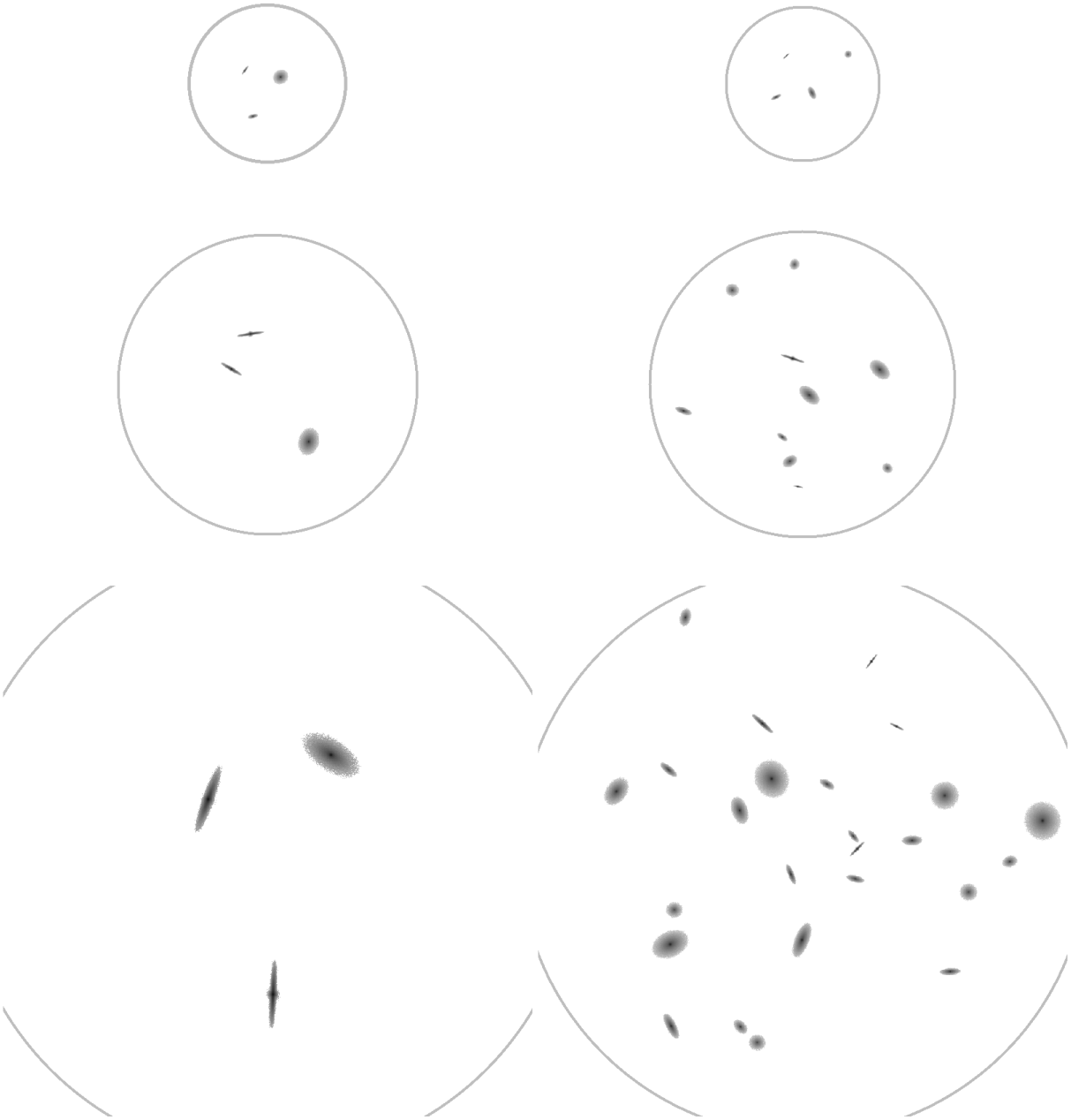

Figure 2.2: Logarithmic surface density maps of the initial conditions for four of the simulated groups. The groups have a nominal total luminosity of 0.125, 1, and 8 L* in each row respectively. The number of galaxies in each group varies from three (leftmost column) to a mass-dependent maximum N_{max} (rightmost column). The maximum radius within which galaxies are spawned (equivalent to $2R_{200,z=2}$) is shown in grey. Images are 1 Mpc across.

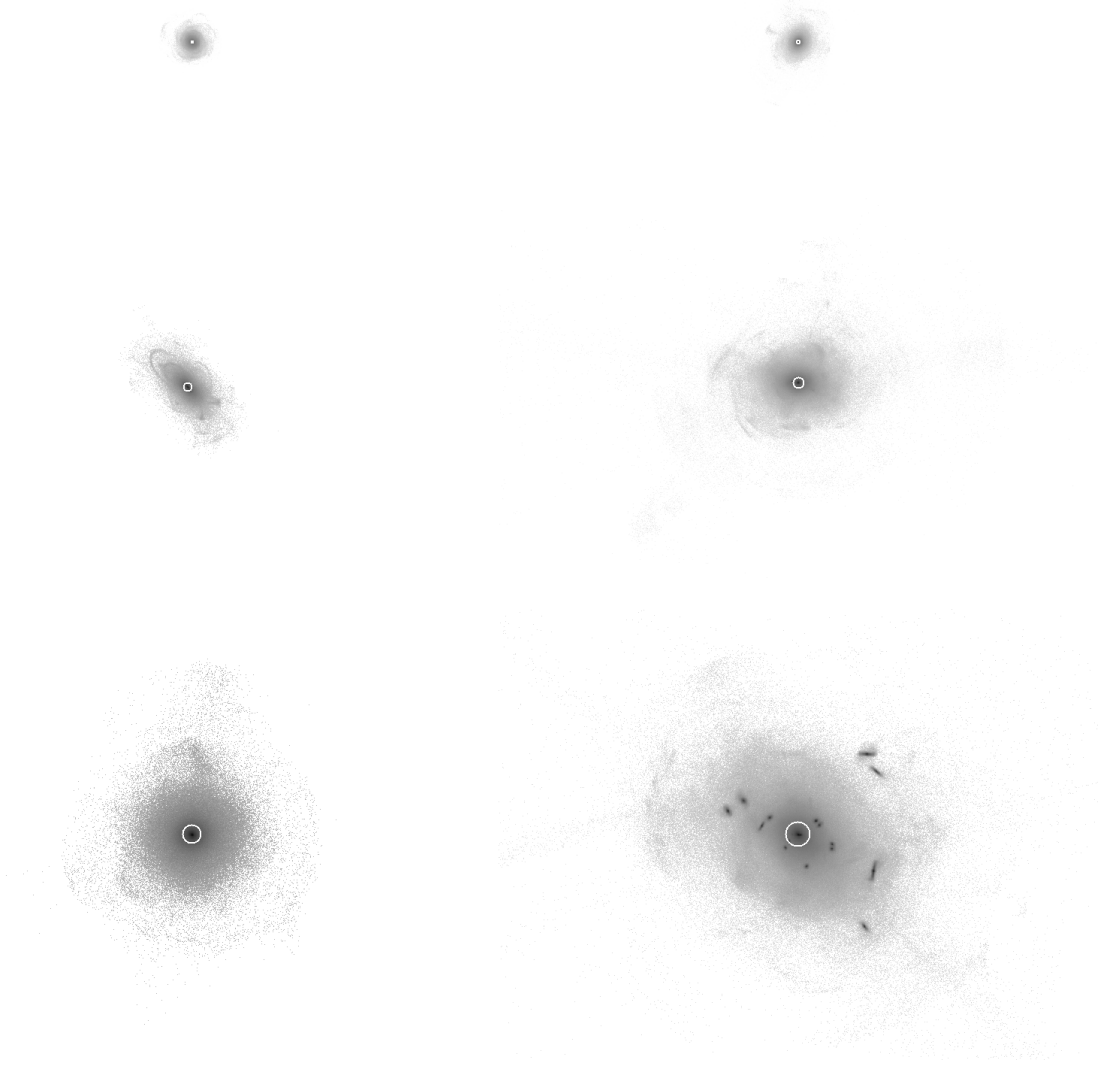

Figure 2.3: Logarithmic surface density maps of nine of the simulated groups after the full simulation time of 52,000 steps (about 10 Gyr). The groups shown are the same as in Fig. 2.2. The effective radius of the central galaxy in each group is shown in white. Images are 1 Mpc across, as in Fig. 2.2.

(Hyde & Bernardi, 2009a) to fit a de Vaucouleurs profile to the sky- and satellite-subtracted image, both for comparison to more general Sersic fits and to the de Vaucouleurs fits of Hyde & Bernardi (2009b). Finally, we create spatially resolved kinematics at the same scale, and use these maps to measure kinematical quantities within the central region and the effective radius of the central galaxy. Although our simulations do not resolve faint satellites particularly well, our pipeline is able to recover the properties of the central ellipticals with precision comparable to SDSS observations.

Simulations are processed with our own imaging pipeline, which is intended to create images of the central galaxy in each group equivalent to those produced by the SDSS. We convert mass to luminosity to create nominal r-band images, using fixed stellar mass-to-light ratios for the bulge and disk components. We then extract a one-dimensional profile of the central galaxy in circular bins, masking out the central regions of satellite galaxies. A single Sersic profile is then fit to produce a rough estimate of the effective radius of the central galaxy ($R_{e,est}$).

Next, we create a FITS image out to $8R_{e,est}$ around the central galaxy. The image is smoothed by a point spread function (PSF) with a full-width at half-maximum (FWHM) of 1.43 arcseconds, typical for SDSS r-band observations (Stoughton et al., 2002; Abazajian et al., 2009). Galaxies are imaged at a mock redshift of $z_{obs} = 0.025$, typical for the SDSS spectroscopic sample used in (e.g. Hyde & Bernardi, 2009a; Nair & Abraham, 2010). Fig. 2.4 shows an example image of a typical galaxy, along with a Sersic profile fit (as will be described shortly). The pixel scale is identical to that used by SDSS, 0.396 arcsec/pixel. Most importantly, we add a sky background with both a mean surface brightness and variations comparable to SDSS observations. In the r band, the mean sky value is 20.86 and variations are Gaussian distributed with a standard deviation of 2.65%, equivalent to the SDSS *asinh* zero-flux magnitude of 24.80 (which itself was chosen to be approximately 1-sigma of typical sky noise). We also create maps of the projected dark matter distribution using the same pixel scale (but no PSF).

In addition to photometry, we create kinematical maps of the first four moments of the luminosity-weighted velocities of particles in each pixel (velocity, rms velocity dispersion σ, and v3 and v4). Examples velocity and velocity dispersion maps are show in Fig. 2.5. Although we do smooth these maps by the same PSF and use the same pixel scale as the photometry, we do not add a sky background or any instrument-specific noise. We do not perform any fitting to the kinematic quantities, choosing rms velocity dispersions rather than fitting any profiles, and so the kinematical maps remain largely instrument-agnostic beyond the choice of pixel scale and PSF. The maps can then be used both to measure central velocity dispersions and spatially resolved kinematics, comparing to SDSS and ATLAS3D respectively.

Finally, we create an error map for the photometry, which is used to perform χ^2 minimization in fitting profiles to the galaxies. The error is the square root of the luminosity in each pixel multiplied by some constant factor, which scales the signal-to-noise ratio across the image. The constant itself is simply related to the image exposure time, given a certain zero-point equivalent to 1 count per second (for SDSS r-band, this is about 26.7) and mean sky variation.

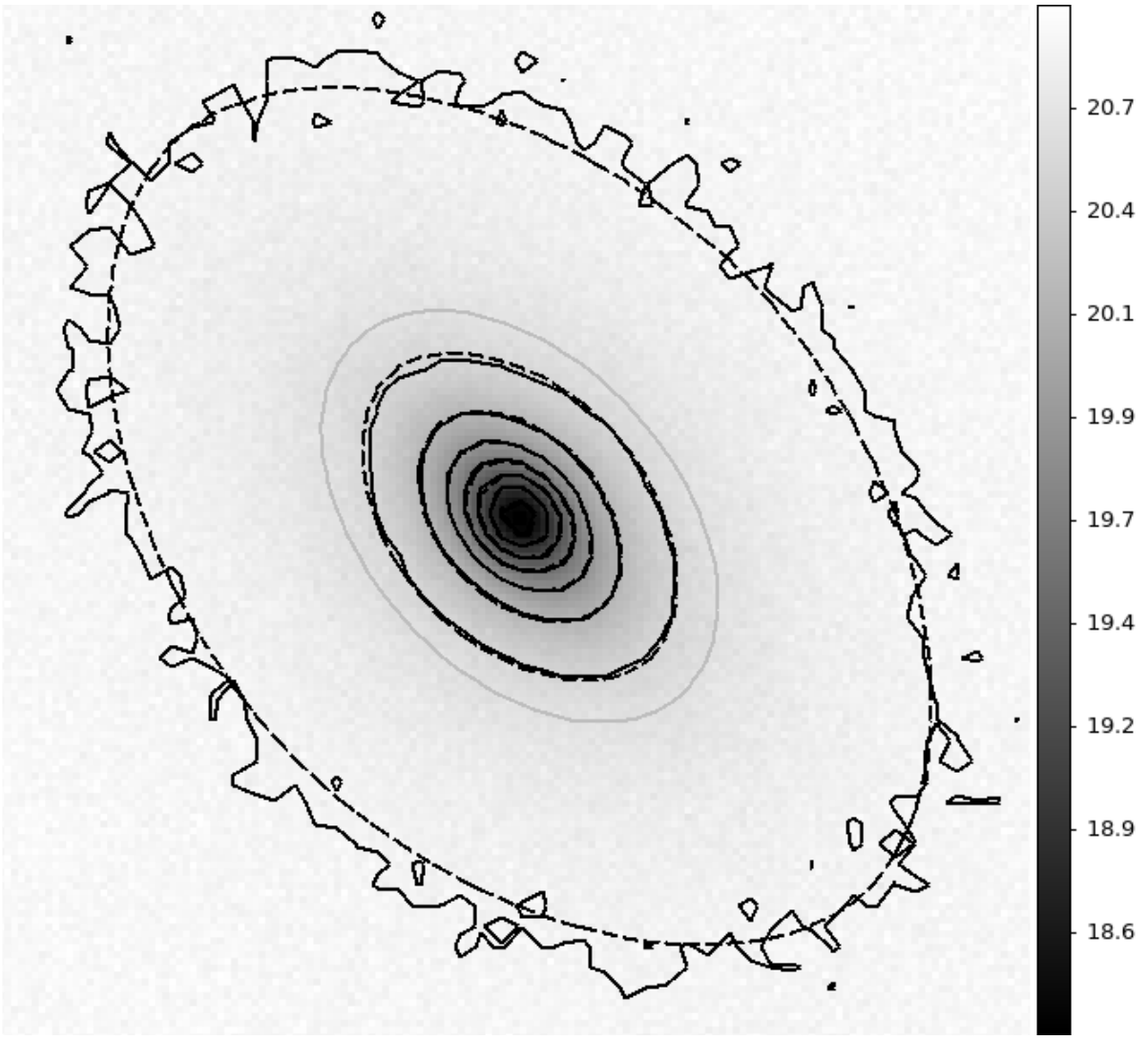

Figure 2.4: Example mock image of the major axis projection of the central galaxy from a typical L* group after 10 Gyr of simulation. The image shows SDSS-equivalent r-band photometry down to the mean sky level, overlaying contours from the image itself (dashed, black) and the best fit GALFIT Sersic model (solid, black). The gray ellipse shows the effective radius but with no boxiness parameter altering its shape. The image is 29 kpc or 150 SDSS pixels across.

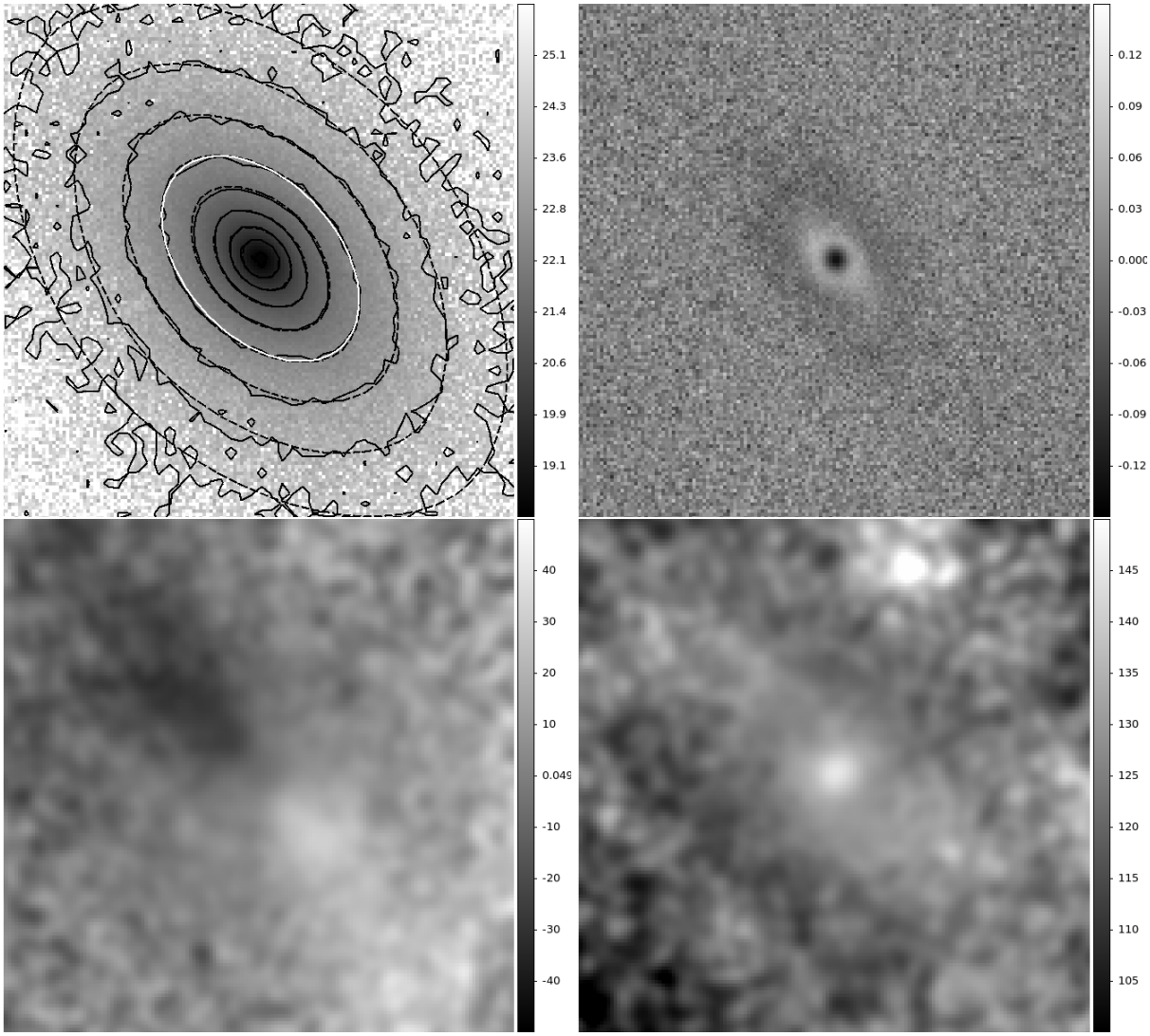

Figure 2.5: Example images of a typical galaxy. The leftmost image is as Fig. 2.4 but now sky subtracted. The remaining panels show the GALFIT Sersic model residuals ((image - model)/image) at top right, and the velocity and velocity dispersion maps in units of kms^{-1} (bottom left and right, respectively). All images are 29 kpc or 150 SDSS pixels across, as in Fig. 2.4.

This scheme contrasts with, e.g., Feldmann et al. (2011), and other simulations which use the square root of the number of particles in each pixel as the error. The per-pixel errors do not scale directly with the resolution of the simulation but should instead converge with increasing resolution. Similarly, setting a non-zero floor to the error map ensures that pixels with no signal are not ignored in the fit, which is necessary since the absence of a signal is meaningful.

For each galaxy, we create images in 10 randomly oriented but evenly spaced projections. These are the ten projections passing through opposite faces of a regular icosahedron, but arbitrarily rotated with respect to the central galaxy. We also use the three projections corresponding to estimates of the principal axes of the central galaxy. We fit every galaxy in the image with a single Sersic profile using GALFIT; an example of the residuals from such a fit is shown in Fig. 2.5.

The Sersic profile defines a total luminosity L for the galaxy, as well as an effective radius R_e containing half of the light, and has been shown to be a suitable parameterization for the surface brightness profiles of elliptical galaxies (for a thorough review, see Graham, 2013). A circularly-symmetric Sersic profile can be written in several ways, but a convenient formulation is:

$$\mu(R) = \mu_{R_e} + 2.5b_n/\ln(10)[(R/R_e)^{(1/\mathrm{n_s})} - 1], \tag{2.1}$$

where the free parameters are the Sersic index $\mathrm{n_s}$, the effective half-light radius R_e, and the surface brightness μ_{R_e} at this radius. μ_{R_e} is not to be confused with μ_e, our notation for the mean surface brightness within R_e. b_n is an analytic function of $\mathrm{n_s}$ meant to ensure that R_e contains exactly half of the luminosity L. The Sersic index n_s reduces the surface brightness profile to an exponential for $\mathrm{n_s} = 1$ and the classic de Vaucouleurs $R^{1/4}$ profile for $\mathrm{n_s} = 4$. A full reference to Sersic-related quantities is available in Graham & Driver (2005).

The two-dimensional ellipsoidal fits have three main additional free parameters: an ellipticity ϵ (which does not vary with R), a position angle, and a boxiness parameter C0. The two coordinates of the centre of the galaxy can vary as well, but typically do not change by more than a pixel from the initial guess. Only sufficiently large galaxies ($R_e < 20$ pixels) fit the boxiness parameter (C0). C0 allows for elliptical isophotes to vary from diamond-shaped (C0 < 0) to rectangular- or box-shaped (C0 > 0), but can be degenerate with the ellipticity for very small galaxies. For highly inclined disks with a bulge, fits with a negative C0 provide a better fit than an unmodified ellipse. The GALFIT fits also include a fixed sky background equal to the mean sky brightness. We do not allow for the sky value to vary, as doing so would result in over-fitting the sky, a common problem in observations. Since different surveys and even different data releases of the SDSS have employed various methods for fitting sky backgrounds, we opt to avoid the difficulty of reproducing each methodology and simply fit with the known mean sky value. This does not, however, remove the pixel-to-pixel variation in sky brightness, which sets the effective limiting surface brightness in the image.

We use the GALFIT fits to create a sky- and satellite-subtracted image of the central galaxy in each frame. This image is used to measure various quantities, including alternative

non-parametric half-light radii. We also use GALMORPH to fit a single de Vaucouleurs profile to this sky-subtracted image. This provides a direct comparison to the methodology used in Hyde & Bernardi (2009b), with the caveat that our use of GALFIT to fit the profiles of satellite galaxies may not match the exact methodology employed in masking nearby sources in SDSS or other surveys.

2.2.2 Photometric and Kinematic Measures

Sizes and luminosities of the central remnants are measured several different ways. The preferred luminosity measure is the total luminosity within the deconvolved model image of the central galaxy, roughly equivalent to model magnitudes in SDSS and other surveys. For comparison, we also measure several other sizes and luminosities, including non-parametric Petrosian radii (Petrosian, 1976) (see Abazajian et al. (2004) for the SDSS implementation and Graham et al. (2005) for analysis thereof). A thorough analysis of the suitability of these measures is presented in Appendix A.1.

Kinematical maps are used to measure the velocity distributions - mean velocities (for rotation measures), dispersions, and higher order moments. Generally, we use central dispersions within 1/8 R_e and rotation measures within R_e. Velocity dispersions in the central remnants do vary radially, generally dropping from peak central values. Integral field surveys such as ATLAS3D can measure dispersions out to 0.5 to 1 R_e, whereas fibre dispersions from SDSS are measured within fixed angular diameters, and hence variable fractions of R_e. Aperture corrections are often applied to fibre dispersions to convert them to a fixed fraction of R_e, with 1/8 R_e a typical choice for SDSS observations (Hyde & Bernardi, 2009a). However, we find that central dispersions are nearly identical to effective dispersions (within 1 R_e), with most galaxies lying on a linear relation and only a handful of outliers, so aperture corrections are not necessary for the simulations.

The central velocity dispersions in simulations can be artificially depressed by softening of the gravitational potential. We mask out the central 300 pc in projection to compensate, and measure central dispersions within 1/8 R_e where possible. For the few galaxies where 1/8 R_e is smaller than 300 pc, we enlarge the aperture by factors of 1/8 R_e until a reliable estimate is obtained.

2.3 Observational Data

Our simulation results are compared to three published data sets for nearby galaxies. The ATLAS3D survey (Cappellari et al., 2011, hereafter A3D) is a volume-limited integral field unit survey of the kinematics of 260 nearby early-type galaxies. A3D provides kinematical maps (Emsellem et al., 2011) with a pixel size about twice as large as that of SDSS. This is mitigated by the larger aperture and very low redshifts (z<0.01) of the sample as compared to our nominal mock sample redshift (0.025). Sersic profile fits are also available from Krajnović et al. (2012),

with photometry from a variety of sources but typically comparable to or better than SDSS.

Simard et al. (2011, hereafter S+11) published three different profile fits for over a million SDSS galaxies. We use the single Sersic decompositions for direct comparison and the free Sersic (bulge) plus exponential (disk) decompositions for diagnostic purposes. Although these fits were performed with a different code - GIM2D (Simard et al., 2002) - the fitting procedure is similar to our GALFIT fits. We select galaxies with spectroscopic redshifts $0.01 < z < 0.3$ to ensure availability of a reliable V_{max} volume correction term. We use the logarithmic median velocity dispersion between two sources - the SDSS DR7 and Princeton measurements (both included in DR7, Abazajian et al. (2009)). Stellar masses are based on the MPA-JHU DR7 catalogue [1], using fits to the multi-band photometry.

Detailed visual classifications for nearly 6,000 early-type galaxies from SDSS with z<0.1 are provided by Nair & Abraham (2010, hereafter N+10). Volume corrections are applied with the standard $1/V_{max}$ weighting scheme (Schmidt, 1968). Profile fits from this catalogue include Petrosian sizes from the SDSS pipeline (Stoughton et al., 2002) and Sersic fits from S+11. Although the original catalogue of N+10 contained over 14,000 galaxies, eliminating bad fits and unmatched/misclassified objects provides just over 11,000 galaxies, of which nearly 5,000 are early-types.

We exclude all SDSS galaxies with extreme velocity dispersions ($\sigma < 20$ kms^{-1}or $\sigma > 400$ kms^{-1}) or effective radii smaller than 0.3 kpc. Where visual classifications are available (A3D, N+10) we select galaxies with Hubble T-types (de Vaucouleurs, 1959) less than 0 as early-types. T-types less than -3 are included in the elliptical sample while the remainder are classified as S0s. The majority of the S+11 sample does not have visual classifications, other than the small subset classified by N+10. We adopt a series of empirical cuts similar to those of Dutton et al. (2011) to identify early-type galaxies, testing these against the N+10 subset. The early-type sample contains galaxies with $n_s > 1$, and – from the disk plus free n_s fits – r-band bulge to total luminosity ratio $B/T_r > 0.4$, disk inclination less than 63 degrees, and bulge $R_e > 0.5$kpc. Early-types must also have a spectroscopic eclass value less than -0.1 (see Yip et al. (2004), but note that the sign convention in SDSS is opposite), which selects galaxies with spectra consistent with a passive population. This early-type sample is subdivided into an elliptical subset, which imposes further cuts based on the single Sersic fits: g-band image smoothness S2 < 0.08, or g-band image smoothness S2 < 0.12 and $B/T_r < 0.6$. These cuts are similar to those suggested by Simard et al. (2009) to select early-type galaxies from morphology alone, but also serve to decrease contamination from S0s and early-type spirals in the elliptical sample. All galaxies not classified as early-type but meeting the dispersion and R_e cut are identified as spirals.

The samples obtained by applying these cuts to the N+10 catalogue are listed in Tab. 2.2. The elliptical sample is 86% complete. While it is only 61% pure, the contamination mainly comes from S0s and not spirals. No cuts appear to be able to reliably classify S0s, which

[1] Available at http://www.mpa-garching.mpg.de/SDSS/DR7/

Table 2.2: Morphological types of cuts used for the Simard et al. (2011) sample

S+11 Subsample	N+10 Es	N+10 S0s	N+10 Spirals
Es	1874	1095	93
S0s	98	350	323
Spirals	193	1265	5272
Unclassified	13	54	604
Total	2178	2764	6292

Each row lists the breakdown of visual morphological classifications from N+10 of each of the subsamples from S+11, which are based on empirical cuts on various parameters rather than visual classification. Empirical cuts generally produce complete but impure samples of ellipticals and spirals, with substantial contamination by S0s.

contaminate both elliptical and spiral samples. In principle, we could instead use the S+11 cuts on the N+10 sample rather than relying on visual classifications at all; however, visual classifications are repeatable and fairly robust (see Nair & Abraham (2010) for comparisons to previous classifications), and as seen in A3D, there are significant differences in rotational support between the elliptical and S0 population (Krajnović et al., 2012), even if no automated morphological classification can separate them.

Additional weightings are necessary to compare these catalogues to our own simulations, which probe a range of about 5 in absolute magnitude but have a nearly flat luminosity function. We produce r-band luminosity functions for each sample, then weight by the ratio of the simulated luminosity function to the observed one. Elliptical and S0 subsamples use all simulated galaxies versus E/S0 classifications from observed catalogues - i.e., we do not morphologically classify simulated merger remnants. This weighting procedure turns each observational sample into a catalogue with equal numbers of galaxies at each luminosity, directly comparable to our simulations. Although the weightings are not vital for tight scaling relations like the fundamental plane, they are necessary for fair comparisons of weaker correlations and histograms marginalizing over luminosity.

2.4 Fitting Data

For fitting of all scaling relations, we perform linear least-squares regression using MATLAB's svd (singular value decomposition) function. Errors on the fit parameters are estimated from bootstrapping with random resampling, allowing for duplicates and using at least 1,000 bootstrapped samples. We also perform weighted fits to compensate for the shallower luminosity function of the simulated galaxies, using MATLAB's svds function. Scatter is measured as the root mean square (rms) of distances orthogonal to the best-fit relation.

Chapter 3

Morphology, Kinematics and 2D Scaling Relation Results

The necessary ingredients are now in place to begin comparing the results of the group simulations with nearby ellipticals. The simulated and observed catalogues both have structural and kinematic parameters compiled, including sizes, luminosities, ellipticities, Sersic indices, velocity dispersions, and in the case of ATLAS3D, measures of rotational support.

The results presented in this chapter are for the morphologies and kinematics of central group galaxies. Although we do fit satellites as well, this is mainly to exclude their contributions to the profiles of the central galaxies. Few satellite galaxies are sufficiently well resolved to recover sizes and Sersic indices accurately, but we only require their total luminosities to be recovered and subtracted from the central galaxy's profile. Unless otherwise noted, all radii measured with elliptical annuli are $\sqrt{(a \times b)}$, where a and b are the major and minor axis lengths.

3.1 Results

3.1.1 Morphology

Surface Brightness Profiles

While the actual profile fitting is done in two dimensions, we begin by showing the customary one-dimensional surface brightness profiles for four central merger remnants (Fig. 3.1) and corresponding model fits. Most profiles are well-fit by a single Sersic function, while in some cases a de Vaucouleurs model is insufficient to capture both the inner and outer extremes of the profile. For the majority of galaxies, the Sersic model reduced χ^2 values are no larger than 1.2 and thus are formally good fits to SDSS-quality imaging. For many (about 50%) of the galaxies, the de Vaucouleurs fits are sufficient, with χ^2_{red} less than 5% larger than for the Sersic fit - unsurprising, since many galaxies have n_s close to 4. However, we use Sersic fit parameters in all cases, both to maintain consistency with observational works, and because they generally

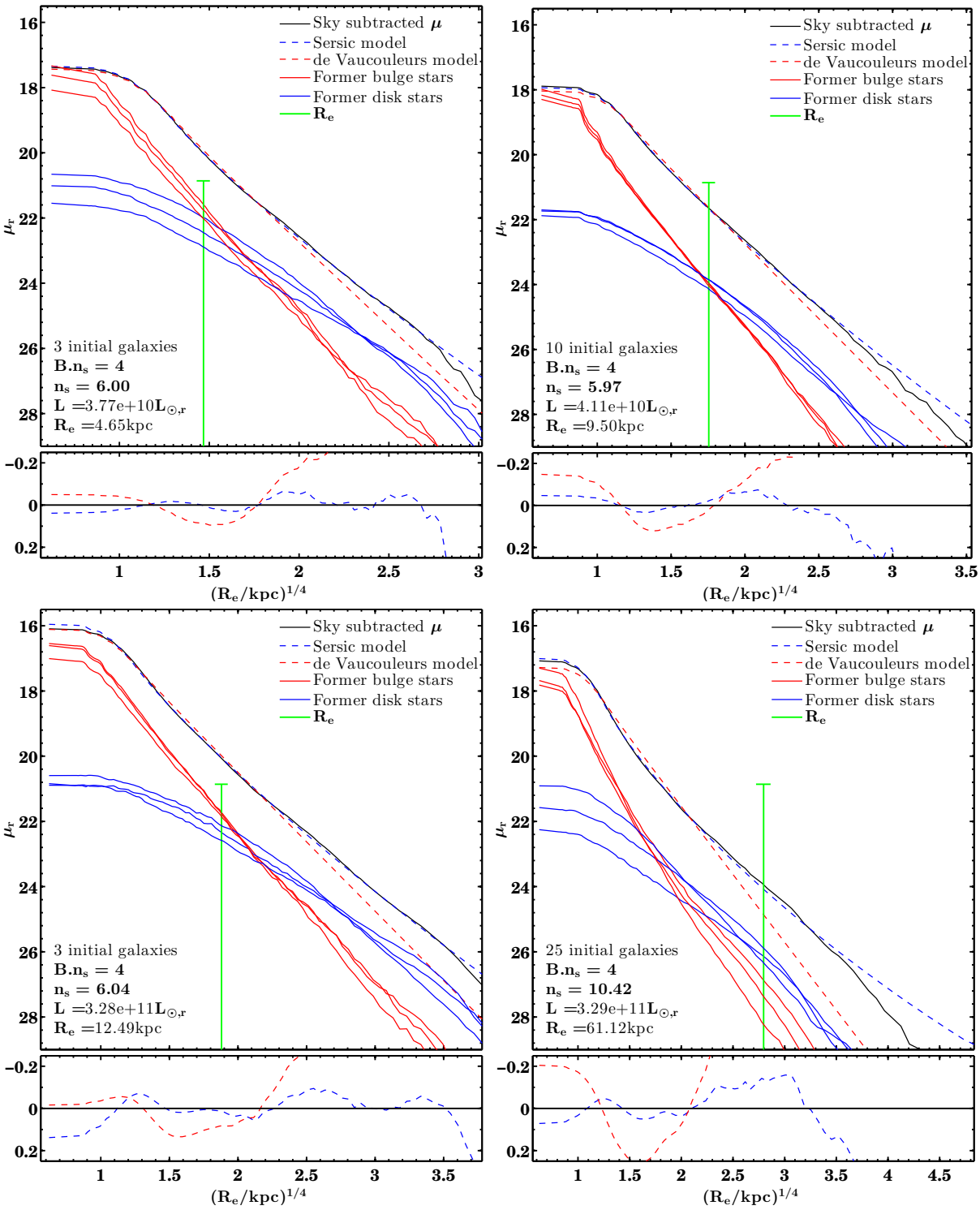

Figure 3.1: Surface brightness profiles of selected merger remnants. Four groups are shown - two each from the L* and 8L* bins. Also shown are contributions to the surface brightness profile from the former disk and bulge stars of the three most massive original spiral galaxies (without PSF convolution). The GALFIT Sersic model and GALMORPH de Vaucouleurs model fits are overlaid, along with residuals (data - model) in the insets. Finally, a green vertical line marks the effective radius, capped at the mean sky background level.

contain less structure in the residuals, with surface brightnesses rarely deviating by more than 0.1 mags/arcsec^2 from the observed profile. The largest deviations are seen in the outermost regions of the profile, but these are generally inaccessible to SDSS-quality imaging even with perfect sky subtraction. This point will be expanded on in §3.2. For the moment, it suffices to say that single Sersic profiles are good fits to the vast majority of merger remnants.

Fig. 3.1 also re-confirms a well-known early result, namely that stellar particles partly preserve their original binding energies even after a merger. This is seen by the fact that the inner regions of the surface brightness profiles are dominated by former bulge stars, most of which were originally tightly bound, while the outer profile is composed mainly of former disk stars, which were originally less tightly bound and which are also more susceptible to resonant stripping. The main consequence of this result is that any differences between stellar populations in original disk and bulge stars will be partially preserved in the merger remnant, a point which will also be discussed further in §3.2.

Sersic Indices

As detailed in §2.2.1, all galaxies are fit with a single Sersic profile. We begin by examining the Sersic indices of the central remnants. Figure 3.2 shows various histograms of the Sersic index distribution for the samples with bulge Sersic indices B.n$_s$=1, B.n$_s$=4 and B.n$_s$=all, where "all" is simply the sum of B.n$_s$=1 and B.n$_s$=4. Each individual bulge type produces a narrow distribution of Sersic indices. The B.n$_s$=4 sample's distribution is narrower and peaked at a larger value of $n_s = 5$ than the observational distributions. The B.n$_s$=1 sample's peak at $n_s = 3$ is significantly lower than those of N+10 and A3D ellipticals, and the distribution is narrower still than that of B.n$_s$=4. The combined B.n$_s$=all sample's n_s distribution is nearly bimodal due to this separation and approximately twice as broad as B.n$_s$=1 alone. By contrast, most observed distributions are unimodal, although the S+11 distributions show a larger peak of high n_s galaxies, which is only reproduced in the B.n$_s$=4 sample. There is also a hint of bimodality in the S0 distributions, which we have diminished by setting a lower limit of $n_s = 1$. The peak of the S0 distribution is best reproduced by the B.n$_s$=1, but, as will be demonstrated in §3.1.3, the remnants' rotational support is far lower than that of typical S0s. None of the simulation samples can reproduce the width of the observed S0 distributions.

Although each of the B.n$_s$=1 and B.n$_s$=4 samples are individually a poor fit to the elliptical data - particularly being too narrow of a distribution - the naive linear combination of the two (B.N$_s$=all) provides a better match. The B.n$_s$=all sample is also a better match to the elliptical distributions than the S0, the latter of which tend to smaller Sersic indices. While it is not a particularly realistic distribution - assuming that half of the groups in the universe contain galaxies with only exponential bulges while the other half contain de Vaucouleurs bulges - we will elaborate on the implications for more realistic bulge profile distributions in §3.2.

The difference in Sersic index between the Many- and Few-merger subsamples is small in the L.F.-sampled case but is maximized at about 0.5 for equal-mass mergers. Furthermore,

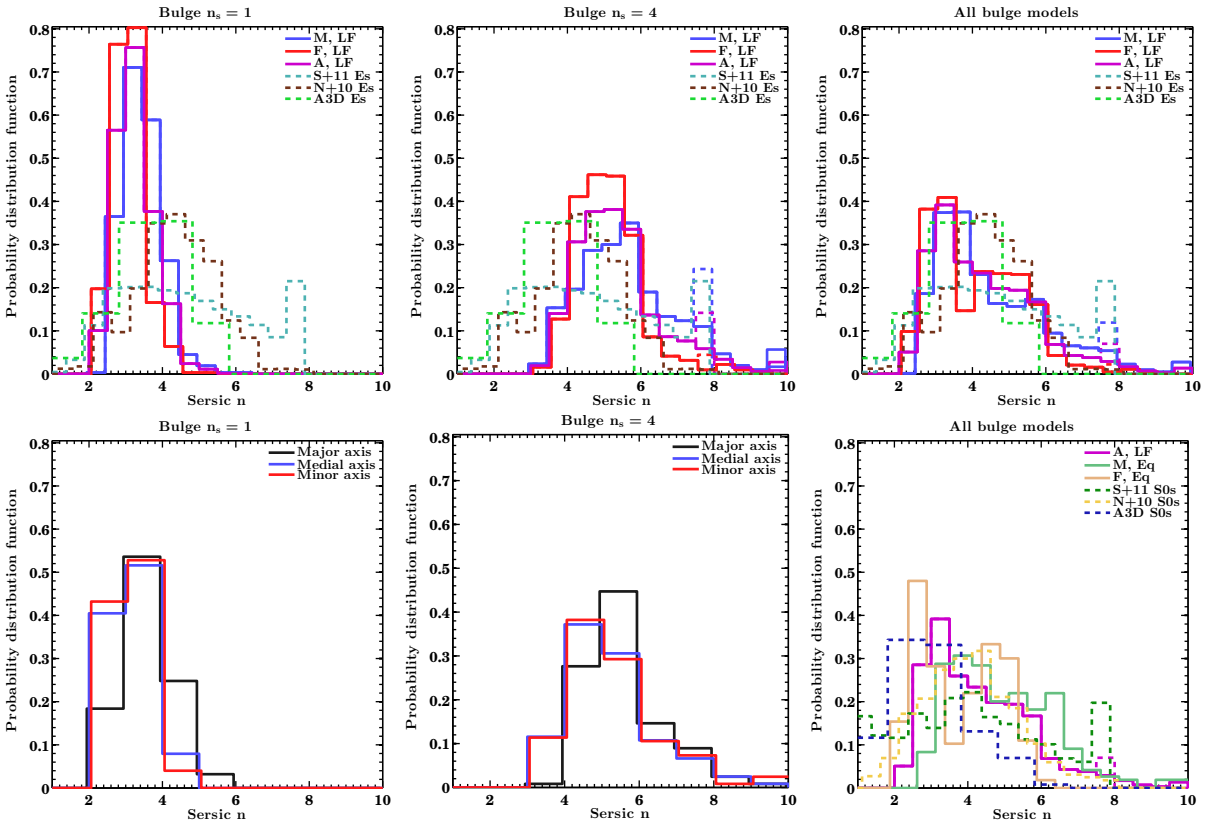

Figure 3.2: Sersic indices of central ellipticals. The top row shows comparisons to observed elliptical galaxies. The bottom right panel shows distributions for equal mass mergers as well, as compared to observed S0 galaxies. The bottom left and middle panels show principal axis projections only. Histograms are offset slightly on the x-axis to prevent overlap. Simulation data are shown with several maximum n_s: 8 (dashed line) for comparison with N+10 and S+11, and no limit (solid line) for the simulations themselves. B.n_s=4 mergers match observed ellipticals best, but a range of bulge types appears to be required to reproduce the observed distributions.

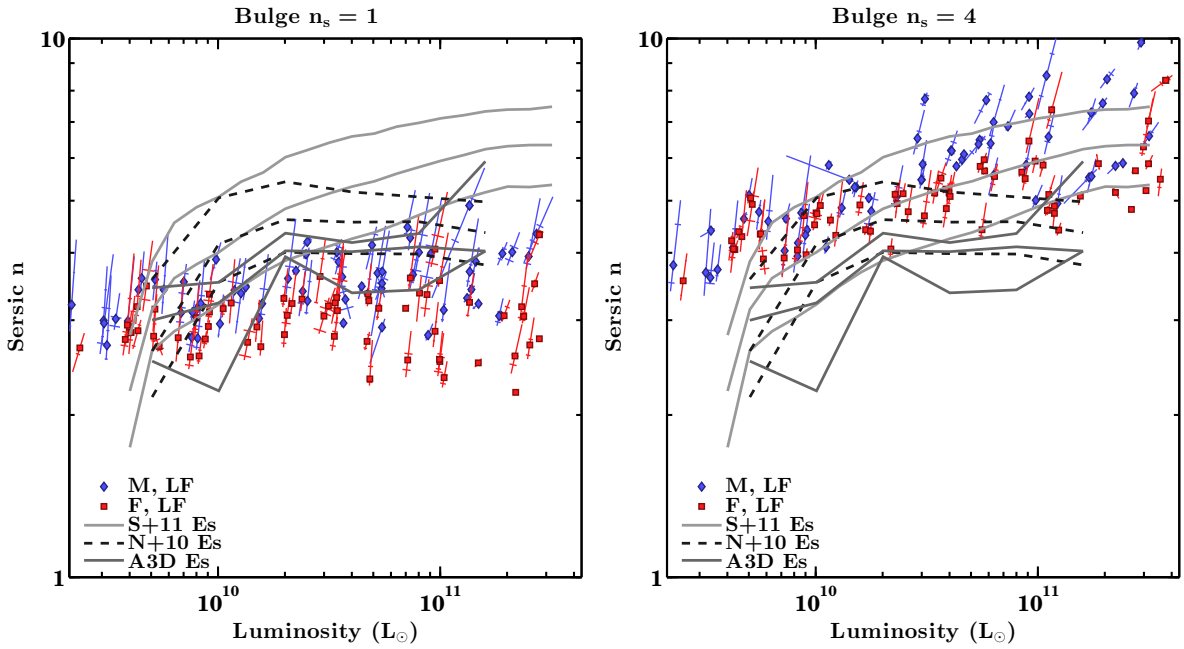

Figure 3.3: Sersic indices of central ellipticals by galaxy luminosity. Classical-bulge mergers (right) have larger n_s for the same initial conditions and show a strong dependence of n_s on galaxy luminosity, as with observed ellipticals from S+11 but unlike exponential-bulge mergers (left) and N+10 ellipticals. Different projections of the same group are shown as lines of best fit for clarity, with a single point marking the median projection. The length of the line shows the range of values from 10 random projections. Perpendicular lines cross at the 25th and 75th percentiles, with a length equivalent to the r.m.s. dispersion of points perpendicular to the line of best fit.

the distributions of the Few-, equal-mass merger remnants in the different bulge samples are sufficiently narrow that the combined B.n_s=all, Few-merger subsample is distinctly bimodal. Thus, it appears that multiple mergers are sufficient to broaden the distributions of remnant Sersic indices, but sampling progenitors from a realistic luminosity function can accomplish the same purpose, even with relatively few mergers.

Major axis projections of central remnants have systematically larger Sersic indices than the medial or minor axis projections (bottom left and middle panels of Fig. 3.2), with the peak of the distribution shifted by about 1. Medial and minor axes have nearly identical distributions, even though their ellipticities and semi-major axes are not necessarily the same. As Fig. 3.3 shows, the variation in Sersic index for a single galaxy over different viewing angles is not usually much larger than one (and often smaller), so projections aligned near the major axis appear to produce the largest n_s profiles.

Only B.n_s=4 mergers produce a correlation between luminosity and n_s, as shown in Fig. 3.3. This is partly a result of more massive ellipticals being produced by more mergers. In both B.n_s samples, Many-merger remnants tend to have larger n_s at fixed luminosity. However, in the B.n_s=4 sample, even the Few-merger subsample shows a small positive slope in Sersic index,

whereas the trend is flat or even slightly negative for B.n_s=1. The overall trend is dependent both on the initial bulge profile and the number of mergers. A positive dependence of merger rate on halo mass is a prediction of ΛCDM cosmology (e.g. Hopkins et al., 2010). Exponential bulges, however, are simply not concentrated enough to create merger remnants with $n_s > 4$, even with repeated merging. Thus, luminous ellipticals are unlikely to be the product of only exponential bulge mergers.

The degree of agreement between simulations and observations is difficult to judge, since the observational samples do not completely agree. The N+10 $n_s - L$ relation appears to flatten above $10^{10} L_\odot$. This could be due to the larger redshift range of the S+11 sample; however, we find that GALFIT-derived Sersic fits to mock images at higher redshift tend to fit lower Sersic indices, so this systematic trend would have to be reversed in observed ellipticals to explain the shift.

Ellipticities

Ellipticities of the remnants are on average slightly larger than observed elliptical samples but lower and more sharply peaked than S0s. Fig. 3.4 shows that there is only a small difference between the Many- and Few-merger subsamples, while there is about a 0.05 shift towards rounder remnants from the B.n_s=4 to B.n_s=1 samples. On the whole the distributions are not unreasonable, lying closer to observations of ellipticals than of S0s, while lacking the tail of highly elliptical shapes found in S0s. Although the Many-merger remnants are slightly rounder on average than the Few-merger, the difference is not large even in equal-mass mergers. This is somewhat surprising, considering that the progenitor galaxy orbits are nearly isotropic and should tend to produce spheroidal remnants as the number of mergers increases. We will elaborate on this point further in §3.2.

The intrinsic ellipticities of the remnants along the principal axis projections are also shown in the bottom left and middle panel of Fig. 3.4. The distributions are consistent with the remnants being triaxial, with the median value in each projection being both different than the others and greater than zero. The smallest axis ratios are found for the minor axis projection, which would be the case for ellipsoids closer to oblate than prolate. At the same time, the major axis projection ellipticities are significantly lower than the medial axis projection, as in prolate ellipsoids, so most of the remnants are triaxial rather than strictly oblate or prolate. Most galaxies have a medial axis ellipticity of around 0.4, with few being rounder than 0.2, indicating that almost all galaxies have a significantly shorter minor axis than the major axis.

In addition to having larger Sersic indices, brighter galaxies trend toward smaller ellipticities and rounder shapes (Fig. 3.5). This trend might be expected for more luminous galaxies with many mergers. If the orbits of the merging galaxies are isotropically distributed, the resulting remnant should be close to spherical. Such a trend is present in the simulations, although it appears stronger for the B.n_s=4 sample. Much of the scatter in the relation appears to be due to projection effects of the inherently triaxial simulated galaxies, although median ellipticities

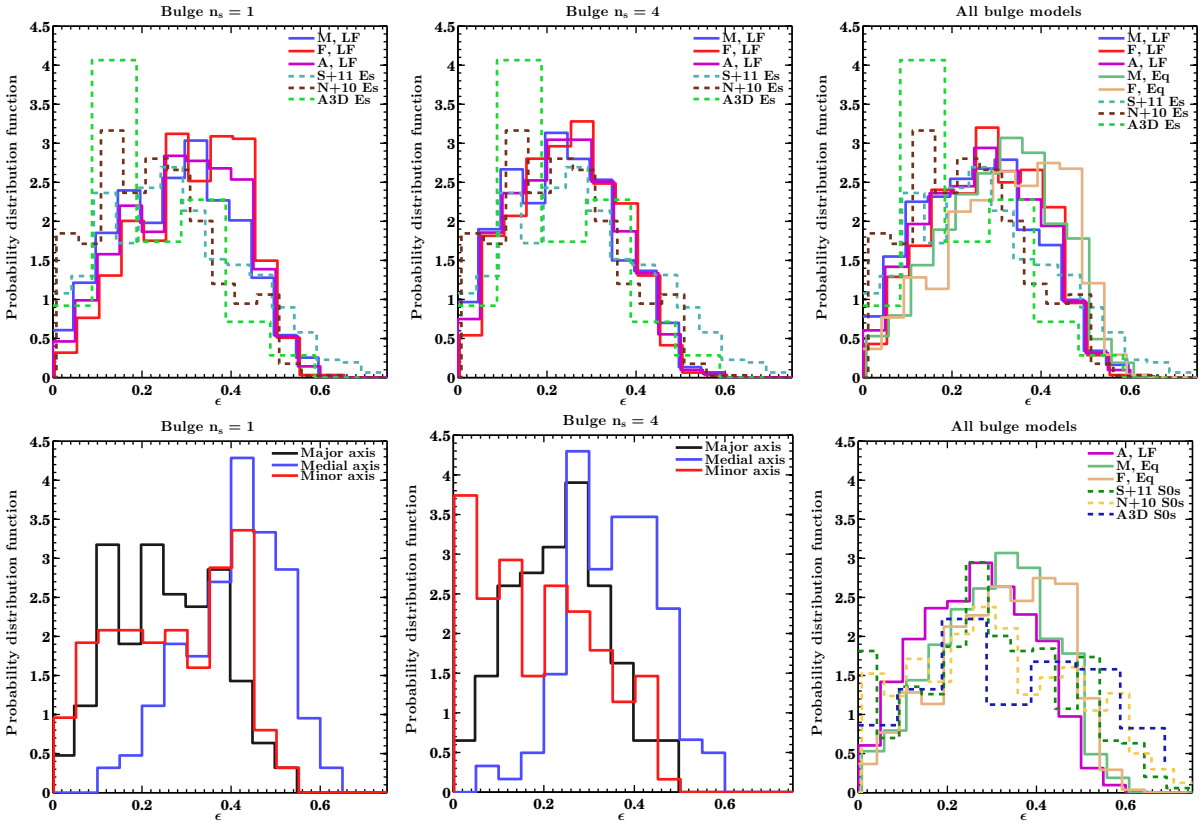

Figure 3.4: Ellipticities of central ellipticals, displayed in a similar format as Fig. 3.2. Top panels show randomly oriented, evenly spaced projections of various models compared with observed ellipticals. Bottom left and middle panels show principal axis projections only, while the bottom right panel shows equal mass mergers and compares with observed S0s. Ellipticities of central galaxies are largely consistent with the observed distributions, though slightly more flattened on average. Simulated galaxies are intrinsically triaxial, with the minor axis projection being the roundest on average. The remnants are rounder than observed S0s and lack a tail of highly flattened ($\epsilon > 0.5$) objects.

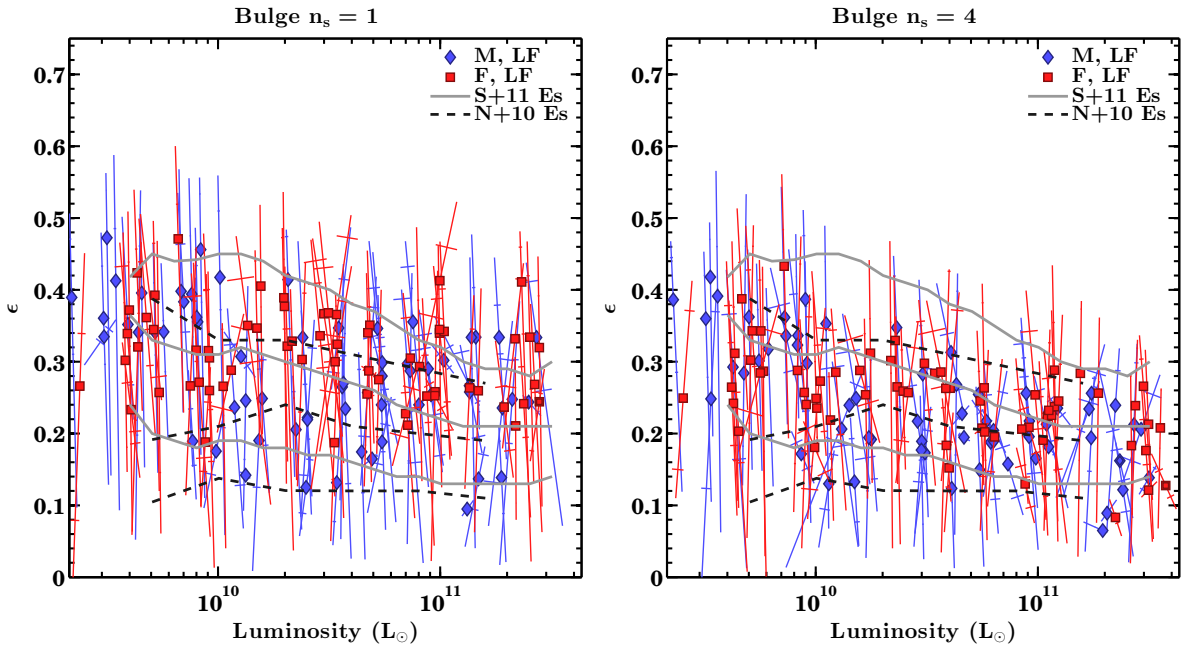

Figure 3.5: Ellipticities of central ellipticals by galaxy luminosity. Median ellipticities tend to decrease slightly with luminosity, both in simulations and observations, while B.n$_s$=4 mergers are slightly rounder on average. Projection effects for single galaxies are quite large, with spreads of 0.2-0.3 in ellipticity being common. Line types are as in Fig. 3.3.

show significant scatter as well. The B.n$_s$=1 sample also appears to have few very round ($\epsilon < 0.1$) remnants, especially at low luminosities.

3.1.2 Scaling Relations

Size-Luminosity/Stellar Mass and Kormendy Relations

Fig. 3.6 shows the Sersic model size-luminosity relation for principal axis projection of simulated galaxies after 10.3 Gyr, connecting otherwise identical groups with different spiral bulges. All relations have very small scatter. Part of the scatter is caused by the B.n$_s$=1 sample having smaller sizes (a real effect) and lower luminosities (partly a real effect, but largely systematic, as will be shown in Appendix A.1). Regardless, both projection effects and different progenitor bulge profiles contribute to the scatter in the relation.

Table 3.1 lists best-fit Sersic model size-luminosity relations for simulations and observations alike, obtained by least-squares minimization of the orthogonal scatter. In all of the simulation samples, the scatter is relatively small at about 0.1 dex. The scatter does not appear to be mainly due to projection effects or combining progenitors. Fits to major axis projections have similar scatter to the ten equidistant but randomly aligned projections. Similarly, though some groups show projection-dependent sizes and luminosities, these variations are smaller than the scatter in median values, and are likely a result of the mild correlation between Sersic index and

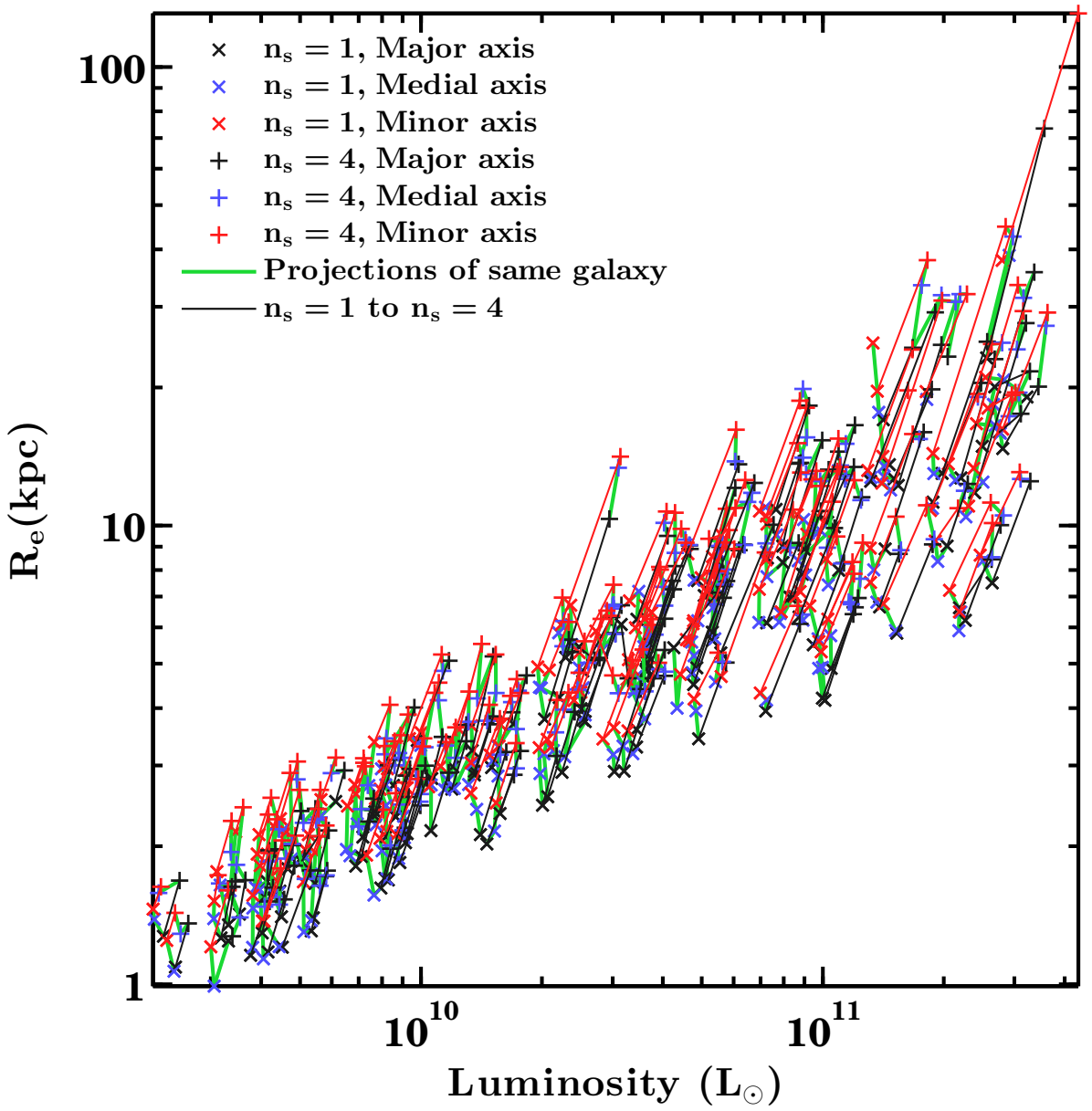

Figure 3.6: The size-luminosity relation of merger remnants after 10 Gyr. Each point shows one of the principal axis projections. Light (green) lines connect different projections of the same galaxy. Darker (red and black) lines connect the same projection for groups with different progenitor bulge profiles but otherwise identical initial conditions. The light (green) lines can be viewed as contributions to scatter in the relation from projection effects, while the darker lines show differences from progenitor galaxies.

Table 3.1: Sersic model size-luminosity relations

Simulations: Ten equally-spaced projections, randomly oriented

$B.n_s$	Subsample	Slope	Intercept	R.M.S.
1	Unweighted	0.53 ± 0.01	-4.89 ± 0.07	0.10
1	Weighted	0.58 ± 0.01	-5.36 ± 0.06	0.10
1	Many	0.55 ± 0.01	-5.08 ± 0.05	0.07
1	Few	0.50 ± 0.01	-4.67 ± 0.08	0.10
4	Unweighted	0.61 ± 0.01	-5.66 ± 0.10	0.12
4	Weighted	0.67 ± 0.01	-6.20 ± 0.07	0.12
4	Many	0.65 ± 0.01	-5.95 ± 0.08	0.09
4	Few	0.55 ± 0.01	-5.11 ± 0.11	0.11
All	Unweighted	0.58 ± 0.01	-5.32 ± 0.06	0.12
All	Weighted	0.63 ± 0.01	-5.92 ± 0.06	0.12
All	Many	0.62 ± 0.01	-5.69 ± 0.06	0.10
All	Few	0.54 ± 0.01	-4.96 ± 0.08	0.12

Principal axis projections, unweighted

$B.n_s$	Projection	Slope	Intercept	R.M.S.
1	Major axis	0.55 ± 0.02	-5.12 ± 0.19	0.10
1	Minor axis	0.52 ± 0.02	-4.70 ± 0.21	0.10
4	Major axis	0.60 ± 0.02	-5.53 ± 0.24	0.11
4	Minor axis	0.58 ± 0.02	-5.25 ± 0.29	0.11

Observations

Cat.	Type	Weight	Slope	Intercept	R.M.S.
S+11	E	N	0.85 ± 0.00	-8.34 ± 0.01	0.12
S+11	E	Y	0.80 ± 0.00	-7.82 ± 0.02	0.12
N+10	E	N	0.66 ± 0.01	-6.40 ± 0.10	0.09
N+10	S0	N	0.63 ± 0.01	-6.03 ± 0.11	0.12
N+10	E	Y	0.65 ± 0.02	-6.29 ± 0.21	0.09
N+10	S0	Y	0.61 ± 0.02	-5.82 ± 0.24	0.12
A3D	E	N	0.72 ± 0.03	-6.90 ± 0.35	0.12
A3D	S0	N	0.57 ± 0.05	-5.41 ± 0.24	0.12
A3D	E	Y	0.72 ± 0.04	-6.97 ± 0.65	0.12
A3D	S0	Y	0.60 ± 0.05	-5.70 ± 0.44	0.12

Slopes are given in log space, i.e., for $\log(R_e)$ as a function of $\log(L)$. Simulation data are from analyses after 10.3 Gyr, including various subsamples of randomly oriented (but equally spaced) projections, as detailed in the text, as well as principal axis projections. Observational data for each catalogue (Cat.) are $1/V_{max}$ corrected, with fits optionally weighted (Weight) or not by the difference between the simulated and observed luminosity functions. R.M.S. lists the r.m.s. orthogonal scatter of all points from the best-fit relation.

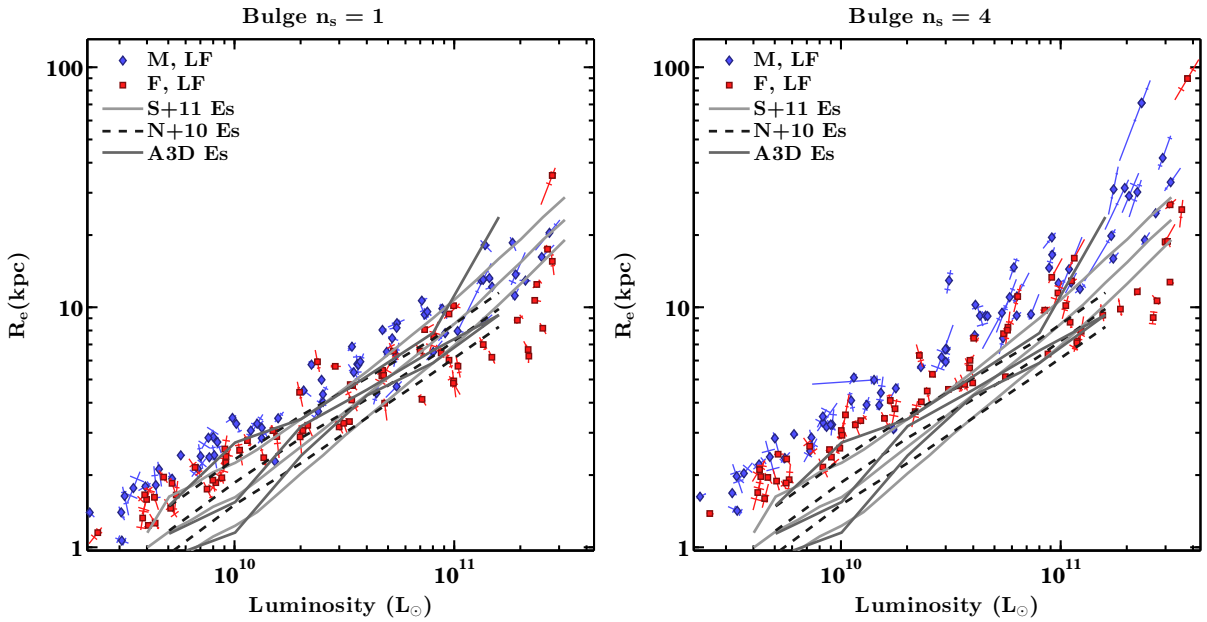

Figure 3.7: Sersic model size-luminosity relation of central ellipticals after 10 Gyr. The simulated relations have small scatter and a similar slope to observations but are offset slightly, being too large at fixed luminosity. Many merger galaxies appear to be a better fit for luminous ellipticals, whereas few mergers match low luminosity ellipticals better. Line types are as in Fig. 3.3.

luminosity of projections of the same galaxy (evidenced in Fig. 3.3). If sizes and luminosities are generally accurate to within 10-20% or 0.04-0.08 dex, as suggested by our testing, then some of the scatter could be intrinsic. The scatter in the unweighted simulation data is comparable to that in observed ellipticals (slightly larger than N+10), while the slope is considerably shallower and the intercepts larger.

Separate fits to the Many- and Few-merger subsamples show a large difference of 0.05 to 0.1 in slope. Also, as Fig. 3.7 demonstrates, the Many-merger subsample is larger at fixed luminosity than the few merger sample. Thus, the slope of the predicted relation can be maximized by giving a larger weight to luminous, Many-merger remnants (and a smaller weight to faint galaxies), while applying the opposite weighting to groups of relatively few galaxies, such that their weights are largest at low luminosities. We apply such a weighting in Tab. 3.1 and find that it can steepen the slope of the size-luminosity relation further than even the Many-merger subsample alone, bringing it close to observed values for N+10 but still short of S+11 and A3D.

Table 3.1 also lists values for observational data, with both $1/V_{max}$ corrections and optional weighting to match the luminosity function of the simulations. This weighting scheme only makes a significant difference in the S+11 sample - otherwise, most scaling relations are insensitive to weighting method, as one would expect if they are truly linear with uniform scatter. Some curvature may exist at the low- or high-luminosity extremes, but it is unclear whether it is real or systematic.

Table 3.2: Petrosian size-luminosity relations

B.n_s	Subsample	Slope	Intercept	R.M.S.
Simulations: Ten equally-spaced projections, randomly oriented				
1	Unweighted	0.50 ± 0.01	-4.62 ± 0.06	0.10
1	Weighted	0.54 ± 0.01	-5.06 ± 0.05	0.10
1	Many	0.52 ± 0.01	-4.81 ± 0.06	0.08
1	Few	0.48 ± 0.01	-4.43 ± 0.09	0.09
4	Unweighted	0.49 ± 0.01	-4.47 ± 0.05	0.10
4	Weighted	0.54 ± 0.01	-4.99 ± 0.06	0.10
4	Many	0.52 ± 0.01	-4.72 ± 0.07	0.08
4	Few	0.46 ± 0.01	-4.22 ± 0.07	0.09
All	Unweighted	0.49 ± 0.00	-4.50 ± 0.04	0.10
All	Weighted	0.54 ± 0.01	-5.04 ± 0.04	0.10
All	Many	0.52 ± 0.00	-4.76 ± 0.06	0.08
All	Few	0.47 ± 0.01	-4.34 ± 0.06	0.09

Cat.	Type	Weight	Slope	Intercept	R.M.S.
Observations					
N+10	E	N	0.62 ± 0.01	-6.04 ± 0.07	0.08
N+10	S0	N	0.57 ± 0.01	-5.53 ± 0.07	0.10
N+10	E	Y	0.58 ± 0.01	-5.61 ± 0.22	0.08
N+10	S0	Y	0.54 ± 0.01	-5.14 ± 0.09	0.10

Column definitions are as in Tab. 3.1.

Table 3.3: Sersic size-stellar mass relations

Cat.	Type	Weight	Slope	Intercept	R.M.S.
S+11	E	N	0.78 ± 0.00	-7.95 ± 0.02	0.13
S+11	E	Y	0.75 ± 0.00	-7.53 ± 0.03	0.13
N+10	E	N	0.64 ± 0.01	-6.39 ± 0.06	0.09
N+10	S0	N	0.57 ± 0.01	-5.61 ± 0.09	0.12
N+10	E	Y	0.60 ± 0.02	-5.89 ± 0.20	0.09
N+10	S0	Y	0.48 ± 0.02	-4.63 ± 0.17	0.13

Column definitions are as in Tab. 3.1.

The Petrosian R_{50} size-luminosity relation (Tab. 3.2) shows smaller scatter than Sersic sizes, despite the fact that uncorrected Petrosian half-light radii systematically underestimate the luminosities of pure Sersic profiles and simulated galaxies alike. This is especially true for the B.n_s=4 sample, which has slightly lower scatter than B.n_s=1 mergers, despite having greater systematic errors on R_e due to its larger mean n_s. The slopes are still shallower than those observed in N+10, but the difference can shrink to less than 0.05 if considering weightings for both simulations and observations. The implications of these results will be discussed further in §3.2.

The best-fit relations between size and stellar mass for the S+11 and N+10 catalogues are listed in Tab. 3.3. The slopes are slightly shallower than those for the size-luminosity relations and closer to (but not quite matching) those predicted by the simulations, which do not have significant variations in the stellar mass-to-light ratio. Thus some of the tension between the

Table 3.4: Petrosian model size-stellar mass relation

Cat.	Type	Weight	Slope	Intercept	R.M.S.
N+10	E	N	0.59 ± 0.01	-5.97 ± 0.09	0.09
N+10	S0	N	0.50 ± 0.01	-4.922 ± 0.08	0.11
N+10	E	Y	0.52 ± 0.02	-5.21 ± 0.21	0.09
N+10	S0	Y	0.41 ± 0.01	-4.03 ± 0.11	0.12

Column definitions are as in Tab. 3.1.

slopes of the simulated and observed size-luminosity relations can be resolved by accounting for the variable stellar mass-to-light ratio of observed galaxies, which increases in more luminous observed ellipticals but is nearly constant by construction in the simulated remnants.

The Petrosian size-stellar mass relation shows slightly shallower slope, as with Sersic models. In fact, the slope and scatter of the weighted simulations (0.52 and 0.09) are within the quite small bootstrap errors (0.01) of the weighted observations (0.51 and 0.09), while the intercept is higher (-4.81 versus -5.08) but still also within the more generous error bars. Thus, it is entirely possible to match the slopes, and, to a lesser extent, the intercepts of the size-mass relation, depending on the fitting technique and sample weights. However, this alone does not justify either weighting scheme. The observational scheme is reasonable, since matching luminosity functions is necessary in order to make a fair comparison. The simulation scheme is not as well justified, since the number of mergers per group is somewhat arbitrary.

The Kormendy relation (Kormendy, 1977), shown in Fig. 3.8, has large scatter and shallow slope, especially for the B.n_s=1 relation, which is nearly flat. None of the observed relations are quite linear. While the kink at small sizes is likely a systematic artefact, the curvature near 5-6 kpc appears more robust and also more significant than the equivalent curvature in the size-luminosity relation. As in the size-luminosity relation, it appears as if the simulated galaxies are either too faint for their size or too large to be so faint. Interestingly, the relation for large ellipticals appears to asymptote towards the slope of constant luminosity ($\mathrm{d}\log(\mu_\mathrm{e})/\mathrm{d}\log(\mathrm{R_e})$ = 5), which suggests that bright ellipticals can grow significantly in size without adding a large amount of stellar mass. In fact, many BCGs have exceptionally large effective radii and faint mean surface brightnesses. However, most of the similar simulated remnants in Fig. 3.6 are mergers of many equal-mass spirals, rather than luminosity function-sampled remnants - without this M-Eq subsample, the simulated Kormendy relation is rather weak, especially for the B.n_s=1 sample.

Faber-Jackson Relation

The Faber-Jackson (velocity dispersion-luminosity, Faber & Jackson (1976)) relation is shown in Fig. 3.9, with best fits tabulated in Tab. 3.5. The simulated relations have slopes fairly close to the observations, though the intercepts are significantly lower. The turnover or curvature at low velocity dispersions (<100 kms^{-1}) is likely not entirely real, since such low dispersions are near the spectrograph's resolution limit and unlikely to be reliable (Aihara et al., 2011). The

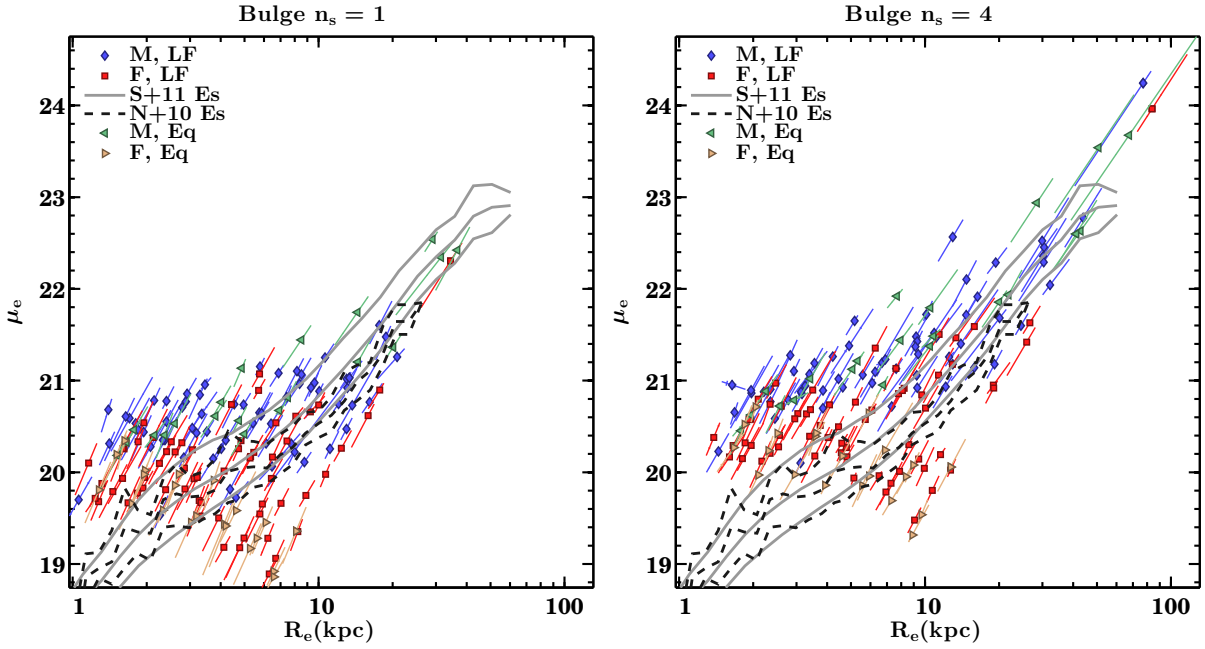

Figure 3.8: The Kormendy relation of central ellipticals. Only B.n$_s$=4 simulations show a distinct Kormendy relation, but they are also too faint at a fixed size. The observed relation can be better reproduced if few mergers and B.n$_s$=1 are the preferred source of small galaxies and many/B.n$_s$=4 produced large ellipticals. Line types are as in Fig. 3.3.

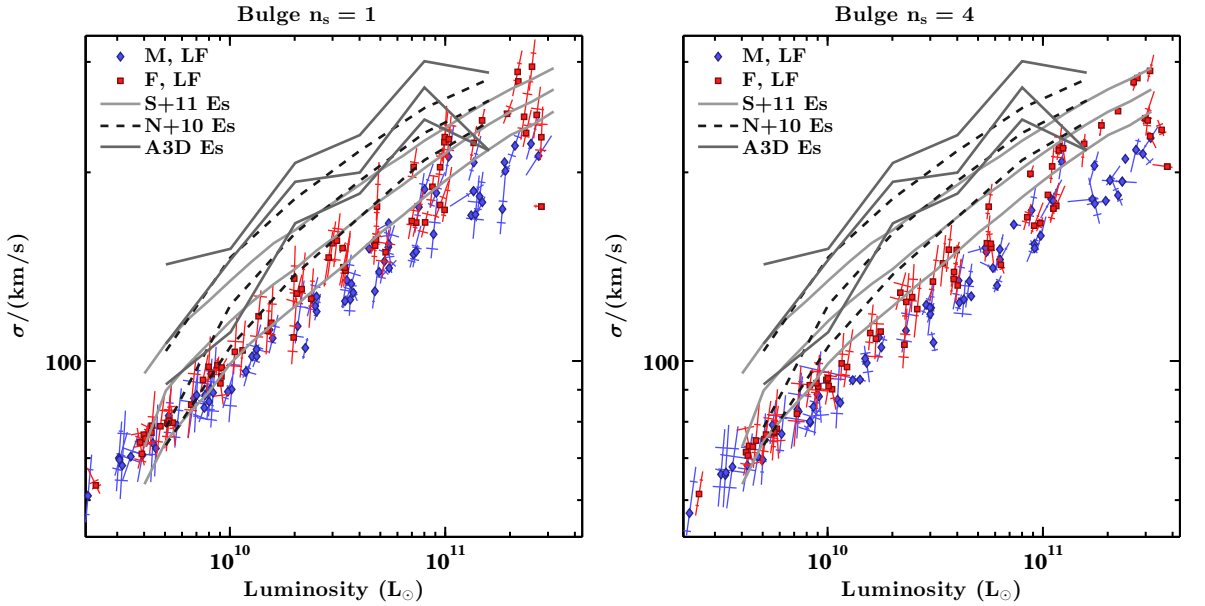

Figure 3.9: The Faber-Jackson relation. Both simulation samples follow a similar slope to observations but are offset to lower dispersions, regardless of which subsample is used. The scatter in simulations is tighter than observations, since the observed relations show 25th, 50th and 75th percentiles. Line types are as in Fig. 3.3.

Table 3.5: Sersic model Faber-Jackson relations

Simulations: Ten equally-spaced projections, randomly oriented

$B.n_s$	Subsample	Slope	Intercept	R.M.S.
1	Unweighted	0.28 ± 0.00	-0.85 ± 0.02	0.04
1	Weighted	0.27 ± 0.00	-0.68 ± 0.02	0.05
1	Many	0.27 ± 0.00	-0.68 ± 0.03	0.03
1	Few	0.30 ± 0.00	-0.98 ± 0.04	0.04
4	Unweighted	0.29 ± 0.00	-0.90 ± 0.02	0.04
4	Weighted	0.27 ± 0.00	-0.74 ± 0.02	0.04
4	Many	0.27 ± 0.00	-0.75 ± 0.02	0.03
4	Few	0.30 ± 0.00	-0.99 ± 0.03	0.04
All	Unweighted	0.28 ± 0.00	-0.86 ± 0.02	0.04
All	Weighted	0.27 ± 0.00	-0.71 ± 0.02	0.05
All	Many	0.27 ± 0.00	-0.72 ± 0.02	0.04
All	Few	0.30 ± 0.00	-0.98 ± 0.03	0.04

Principal axis projections, unweighted

$B.n_s$	Projection	Slope	Intercept	R.M.S.
1	Major axis	0.27 ± 0.01	-0.70 ± 0.06	0.04
1	Minor axis	0.30 ± 0.01	-1.01 ± 0.06	0.04
4	Major axis	0.27 ± 0.01	-0.69 ± 0.05	0.04
4	Minor axis	0.30 ± 0.01	-1.12 ± 0.06	0.04

Observations

Cat.	Type	Weight	Slope	Intercept	R.M.S.
S+11	E	N	0.27 ± 0.00	-0.63 ± 0.01	0.08
S+11	E	Y	0.30 ± 0.00	-0.92 ± 0.02	0.08
N+10	E	N	0.28 ± 0.01	-0.67 ± 0.10	0.07
N+10	S0	N	0.36 ± 0.01	-1.57 ± 0.09	0.10
N+10	E	Y	0.37 ± 0.01	-1.67 ± 0.31	0.08
N+10	S0	Y	0.48 ± 0.03	-2.85 ± 0.20	0.11

Column definitions are as in Tab. 3.1.

Table 3.6: Velocity dispersion-stellar mass relations

Cat.	Type	Weight	Slope	Intercept	R.M.S.
S+11	E	N	0.26 ± 0.00	-0.60 ± 0.01	0.07
S+11	E	Y	0.28 ± 0.00	-0.88 ± 0.01	0.07
N+10	E	N	0.29 ± 0.00	-0.89 ± 0.05	0.06
N+10	S0	N	0.36 ± 0.01	-1.74 ± 0.08	0.09
N+10	E	Y	0.36 ± 0.03	-1.70 ± 0.26	0.07
N+10	S0	Y	0.43 ± 0.01	-2.45 ± 0.10	0.09

Column definitions are as in Tab. 3.1.

luminosity function weightings make a significant difference in slope for the N+10 sample, which is likely due to this same curvature. The scatter appears to be mostly due to projection effects at the low-luminosity end but increases at high luminosities, where the Many- and Few-merger samples appear to diverge. The most robust conclusions from the data are that the slope for the S0 sample is significantly steeper than that for ellipticals, which in turn is slightly steeper than the canonical slope of 0.25, depending on the weighting scheme used. The scatter in the simulated relations is also significantly lower than in the observations, even when both bulge samples are combined.

Unlike the size-mass/luminosity relations, the velocity dispersion-stellar mass relation (Tab. 3.6) is hardly changed from the velocity dispersion-luminosity relation, although the scatter shrinks slightly. The velocity dispersion-stellar mass relation also deviates from the canonical Faber-Jackson relation slope of 0.25, showing a scaling closer to $\sigma \propto M_*^{0.3}$.

3.1.3 Rotational Support

We measure v/σ as the luminosity-weighted average within R_e, as used in IFS observations like ATLAS3D (Cappellari et al., 2011). Most simulated ellipticals are slow rotators (Fig. 3.10). However, some projections show v/σ as large as 0.35 and can be classified as fast rotators despite having been formed from dry mergers. Cox et al. (2006) found that dry binary mergers only form slow rotators ($v/\sigma < 0.1$), whereas some group mergers are clearly capable of producing fast rotators. Nonetheless, the scarcity of remnants with $v/\sigma > 0.3$ strongly suggests that dissipation is necessary to form fast rotators, as will be elaborated further in §3.2.

We also measure rotation in Fig. 3.11 by the more physically motivated measure λ (Emsellem et al., 2007; Cappellari et al., 2011) - essentially a radially-weighted v/σ tracing net projected angular momentum. While the distribution of rotational support is not wildly different from ATLAS3D, there is a significant excess of slow rotators (especially flattened ones) and a complete absence of simulated galaxies with $\lambda > 0.4$. B.n$_s$=1 mergers and Many-merger remnants tend to be slightly slower rotators, but the differences in both cases are not large.

Figure 3.12 shows rotational support for the principal axis projections. The minor axis projection shows minimal rotation, which is expected if there are no stable orbits about the major axis. In general, B.n$_s$=4 mergers are rounder despite having faster rotation for the same

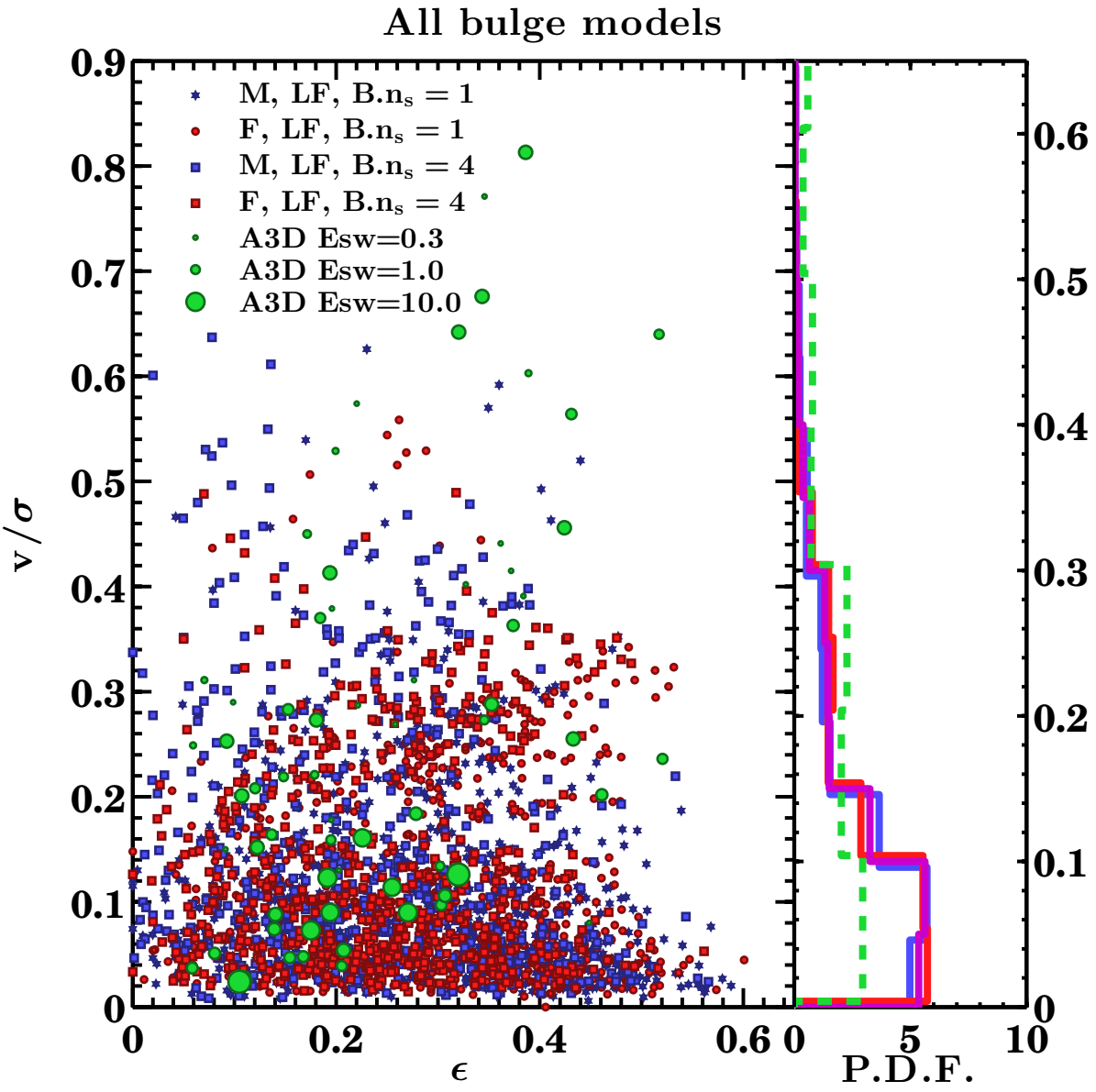

Figure 3.10: Rotational support of simulated galaxies by classical v/σ measure. ATLAS3D ellipticals are shown with areas of points roughly corresponding to their relative weights on a logarithmic scale. Most simulated ellipticals are slow rotators, but some have modest rotational support.

set of initial conditions. As with random projections, there appear to be two distinct tracks for galaxies, which is more readily apparent in the B.n$_s$=4 mergers. Most galaxies have a range of ellipticities in their major axis projections but only show modest increases in rotational support from the minor to medial axis projections. These appear as horizontal lines with a shallow slope near the bottom of the figure. A smaller subset of galaxies are nearly round in the minor axis projection, with very modest rotation ($\lambda < 0.1$), but are significantly flattened ($\epsilon > 0.2$ and rotationally supported ($\lambda > 0.2$) in major and medial axis projections alike. In fact, for most of these galaxies it appears as if the major and medial axis projections are nearly identical, and so these galaxies are probably oblate spheroids. In this case, the distinction between major and medial axis projection is not very meaningful.

Rotational support decreases with increasing luminosity in A3D ellipticals but not in simulations, as shown in Fig. 3.13. This is largely due to the inability of dry mergers to produce fast rotating, faint ellipticals. Furthermore, even if the morphological properties of some remnants (particularly Sersic indices of B.n$_s$=1 remnants) are more consistent with S0s than ellipticals, observed S0s have far more rotational support than the vast majority of the simulated galaxies.

There does not appear to be any strong correlation between rotational support and number of mergers in Fig. 3.10, or with total group mass or central galaxy luminosity. One might expect rotational support to at least correlate with net group specific angular momentum, assuming most of the halos merge and this angular momentum is conserved - however, Fig. 3.14 does not show any such correlation. It appears that repeated, mostly isotropic mergers cannot produce very fast rotators, even if the group itself has some net orbital angular momentum in one or more satellite galaxies.

3.2 Discussion

The main results of §3.1 are that collisionless mergers in groups can produce central remnants with properties very similar to nearby elliptical galaxies. However, we do note several key differences between the simulation predictions and observed elliptical galaxies, not all of which are easily reconciled with dissipationless merging. We will also highlight how and why these results differ from previously published simulations.

3.2.1 Morphology

In Appendix A.1, it is shown that at the resolutions used in this study, luminosities, sizes and Sersic indices of spherical Sersic model galaxies can be recovered within about 5%, usually underestimating the true values. For group merger remnants, Sersic fits typically recover luminosities and sizes to within 10%, although luminosities tend to be more precisely recovered. By contrast, Petrosian radii systematically underestimate galaxy sizes and luminosities, negating the advantage of a non-parametric fit unless corrected for. Thus we conclude that single Sersic model fits are suitable for the simulated galaxies and can be compared directly to S+11 cata-

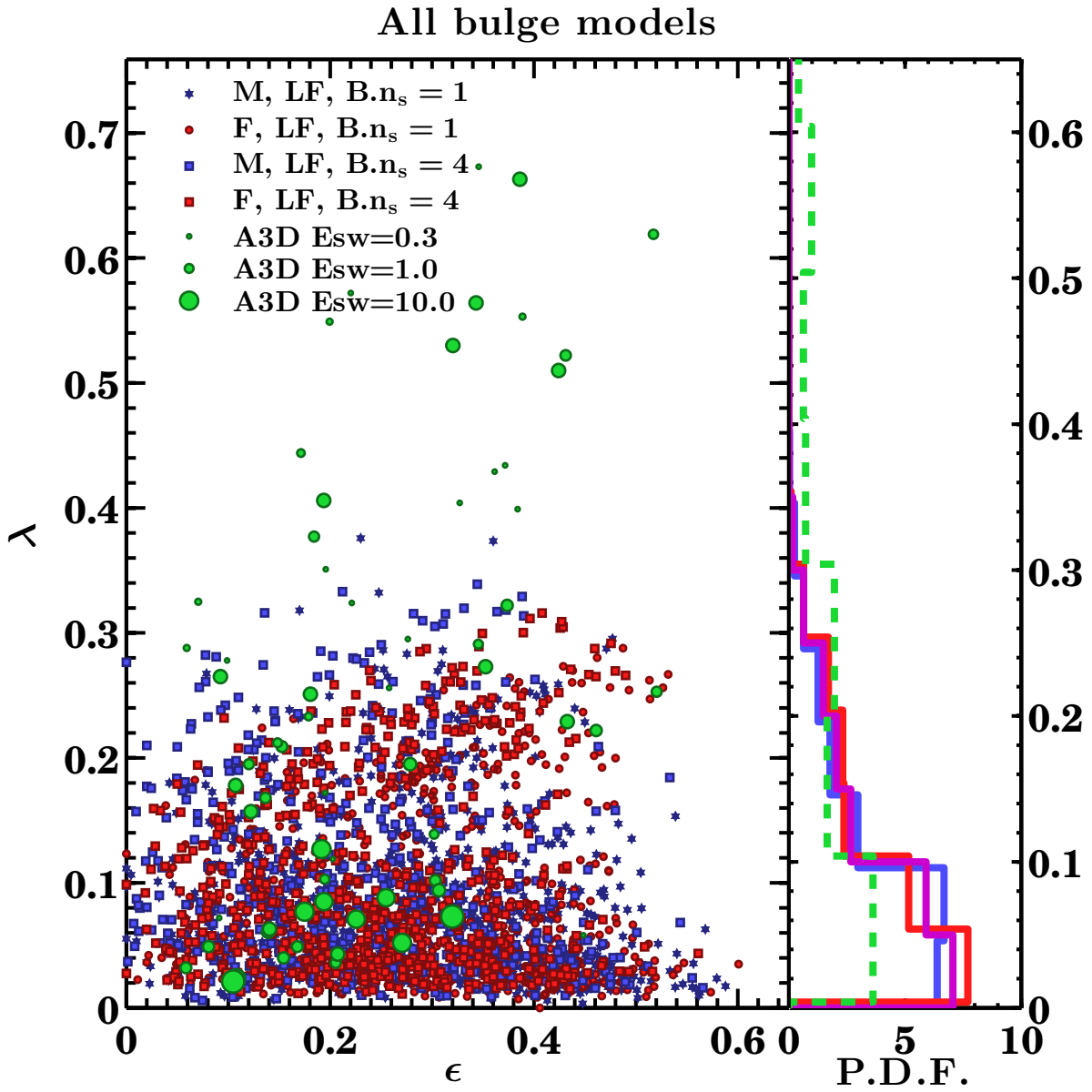

Figure 3.11: Rotational support of simulated galaxies by dimensionless angular momentum measure λ. Observed data are shown with point sizes proportional to the logarithm of the relative weights to match the luminosity function of the simulated galaxies. Despite this weighting scheme, too many simulated galaxies have low rotational support, and none have very high support ($\lambda > 0.4$).

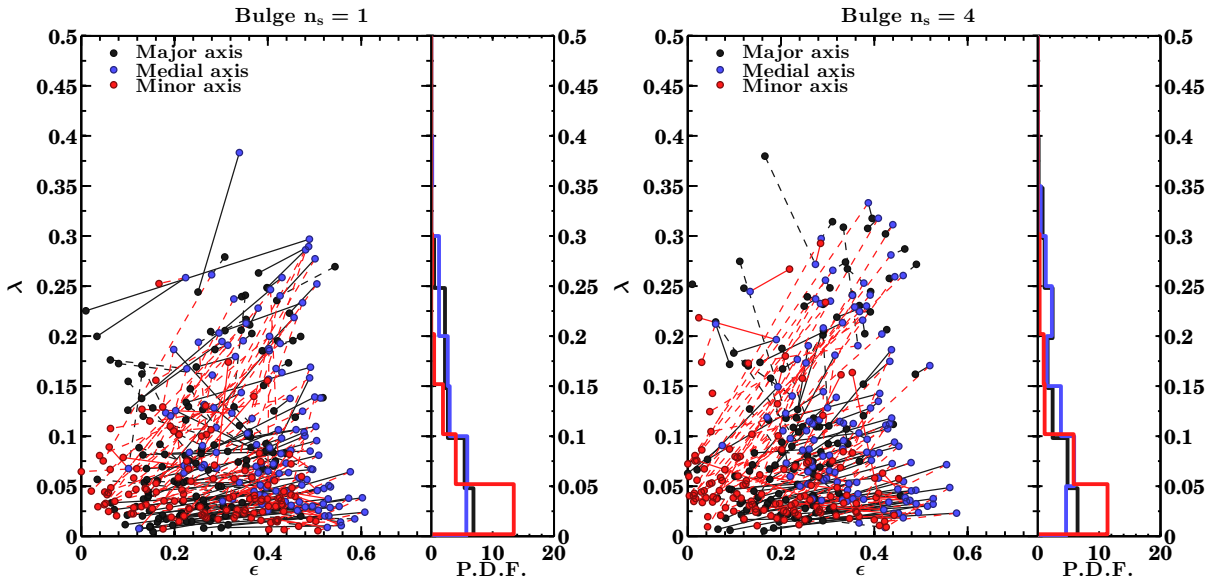

Figure 3.12: Rotational support of principal axis projections of simulated galaxies by dimensionless angular momentum measure λ. Different projections of the same galaxy are connected by lines, with dashed lines if the second point is lower on the y-axis than the first. Minor axis projections show very little rotation, while medial and major axis projections have similar amounts of rotational support, with medial axis projections being slightly more flattened.

logue fits, with the caveat that Sersic indices are the least robust parameter at low resolutions and are likely systematically underestimated. However, it is also true that in practice, Sersic fits can produce larger scatter on size than on luminosity, whereas Petrosian half-light radii appear to limit scatter in sizes - likely because they systematically underestimate the total luminosity of galaxies with large Sersic indices. Given these issues, our solution is to compare sizes between simulations and observations as fairly as possible, so that any systematic errors are likely to be shared between simulated and observed galaxies.

We have compared Sersic index and ellipticity distribution to single Sersic profile fits of local (A3D) and SDSS (N+10, S+11) galaxies. Neither B.n$_s$ sample is a good fit to observed ellipticals alone, but the naive linear combination of the two is a better fit while remaining inconsistent with S0s. However, such a naive combination still produces a near-bimodal distribution, in contrast to the single peak typical of observed ellipticals. A more natural choice of progenitors would likely smooth out this bimodality. For example, groups with half of the spirals having exponential bulges and the other half de Vaucouleurs would likely produce remnants with intermediate properties, filling in the gap between the two peaks of single-progenitor distributions. A smooth, realistic distribution of bulge profiles and bulge fractions would likely flatten the peaks and further broaden the distribution of remnant Sersic indices.

Sersic indices of observed ellipticals are generally larger for more luminous galaxies, a trend reproduced by the simulated galaxies in Fig. 3.3. Hopkins et al. (2009) predicted that the dissipationless component in mergers (including both binary spiral mergers and some re-mergers of

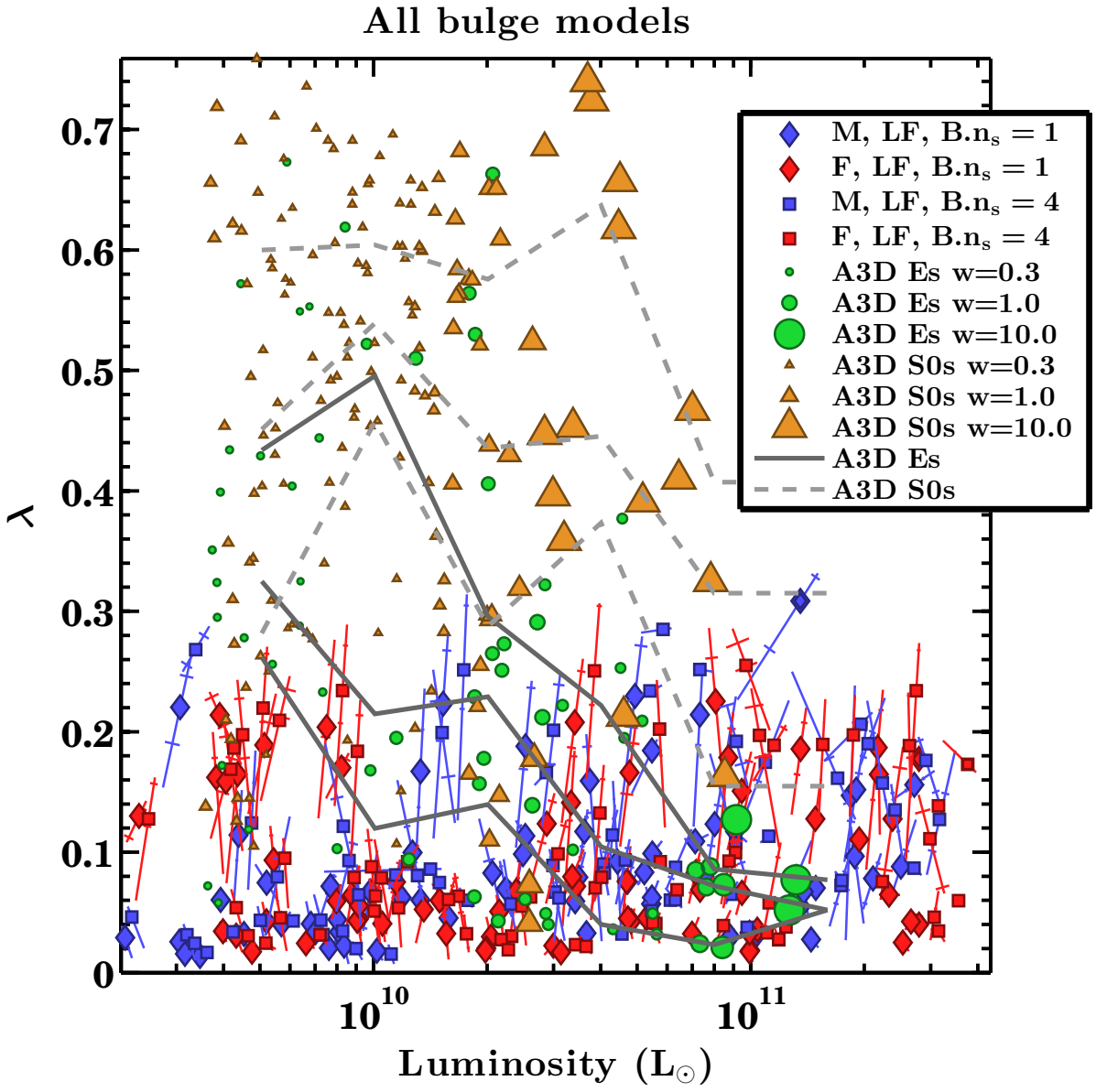

Figure 3.13: Rotational support of elliptical galaxies by dimensionless angular momentum measure λ as a function of luminosity. Observational data show a trend of lower rotational support at higher luminosity, whereas the simulated trend is nearly flat. Almost all S0s are faster rotators than simulated remnants.

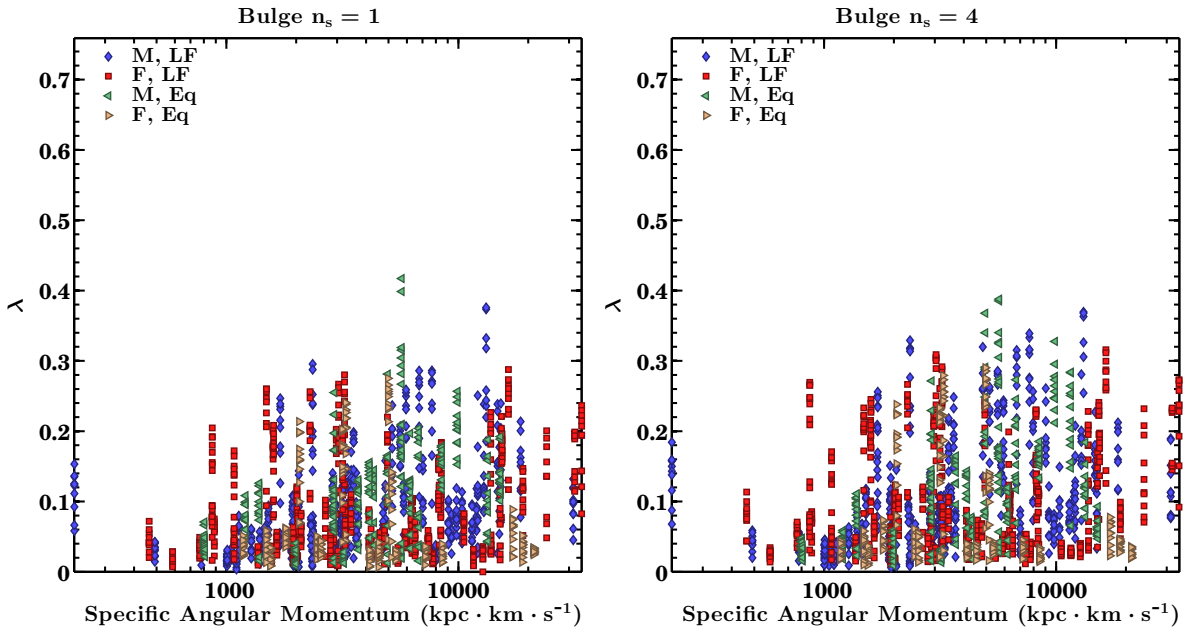

Figure 3.14: Rotational support of simulated galaxies as a function of initial group orbital angular momentum per unit mass. For reference, M31's estimated orbit about the Milky Way with a tangential velocity of 30 kms^{-1}and a distance of 700 kpc would be amongst the smaller values in the sample.

the resulting remnants) should show only a weak increase with luminosity and have low median values of about n_s=3, with scatter of about 1. We find similar results for the B.n_s=1 sample, for which n_s is nearly constant with luminosity at a mean of 3 and with a range from 2 to 4. By contrast, the B.n_s=4 sample not only has larger mean n_s at about 5, but the median n_s increases with luminosity by ∼0.5-1 per dex. This slope is close to that observed for N+10 and shallower than that in S+11, the discrepancy between these two samples having no obvious cause beyond probable contamination by S0s in the S+11 elliptical sample. Since the simulations have the same initial conditions other than their bulge profiles, this demonstrates that sufficiently concentrated progenitors can produce remnants with large n_s through dissipationless merging. Furthermore, bulge n_s=4 mergers appear to be a better fit for luminous ellipticals, while bulge n_s=1 remnants match the less luminous ellipticals. If progenitor bulge profiles scale with luminosity (i.e., luminous spirals have larger bulge n_s and merge to form luminous ellipticals), the scaling of elliptical Sersic index with luminosity can be matched more closely.

Both simulations and observations show a slight tendency for more luminous ellipticals to be rounder, especially above $10^{11}L_{\odot}$ (Fig. 3.5). Again, the S+11 sample differs from N+10, in this case being more flattened on average - likely due to S0 contamination. Nonetheless, we also find similar luminosity-dependent behaviour as for Sersic indices, as the B.n_s=4 sample is a better match for bright, rounder ellipticals. The B.n_s=1 sample has a shallower slope and appears to be too flattened on average. The observed distribution does not obviously require a combination of both simulation samples in the same way as the Sersic index-luminosity relation

does, but such a combination does not disagree with the S+11 relation either. The N+10 ellipticity-luminosity relation is considerably flatter and could be reproduced by the B.n$_s$=4 sample alone, with the scatter due to the substantial projection effects.

A careful examination of Fig. 3.1 shows that while most remnants' surface brightness profiles are well-fit by a single Sersic profile, there can be structure in the residuals, especially for the most massive merger remnants in groups of many galaxies. Kravtsov et al. (2014) found that many nearby BCGs cannot be well-fit by a single Sersic profile, especially in the outer regions; this result is qualitatively similar to our own findings, since BCGs are more massive and likely formed in even richer groups or clusters than our own merger remnants.

Using GALFIT fits, Huang et al. (2013) have argued that nearby ellipticals' surface brightness profiles are best fit by multiple Sersic components, usually at least 3. Kormendy et al. (2009) suggest instead that most ellipticals are well-fit by a single Sersic component, except for the central regions which can contain either a cusp or core - only the former of which is likely to be a physically distinct component. Unfortunately, their samples do not overlap significantly, so their analyses cannot be directly compared.

Huang et al. (2013) note that multiple components are usually required to fit radially varying ellipticities and position angles, since each of their components has a single, fixed ellipticity and position angle (as in our own fits). Kormendy et al. (2009) avoid this problem by extracting one-dimensional surface brightness profiles with varying ellipticities and position angles. We cannot comment on which approach is preferable, since in most of our remnants, a single Sersic profile is sufficient. The largest deviations tend to occur at significant distances from the centre of the galaxy ($R > 5R_e$) and at faint surface brightnesses ($\mu_r > 24$), where real SDSS imaging would be overwhelmed by sky noise. Without our simplified uniform sky background with Gaussian noise, it would not have been possible to plot surface brightness profiles to nearly 30 mags/arcsec^2, as in Fig. 3.1.

Finally, we have chosen to fix the sky background in our GALFIT fits because allowing for a variable sky inevitably leads to overestimation of the sky background level. In principle, we could have reproduced the sky estimation methods used in S+11; however, this would be insufficient without also reproducing the same variability and structure found in typical SDSS observations - a much more challenging task. Bernardi et al. (2013) have argued that the sky estimations of S+11 result in absolute magnitudes biased by as much as 0.4; however, such extreme errors are only for the most massive BCGs. For more typical ellipticals with $M_r > -23$, $|\Delta M_r| < 0.05$ mags, so the sky estimations of S+11 appear reasonably robust and are likely accurate for all but the very most luminous galaxies.

3.2.2 Scaling Relations

Size-Luminosity Relation

Despite having randomized initial conditions, the simulated galaxies typically produce tight size-luminosity relations, with slight dependence on which size measure is used and whether different

B.n$_s$ samples are combined. The Sersic model relations are somewhat tighter ($\sim 0.1-0.12$ dex scatter) than those reported by Nair et al. (2011) ($\sim 0.12-0.15$ dex scatter). This is partly systematic, since Nair et al. (2011) used circular Sersic fits provided by Blanton et al. (2005). Using the elliptical Sersic model fits of S+11 - which are more directly comparable to our own methodology and overlap with the N+10 sample - yields smaller scatter in the N+10 size-luminosity relation of ~ 0.09 dex. We also find slightly tighter scatter in the remnant Petrosian size-luminosity relation (~ 0.09 dex), whereas the scatter for N+10 ellipticals remains largely unchanged whether Sersic or Petrosian model sizes are used.

The small scatter in the size-luminosity relation should allay concerns that stochastic merging processes cannot produce tight scaling relations. Nipoti et al. (2009a) used simulations with multiple mergers of spheroidal galaxies to conclude that "a remarkable degree of fine tuning is required to reproduce the tightness of the local scaling relations with dry mergers". Instead, we find that mergers of many galaxies typically produce slightly tighter correlations than those with fewer galaxies, and the relations are tight regardless of which formation time is assumed for the groups (Appendix B.1). No fine tuning in galaxy orbits, number of mergers or any other parameters are required to produce tight scaling relations. Moreover, the Faber-Jackson relation has even tighter scatter than the size-luminosity relation. Rather than scattering galaxies away from existing scaling relations, multiple mergers appear to converge remnants towards a common relation, a behaviour somewhat like the central limit theorem. However, it is still true that dry mergers of spirals in groups produce remnants with larger sizes and smaller velocity dispersions at fixed mass or luminosity, a problem shared with mergers of spheroids (e.g. Nipoti et al., 2003; Boylan-Kolchin et al., 2006; Nipoti et al., 2009b). Also, the scatter does appear to increase slightly with luminosity. This could simply be a reflection of the wide range of galaxy and merger counts for the luminous groups, which may not match the true range of cosmological merger histories for galaxy groups.

We have tested mergers of spirals following a zero-scatter Tully-Fisher relation. The estimates for the scatter of merger remnant scaling relations can be considered lower limits, as they would likely have been higher had progenitors followed Tully-Fisher relations with intrinsic scatter and/or evolving slope and scatter. The observed Tully-Fisher relation does have significant scatter, even at low redshift (about 0.12 dex, from Courteau et al. (2007)), but the intrinsic scatter could be much lower. Hopkins et al. (2008) estimate that a scatter of 0.1 dex in the Tully-Fisher relation contributes about 0.04 dex scatter in the Fundamental Plane scaling relation; comparable scatter added to the existing size-luminosity relation scatter of 0.10-0.12 dex would make little difference if added in quadrature.

While limiting scatter does not appear to be a challenge, in almost all cases the slope of the size-luminosity relation is shallower than observed and the intercept larger, so most galaxies are too large for their luminosities. The slopes of the remnant size-luminosity relations (typically $R \propto L^{0.5-0.6}$) are steeper than the progenitor spiral scaling relation ($R \propto L^{0.42}$) and the group scaling relation (ρ=constant, $R \propto L^{1/3}$). However, the remnants slopes are still shallower

than those for the observations, which range from $R \propto L^{0.6}$ to $R \propto L^{0.8}$ depending on the observational sample and size measure. Encouragingly, the best matches are found between simulated remnants and N+10 ellipticals ($R \propto L^{0.66}$), the largest sample for which visual classifications are available.

The steeper slope of the S+11 elliptical Sersic size-luminosity relation (0.75 to 0.78) is of some concern. However, the elliptical classification for S+11 is based on empirical cuts on various parameters and results in significant ($\sim$ 30%) contamination by S0s (Tab. 2.2). The much smaller A3D elliptical sample also has a slightly larger slope than N+10, and the luminosity function weighting does not change the slope. Since A3D used a slightly different fitting methodology with a much smaller volume sample, it is not clear whether this discrepancy is significant.

The size-luminosity relation slopes for the simulated remnants are also steeper than that of $R \propto L^{\sim 0.3}$ predicted for binary mergers remnants by Hopkins et al. (2009). However, those simulations began with a spiral scaling relation of similar slope (0.3), and so the merging process did not steepen the size-mass relation. By contrast, we have shown that group mergers are capable of steepening the slope of the size-luminosity relation by $\sim 0.1-0.2$ from progenitors to merger remnants without dissipation.

Our models predict virtually no dependence of stellar mass-to-light ratio on luminosity - while the bulge and disk stellar mass-to-light ratios have different values, the fraction of disk stars within the effective radius varies little. However, luminous ellipticals do tend to have larger stellar mass-to-light ratios, so comparing to observed size-stellar mass relations lessens the discrepancies in the slopes by about 0.05 dex, depending on the sample and size measure. Such a dependence could be produced by more massive progenitor spirals having larger mean stellar mass-to-light ratios. We also did not include any scatter in the progenitor spiral Tully-Fisher relation or any scatter or luminosity dependence in bulge fractions. Extra scatter in either of these input galaxy properties would likely result in increased scatter in the remnant scaling relations. Any realistic luminosity dependence in the large M31 model bulge fraction would likely flatten the size-luminosity slope still further, since faint ellipticals would be produced by faint spirals with weak bulges.

Dissipation is a tempting solution to the shallow size-luminosity relation slope problem. Dissipation should decrease sizes at fixed luminosities and preferentially shrink faint ellipticals if their progenitors had larger gas fractions, resulting in a remnant with a larger fraction of stars formed in a central starburst. Luminosity-dependent gas fractions have been proposed by Robertson et al. (2006) and Hopkins et al. (2008) as the source of the tilt in the fundamental plane scaling relation, a hypothesis which will be addressed in the next chapter.

Another possible remedy to the shallower slopes of the simulated size-luminosity relations is to weight the contributions from various simulation subsamples differently. Applying a simple linear weighting scheme of favouring B.n$_s$=1 groups at low luminosity and B.n$_s$=4 at high luminosities yields a steeper slope than a uniform weighting and a closer match with observations.

Such a weighting also produces steeper slopes than either the Few- or Many-merger relations alone and can be justified if more massive halos undergo more mergers. While average halo merger rates are not strongly mass dependent (Stewart et al., 2008; Fakhouri et al., 2010), the groups we have simulated here would likely be those with higher than average merger rates.

Although these schemes could resolve the mismatch in slopes, none save dissipation are viable solutions to the problem that simulated remnants are generally too large at fixed luminosity (Fig. 3.7). Our estimated stellar mass-to-light ratios are already quite low, so making small galaxies brighter appears to be out of the question. Numerical resolution effects are not large (Appendix A.2). Barring a strong redshift dependence in the sizes of observed ellipticals, this discrepancy is real. As a result, the Kormendy relation (Fig. 3.8) is poorly reproduced. Remnants are too faint at fixed sizes, so their effective surface brightnesses are also too faint by about a magnitude for small galaxies. The shallower slopes of the size-mass relation also translate into a weak simulated Kormendy relation (nearly non-existent in the case of the B.n$_s$=1 sample).

Faber-Jackson Relation

The Faber-Jackson relation of simulated galaxies shows even smaller scatter (0.04 dex) than their size-luminosity relation or any observed Faber-Jackson relation (typically 0.08 dex, as in Fig. 3.9 and Tab. 3.5). The simulated remnants also have slightly shallower slopes ($\sigma \propto L^{0.28}$) than the observations ($\sigma \propto L^{0.27-0.37}$), again depending on sample and weighting scheme. Curiously, the slope of the Faber-Jackson relation is nearly identical to that of the progenitor spiral Tully-Fisher relation ($V \propto L^{0.29}$), so multiple mergers appear to preserve the scaling of orbital velocity with mass while converting ordered rotation into random motions. This is despite the fact that the virial ratio in each group varies significantly, and so galaxy orbits within each group are not scaled uniformly the same way that stellar orbits within galaxies are.

In virtually all cases, the slope of the remnant Faber-Jackson relation is steeper than the canonical value of 0.25 (or $L \propto \sigma^4$). However, the observed relations show similar deviations and there is no compelling reason why ellipticals should follow this canonical relation. Indeed, the simulations of Boylan-Kolchin et al. (2006) predict scalings as steep as $M \propto \sigma^{12}$ for major mergers with very small pericentric distances, so such deviations from the canonical relation are not unexpected.

In most samples, the simulations have smaller dispersions than observed galaxies of the same luminosity. No weighting scheme can resolve this mismatch in the intercept of the Faber-Jackson relation, which is of similar magnitude (but opposite sign) as the offset in the intercept of the size-luminosity relation. Increasing the stellar mass-to-light ratios of the simulations would make galaxies of the same dispersion fainter but would worsen the match to the size-luminosity relation by making small remnants even fainter. Dissipation appears to be necessary here - central starbursts have been shown to increase velocity dispersions and shrink effective radii compared to purely dissipationless mergers (Hopkins et al., 2009). However, it is not clear

whether a mass-dependent gas fraction would preserve the slope or flatten it. The mild curvature in the observational relations may be a systematic effect at low dispersions, although we have attempted to minimize such systematics by including two independent dispersion measurements. On the other hand, the simulated relations are insensitive to the choice of velocity dispersion measure (central or effective; including rotational support or not) and most observed relations are insensitive to various weighting schemes.

Time or Redshift Dependence

All of the results presented above apply to simulations analysed after 10.3 Gyr, assuming an initial formation redshift of z=2.0 - a redshift at which pure dry mergers of disks are not likely to be common. However, the first merger in the group typically only occurs after another 1-2 Gyr. The scaling relations of remnants after 5 and 7.7 Gyr are similar to those at 10.3 Gyr, as shown in Appendix B.1, and so similar conclusions would be reached by assuming that the first merger occurred at z=0.5, when mergers were more likely to be dry or gas-poor. At face value, this also implies that the evolution in scaling relations is minimal; however, we caution that all of the groups are effectively the same age, so this prediction does not include any evolution from varied ages and assembly histories of real group galaxies.

3.2.3 Spiral Progenitors and Their Bulges

In the case of Sersic index distributions and scaling relations, it is tempting to consider whether a combination of progenitor bulge types (and possibly bulge fractions) could resolve the tensions with observations. To examine this further it is useful to ask what the distributions of bulge Sersic index and bulge fraction are for spirals as a function of luminosity.

Not all S+11 spirals have a distinct bulge, nor are most images of sufficient quality to accurately measure bulge properties, so we consider the subset for which a bulge plus disk fit is required - that is, those with an F-test probability that a de Vaucouleurs bulge is not required is less than 0.32. This is about half of the spiral sample. The proportion for which a free Sersic bulge is required over a de Vaucouleurs bulge is much smaller, so we do not limit the sample any further, except to exclude galaxies with extreme bulge fractions ($0.1 < B/T_r$ or $B/T_r \geq 0.9$). Fig. 3.15 shows the probability densities of bulge Sersic indices as a function of galaxy luminosity, split into different bulge fraction bins. In all bins, classical (n_s=4) bulges are at least a local maximum, although extreme bulge Sersic indices (n_s=0.5 and n_s=8, which are the lower and upper limits for S+11) are often the most common. The dependence on luminosity is not very strong, but in most bulge fraction bins, fainter spirals are slightly more likely to have low Sersic index bulges than high.

The S+11 spiral sample is known to be contaminated by S0s. In Fig. 3.16, we instead use the much smaller but visually classified sample of spirals from N+10. This smaller sample does show slight evidence for a correlation between luminosity and bulge Sersic index, at least for more bulge-dominated spirals. Also, the large fraction of bulge Sersic indices below 1 is greatly

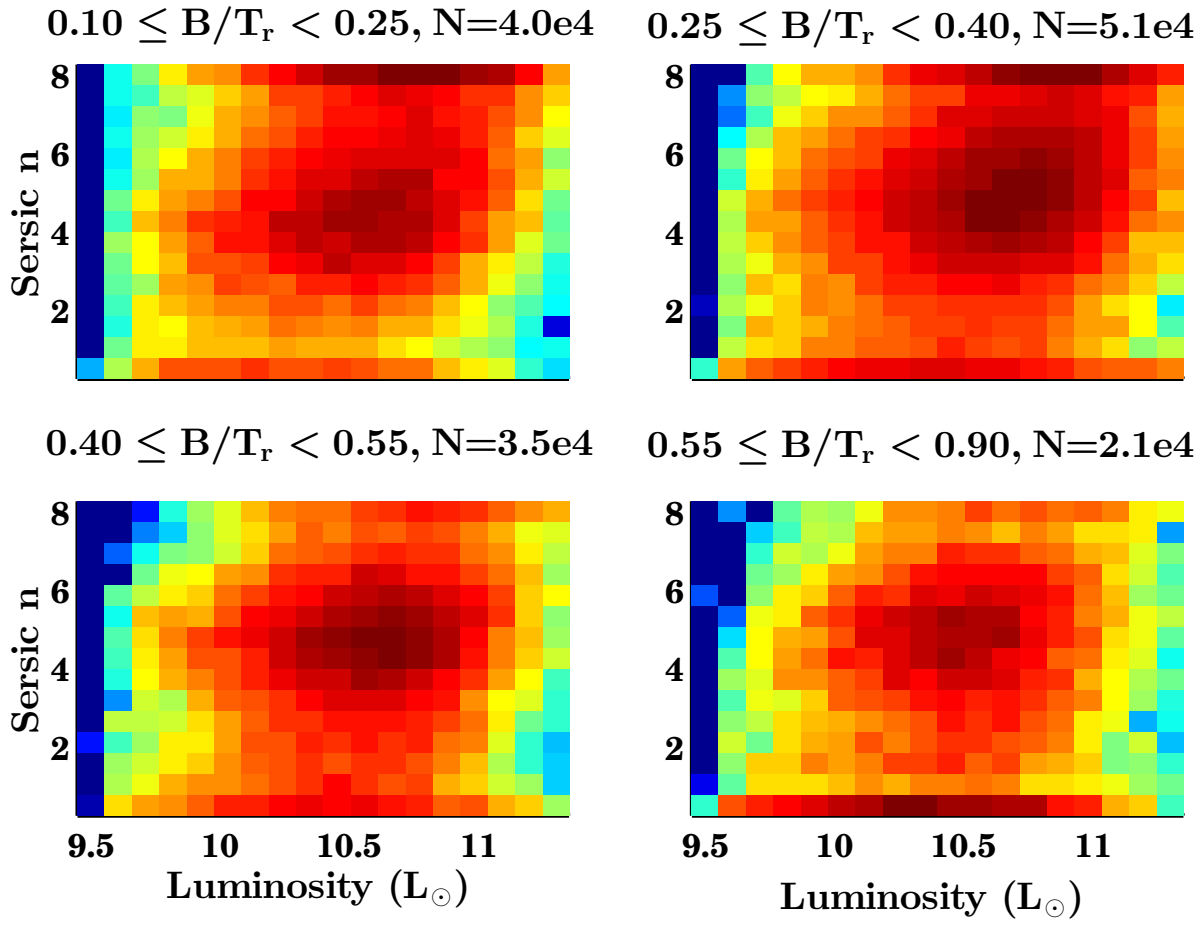

Figure 3.15: Relations between total luminosity and best-fit bulge Sersic index as a function of r-band bulge-to-total luminosity ratio in S+11 spiral galaxies. Plots show probability density on a logarithmic scale, with dark red the highest and blue the lowest densities. Only galaxies with a distinct bulge component are included. All galaxies have an F-test probability that a bulge component is not required for a good fit of less than 0.32, as well as $0.1 \leq B/T_r < 0.9$. Each galaxy is weighted by $1/\mathrm{V_{max}}$ to correct for incompleteness.

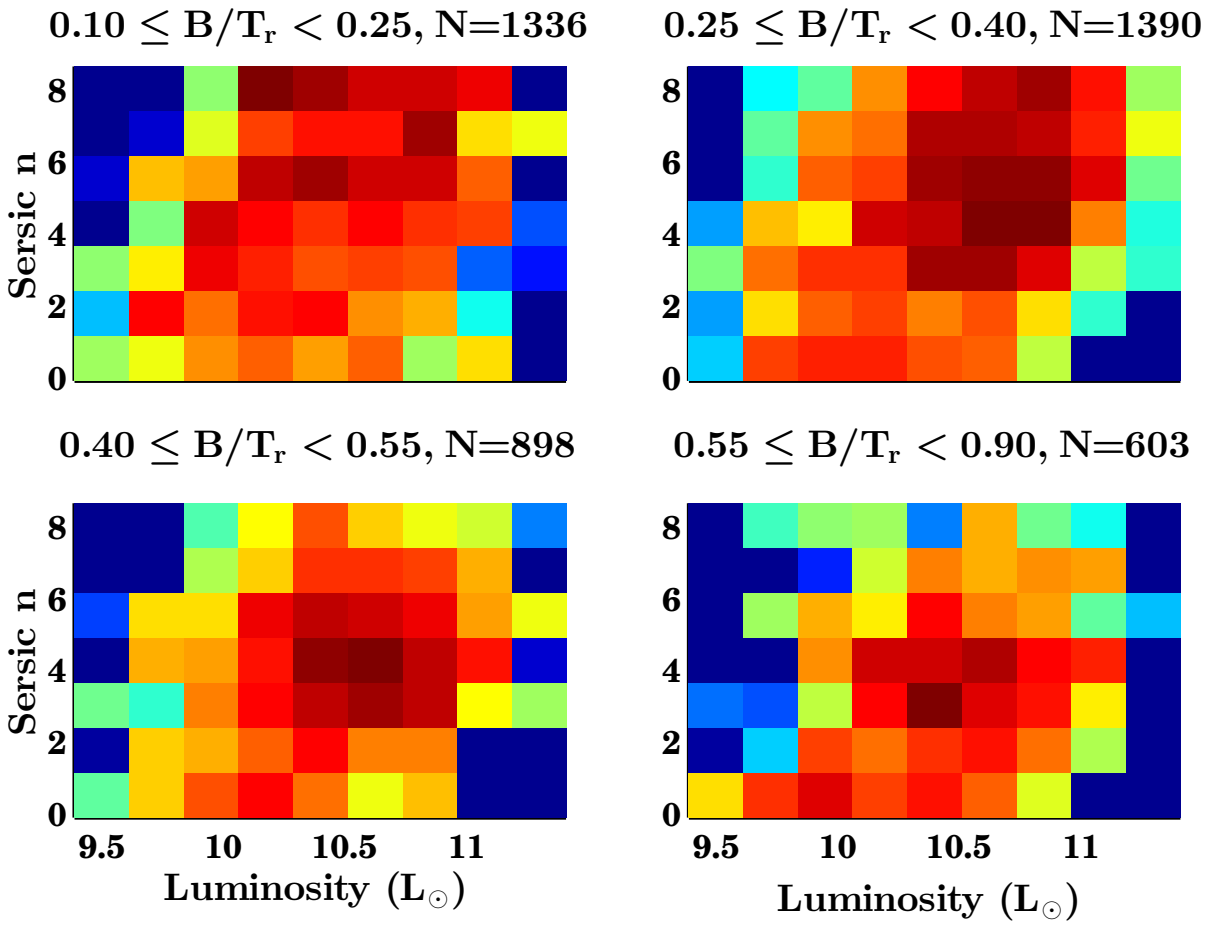

Figure 3.16: Spiral galaxy bulge properties as in Fig. 3.15, but now for visually classified N+10 spirals. Although the statistics are barely sufficient, there does appear to be a weak correlation between luminosity and bulge Sersic index for spirals with large bulge fractions, more so than in Fig. 3.15.

diminished, suggesting that those could be primarily S0 contaminants in the S+11 sample, or possibly more poorly resolved, higher-redshift spirals which appear in S+11 but not N+10. In either case, both samples contain substantial fractions of spirals with large bulge fractions.

The M31 model used in our simulations has a large bulge mass fraction (0.33) and luminosity fraction (0.5). Such fractions are not uncommon, even at low luminosities. de Vaucouleurs bulges are also quite common, whereas exponential bulges are at least not exceptionally rare, especially for bulge-dominated spirals. Even if groups of spirals have broad distributions of bulge profiles, as in Fig. 3.15, their median values could also lie close to the limiting cases of exponential or de Vaucouleurs in our simulations. Also, a wide distribution of bulge profiles is indeed a realistic solution to the problem of single-progenitor mergers producing remnants with narrow Sersic index distributions. Real mergers in groups would likely produce wider, less bimodal distributions of Sersic indices than the single-progenitor simulations.

3.2.4 Rotational Support

The abundance of fast-rotating, faint ellipticals is at odds with the simulation predictions. However, as Figs. 3.10 and 3.11 show, multiple mergers can product remnants with moderate rotational support. This contrasts with the results of Cox et al. (2006) that dissipationless binary mergers only produce slow-rotating remnants with $v/\sigma < 0.15$ - all the more so because Cox et al. (2006) measured major axis rotation curves, whereas our simulations (and A3D) average over R_e. Nonetheless, our simulations are unable to produce any remnants with $\lambda > 0.35$. The simulated remnants show little or no change in rotational support as a function of luminosity (Fig. 3.13), unlike observations, and do not produce any of the fast-rotating, moderately luminous S0s found in A3D. There is also an abundance of flattened remnants with minimal rotation, unlike in A3D. Cox et al. (2006); Bois et al. (2011) and others have shown that significant rotation can be easily produced in gas-rich mergers. Dissipation is likely necessary to produce some ellipticals, particularly faint ones, and most likely a large fraction of S0s - if S0s are formed through mergers. However, it should emphasized that many of the simulated galaxies are consistent with the properties of some A3D galaxies, particularly bright ellipticals, so dissipation may not be necessary in all cases.

3.3 Conclusions

We have investigated the hypothesis that elliptical galaxies can form through collisionless mergers of spiral galaxies by creating a sample of numerical simulations of such mergers and comparing the results directly with observations of local ellipticals. We draw the following key conclusions:

1. For a given fixed bulge type, central remnants have narrow distributions of Sersic indices, with mergers of spirals with exponential bulges producing less concentrated remnants ($\sim$

n_s=3) than classical-bulge merger remnants ($\sim$ n_s=5). Although classical-bulge mergers alone are a better fit than exponential-bulge mergers, a combination of progenitor bulge profiles is required to reproduce observed Sersic index distributions.

2. Classical-bulge mergers produce a correlation between luminosity and Sersic index, whereas exponential bulge mergers do not. The observed correlation is best reproduced if exponential bulge mergers preferentially produce faint ellipticals and classical bulge mergers produce bright ellipticals.

3. Every simulation sample produces tight scaling relations, with approximately 0.1 dex scatter for the size-mass relation and 0.04 dex scatter in the Faber-Jackson relation. Thus, even multiple dry mergers can produce ellipticals with exceptionally tight scaling relations. However, the scatter estimates represent a lower limit, because the progenitor spirals in our simulations follow a fixed, zero-scatter Tully-Fisher relations. The scatter in the remnants scaling relations would likely increase (though not necessarily significantly) if the progenitor scaling relations had larger intrinsic scatter or evolved with redshift.

4. The remnant size-luminosity relation typically has a shallower slope ($R \propto L^{0.5-0.6}$) than observed relations ($R \propto L^{0.6-0.8}$), depending on the sample and weighting scheme used. The simulated slope is also steeper than that of the progenitor spiral size-luminosity relation ($R \propto L^{0.42}$), suggesting that mergers can steepen the size-luminosity relation.

5. As a consequence of the shallower slopes and larger intercepts of the simulated size-luminosity relation, the simulated Kormendy relation is shallower than observed - nearly flat for exponential bulge mergers - and has larger scatter.

6. The remnant Faber-Jackson relation has a slightly shallower slope ($\sigma \propto L^{0.28}$) than most of the observed relations ($\sigma \propto L^{0.27-0.37}$), but is virtually unchanged from the progenitor spiral Tully-Fisher relation, $V \propto L^{0.29}$.

7. The slopes of the scaling relations can be better reproduced if massive ellipticals are produced by many mergers and less massive by fewer mergers, or if stellar mass is compared instead of luminosity.

8. The intercepts of the size-mass and Faber-Jackson relations can be individually matched by adjusting the stellar mass-to-light ratios of the galaxies; however, each relation requires adjustment in the opposite sense (remnants of a fixed luminosity being too large and having too low of a velocity dispersion), so it is not possible to match both intercepts simultaneously.

9. Multiple mergers can produce remnants with modest rotational support ($v/\sigma > 0.1$); however, most remnants are slow rotators, and there is no correlation between luminosity and v/σ, whereas such a correlation is found in ATLAS3D ellipticals.

These results demonstrate that many of the properties of elliptical galaxies are consistent with their emergence through multiple dry mergers of spiral galaxies. Perhaps most importantly, these properties also differ significantly from those of remnants formed through binary dry mergers of spirals, as reported in previous studies. This not only adds to an increasing body of evidence supporting the case for multiple mergers (e.g. Bournaud et al., 2007; Naab et al., 2009; Trujillo et al., 2011; Hilz et al., 2013) but also demonstrates that such mergers can produce tight scaling relations - in some cases tighter than observed ellipticals - as long as the progenitor spirals are drawn from a realistic luminosity function and scaled appropriately.

Several major concerns remain for a purely dissipationless formation scenario for elliptical galaxies. The first is the limited amount of rotational support in the merger remnants and the absence of any correlation between rotation and luminosity. The second is the large sizes (and low velocity dispersions) of faint ellipticals, which result in a shallow size-luminosity relation and poorly reproduced Kormendy relation. While this second point could be resolved without dissipation (e.g. by merging more compact disks at high redshift), dissipation does appear to be necessary to produce fast-rotating ellipticals. Dissipation could also solve the second problem, as central starbursts would produce more compact remnants with higher dispersions.

Perhaps the greatest challenge for dry mergers lies in matching the tilt of the fundamental plane with respect to the virial relation. Previous work has suggested that dissipational processes are the cause of this tilt and that dry mergers cannot produce any tilt (Robertson et al., 2006; Hopkins et al., 2008). This point will be addressed in the following chapter.

Chapter 4

The Fundamental Plane of Elliptical Galaxies

In §1.3, we introduced the fundamental plane of elliptical galaxies as a key scaling relation providing strong constraints on the formation histories of ellipticals. The fundamental plane is an empirical relation between the velocity dispersion σ, mean surface brightness μ and size R of elliptical galaxies. This relation, introduced by Djorgovski & Davis (1987) and Dressler et al. (1987), is sufficiently important that it warrants a more thorough derivation and review, which will serve as an introduction to this chapter. Following this review are detailed results relating to the fundamental plane, virial theorem and dynamical masses.

4.1 Review

4.1.1 The Tilt of the Fundamental Plane

Taking the liberty of assuming a consistent set of units of size (kpc), velocity (km s^{-1}), mass ($M_\odot$), luminosity ($L_\odot$), and surface brightness (mag/arcsec^2), and omitting these units from logarithms, one can write the FP as:

$$\log R = a \log \sigma + b\mu + c, \text{or:} \tag{4.1}$$

$$\log R = \alpha \log \sigma + \beta \log L + \gamma, \text{where:} \tag{4.2}$$

$$\alpha = a/(1-5b),\ \beta = -2.5b/(1-5b), \tag{4.3}$$

and γ and c are related by a unit-dependent constant. These relations can be tied to the scalar virial theorem (SVT) for a relaxed object, which states that $2T + W = 0$, where T and W are the total kinetic and potential energy, respectively. We distinguish between the SVT and the full (or tensor) virial theorem, which contains additional terms. Now if $T \propto M\sigma^2$, and

$W \propto M^2/R$, then $M\sigma^2 \propto M^2/R$, and $R \propto M/\sigma^2$. This yields the virial scaling:

$$\log R = -2\log\sigma + \log M + c_v. \tag{4.4}$$

Now Eqn. 4.2 can be rewritten as:

$$\log R = \alpha\log\sigma + \beta\log M + \beta[\log(M_\star/M) - \log(M_\star/L)] + \gamma. \tag{4.5}$$

The term $M_\star/L$ is simply the stellar mass-to-light ratio (sometimes written as $\Gamma_\star$), whereas $M_\star/M$ is the stellar mass fraction within R. If these two terms are constant, and if the assumptions of virial equilibrium and the scalings of T and W that yielded Eqn. 4.4 all hold, then equating Eqn. 4.4 and Eqn. 4.5 immediately yields $\alpha = -2$ and $\beta = 1$, the "virial" coefficients. Similarly, the virial coefficients $a = 2$ and $b = 0.4$ for Eqn. 4.1.

One can also begin with a dimensional equality $\sigma^2 = kGM/R$. The term k is often referred to as the "structural non-homology" parameter, because it is constant for self-similar (homologous), virialised systems, but can vary if the assumptions that yielded Eqn. 4.4 do not hold. It is also referred to as the "virial parameter", because its definition is an equality between kinetic and potential energy (per unit mass), at least dimensionally. This equality can be arranged into the virial FP by taking logarithms of both sides:

$$\log R = -2\log\sigma + \log M + \log(kG), \tag{4.6}$$

or:

$$\log R = -2\log\sigma + \log L + \log(M/M_\star) + \log(M_\star/L) + \log(kG). \tag{4.7}$$

These forms are identical to Eqn. 4.4, except that the previously arbitrary intercept c_v is composed of a constant G and a potentially variable term, k. However, fitting a FP of the form of Eqn. 4.2 to observational data consistently yields coefficients $\alpha \neq -2$ and $\beta \neq 1$. This is the tilt of the FP, and it exists because the tilt terms $\log(M_\star/L)$, $\log(M/M_\star)$ and $\log k$ depend on some combination of R, L and σ.

Up to this point, we have not been specific about the exact definitions of M, L, R or σ. To some extent the definitions are arbitrary, especially for the size R. Even the total mass and luminosity are difficult to define, since galaxies typically do not have well-defined limits or edges, and also because the total mass must be inferred from kinematics and/or gravitational lensing. The dispersion σ is necessarily limited to a line-of-sight measurement, though can be corrected for rotation. Nonetheless, it is necessary to define a size and luminosity measure, so we will continue to use the parametric Sersic (1968) profile fits described in §2.2.1.

In keeping with convention, the dispersion σ is the central, luminosity-weighted, line-of-sight dispersion within $R_e/8$, whereas the luminosity-weighted dispersion within R_e is written as σ_e. Observers often prefer to use surface brightnesses rather than luminosities, mainly because surface brightnesses are nearly distance-independent and allow for the calibration of the FP

as a distance indicator. A common choice derived from the Sersic profile is the mean surface brightness within R_e, which is:

$$\mu_e = -2.5\log[(L/2)/(\pi R_e^2)] + 21.572 + 15 + M_{P,\odot}, \tag{4.8}$$

where $M_{\odot,P}$ is the absolute magnitude of the sun in a given photometric band P. The factor of 15 is for units of $L_\odot$ and kpc. Substituting into Eqn. 4.7 gives:

$$\log R_e = 2\log\sigma + 0.4\mu_e - \log(M_\star/L) - \log k + \log(M_\star/M) - \log(G) - 0.4M_{\odot,P} - 15.427. \tag{4.9}$$

This is exactly the fundamental plane relation, plus four tilt terms and a fixed constant offset to return it to the virial scalings. Note that the tilt terms are not unique, and can be further subdivided, rearranged, combined or restated. For example, Hyde & Bernardi (2009a) write the non-homology term k as a ratio between dynamical and total mass, M_{dyn}/M_{tot}. Nonetheless, the stellar/dark mass fraction, stellar mass-to-light and non-homology terms are fairly universally, if not intuitively, understood in the literature.

One additional tilt term which can be considered is a correction for ordered rotation. Although ellipticals are mostly dispersion-supported, some can have significant rotation of $v/\sigma \sim 0.5$, often (but not always) aligned with the photometric major axis. This net rotation contributes to the stellar kinetic energy, which may otherwise be underestimated if only σ is measured. A corrected velocity V_{rms} (e.g. Cappellari et al., 2006) including rotation is often used in place of σ. We define a similar term S as $S^2 = \sigma_e^2(1+ < v/\sigma >^2)$, where σ_e is the luminosity-weighted dispersion within R_e rather than the central dispersion. The mean v/σ can be measured in a number of different ways depending on the source of the data; we opt for a similar luminosity-weighted average within R_e for consistency with Cappellari et al. (2011). Incorporating S modifies Eqn. 4.7 to:

$$\log R_e = -2\log\sigma + \log L + \log(M_\star/L) + \log k_S - \log(M_\star/M) + 2\log(\sigma/S) + \log(G), \tag{4.10}$$

where $k_S = S^2R/(GM) = k(S/\sigma)^2$.

4.1.2 Results from Observations

Since the original publication of Djorgovski & Davis (1987), numerous works have expanded on the FP and its tilt, both from theoretical considerations and observationally attempting to decompose the various contributors to the tilt. Bender et al. (1992) proposed an alternative coordinate system to the usual R, σ, and μ, dubbed k-space, emphasizing the need to consider both face-on and edge-on projections of the FP. Bender et al. (1993) and Guzman et al. (1993) were amongst the first to detail the importance of stellar populations (age and metallicity) in determining the $M_\star/L$ term's contribution to the tilt. Guzman et al. (1993) also quantified the spatial extent of the FP, which cannot be infinite or else its projections would have infinite

scatter.

With limited evidence available to quantify the $M_\star/M$ tilt term, attention turned to the non-homology parameter k. Prugniel & Simien (1996) attributed half of the tilt to $M_\star/L$, and the remaining half to a combination of rotational support (as we will discuss later) and structural non-homology. Prugniel & Simien (1997) derived the non-homology term as originating from non-universal mass profiles, specifically Sersic (1968) profiles with negligible dark matter within R_e. Busarello et al. (1997, see also references therein) expanded on this interpretation, shrinking the $M_\star/L$ contribution to 30% - roughly the agreed-upon modern value.

Most of these early works were limited to samples of around 100 galaxies with measured dispersions and imaging. Order-of-magnitude improvements came with the advent of wide-field surveys like the Sloan Digital Sky Survey (SDSS) and 2 Micron All-Sky Survey (2MASS). Bernardi et al. (2003) analysed a sample of 9,000 galaxies from SDSS, finding evidence for environmental dependence of scaling relations (including residuals from the best-fit FP). Trujillo et al. (2004) used a sample of 911 SDSS and 2MASS galaxies (including K-band imaging insensitive to stellar population variations) to argue that the remaining tilt was entirely caused by the non-homology of (Sersic, 1968) profiles, rather than scale-dependent dark matter fractions. Subsequent work has expanded samples to over 50,000 galaxies (Hyde & Bernardi, 2009a), confirming the exceptionally small scatter of the FP (0.06 dex or less). Nair et al. (2011) used a sample (Nair & Abraham, 2010) of about 4,000 visually classified early-type galaxies (ETGs) to argue that similarly small scatter (and much smaller *intrinsic* scatter) can be found in the size-luminosity relation if Petrosian (1976) sizes are used rather than Sersic fits. Hyde & Bernardi (2009b) concluded that dark matter fraction contributions (specifically $M_{dyn}/M_\star$) are responsible for approximately half of the tilt, and stellar populations the remaining half, with additional non-homology terms being negligible. However, this was based on sizes from de Vaucouleurs (1959) profile fits, implicitly excluding non-homology from varying Sersic indices. Such systematic differences between measures of size, luminosity and stellar mass - as well as sample selection - have contributed to a lack of a general consensus on the origin of the tilt, despite the rapid growth in galaxy catalogues. It is, however, generally accepted that part of the tilt is due to variations in stellar populations - ages, metallicities, or possibly the initial mass function (IMF).

Beyond simply increasing sample sizes, recent studies have begun to quantify each component of the tilt by inferring stellar masses using stellar population models, and *total* masses using spatially-resolved kinematics and dynamical models (Rix et al., 1997; Gerhard et al., 2001; Cappellari et al., 2006, 2013b, e.g.) or from strong gravitational lensing (Bolton et al., 2008; Auger et al., 2010, e.g.). Such analyses have been complicated by the fact that stellar masses are sensitive to the assumed form of the IMF, which recent evidence suggests may be non-universal (e.g.; van Dokkum, 2008; Conroy & van Dokkum, 2012), impacting the tilt of the FP (Dutton et al., 2011). Stellar masses are also be sensitive to the assumed star formation history (Allanson et al., 2009; Graves & Faber, 2010), which is difficult to constrain or

infer even assuming a fixed IMF. The dependence of stellar mass on star formation history can severely bias estimates of the contribution of stellar population variations ($M_\star/L$) to the FP tilt. Allanson et al. (2009) reported that 74% of the I-band FP tilt can be explained by stellar population variations assuming a single-burst (SSP) history (63% in K-band), or 50% (38% in K-band) for a model with continuous star formation followed by abrupt quenching. Graves & Faber (2010) noted that SSP models generally provide an upper limit to the $M_\star/L$ term, quoting a fraction of 58% of the tilt from $M_\star/L$ using an SSP model. A variety of more complex models yielded fractions ranging from as low as 13% to 41%. Even lensing and dynamical masses must be modelled and inferred and cannot be directly measured, so the details of the modelling technique are important to deriving total masses even if the stellar mass is known.

Nonetheless - and given these important caveats - several studies have measured some form of mass FP comparable to Eqn. 4.4. Using the projected mass density Λ within $R_e/2$, and the mean σ within $R_e/2$, $\sigma_{e/2}$, Auger et al. (2010) found a relation $\log R_e \propto (1.83 \pm 0.13) \log \sigma_{e/2} - (1.30 \pm 0.06) \log \Lambda$. This is equivalent to $\log R \propto \alpha \log \sigma_e + \beta \log M$ with $\alpha = -1.14$ and $\beta = 0.81$. Neither of these coefficient pairs are exactly the virial FP coefficients.

In an independent sample of local early-type galaxies with spatially resolved kinematics, Cappellari et al. (2013b) inferred total masses from dynamical modelling of stellar kinematics. This yielded a best-fit plane of the form $\log M_{model} \propto \alpha \log \sigma_e + \beta \log R_e$, with $\alpha = 1.928 \pm 0.026$ and $\beta = 0.991 \pm 0.024$, which is very nearly the virial plane. While this would seem to imply that the FP is simply a reflection of the fact that galaxies are virialised, recall that Eqn. 4.4 required the assumption that $M\sigma^2 \propto T$, and that $M^2/R \propto T$. Both assumptions have yet to be validated directly. Indeed Cappellari et al. (2013b) point out that the fact that k appears to be constant for their particular choice of mass (and radius) definition is not necessarily an obvious extension of the virial theorem, since real galaxies can be complex, multi-component systems. We will return to this point later.

4.1.3 Results from Theory

Galaxy mergers have long been thought to form elliptical galaxies, and numerical simulations - especially N-body simulations - have been a particularly powerful tool for testing this hypothesis (see Struck (1999) and Struck (2006) for excellent reviews). However, a much smaller fraction of the literature has attempted to predict or explain the nature of the FP and its tilt. Weil & Hernquist (1996) presented detailed simulations of mergers in groups, but their predictions for the FP were left unpublished (see Weil, 1995). Bekki (1998) presented one of the first analyses of the FP tilt in dissipational binary spiral merger simulations, suggesting that dissipation could establish non-homology. A number of studies alternatively focused on mergers of spheroidal galaxies, including Capelato et al. (1995), Nipoti et al. (2003), Boylan-Kolchin et al. (2005, 2006) and more recently Hilz et al. (2013). Most of these studies have focused on determining whether the FP and its tilt can be preserved in subsequent mergers of spheroids - so far, the answer is "maybe," depending on the number of mergers, mass ratios, orbital parameters and

properties of the merging systems.

Elliptical galaxies are still thought to form primarily from mergers of spirals (but see Naab & Ostriker, 2009); so, such simulations of mergers of spheroids have not determined how the FP is established in the first place. Aceves & Velázquez (2005) presented simulations of binary mergers of spirals scaled to follow the observed Tully-Fisher (TF) relation (Tully & Fisher, 1977). These merger remnants were similar to ellipticals and followed a tilted FP even in the absence of gas dissipation, owing to the precise scaling of the progenitor spirals. By contrast, Robertson et al. (2006) reported that dissipational binary mergers were sufficient to create a tilted FP ($a = 1.55$ and $b = 0.33$) with 0.06 dex scatter. Hopkins et al. (2008) went a step further in claiming that dissipation is both necessary and sufficient to create the FP. However, such binary merger simulations did not incorporate truly hierarchical cosmological merger histories and so did not consider the impact that repeated, mainly minor mergers may have on the size and mass growth of ellipticals. Although a few consecutive re-mergers of merger remnants were included, binary mergers alone do not capture the full range of possible merger histories of ellipticals, and so are at risk of overestimating the role of dissipation over structural non-homology from dissipationless merging, as reported by Aceves & Velázquez (2005).

A relatively new class of cosmological "zoom" simulations can in principle follow realistic merger histories and form elliptical galaxies self-consistently. Zoom simulations have been used to study 2D scaling relations (Naab et al., 2009; Oser et al., 2012) and detailed kinematics (Naab et al., 2013), but not the fundamental plane, as far as we are aware - perhaps due to the necessarily limited resolution of full cosmological simulations. Oñorbe et al. (2006) presented scaling relations from cosmological simulations in small volumes (10 Mpc-side boxes), but with low resolution by today's standards (64^3 gas and dark matter particles each). Feldmann et al. (2011) and Dubois et al. (2013) compared their central group galaxies to the projected fundamental plane, but with 6–7 galaxies each, neither study had the statistics to fit scaling relations. As a compromise, Chapter 2 presented controlled merger simulations of spirals in groups, incorporating cosmologically-motivated merger histories and measuring accurate sizes, dispersions and luminosities for central group ellipticals. We now aim to extend the analysis of the morphologies and kinematics of these galaxies to discern the relative importance of dissipationless merging to the FP.

4.2 Methods

The simulation methods and data are essentially identical to those presented in §2.1, while the observational data are from the same sources as in §2.3, with some updates to SDSS. Any changes to the methodology are detailed below.

To summarize, all sizes, ellipticities and Sersic indices are derived via two-dimensional, single Sersic profile fits, where possible. Unless otherwise specified, we define R_e as $\sqrt{ab}$, where a and b are the major and minor axes of the best-fit Sersic ellipse, respectively. All projected quantities

measured within R_e are measured within the best-fit ellipse, not a circle. By convention, the central dispersion σ is defined as the projected velocity dispersion within $R_e/8$; we refer to the luminosity-weighted dispersion within R_e as σ_e. All magnitudes and luminosities are for the SDSS r-band.

In keeping with previous works, we assume that the dynamics of the galaxy are related to the total mass within R_e, rather than the total mass of the galaxy. We refer to projected total mass within the ellipse defined by R_e and the ellipticity e as $M_{R_e,2D}$ - similar to a lensing mass. We also define the mass enclosed within a sphere of radius $\langle R_e \rangle$ as $M_{R_e,3D}$, where $\langle R_e \rangle = \sqrt[3]{R_{maj}R_{med}R_{min}}$ - the cube root of the product of R_e from each principal axis projection. $M_{R_e,3D}$ is then the mass contained within a sphere which encloses roughly half of the galaxy's light in any given projection, and slightly less than half in three dimensions.

4.2.1 Simulation Data

The simulation data are identical to those presented in §2.1. The simulations consist of over a hundred galaxy groups, initially comprising three to thirty spiral galaxies sampled from a realistic luminosity function. Each group was designed to collapse like a high redshift (z=2) group at the turnaround radius, inducing mergers and forming a central elliptical. Unlike previous merger simulations, the groups were meant to sample a variety of plausible cosmological accretion histories, albeit not an unbiased sample. The initial galaxies were also chosen to follow the observed Tully-Fisher relation (Tully & Fisher, 1977) with no intrinsic scatter.

The initial conditions in the simulations were tightly controlled, allowing only a few parameters to vary. All of the galaxies were self-similar, re-scaled models of M31 (Widrow et al., 2008). Two versions of each simulation were run: one where the spirals began with an exponential bulge (the "bulge Sersic index=1" or B.$n_s = 1$ sample), and another otherwise identical run with de Vaucouleurs profile bulges (B.$n_s = 4$). This roughly brackets the range of realistic bulge profile in spiral galaxies, allowing us to test the impact of input galaxy structure on the properties of the final remnant. Additionally, groups of a given mass were seeded with varying numbers of galaxies, in order to test the impacts of multiple, mostly minor mergers versus a few mostly major mergers. We distinguish between these subsamples as "Many" (M) and "Few" (F), where the former groups began with a larger-than-average number of galaxies for their mass. Similarly, the main group sample had galaxy luminosities drawn from a realistic luminosity function ("LF"), whereas a smaller control sample featured equal-mass mergers ("Eq").

4.2.2 Observational Data

We use 2D Sersic fits from Simard et al. (2011, hereafter S+11) and visual morphological classifications from Nair & Abraham (2010, hereafter N+10), both based on SDSS data. We also use spatially resolved kinematics for 65 nearby ellipticals from ATLAS3D (Cappellari et al., 2011), including kinematic measures from Cappellari et al. (2013b), and stellar mass-to-light

ratios and dark matter fractions from Cappellari et al. (2013a). In Chapter 3, we used 2D GALFIT fits described in the appendix of Krajnović et al. (2012). In this chapter, we will use the values of L and R_e tabulated in Cappellari et al. (2013b), as recommended by the authors of that paper. Although these are not derived from 2D Sersic fits, they are generally similar for most galaxies and allow for more direct comparison to Cappellari et al. (2013b). Since spatially resolved kinematics are unavailable for most SDSS galaxies, we use central velocity dispersions σ unless otherwise specified.

Wherever possible, we have opted to use similar methodologies in all cases. The simulation sizes and luminosities are based on single Sersic fits using GALFIT (Peng et al., 2002, 2010). SDSS data use single Sersic fits from GIM2D (Simard et al., 2002). SDSS stellar masses are based on fits to photometry (Mendel et al., 2014), using a Chabrier (2003) initial mass function (IMF). These stellar masses are on average marginally but not significantly different from those used in §2.3, and we refer to Mendel et al. (2014) for full details. A3D stellar masses are derived by multiplying the model L_r with the M/L_r derived from fits to spatially resolved spectra assuming a Salpeter (1955) IMF (Cappellari et al., 2012, 2013a). To maintain consistency with the normalization of M/L values with different IMFs, we divide the A3D M/L_r by a factor of 1.7, which compensates for the systematically larger M/L_r in a Salpeter IMF for an old, solar-metallicity population. This does not entirely account for systematic differences between stellar masses from the two samples, and Mendel et al. (2014) caution that stellar masses derived from photometric fits are subject to up to 60% systematic errors. We similarly caution against over-interpretation of trends based on stellar masses with a fixed IMF.

4.3 The Fundamental Plane and the Virial Theorem

4.3.1 The Fundamental Plane

The FP relation is typically written as $\log R_e = a \log \sigma + b\mu + c$, as in Eqn. 4.1. We derived this relation from the SVT in the traditional way in §4.1.1. The FP can also be expressed in terms of L instead of μ. This formulation is equivalent to using μ, and Eqn. 4.3 gives simple transformations between the luminosity and μ FPs. While luminosity is arguable a more fundamental variable, being independent of R_e, we will use μ for the moment for consistency with previous studies.

Fig. 4.1 shows the projected FP, with two variables (σ and μ_e) collapsed onto the x-axis, as in Hyde & Bernardi (2009a). This visually demonstrates the exceptionally small orthogonal scatter of the FP, even for the exponential bulge ($\mathrm{B.n_s} = 1$) sample, which is not shown exactly edge-on. Similarly, the tilt does depend on the structure of the progenitors, since it is larger in magnitude for the $\mathrm{B.n_s} = 4$ sample, as is the extent of the FP.

Tab. 4.1 tabulates best-fit FP parameters for simulations and observations alike. Several trends are clear from the simulations. First, the tilt is smaller than observed but definitely in the correct sense: $a < 2$ and $b < 0.4$. The scatter in the simulations is exceptionally small (0.02

Table 4.1: Sersic model Fundamental Plane fits

Simulations: Ten equally-spaced projections, randomly oriented

$B.n_s$	Subsample	a	b	Intercept	R.M.S.
1	All	1.74	0.32	-9.50 ± 0.06	0.02
1	Many	1.80	0.31	-9.49 ± 0.10	0.02
1	Few	1.70	0.31	-9.26 ± 0.11	0.02
4	All	1.64	0.29	-8.65 ± 0.04	0.02
4	Many	1.67	0.28	-8.60 ± 0.06	0.02
4	Few	1.64	0.29	-8.62 ± 0.08	0.02
All	All	1.69	0.29	-8.89 ± 0.04	0.02
All	Many	1.75	0.28	-8.71 ± 0.05	0.02
All	Few	1.66	0.29	-8.85 ± 0.07	0.02

Principal axis projections, unweighted

$B.n_s$	Projection	a	b	Intercept	R.M.S.
1	Major axis	1.76 ± 0.03	0.30	-9.22 ± 0.25	0.03
1	Minor axis	1.71 ± 0.02	0.31	-9.30 ± 0.29	0.02
4	Major axis	1.71 ± 0.02	0.28	-8.74 ± 0.14	0.02
4	Minor axis	1.58 ± 0.01	0.28	-8.36 ± 0.12	0.01

Observations

Cat.	T.	W.	a	b	Intercept	R.M.S.
S+11	E	N	1.35 ± 0.00	0.28	-7.89 ± 0.01	0.06
S+11	E	Y	1.28 ± 0.00	0.29	-7.95 ± 0.01	0.06
N+10	E	N	1.36 ± 0.04	0.22	-7.88 ± 0.12	0.06
N+10	S0	N	1.08 ± 0.02	0.27	-7.11 ± 0.08	0.07
N+10	E	Y	1.08 ± 0.10	0.28	-7.40 ± 0.28	0.06
A3D	E	N	1.29 ± 0.09	0.33	-9.12 ± 0.55	0.07
A3D	S0	N	0.96 ± 0.07	0.30	-7.63 ± 0.38	0.07
A3D	E	Y	1.31 ± 0.09	0.33	-9.09 ± 0.52	0.07

Slopes are given in log space, i.e., for $\log R_e$ as a function of $\log L$. Simulation data are from analyses after 10.3 Gyr, including various subsamples of randomly oriented (but equally spaced) projections, as detailed in the text, as well as principal axis projections. Simulated data include subsamples for relatively many or few mergers. Observational data for each catalogue (Cat.) and Hubble type (T.) are $1/V_{max}$ corrected, with fits optionally weighted (W.) or not by the difference between the simulated and observed luminosity functions. R.M.S. lists the r.m.s. orthogonal scatter of all points from the best-fit relation. Errors on a for simulations and on b for simulations, N+10 and S+11 are uniformly 0.01 or smaller and are omitted for brevity; for A3D, errors on b are 0.02.

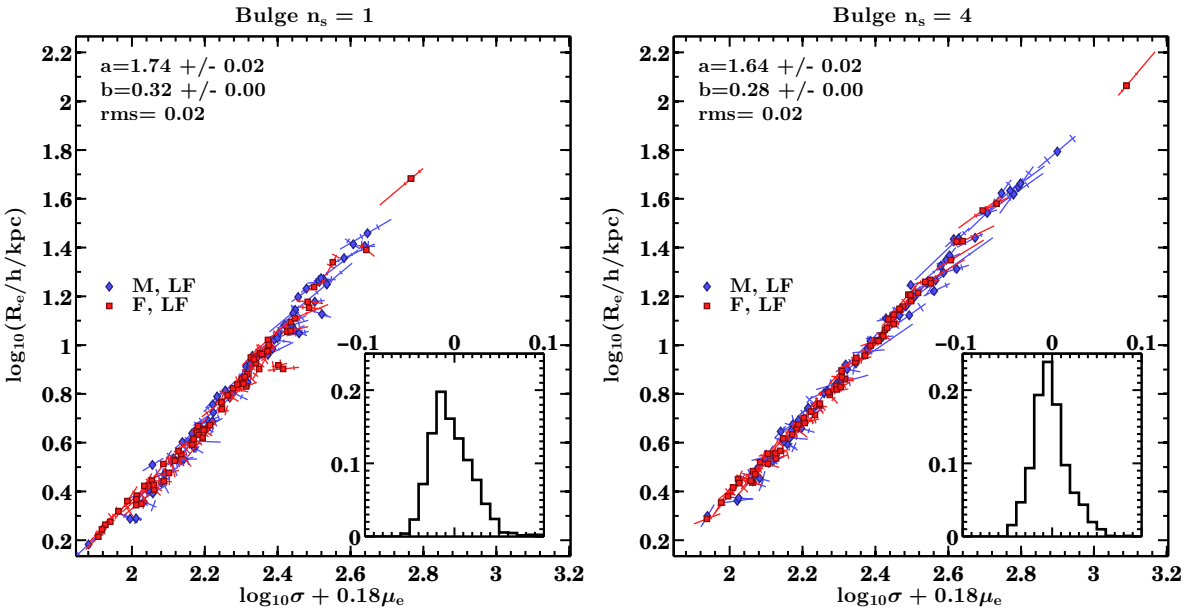

Figure 4.1: Projected FP for B.n$_s$ = 4 and 1 samples, plotted in the style of Hyde & Bernardi (2009a). The μ_e term in the x-axis includes only deviations from the mean μ_e (i.e. it is really $\mu_e - \langle\mu_e\rangle$). The coefficient 0.18 matches the average value of b/a for both panels. As in Fig. 3.3, different projections of the same group are shown as lines of best fit, with the data point marking the median projection. Inset shows the PDF of orthogonal scatter from the best-fit FP.

dex), even when combining different progenitor subsamples, and is considerably smaller than for the observations (0.06 – 0.08 dex). For the most part, the different observational samples are consistent with one another, other than unusually small a parameters for the N+10 weighted subsample and b for the unweighted (both possibly due to the undersampling of faint and small ellipticals in N+10). Nonetheless, S+11 is largely consistent with the completely independent measurements from A3D, although the A3D intercepts are slightly lower and scatter slightly larger. It is also clear that the FP of S0 galaxies is quite different from that of ellipticals; since the simulated galaxies show no signs of being genuine bulge plus disk systems, we will not consider further comparisons with S0s. It should be noted, however, that the S+11 sample is likely contaminated with S0s, which is unavoidable since no automated classification can separate them (see §2.3).

In §3.1.2, we presented optional weighting schemes which can have a significant impact on 2D scaling relations - i.e., projections of the FP. For the simulations, we weighted the "Many" merger sample more heavily at the more luminous end, and the "Few" merger sample at the faint end. This weighting does not impact the simulated FP fits, because all of these points really do lie on a single plane with minimal scatter. No weighting scheme will make a significant difference unless it changes the weights where there is curvature in a scaling relation, and there is no curvature in the simulated FP. We omit these weighted fits from Tab. 4.1, as all of the parameters are within the errors of the unweighted fits.

Table 4.2: Sersic model stellar mass Fundamental Plane fits

Simulations: Ten equally-spaced projections, randomly oriented

$B.n_s$	Subsample	a	b	Intercept	R.M.S.
All	All	1.72	0.31	-9.07 ± 0.04	0.02
All	Many	1.78	0.30	-8.91 ± 0.05	0.02
All	Few	1.69	0.32	-9.05 ± 0.07	0.02
All	All-S	1.78	0.29	-8.69 ± 0.05	0.02

Observations

Cat.	T.	W.	a	b	Intercept	R.M.S.
S+11	E	N	1.48 ± 0.00	0.28	-7.87 ± 0.01	0.06
S+11	E	Y	1.42 ± 0.01	0.28	-7.96 ± 0.01	0.06
N+10	E	N	1.56 ± 0.04	0.27	-8.09 ± 0.11	0.06
N+10	S0	N	1.26 ± 0.02	0.28	-7.76 ± 0.06	0.06
N+10	E	Y	1.25 ± 0.06	0.28	-7.67 ± 0.20	0.06
A3D	E	N	1.71 ± 0.08	0.36	-10.13 ± 0.49	0.05
A3D	S0	N	1.56 ± 0.09	0.28	-8.29 ± 0.45	0.06
A3D	E	Y	1.73 ± 0.08	0.36	-10.10 ± 0.48	0.06
A3D-S	E	N	1.78 ± 0.11	0.37	-10.04 ± 0.67	0.06
A3D-S	S0	N	1.87 ± 0.14	0.30	-9.42 ± 0.61	0.07
A3D-S	E	Y	1.83 ± 0.11	0.37	-10.50 ± 0.61	0.06

Column headings and notes are as in Tab. 4.1, but surface brightnesses/magnitudes are now based on stellar masses instead of luminosities. See text for details on sources of stellar masses. A3D-S and All-S use the kinematic measure S in place of σ, correcting for ordered rotation - see Eqn. 4.10.

A second scheme weighted the *observed* data to match the much flatter LF of the simulations. This scheme can make a significant difference (especially for N+10), which is possible if there is some curvature in the observed plane at the high mass end. In the N+10 case specifically, it may also be due to the sample selection, which selected roughly a log-normal distribution around L* rather than a magnitude- or volume-limited sample.

The FP parameters also depend on the projection angle. Choosing only minor axis projections yields the steepest FP, whereas major axis projections minimize the tilt. They can also be sensitive to the orbits of the merging galaxies - we leave this analysis to Appendix C.2. Regardless, the tilt in the simulations is weaker than observed. This difference can be quantified in various ways. One methods is to project the vector between the unit normal of the simulated plane (-1, $a \approx 1.69$, $b \approx 0.29$) and the unit normal of the virial plane (-1, $a = 2$, $b = 0.4$) onto a similar vector between the observed (-1, $a \approx 1.3$, $b \approx 0.29$) and virial plane's unit normals. This gives a "tilt fraction" of 37%. Any other quantification of the tilt fraction would yield a similar result, and so this difference requires an explanation.

The discrepancy between the predicted and observed tilt is mainly in the a parameter and is lessened if one considers the stellar mass FP (Tab. 4.2). This is justifiable because the simulations effectively do not include any stellar population variations and have a constant $M_\star/L$, whereas luminous ellipticals tend to have larger $M_\star/L$ in general (and $M_\star/L_r$ in particular),

assuming a universal IMF. This implies that a substantial portion of the tilt is due to variations in stellar populations along the FP. Once this is accounted for, the gap between the observed tilt and the $B.n_s = 4$ sample's tilt is considerably smaller. In fact, for A3D, the observed tilt in the stellar mass FP is *smaller* than in the $B.n_s = 4$ sample, as A3D has a significantly larger value of $b \approx 0.36$ than the other samples. This b value is consistent with the near-infrared J-band FP fits from the 6dF survey (Magoulas et al., 2012) of $a = 1.52 \pm 0.03$ and (effectively) $b = 0.36 \pm 0.02$, which are close to a stellar mass FP (since $M/L_{\star,J}$ is less sensitive to age and metallicity than $M/L_{\star,r}$).

It is clear that multiple dissipationless mergers can produce a tilt in the FP, and that this tilt could be a significant fraction of the observed tilt. However, we caution again that the stellar mass FP is sensitive to the assumption of a universal IMF and/or star formation history. Furthermore, the stellar masses for A3D are based on fits to spatially resolved spectra assuming a Salpeter IMF, whereas SDSS stellar masses are based on fits to photometry assuming a Chabrier IMF instead; both methods have their caveats and we make no judgement as to which are more likely to be accurate.

Finally, Tab. 4.2 includes a fit to the FP using S in place of σ, for A3D and the simulations. Using S lowers the tilt slightly in A3D, although only significantly for the S0s - not surprisingly, since they show more rotational support and are more affected by the v/σ correction. Using S in the simulations makes little difference in a and actually lowers b to 0.29. This is likely because the simulated ellipticals generally have less rotational support than A3D ellipticals, as shown in §3.1.3.

4.3.2 The Tilt of the Fundamental Plane

Having established that the FP of the simulations is tilted from the virial relation, we will now decompose the FP and fit the various tilt terms from Eqn. 4.5. We use $M_{r,\odot} = 4.68$ throughout, which sets the constant in Eqn. 4.5 to -11.93.

The full tilt of the FP can be characterized from the equality $\sigma^2 = \Gamma_t GL/R_e$, where the tilt factor $\Gamma_t = k(M/L)$ is a mass-to-light ratio that encompasses the entirety of the tilt, including non-homology (k), stellar population variations ($\Gamma_\star$) and variable dark matter fractions ($M_\star/M_{R_{e,3D}}$). Fig. 4.2 shows Γ_t as a function of luminosity for the entire sample. The term clearly varies with luminosity in both observations and simulations, although the variation is shallower for simulations (unsurprisingly, since the tilt is also smaller). Nonetheless, the intercept and median values of Γ_t are consistent with S+11, though somewhat offset from A3D. This is mainly because the simulated galaxies have lower σ than observed, and A3D galaxies have slightly larger σ than the other samples. Sample selection is evidently important, since the N+10 is a subset of the S+11 samples and uses the same σ, R_e and L measures, but shows an anomalous break in Γ_t at $2 \times 10^{11} L_\star$. This break is likely to be the cause of the difference between weighted and unweighted N+10 fits. We do not speculate further on the causes of these systematic differences and simply re-assert that the simulated tilt is at least broadly consistent

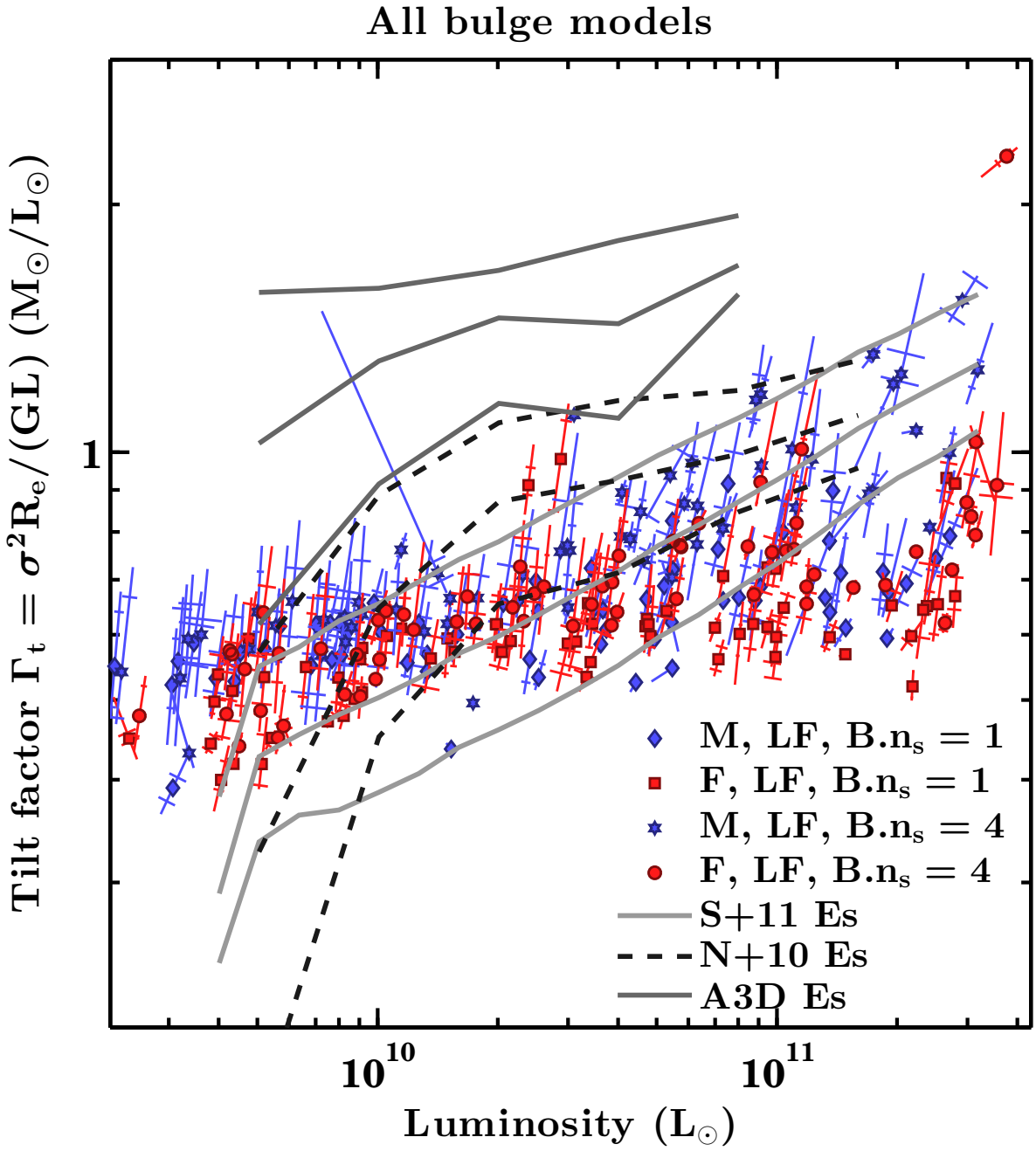

Figure 4.2: The tilt factor Γ_t for simulated and observed ellipticals. The lines for observational catalogues separate quartiles. ATLAS3D ellipticals are somewhat discrepant from both the simulated trend and observed trends for SDSS ellipticals, while the visually-classified N+10 ellipticals show a sharp drop at low luminosities (in part because N+10's sample was biased to select brighter galaxies). Nonetheless, all relations show a positive trend.

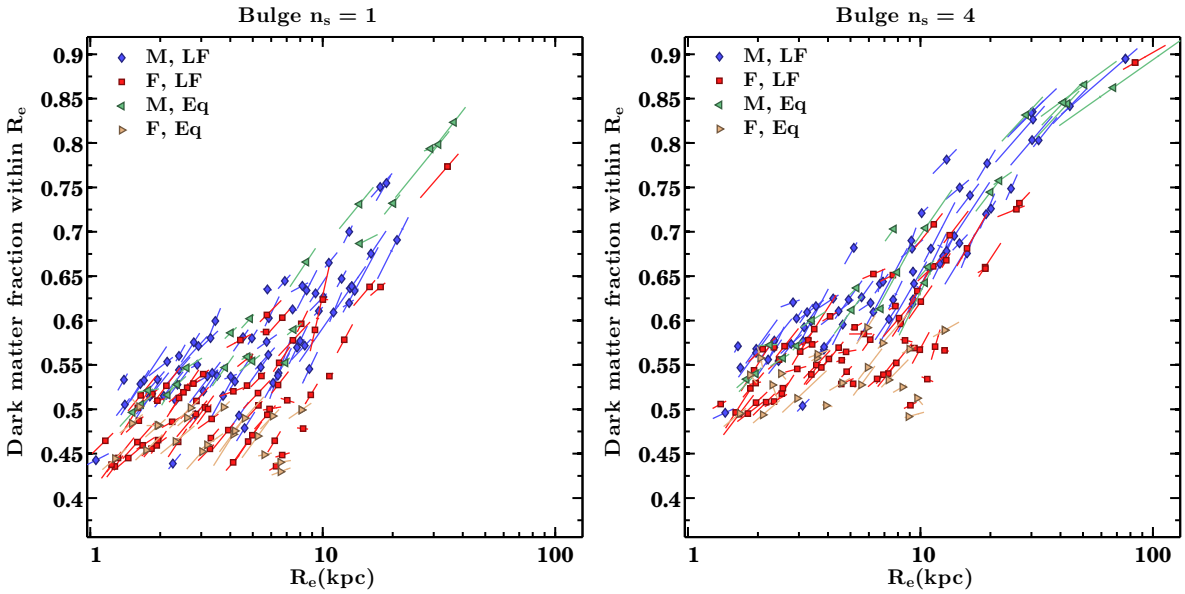

Figure 4.3: Projected dark matter fraction within R_e. The dependence of baryonic fraction with R_e ($M_\star/M$ = 1-M_{DM}/M) on size and mass is a major contributor to the tilt of the fundamental plane.

with the observed intercept and shallower in the slope.

We now turn to identifying which of the tilt terms contribute to the variable Γ_t. Fig. 4.3 shows projected dark matter fractions, i.e. $1 - M_{\star,R_e,2D}/M_{R_e,2D}$. Similar fractions of order 2–5% smaller are found for $1 - M_{\star,R_e,3D}/M_{R_e,3D}$. Dark matter fractions increase for larger galaxies, because the effective radii extend further out to regions dominated by the halo. This is evidenced by the fact that independent projections of the same galaxy with larger R_e have larger dark matter fractions - not surprising, since the dark matter fraction will increase with radius as long as the stellar density profile is steeper than the halo profile.

The non-trivial discovery here is that $M_\star/M_{R_e,2D}$ is significantly smaller in larger/more luminous galaxies, driving what would appear to be a large fraction of the tilt. This is partly caused by the fact that galaxies undergoing many mergers (M) are larger at fixed luminosity than those formed from few mergers (F; see Fig. 3.7); similarly, at a fixed size, the M subsample is less luminous and so contains a smaller stellar mass fraction. For the whole sample, we find that $M_{DM,R_e,3D} \propto R_e^2$ nearly exactly, whereas $M_{\star,R_e,3D} \propto R_e^{1.72}$, with a slightly shallower slope for the most luminous galaxies. The enclosed dark matter mass in different galaxies scales more steeply with R_e than does the stellar mass.

The full explanation for the origin of this trend in dark matter fractions is complicated by the fact that neither the stellar density profiles nor the dark halo profiles are self-similar in the merger remnants. Nonetheless, we have demonstrated that merging multiple self-similar galaxies produces a particular scaling relation for $M_\star/M$ within R_e, rather than retaining the same constant fraction that they began with (roughly 30–35%, depending on how one defines

R_e for a spiral galaxy). We will discuss the absolute values of these dark matter fractions and compare them to observations further in §3.2; for now, what matters is that the trend lies in the correct sense to cause some part of the tilt in the FP.

The three remaining terms that can contribute to the tilt are shown in Fig. 4.4, beginning with the virial parameter k_S. For a dispersion-supported, uniform unit sphere, $k_S \simeq k = 0.2$; the fact that most of the simulated galaxies have $k > 0.2$ is simply a reflection that they are centrally concentrated. We will discuss this shortly in §4.3.4. For the most part, k_S does not vary strongly with any of the FP parameters, although it tends to be larger for more luminous galaxies. At the most luminous end, a number of outliers appear with unusually low values of k_S. These tend to be systems which were shown to have overestimated R_e (see Fig. A.2), and their k_S values are small only because the $M^2_{R_e,3D}$ term in the denominator increases more rapidly than R_e. The outliers with large k_S tend to be triaxial systems with strongly projection-dependent S.

The remaining two tilt terms are also shown in Fig. 4.4 and contribute little to the tilt in simulations. The σ/S term (left panel) is nearly constant at unity in both simulations and in A3D. Again, the main outliers are groups for which R_e has been overestimated. Since projected dispersions tend to drop with radius, σ_e/σ becomes significantly smaller than unity if R_e is overestimated. While σ_e is typically quite small in A3D, it is often offset by a substantial rotation correction in v/σ. This correction is much smaller in the simulated ellipticals, since most are slow rotators (see §3.1.3).

In the simulations, $M_\star/L$ is nearly constant by construction; the only outliers are groups for which a massive satellite appears within R_e, since we have not masked or fit satellites in the stellar mass maps. By contrast, both observed data sets show a trend of increasing $M_\star/L$ with L. The A3D ellipticals appear to have a steeper slope, which may be partly due to systematics. A3D $M_\star/L$ are derived from fits to spatially-resolved spectra, whereas the SDSS $M_\star/L$ is based on fits to broadband colours. The A3D fits also assume a Salpeter IMF rather than the Kroupa IMF used in SDSS; we have adjusted the normalization of the A3D $M_\star/L$ by dividing by a factor of 1.7 to correspond to an old, Kroupa IMF, but this normalization may not be self-consistent.

4.3.3 The Virial Fundamental Plane

Having established that the dark matter fraction is likely a major contributor to the tilt, we will now fit various permutations of the FP including each tilt parameter to determine which are closest to the virial FP. To do so, one can fit an FP with R_e, a velocity (σ, σ_e or S), and a third parameter other than the usual L or μ_e. The values of the parameters are then compared to the expected virial coefficients $a = 2$, $b = 0.4$ or $\alpha = -2$ and $\beta = 1$, depending on whether the third parameter is a mass/luminosity or surface density. In principle, the fits should be convertible using Eqn. 4.3, but in practice the choice can be significant. As an example, one fit

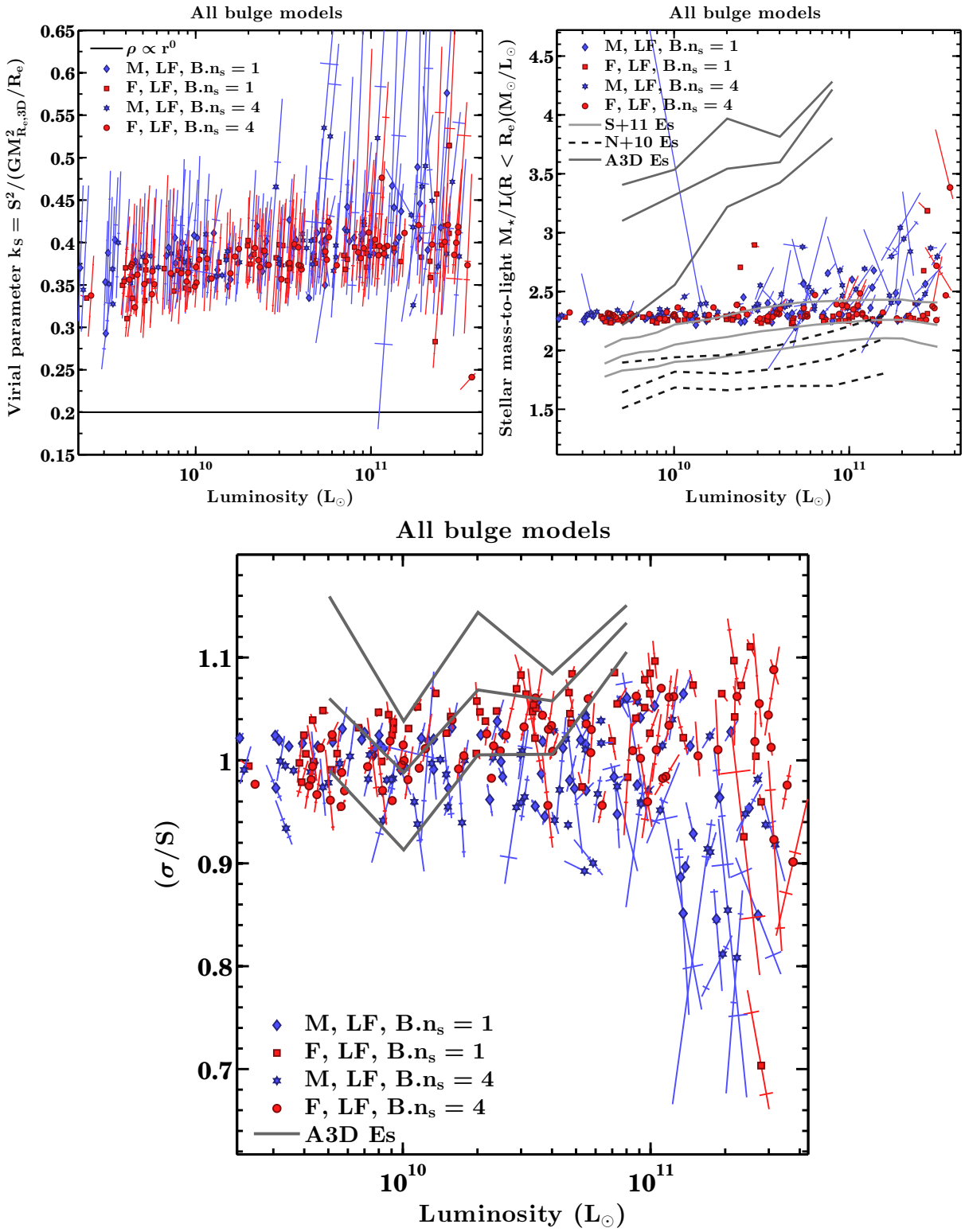

Figure 4.4: Three possible tilt terms k_S (top left), $M_\star/L$ (top right) and σ/S (bottom) - the virial parameter, stellar mass-to-light ratio and dispersion-to-orbital velocity ratio, respectively. Only the virial parameter varies significantly along the simulation FP. Stellar mass-to-light ratios are constant by construction, although some galaxies with substructure have (spuriously) larger ratios. Since most remnants rotate slowly, the S term - σ corrected for ordered rotation - is near unity, even for the relatively more rapidly-rotating, faint A3D ellipticals.

close to the virial plane in the simulations is:

$$\log R_e = \alpha \log S + \beta \log M_{R_e,3D} + \gamma, \tag{4.11}$$

with $\alpha = -1.97 \pm 0.03$, $\beta = 1.02 \pm 0.01$ and just 0.023 dex scatter. This fit is tabulated as fit #3 in Tab. 4.3, along with the dynamical mass coefficient c, which will be discussed further in §4.3.5. The fit is almost exactly the virial FP in Eqn. 4.4, and should yield parameters of $a = 1.89$, $b = 0.39$. Fitting the same FP with $-2.5 \log (M_{R_e,3D}/R_e^2)$ as the third parameter yields $a = 1.90 \pm 0.01$, $b = 0.379 \pm 0.003$. These are nearly precisely the expected values, but the errors on a and b are smaller, so that the FP tilt is small but significant. Using σ_e in place of S gives very similar results, so both are acceptable choices for relatively slowly-rotating galaxies. However, it is not always the case that a and b transform to α and β exactly. For example:

$$\log R_e = a \log \sigma - 2.5b \log (M_{R_e,3D)}/R_e^2 + c, \tag{4.12}$$

yields $a = 1.94 \pm 0.01$, $b = 0.43 \pm 0.01$, and 0.028 dex scatter. However, fitting a similar FP as in Eqn. 4.11 returns $\alpha = -1.55 \pm 0.02$, $\beta = 0.90 \pm 0.01$, with 0.025 dex scatter (fit #1 in Tab. 4.3). This is quite far from the virial plane and even more discrepant from the simple conversion using Eqn. 4.3. It is not generally the case that fits using mass versus mass surface density are identical, and it appears that using σ_e or S is necessary to obtain a virial FP in both cases.

Even using the *projected* mass $M_{R_e,2D}$ and σ_e in Eqn. 4.12 returns $a = 1.98 \pm 0.01$ and $b = 0.43 \pm 0.01$, with 0.020 dex scatter; however, the values (α,β) = (-1.65,0.92) are even further from the virial FP (fit #13 in Tab. 4.3). Notably, they also differ from the values quoted by Auger et al. (2010) using $\sigma_{e/2}$ and $M_{R_e/2}$. These are effectively (a,b) = (1.83,0.52), or (α,β) = (-1.13,0.81), if transformed with Eqn. 4.3. It is not clear if systematics or sample selection contribute to the differences, as we have not attempted to match methods with this particular sample or model gravitational lensing.

The one common conclusion from these fits is that most FPs using a total mass of some sort are close to the virial plane; however, reproducing (α, β) = (-2,1) is more difficult than (a, b) = (2,0.4). If the goal is to get as close to the virial FP as possible using both mass and mass surface density, then R_e, $M_{R_e,3D}$ and S or σ_e are appropriate choices for FP variables.

4.3.4 The Virial Theorem

We have now demonstrated in a number of different ways that the virial FP can be recovered from the total mass within R_e. Amongst others, Cappellari et al. (2013b) obtained very similar results through dynamical modelling of A3D galaxies. The fact that various mass estimators result in near-virial FP has been interpreted as a simple or uninteresting application of the SVT.

However, as Cappellari et al. (2013b) point out, the SVT only states that $-2T = W$, where

T is the total kinetic energy of the galaxy and W is the total potential energy of the galaxy. Much of this energy is bound in the dark matter halo. Furthermore, observers only measure stellar kinetic energy and infer the potential energy from the stellar mass within a specific radius such as the effective radius, which is not the same as the total potential energy and which also depends on the dark matter halo profile. Even worse, the SVT only holds for the total energy of the object. There is no guarantee that the material within an arbitrary radius (such as R_e) is exactly virialised as well. The SVT should hold for any unbiased tracer of the potential of a galaxy, but the material within R_e is certainly not an unbiased tracer. Stars are not an unbiased tracer either, unless they follow the halo profile exactly - this is unlikely and contrived, even within R_e. Thus, to be certain that the FP truly follows from the SVT, we must ask the following questions:

1. Does the stellar velocity dispersion trace the stellar and/or total kinetic energy?
2. Can the potential energy be estimated from any combination of size and mass or luminosity?
3. Does the SVT hold for the stars and/or the material within R_e? More generally, does $-2T = W$ for biased subsets of the galaxy?

The first point appears most likely to be true for a dispersion-supported system like an elliptical galaxy, but the final two points are neither trivial nor self-evidently true. We will now address all three questions in order.

Kinetic Energy

The left hand side of the virial theorem is the total kinetic energy of the system. However, observations typically only probe the stellar velocity dispersion across a long slit, within a fixed angular radius (if using a fibre as in SDSS), or at best within about R_e for integral field units (as in SAURON/ATLAS3D). We now test whether one can recover the actual stellar kinetic energy content within $r < R_e$ from the projected stellar velocity dispersion.

As Fig. 4.5 shows, the total stellar kinetic energy within R_e can be accurately estimated, as long as $M_{R_e,3D}$ is known. The central dispersion σ traces the kinetic energy within $R_e, 3D$ for most galaxies, with a median ratio of 0.99 but significant scatter of about 15%. Using the parameter S (σ_e corrected for $\langle v/\sigma \rangle$), we find a slightly smaller ratio and scatter of $0.97 \pm 13\%$. The ratio is smaller because for the simulated galaxies, σ_e is generally smaller than σ by an amount greater than the rotation correction. Either way, the central dispersion is sufficient to estimate stellar kinetic energy. Although σ can be significantly projection dependent, it is at least generally maximized in minor-axis projections (and minimized in major-axis projections), so axisymmetric models can in principle attempt to correct for this bias.

In principle, one can also estimate the total kinetic energy within any radius, given an accurate halo mass within that same radius. However, the halo dispersion is generally higher

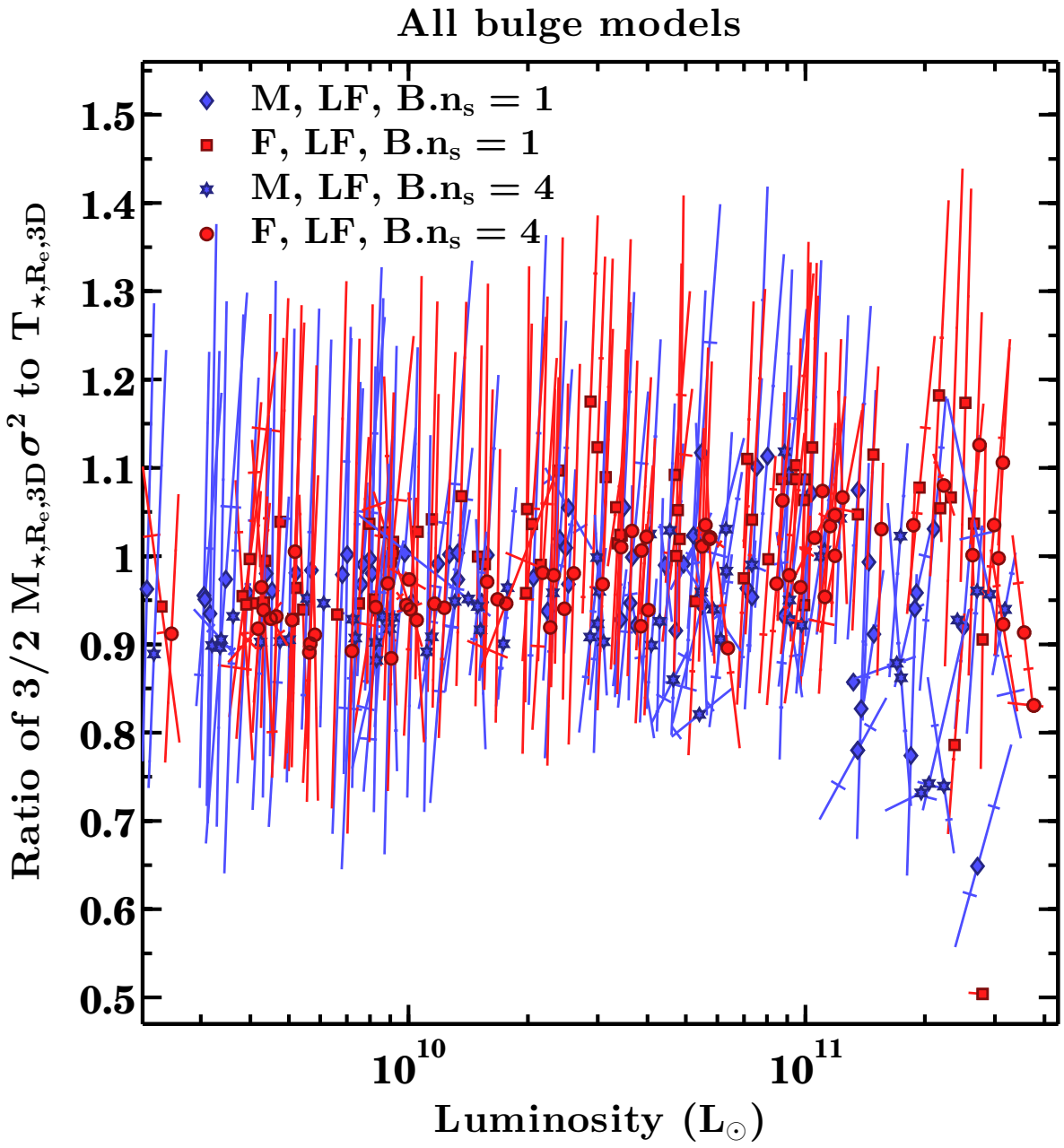

Figure 4.5: The ratio of estimated to actual stellar kinetic energy within R_e, based on the projected central dispersion σ, the stellar mass within a sphere of radius R_e, $M_{R_e,3D}$, and the stellar kinetic energy within that same sphere.

than σ, by approximately 20% in our simulations, so this bias must be taken into account for larger radii within which the mass is mostly dark.

Potential Energy

The potential energy term of the virial theorem is strictly the total gravitational potential energy of the galaxy, with the boundary condition that the potential is zero at infinity. This potential is dominated by the halo, since its mass greatly exceeds the stellar mass. Nonetheless, we can still measure the gravitational potential energy of the mass (total or stellar) within R_e, or effectively the binding energy.

This potential energy is typically equated to $\beta GM^2/R$, where β is a parameter dependent on the density profile in a spherical system. For a *finite*, uniform sphere, $\beta = 0.6$; for more centrally concentrated profiles, the values increase (e.g. to β=2/3 for $\rho \propto r^{-1}$ and β=1 for $\rho \propto r^{-2}$). For a virialised, isotropic, dispersion-supported sphere, $\beta = 3k$, where the factor of 3 arises if σ is measured in projection. In principle, then, if one treats the mass interior to $R_e, 3D$ as an isolated sphere, one can infer a value of β from k and estimate the power-law density profile.

We can test this by measuring the potential energy between particles within $R_e, 3D$, treating this mass as isolated and ignoring the contribution to the potential from the mass outside $R_e, 3D$ (by analogy to a finite sphere). Doing so yields a median value of $\beta = 0.92$ for the entire simulation sample, which is a factor of 2.45 (not 3) larger than the median $k = 0.41$, and naively corresponds to a density profile slightly shallower than r^{-2}.

While conceptually simple, this analysis is flawed. In a spherically symmetric galaxy, the material outside $R_e, 3D$ would not contribute any net gravitational force to particles within $R_e, 3D$. However, such particles are not physically bounded by $R_e, 3D$, and their orbits can be sensitive to the potential beyond $R_e, 3D$. Also, any deviations from spherical symmetry can apply a net force. Hence, we will measure all potentials including the full potential of the galaxy, and define $W_{R_e,3D}$ as the gravitational potential energy of all particles within $R_e, 3D$.

In the left panel of Fig. 4.6, we plot the ratio β of this potential $W_{R_e,3D}$, including the potential from mass outside R_e, to the estimated potential $GM^2_{R_e,3D}/R$. The potential within R_e can be reasonably accurately estimated with a single value for $\beta = 3$, with some scatter and outliers in systems where R_e and $M_{R_e,3D}$ are not accurately estimated.

Finally, we test whether the total potential energy of the galaxy correlates with the estimated potential from the mass interior to R_e, showing this ratio in the right panel of Fig. 4.6. Although this ratio is close to 50 for most galaxies, the scatter is rather large and the outliers are more extreme.

The Virial Ratio

Having demonstrated that the kinetic and potential energies interior to R_e can be estimated, at least in principle, we now consider whether the SVT is obeyed by those same subsets of the

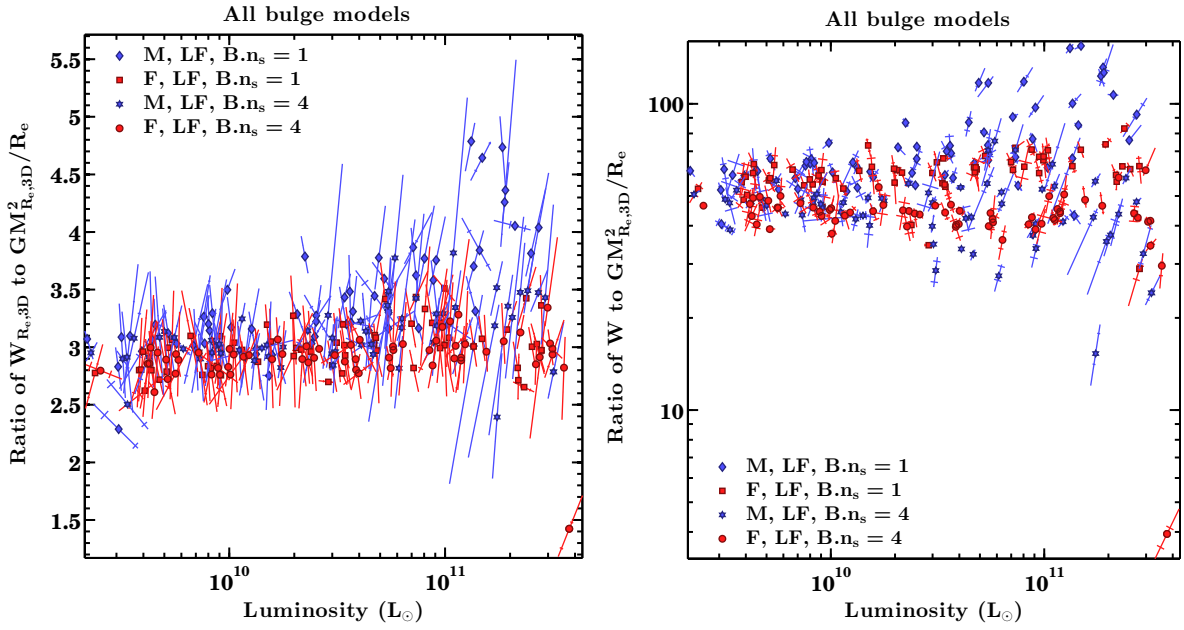

Figure 4.6: Ratios of actual to estimated potential energy. In the left panel, the potential is calculated within $\langle R_e \rangle$ (spherical, following the same definition of $M_{R_e,3D}$), including the contribution from mass exterior to $\langle R_e \rangle$. The ratio is nearly constant, but can only be estimated accurately with the true value of $M_{R_e,3D}$. In the right panel, the potential is the total potential energy of the entire galaxy.

galaxy. If so, then we can justify the interpretation that the FP is simply a reflection of the fact that the mass interior to R_e obeys the SVT.

First, we consider the stellar virial ratio within R_e: $q_{\star,R_e,3D} = -2T_{\star,R_e,3D}/W_{\star,R_e,3D}$, *excluding* the potential from the mass exterior to R_e. Next, we tally the total stellar virial ratio, $q_\star = -2T_\star/W_\star$; and finally the total virial ratio within R_e, $q_{R_e,3D} = -2T_{R_e,3D}/W_{R_e,3D}$, both *including* the potential from the entire galaxy. Fig. 4.7 shows that none of these virial ratios are unity. Neglecting the potential from mass exterior to R_e still does not yield a virial ratio of unity - the median $q_{\star,R_e,3D}$ is about 1.3, and the median $q_{R_e,3D}$ with this underestimated potential is 1.7 (not shown in Fig. 4.7), both with significant scatter. Including the total potential yields values with lower scatter but significantly smaller than unity, and with more extreme outliers.

The fact that none of the virial ratios within R_e equal to exactly unity is not surprising. If one includes the full galaxy potential, then both the stars and the stellar or total mass within R_e are a biased subset of particles, with much larger binding/potential energies than the mass exterior to R_e. One might expect the virial ratios neglecting the potential from mass exterior to R_e to be closer to unity. They are not, which simply reflects the points mentioned earlier - firstly, that all of the galaxies depart from spherical symmetry, and secondly, that the mass within R_e is not physically bounded within R_e. Indeed, one should expect some of the stars within R_e to have orbits that pass outside of R_e. Similarly, since the virial ratios are above

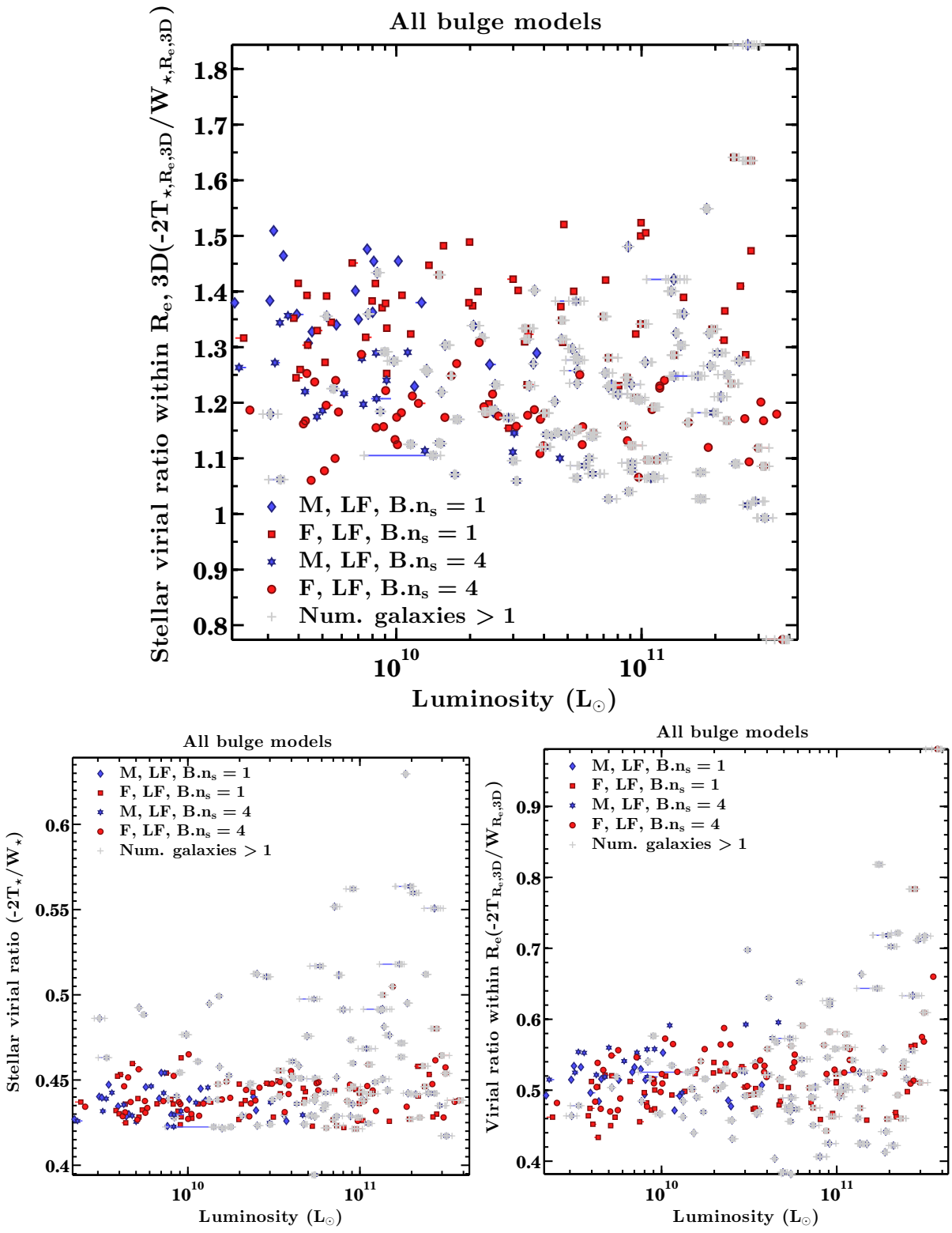

Figure 4.7: A variety of possible virial ratios are shown: $q_{\star,R_e,3D}$ (top), $q_\star$ (bottom left) and $q_{R_e,3D}$ (bottom right). Although most are fairly constant, especially when excluding systems potentially contaminated by satellites, none of their medians are unity.

1, this implies that if the mass outside of R_e were to suddenly be removed, the galaxy would expand - a reasonably intuitive result.

None of this is to suggest that the galaxies themselves are not virialised. To emphasize this point, we show the total virial ratios q=$-2T/W$ in Fig. 4.8. For most galaxies, $q = 1$ with just 1% scatter. The only exceptions are groups with remaining substructures or satellites, but even those groups are typically virialised within 2% as well, as the surviving satellites have had their orbits nearly virialised.

4.3.5 Dynamical Masses

The existence of a tight mass FP with the virial coefficients implies that one can extract a dynamical mass of the form $M_{dyn} = c\sigma^2 R/G$. In §4.3.3, we showed that Eqn. 4.11 is very nearly a virial FP, and so one should be able to derive an accurate value for $M_{R_e,3D}$ from S and R_e alone. However, the precise value of c depends on the structure of the galaxy, while the constancy of c relies on the assumption of homology. We already showed in Fig. 4.4 (top left panel) that the virial parameter is not exactly constant and has significant projected-dependent scatter. We also demonstrated in the previous section that stellar virial ratios and virial ratios within R_e are neither exactly constant nor unity, so these assumptions must be tested.

Values of c for a variety of dynamical mass estimators are shown in Fig. 4.9. For the projected mass $M_{R_e,2D}$, values of c=3.5–5 are appropriate when using σ and R_e; for $M_{R_e,3D}$, c=2.5–3 is more suitable. The tightest correlations are found by replacing σ. Using S gives a median c of 2.58 and 0.06 dex scatter, while σ_e produces $c = 2.63$ with 0.05 dex scatter. As Fig. 4.9 demonstrates, using S lowers the projection-dependent scatter but cannot remove it entirely - more extreme projections require values of c as small as 1.5 or as large as 3.5. While the correlation with R_e and S is fairly tight, there are several notable outliers (again, in galaxies where R_e is overestimated) and a hint of a shallow, luminosity-dependent slope in c. Nonetheless, for a typical random projection, R_e and S or σ_e can be used to estimate $M_{R_e,3D}$ to within 10–15%. at least partly due to the fact that these three variables define a tight virial FP with 0.02 dex scatter.

Other dynamical mass definitions have been proposed in the literature. On theoretical grounds, Wolf et al. (2010) advocate the use of $M_{1/2}$, where $M_{1/2}$ is the total mass within $r_{1/2}$, and $r_{1/2}$ is the 3D radius containing half of the total luminosity of the galaxy. Using Jeans models, they derive a relation $M_{1/2} = 3r_{1/2}\sigma^2$, arguing that $r_{1/2}$ is a unique radius at which the effects of anisotropy are minimized. For a Sersic profile with $0.5 < n_s < 10$, $r_{1/2} = 1.34R_e$ is an excellent approximation (Ciotti, 1991), and so one can also write $M_{1/2} = 4R_e\sigma^2$ without having to infer $r_{1/2}$.

Another alternative dynamical mass was defined by Cappellari et al. (2013b). They applied a variant of Jeans modelling ("JAM" models) to A3D galaxies to obtain a mass M_{JAM}, where $M_{JAM} = L[(M/L)_{JAM}(r < R_e)]$. Their Figure 14 suggests that M_{JAM}/M_{vir} shows minimal scatter (0.08 dex), provided that $M_{vir} = 3.9R_{e,maj}\sigma_e^2$, where $R_{e,maj}$ is the major axis (not circu-

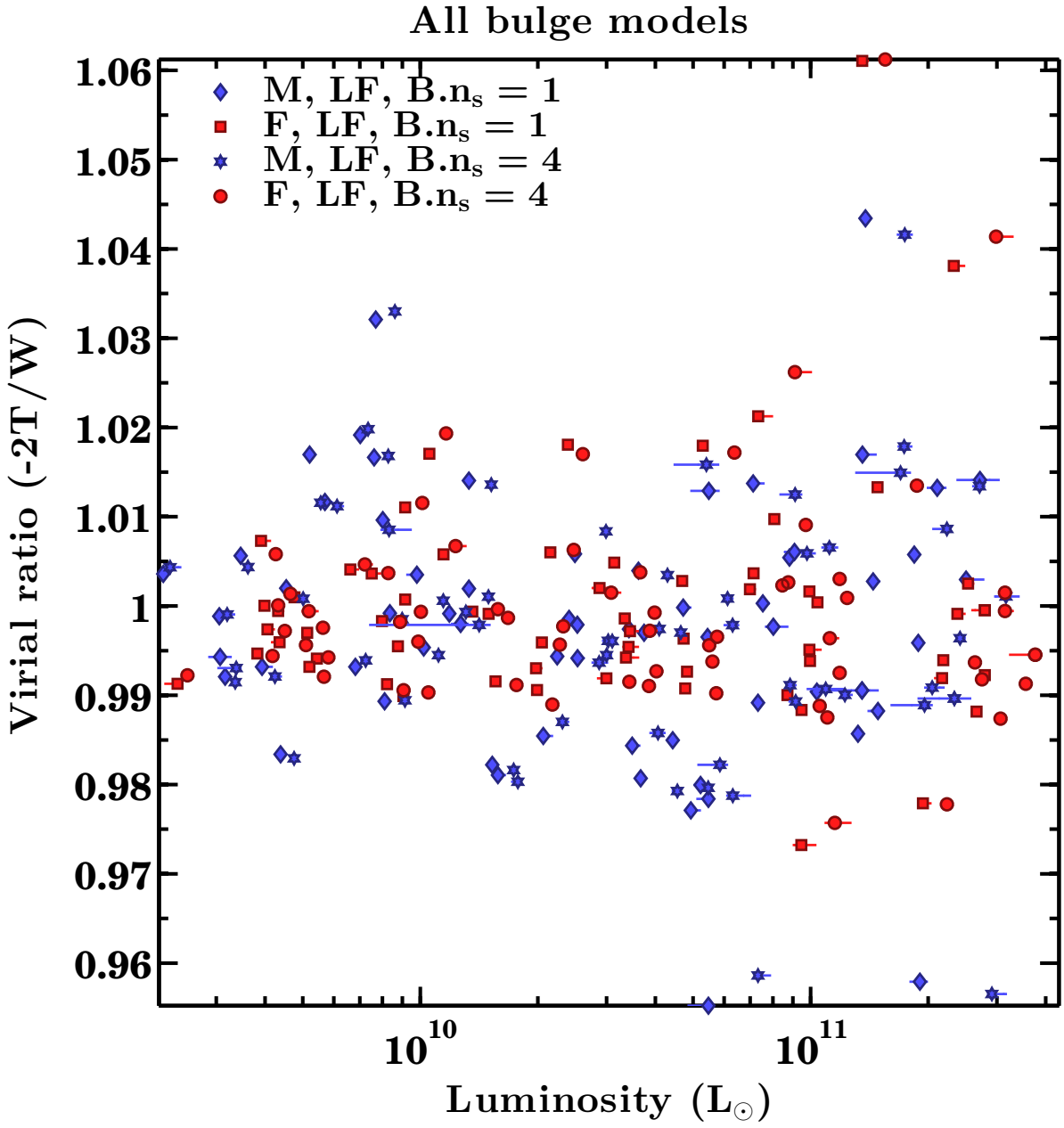

Figure 4.8: The total virial ratio $q = -2T/W$. The virial ratio is unity with percent-level scatter, even for galaxies with satellites.

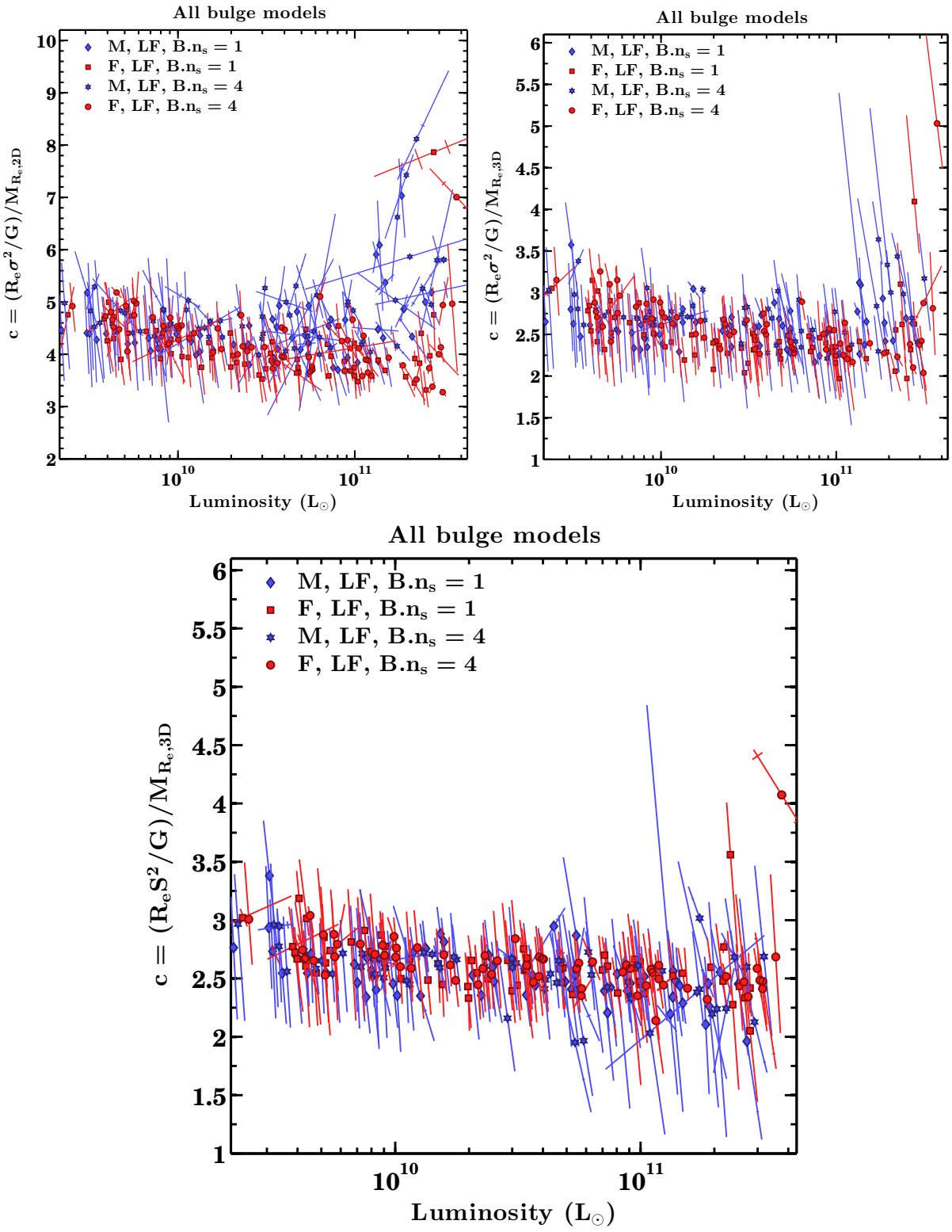

Figure 4.9: Values of c, the dynamical mass coefficient (or the dimensional-to-total mass ratio), for various definitions of the dynamical and total mass. In the top panels, $M_{dyn} = c\sigma^2 R_e/G$; in the bottom panel, S is used in place of σ. The top left panel ratio is to the projected mass, $M_{R_e,2D}$, while the remaining panels use $M_{R_e,3D}$.

Table 4.3: Mass Fundamental Plane and dynamical mass estimators
Simulations: All B.n_s, ten equally-spaced, randomly-oriented projections

#	M	R	K	c	Δc	α	β	γ	Δ
1	$M_{R_e,3D}$	R_e	σ	2.55 ± 0.01	0.065	-1.55 ± 0.022	0.90 ± 0.01	-5.64 ± 0.03	0.024
2	$M_{R_e,3D}$	R_e	σ_e	2.63 ± 0.01	0.053	-1.98 ± 0.032	1.01 ± 0.01	-5.96 ± 0.04	0.021
3	$M_{R_e,3D}$	R_e	S	2.58 ± 0.01	0.058	-1.97 ± 0.03	1.02 ± 0.01	-6.02 ± 0.04	0.023
4	$M_{1/2}$	$r_{1/2}$	σ	2.67 ± 0.01	0.080	-1.22 ± 0.02	0.80 ± 0.01	-5.27 ± 0.02	0.027
5	$M_{1/2}$	$r_{1/2}$	σ_e	2.74 ± 0.01	0.061	-1.55 ± 0.02	0.89 ± 0.01	-5.50 ± 0.02	0.023
6	$M_{1/2}$	$r_{1/2}$	S	2.68 ± 0.01	0.065	-1.54 ± 0.02	0.89 ± 0.01	-5.54 ± 0.03	0.025
7	$M_{1/2}$	R_e	σ	5.04 ± 0.03	0.141	-3.76 ± 0.19	1.39 ± 0.04	-6.66 ± 0.12	0.052
8	M_{model}	$R_{e,maj}$	σ	5.30 ± 0.02	0.061	-1.92 ± 0.02	1.01 ± 0.01	-6.34 ± 0.03	0.024
9	M_{model}	$R_{e,maj}$	σ_e	5.44 ± 0.01	0.060	-2.51 ± 0.04	1.17 ± 0.01	-6.89 ± 0.05	0.021
10	M_{model}	$R_{e,maj}$	S	5.37 ± 0.01	0.067	-2.51 ± 0.04	1.18 ± 0.01	-6.97 ± 0.05	0.024
11	M_{model}	R_e	σ	6.30 ± 0.02	0.059	-1.87 ± 0.02	1.01 ± 0.01	-6.57 ± 0.03	0.021
12	$M_{R_e,2D}$	R_e	σ	4.27 ± 0.02	0.068	-1.32 ± 0.01	0.83 ± 0.01	-5.57 ± 0.02	0.021
13	$M_{R_e,2D}$	R_e	σ_e	4.44 ± 0.01	0.045	-1.65 ± 0.02	0.92 ± 0.01	-5.83 ± 0.02	0.017
14	M_{200}	$r_{1/2}$	σ	53.46 ± 0.32	0.107	-2.94 ± 0.05	1.38 ± 0.02	-9.82 ± 0.09	0.029
15	M_{group}	$r_{1/2}$	σ	68.37 ± 0.34	0.096	-2.78 ± 0.05	1.32 ± 0.01	-9.46 ± 0.08	0.028

Each dynamical mass estimator is based on a mass (M), radius (R), and kinematic (K) tracers. For each estimator, the median c is tabulated, from $c = (RK^2/G)/M$, along with the error on the median and the scatter Δc about the median. Also shown is the best-fit $\log R = \alpha \log K + \beta \log M + \gamma$, with the r.m.s. scatter Δ about this relation.

larized) R_e. Similarly, Cappellari et al. (2013b) argue that M_{JAM} is an appropriate dynamical mass, because it defines a tight virial FP with $R_{e,maj}$ and σ_e (see their Figure 12).

We have tested both of these dynamical mass estimators, listing the values of c and the mass FP parameters α and β for each estimator in Tab. 4.3. $r_{1/2}$ is measured as the radius containing half of the stellar mass within r_{200}. This is equivalent to the half-luminosity radius, since $M_\star/L$ is nearly constant, and for most galaxies, almost all of the bound star particles lie within r_{200}. The median c for $M_{1/2}$, $r_{1/2}$ and σ (fit #4 in Tab. 4.3) is 2.67, with 0.08 dex scatter. This is within 10% of the value of 3 quoted by Wolf et al. (2010), but the scatter with $M_{1/2}$ is larger than for $M_{R_e,3D}$. The scatter is lower if using σ_e, at 0.06 (fit #5), while the median of 2.74 remains lower than 3.

Using R_e in place of $r_{1/2}$ gives a median $c = 5.05$ with 0.14 dex scatter (fit #7 in Tab. 4.3). This value of c is a full 25% larger than the nominal value of 4. Furthermore, the best-fit FP is wildly different from the virial FP, and has much larger scatter than any other mass FP in Tab. 4.3 (using σ_e or S does not improve either fit). This is mainly because the approximation $r_{1/2} = 1.34R_e$ does not hold for our galaxies - instead, $r_{1/2} \approx 1.88R_e$, with 0.13 dex scatter. This limits the usefulness of $M_{1/2}$, since $r_{1/2}$ is not directly measurable. The tight relation between R_e and $r_{1/2}$ only applies for pure, spherical Sersic profiles. Realistic merger remnants and ellipticals alike are not perfectly spherical. Systematic effects in SDSS-quality imaging limit the ability to recover R_e and n_s, even if ellipticals have perfect Sersic profiles, while our

merger remnants evidently only approximately follow Sersic profiles.

We define an analogous mass to M_{JAM} as $M_{model} = L[M/L(r < R_{e,3D})]$, but using the actual M/L within $R_{e,3D}$. M_{JAM} equals M_{model} if the JAM model derives the correct M/L. Note that M_{model} does not really have a physical meaning, as it is a projected luminosity multiplied by a mass-to-light ratio within a sphere. If R_e is correct and truly the half-light radius, *and* if $M/L(r < R_{e,3D}) = (M/L)(r < r_{1/2})$, then $M_{model} = 2M_{1/2}$. In practice, M/L should increase with radius, and so $M_{model}/2$ is really a lower limit on $M_{1/2}$.

Fit #9 in Tab. 4.3, using M_{model}, $R_{e,maj}$ and σ_e, results in a median $c = 5.45$ with 0.06 dex scatter (note that $c = 2.72$ for $M_{model}/2$). M_{model} can be recovered nearly as accurately as $M_{R_e,3D}$; however, the value of c is considerably larger than the value of 3.9 quoted by Cappellari et al. (2013b). This is mainly due to systematics - the values of R_e used by Cappellari et al. (2013b) are not derived from Sersic profile fits and tend to be larger than those from 2D, single Sersic GALFIT fits. Perhaps for similar reasons, we are also unable to recover a tight virial FP using M_{model}. Our best-fit relation for M_{model} is $R_{e,maj} \propto \sigma_e^{-2.51\pm0.04} M_{model}^{1.17\pm0.01}$ (fit #9 again).

We conclude that $M_{R_e,3D}$ is the only dynamical mass that satisfies two broad conditions. First, it can be accurately recovered within 10–15% using R_e and S or σ_e. Secondly, it is linked to the fundamental plane, in that $M_{R_e,3D}$, S and R_e define a nearly exact virial plane (Eqn. 4.11). This latter criterion was advocated by Cappellari et al. (2013b), but using M_{model}; we do not confirm this result using M_{model} and $R_{e,maj}$ based on 2D Sersic fits. M_{model} still defines a tight mass FP, just not with exactly the virial scalings - unless σ is used in place of σ_e, in which case fit #8 comes close.

Still, a nagging question remains - does the fact that $M_{R_e,3D}$, R_e and S (or σ_e) define a virial FP hold any fundamental significance? Similarly, can the value $c \approx 2.6$ be derived from the SVT? To answer this, we begin with the virial ratio $q_{50} = -2T_{R_e,3D}/W_{R_e,3D}$, and note that $q_{50} \approx 0.5$ (Fig. 4.7). Since q_{50} is not constant, it is not surprising that $M_{dyn}/M_{R_e,3D}$ varies slightly too.

Next, we need relations between kinetic and potential energies within R_e and observables. Let $q_{W,50} = W_{R_e,3D}/(GM^2/R_e)$; $q_{W,50} \approx 3.0$ (Fig. 4.5). Then if S traces the total kinetic energy, $2T_{50} = 3\sigma^2 M(S/\sigma)^2$, where $S/\sigma \approx 0.95$ (Fig. 4.4). Inserting these values into the virial ratio yields:

$$M = [3(S/\sigma)^2/(q_{50}q_{W,50})]\sigma^2 R_e/G. \tag{4.13}$$

Thus, the dynamical mass coefficient should be $c = 3(S/\sigma)^2/(q_{50}q_{W,50})$. For typical simulations, this is $3(0.95)^2/(0.5\times3.0) = 1.8$. This is somewhat lower than the value of 2.6 shown in Fig. 4.9. The main reason for this is that $\langle\sigma_{DM}/\sigma\rangle = 1.34$ in the simulations, and so both σ and S underestimate T, which includes the dark matter kinetic energy. This is irrelevant if one simply uses an empirical value of c, but important if one wishes to derive a true virial mass using the SVT. If one is not really deriving a virial mass using the SVT, then it is not clear why one should favour a mass estimator that is best fit by the virial FP in the first place. In principle, any correlation will do, even if it is not strictly a dimensional mass defined by a virial FP.

Finally, having gone through this exercise, it is worth pointing out that none of these dynamical masses are even remotely close to the total mass of the galaxy. This is to be expected, since Fig. 4.6 already showed the total potential is significantly larger than any dimensional potential energy based on R_e. Using $r_{1/2}$ and σ to estimate M_{200} (including substructure), we obtain c=53.5 with 0.11 dex scatter (fit #14 in Tab. 4.3); using R_e yields still larger c and scatter. The dynamical mass estimators we have discussed here are mainly useful for setting limits on the dark matter content within elliptical galaxies, given rather strict assumptions.

4.3.6 Consistency Check

As we have shown, most of the tilt of the FP in the simulated galaxies is caused by varying dark matter fractions, and while the virial parameter k (or k_S) is not exactly constant, it does not contribute much to the tilt. We check the consistency of this result by creating a mock fundamental plane from simple, spherical bulge plus halo systems, using the same GalactICS code (Widrow & Dubinski, 2005; Widrow et al., 2008) as was used to generate the model spirals (see §2.1.3).

Each galaxy consists of a Sersic profile bulge and a dark halo. The stellar component follows a scaling relation of $R_e \propto M_\star^{0.7}$, with σ scaled to create a virial FP and R_e and σ normalized to followed the observed relations for ellipticals. This results in a scaling $\sigma^2 \propto M/R \propto M^{0.3}$. The halo scale radius $r_s = 2R_e$, and the scale velocity $v = 1.2\sigma$, roughly consistent with the simulated ellipticals of Chapter 2. The dark halo has an inner density profile of $\rho \propto r^{-1}$, an outer profile of $\rho \propto r^{-2.5}$, and truncates smoothly to $\rho = 0$ from $30r_s$ to $35r_s$. This is much like a truncated NFW profile (Navarro et al., 1997). The total halo mass is $37M_\star$, equivalent to assuming that $\Omega_\star < 0.01$.

We create 49 such galaxies with bulge $n_s = 4$, $M_\star/L = 2$, and R_e ranging from 1.4 to 27 kpc. Modest intrinsic scatter is added by making some galaxies slightly over- or under-massive for their size. We then generate mock images using the same imaging pipeline as for the group simulations. The FP for these galaxies has $a = 2.06 \pm 0.02$, $b = 0.42$ and negligible scatter. The small deviation from the virial plane is entirely due to systematics. Direct, one-dimensional fits to the surface brightness profile without a variable sky background give $(a, b) = (2.00 \pm 0.01, 0.39)$.

We then repeat this process, introducing non-homology by scaling n_s by a slope of 1 per dex in $M_\star$, roughly consistent with the observed and simulated relations in §3.1.2. Each galaxy keeps the same R_e, $M_\star$ and M. Since $n_s > 4$ profiles are more centrally concentrated, σ is larger than in the $n_s = 4$ case (or smaller if $n_s < 4$), and so σ scales more steeply with $M_\star$. For this sample, we find $(a, b) = (1.94 \pm 0.04, 0.41 \pm 0.01)$ - as expected, the a parameter is lower, since σ scales more steeply with R_e as well. However, a is not significantly smaller than 2, and while the difference between a in this variable n_s sample to the $n_s = 4$ sample is marginally significant, it is mainly systematic. One-dimensional fits give $(a, b) = (1.98 \pm 0.01, 0.40 \pm 0.01)$, at best a barely significant change from the $n_s = 4$ case.

In conclusion, the effect of structural non-homology in galaxies with Sersic stellar mass profiles and fixed halo profiles is negligible. However, this may not necessarily be the case if the stellar profile deviates from a Sersic law, or if the dark halo profiles scale differently from the stellar profiles. For example, one could induce non-homology with otherwise self-similar dark halos if $d\log R_s/d\log R_e > 0$, which would result in larger dark matter fractions in larger galaxies (see Borriello et al., 2003, who conducted a similar exercise). Unfortunately, this interpretation is overly simplistic - the halos in the simulated galaxies are not completely self-similar, and for the common profiles we have fit, $d\log R_s/d\log R_e < 0$ and the central dark matter density $\rho_{0,DM}$ is not constant either. We leave further analysis of dark halo profiles to simulations with fully cosmological merger histories and halo profiles (but see Appendix D.1 for density profiles of an example merger remnant).

4.4 An Alternative Formulation of the Tilt

In §4.3.4, we showed that only the total kinetic energy T and potential W necessarily obey the SVT. We can then re-write the virial parameter $k = \sigma^2 R/(GM)$ as the ratio of two dimensionless parameters:

$$q_T = M_\star\sigma^2/2T \text{ and } q_W = -(GM_\star^2/R)/W, \tag{4.14}$$

such that $k = (q_T/q_W)(-2T/W)$, or simply $k = q_T/q_W$ if the galaxy is virialised. Then the virial plane becomes:

$$\log R = -2\log\sigma + \log M_\star + \log G + \log q_T - \log q_W. \tag{4.15}$$

This form is virtually the same as Eqn. 4.7 if one adds the tilt term $\log(M_\star/L)$ and interchanges k and q_T/q_W. The purpose of the latter substitution is to include the virial ratio $-2T/W$ into two separable tilt terms based on physically meaningful (though not easily measurable) parameters. To illustrate, we use $R = R_e$ and $M = M_{R_e,3D}$ to fit the equation:

$$\log R_e = a\log L + b\log\sigma + d\log q_T + e\log q_W + f\log\Gamma_\star + z, \tag{4.16}$$

yielding $a = -2.04 \pm 0.01$, $b = 1.01$, $d = 1.02$, $e = -1.02$, $f = 0.92 \pm 0.02$ and $z = -5.33 \pm 0.01$, with 0.002 dex scatter. This is nearly exactly the virial plane with 0.4% scatter, except that the constant z is insignificantly larger than $\log G = -5.37$ and the $\Gamma_\star$ term is underfit (likely because the stellar mass maps are not satellite-subtracted). This is in spite of the fact that we have not accounted for any systematics in our definition of R and M, and that there is nothing inherently special about the choice of R_e as a size.

The two tilt terms and their ratio q_T/q_W are shown in a 3D plot in Fig. 4.10. Both terms clearly vary across the plane, although neither term produces a clean gradient individually. However, the total tilt q_T/q_W does vary smoothly across the plane, which is not entirely surprising given how strongly q_T and q_W are correlated: $\log q_T = 0.86\log q_W + 1.40$ with 0.04 dex

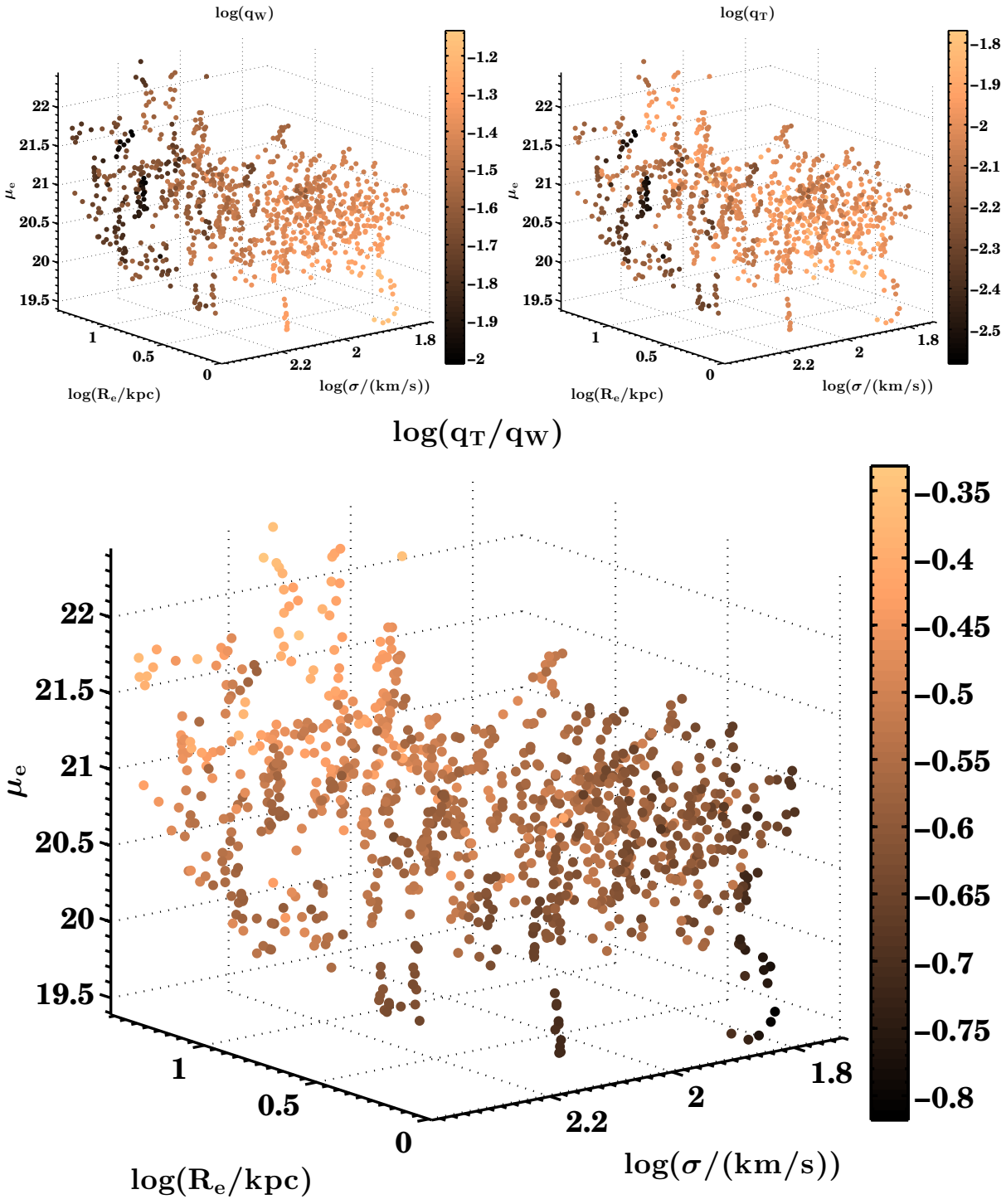

Figure 4.10: The two tilt terms q_T, q_W and the net tilt q_T/q_W as a function of the three fundamental plane parameters, shown roughly face-on.

scatter.

To make the use of these terms more explicit, we split each into two components:

$$q_T = (T_\star/T)M_\star\sigma^2/2T_\star, \tag{4.17}$$

The $M_\star\sigma^2/2T_\star$ term is largely a nuisance parameter - it is equal to 1/3 in a spherical, isotropic, dispersion-supported system, but can vary for more complex systems. Now $M_\star/M$ is the familiar stellar mass fraction term, joined by a very similar ratio in $T_\star/T$, which encompasses non-homology in the stellar kinetic energy fraction. The second tilt term q_W can also be decomposed:

$$q_W = [(-GM^2/R)/W](M_\star/M)^2. \tag{4.18}$$

The dark matter fraction returns as a tilt term alongside another non-homology term: $(-GM^2/R)/W$, which includes structural non-homology in the total mass profile, rather than kinematics. This latter term is, like $T_\star/T$, virtually impossible to measure observationally, but we are free to measure both in the simulations.

4.5 The Origin of the Tilt

We have just shown that the tilt of the stellar mass FP can be restated as originating from three key terms - $M_\star/M$, $T_\star/T$ and $(-GM^2/R)/W$. The first term, the stellar mass fraction, has already been shown to be a major contributor, while the last term was shown to be roughly constant in Fig. 4.5. What about $T_\star/T$?

Fig. 4.11 shows the initial fraction of stellar-to-total kinetic energy, $T_\star/T$ - the main variable component of q_T. The fraction is constant for each individual galaxy, since they are rescaled versions of each other, and only differs for the two bulge models (0.0422 for $n_s = 1$ and 0.0456 for $n_s = 4$). However, the *orbital* kinetic energy is distributed equally between the stars and dark matter, and since the stellar mass fraction is initially about 0.035, the initial value of $T_\star/T$ has a minimum of 0.035 in groups where the orbital kinetic energy dominates over the internal energies of each galaxy.

The fact that more massive groups are dominated by orbital energy and not the internal motions with galaxies is a consequence of the scaling relations imposed on galaxies and groups. The galaxies are scaled to follow a Tully-Fisher relation $V \propto M^{0.29}$ (Courteau et al., 2007). The groups are scaled such that the density within the maximum radius is constant (ρ=constant, $R_{max} \propto M^{1/3}$)), and so $V_{orbital} \propto M^{2/3}$ - a steeper scaling than the Tully-Fisher relation. This effectively imposes a non-homology from the initial conditions of the simulation, and one which is not necessarily present by construction in binary merger simulations.

However, not all of the non-homology measured in the final remnants comes from the initial conditions. Fig. 4.12 shows that the stellar kinetic energy ratio continues to drop in almost all of the galaxies - i.e., that the dark matter gains proportionally more kinetic energy than the

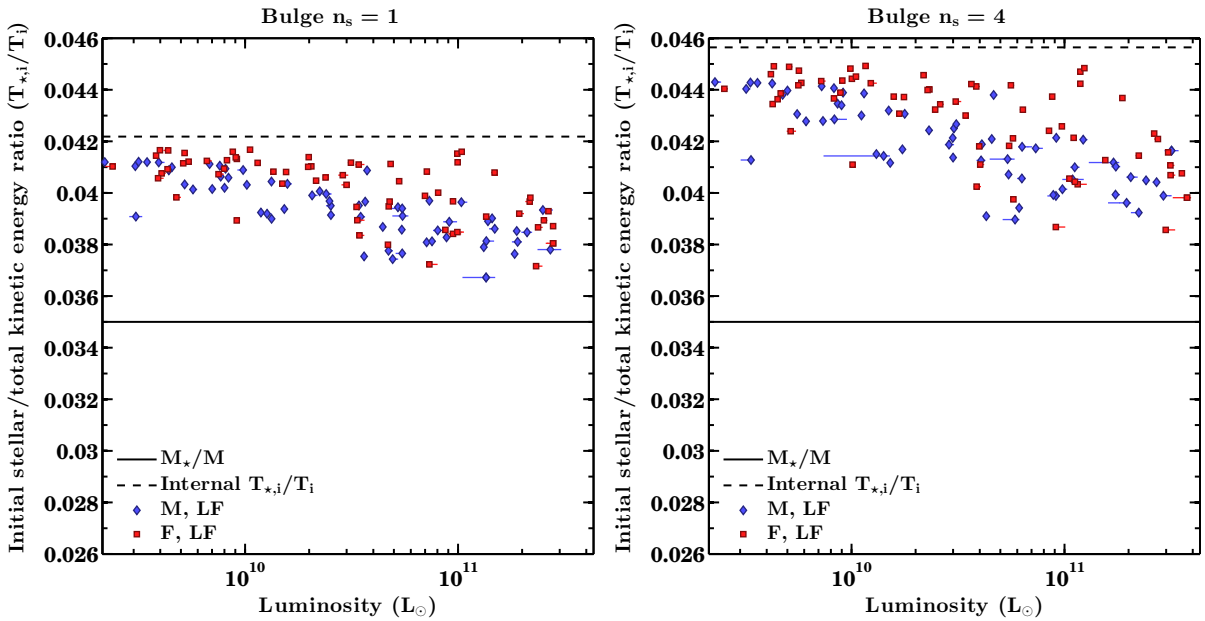

Figure 4.11: Initial stellar kinetic energy ratios. The solid line shows the fraction of kinetic energy in stars for isolated galaxies (which are all self-similar); the points show the totals including orbital energy. More massive groups are dominated by the kinetic energy of the galaxy orbits and lie closer to the stellar mass fraction of 0.035, since orbital energy is equally distributed amongst stars and dark matter.

stars. Furthermore, the stellar kinetic energy fraction drops more in the most massive groups. Interestingly, while all of the galaxies begin with larger $T_\star/T$ than $M_\star/M$ - i.e., a larger specific kinetic energy in stars than dark matter - a small majority end with $T_\star/T < M_\star/M$. This is not unrealistic - after all, most elliptical galaxies must have smaller σ_* than σ_{DM}, since even the most massive ellipticals do not have dispersions larger than about 400 km s^{-1}, whereas the most massive halos in cosmological simulations can have 1000 km s^{-1} dispersions. Nonetheless, it is important that dissipationless merging can convert spirals with large stellar specific kinetic energies into ellipticals with lower specific kinetic energies than their halos. This is possible because the merging galaxies follow different scaling relations from the groups themselves, allowing large groups to be dominated by the orbital energies of whole galaxies, rather than of the orbits of masses within galaxies.

The fractional drop in $T_\star/T$ is about the same regardless of bulge type. The B.$n_s = 4$ sample begins with a slightly stronger trend, simply because the $n_s = 4$ bulge is more centrally concentrated and has a larger velocity dispersion at the same mass. Thus, the tilt is sensitive to the structure of the progenitor galaxies, and the larger tilt observed in the B.$n_s = 4$ sample (Tab. 4.1) is at least partly because the initial spirals began with a larger bulge velocity dispersion at fixed mass. Nonetheless, the initial dependence of $T_\star/T$ on group mass or luminosity only steepens with extra merging, and the final ratios are not very sensitive to the initial values, so the initial conditions are only part of the reason why q_T varies with galaxy and group mass.

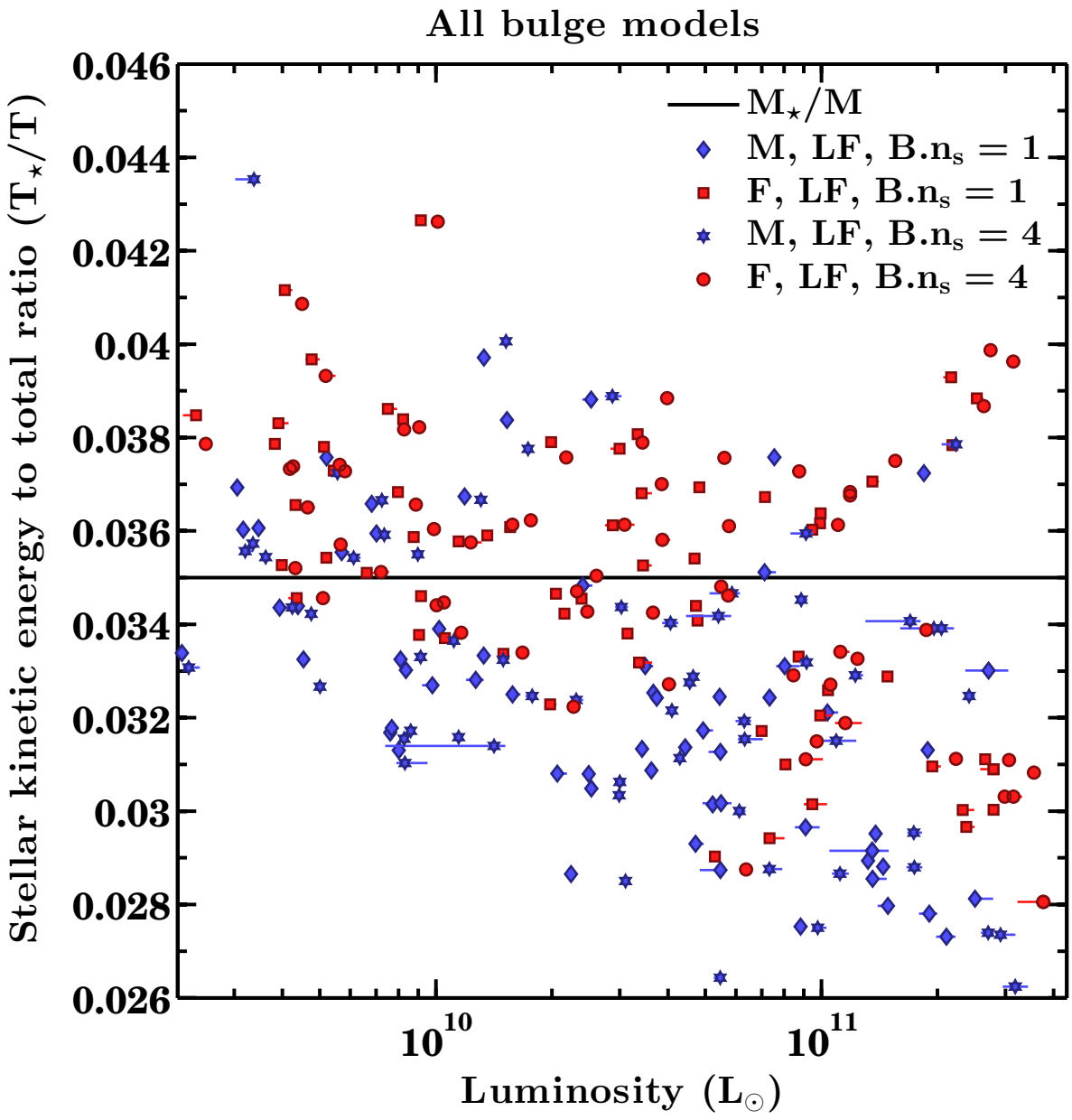

Figure 4.12: Final stellar kinetic energy ratios after 10 Gyr, for comparison to Fig. 4.11.

The weakness of this formulation of the tilt - beyond that $T_\star/T$ is difficult to measure - is that $T_\star/T$ does not really return the observed FP to the virial FP the way that tilt terms like $M_\star/M$ do. Furthermore, the variation of $T_\star/T$ does not explain the trend in $M_\star/M$ itself. Nonetheless, it does illustrate how non-homology can originate from plausible merger histories in groups.

4.6 Discussion

It is clear from the results of §4.3.1 that multiple dry mergers of spiral galaxies can produce a tilted FP, even if the merging galaxies are self-similar. This contrasts with the findings of Hopkins et al. (2008) that "dissipation appears to be both necessary and sufficient to explain the FP tilt". Moreover, the merger remnants show exceptionally tight scaling relations, including just 0.02 dex scatter in the FP. This demonstrates that multiple dry merging is a promising channel for the formation of elliptical galaxies, and one that is certainly plausible for the formation of the most massive ellipticals. However, as §3.1.3 demonstrated, producing less luminous, disky and fast-rotating ellipticals remains a challenge. S0s probably cannot be formed without some dissipation, if they are formed through mergers at all.

One of the major challenges to the merger theory of ellipticals - whether dissipational or not - comes from directly measured or inferred dark matter fractions in real ellipticals. As shown in Fig. 4.3, the dark matter fractions within R_e are quite large - at least 40% in projection (30% in 3D) and up to 80 – 90%. These are not inconsistent with results from the Sloan Lens ACS survey (SLACS), who found similarly large dark matter fractions (Auger et al., 2010) with a strong luminosity-dependent trend (Barnabè et al., 2011), assuming a Chabrier IMF. However, the situation is not as clear if the IMF is not universal. In particular, if the IMF is more "bottom-heavy" for low-mass ellipticals - i.e. closer to Salpeter (1955) - then these large dark matter fractions could be over-estimated, although in some cases a Salpeter IMF is nearly ruled out as it implies a negative dark matter fraction (see also Shu et al., 2014, whose analysis does formally exclude a Salpeter IMF from a number of mainly low-mass lensing ellipticals). If only the most massive ellipticals have an IMF even more "bottom-heavy" or steeper than Salpeter (1955), then some of the dark mass within R_e could simply be faint M dwarfs, making the dark matter fraction still lower. The net effect from such a variable IMF would be to flatten the dark matter fraction relation in Fig. 4.3, which would shrink the tilt from the $M/M_\star$ term.

The small scatter of just 0.02 dex in the simulation FP should be taken as a lower limit, as it is partly a byproduct of the assumption of a zero-scatter Tully-Fisher relation for the progenitor spirals. As discussed in §3.2.2, there is significant scatter in the observed Tully-Fisher relation (about 0.12 dex: Courteau et al., 2007), although the intrinsic scatter could be much smaller. If the Hopkins et al. (2008) estimate that 0.1 dex scatter in the Tully-Fisher relation contributes about 0.04 dex scatter to the FP is correct, then adding this amount to the existing 0.02 dex scatter from the simulations in quadrature would leave the simulation FP scatter consistent

with observed values of 0.05–0.06 dex. Either way, there is room for more scatter to be added to the simulation FP.

The large dark matter fractions in dissipationless mergers would also appear to be at odds with results from dynamical modelling of nearby galaxies Cappellari et al. (2013b), which favour values closer to 20% than 50%. Such dynamical models have yet to be applied to merger simulations - both the Jeans and Schwarzschild modelling methods have only been tested against idealized galaxies (Lablanche et al., 2012) but not triaxial merger remnants. Nonetheless, the low inferred dark matter fractions would seem to support dissipational merging, as such mergers can shrink R_e and thus also lower $M/M_\star$ within R_e significantly (Hopkins et al., 2008). However, this requires the majority of ellipticals to be formed from relatively gas-rich major mergers. It is unclear whether gas fractions are really so high beyond $z > 1$ (Narayanan et al., 2012), even in the most massive disks. Cosmological simulations also suggest that major mergers are less important for the formation of massive ellipticals than late minor mergers (Naab et al., 2009; Oser et al., 2012). Robertson et al. (2006) reproduced virtually the entire tilt of the stellar mass FP with $\tilde{4}0\%$ gas fractions, while our simulations suggest that dissipationless merging can account for half or more of the tilt. Thus, if multiple, dissipationless mergers do occur, then gas-rich mergers must be less common to avoid producing an excessively large tilt in the stellar mass FP, or gas fractions should be lower overall. It is not clear if this would still result in low dark matter fractions.

Although the non-zero tilt of the FP is a robust result of this work, the exact value of the tilt is sensitive to many factors. In §4.3.1, we showed that the degree of tilt depends on the structure of the merging galaxies, such that merging galaxies with more concentrated bulges produces a steeper tilt. The merger history may also have an impact. While the raw number of mergers may not affect the tilt much, as long as it is larger than one, the details of the merger history do have an impact on the tilt, as Appendix C.2 shows. The observed tilt could also vary if $M_\star/M_{DM}$ was a strong function of group mass rather than constant, as we have assumed, and if the bulge fractions and profiles of the merging galaxies were mass-dependent. It remains to be shown whether the exact values of the tilt of the FP emerge naturally from self-consistent cosmological merging, given all of the possible causes for a tilt in the FP - only some of which have been explored in this chapter.

A number of possible interpretations exist for why and how a tilted FP is generated from multiple dissipationless mergers. In §4.3.1, we showed that the majority of the tilt is caused by a variable dark matter fraction, and in turn by the fact that $M_{DM,R_e,3D} \propto R_e^2$, whereas $M_{\star,R_e,3D} \propto R_e^{1.72}$. These scalings clearly result in a dark matter fraction that increases with radius, although it is not obvious why these specific scalings exist in the first place.

In §4.4, we introduced an alternative formulation of the tilt of the FP. In this formulation, the tilt is partly the result of the redistribution of kinetic and potential energy. One possible tilt term examined in §4.5 is the ratio of stellar to total kinetic energy, $T_\star/T$. $T_\star/T$ is mass-dependent, with more luminous galaxies having lower values. This difference is partly embedded

in the initial conditions. More massive groups have a larger fraction of the kinetic energy in the orbital energies of galaxies within the group, rather than in internal motions within individual galaxies. The difference is also enhanced by the merging process, such that many galaxies end up with lower specific stellar kinetic energies ($T_\star/T < M_\star/M$), even though each progenitor galaxy began with $T_\star/T > M_\star/M$. Although $T_\star/T$ alone is not strictly the cause of the tilt of the FP, since it needs to be combined with potential energy terms, this formulation does help to explain why multiple mergers in groups are fundamentally different from the standard self-similar binary merger scenario.

The significant contribution of the $M_\star/L$ term to the tilt remains another major challenge for elliptical galaxy formation theories, and we are unaware of any self-consistent theories for its origin. Robertson et al. (2006) compared their stellar mass FP to near-infrared observations. A fully consistent theory for the formation of ellipticals should explain stellar population variations in visible bands as well. In principle, this could originate from dissipationless merging, if more massive ellipticals are formed from mergers of more massive galaxies with older/more metal-rich stellar populations with larger $M_\star/L$, but it is unknown if this could generate a steep enough tilt.

In §4.3.5, we showed that the virial FP (Eqn. 4.11) defined by $M_{R_e,3D}$, R_e and S (or σ_e) can be used to derive a dynamical mass, $M_{dyn} = M_{R_e,3D} = cS^2R_e/G$, with $c \approx 2.6$ and 0.06 dex scatter. We also examined alternative mass estimators proposed by Wolf et al. (2010) ($M_{1/2}$) and Cappellari et al. (2013b) (M_{model}). Of these various dynamical mass estimators, $M_{R_e,3D}$ is the only one that can both be accurately estimated from projected quantities and derived from a near-virial FP fit. $M_{1/2}$ can be estimated from $r_{1/2}$, the 3D half-light radius; however, $r_{1/2}$ cannot be directly measured, and the approximation $r_{1/2} = 1.34R_e$ for pure Sersic profiles does not hold for our galaxies, where $r_{1/2} \approx 1.88R_e$.

We also find that M_{model} is best reproduced with a constant c=5.45 rather than c=4, and that M_{model} does not define an exact virial FP, although these results may partly be due to systematic differences in R_e. M_{model} can estimated fairly accurately from a near-virial FP using $R_{e,maj}$ and σ, rather than σ_e or S; still, we suggest the use of $M_{R_e,3D}$, as it is a physical mass within a well-defined radius. It is a curious coincidence that all three mass estimators are reasonably well fit by $c \approx 2.6$–2.7 (if using $M_{model}/2$, and particular size and kinematic tracers). Ultimately, though, all of these dynamical masses only trace the total mass or dark matter fraction within R_e, while they underestimate the total mass of the galaxy by at least an order of magnitude.

As a final speculative note, we have limited discussion of the systematics in profile fitting, opting to match methodologies between simulations and observations instead. This is not to say that single Sersic fits are an ideal choice. Some systematic effects from Sersic fits to SDSS-quality images were noted in Appendix A, and there is abundant discussion of observational systematics in the literature (e.g. Meert et al., 2013). More generally, the fundamental plane does not exist just because R_e is a "special" radius. In principle, any size or luminosity measure

should generate a fundamental plane, likely with slightly different tilt. As an example, one could measure fundamental planes with $2R_e$, $R_e/2$, or non-parametric R_{50}, R_{25}, R_{10}, etc. Just as ratios like R_{90}/R_{50} are used as a proxy for concentration, other combinations of sizes would reflect differences in the surface brightness profiles of galaxies, much like the n_s parameter attempts to do. In fact, any theory of elliptical galaxy formation should produce galaxies following *every* observed fundamental plane relation, regardless of the definition of the size, velocity and mass or luminosity parameter.

4.7 Conclusions

Using collisionless simulations of mergers of spiral galaxies in groups, we have investigated whether the central merger remnants follow a similar fundamental plane relation to observed ellipticals. The following points summarize the conclusions:

1. Dissipationless mergers of multiple spiral galaxies in groups produce remnants resembling elliptical galaxies. These remnants lie on a tight fundamental plane (FP) relation with $a \approx 1.7$ and $b \approx 0.3$, which is tilted relative to the virial FP in the same sense as the observed FP.

2. The tilt from collisionless mergers could be responsible for about a third to half of the full observed FP tilt, explaining most of the variation in the b parameter but only part of the change in a.

3. The simulation tilt is closer still to the observed stellar mass FP tilt and could explain most of the tilt that is not attributable to stellar population variations. Mergers of galaxies with more concentrated bulges and with fully randomized orbits both produce a more significant tilt.

4. The primary contributor to the simulation tilt is the variable dark matter fraction within R_e. Structural non-homology from a variable virial parameter k may also contribute a small amount, but this may be mainly due to systematics in extracting R_e from single Sersic profile fits.

5. Since *multiple* collisionless mergers can produce a tilted FP, dissipation is not strictly necessary to create a tilted FP. Some dissipation is likely needed to increase central densities, shrink R_e and raise σ. However, the 40% gas fractions quoted by Robertson et al. (2006) as being necessary to reproduce the FP may be an overestimate.

6. The virial FP is not strictly an extension of the scalar virial theorem, because the virial ratios of biased subsets of particles in collisionless systems (such as stars or the most bound particles within $R_e, 3D$) are not generally unity, or even exactly constant.

7. Although the virial FP does not strictly follow from the scalar virial theorem, the combination of R_e, $M_{R_e,3D}$, and S (or σ_e) do define almost precisely a virial FP with minimal scatter. As a result, the virial FP can be used to estimate a dynamical mass $M_{dyn} = M_{R_e,3D} = cS^2R_e/G$, with $c \approx 2.6$ and 0.06 dex scatter. We find that $M_{R_e,3D}$ is the only true, dimensionally correct dynamical mass of the various mass estimators tested.

Chapter 5

Conclusions and Future Directions

5.1 Conclusions

In Chapter 1, we introduced the hypothesis that ellipticals form through multiple mergers of spiral galaxies in groups, along with the motivation behind this idea. This hypothesis was thoroughly tested using the simulations presented in Chapter 2, accompanied by mock observations suited for comparison to existing survey data.

The general conclusion reached from analyses of the morphology, kinematics and 2D scaling relations (Chapter 3) is that the simulated merger remnants strongly resemble elliptical galaxies. Their surface brightness profiles are well fit by Sersic functions, with a Sersic index weakly but positively correlated with luminosity, as in SDSS (but see also Kormendy et al., 2009, who report a much stronger correlation with deeper and better-resolved imaging). Their ellipticities are comparable to those of SDSS and ATLAS3D ellipticals. The merger remnants are generally slowly-rotating and dispersion-supported, like most luminous ellipticals. Their 2D scaling relations have similar slopes to the observed relations as well, though slightly shallower in some cases.

At first glance, these results would seem to confirm the hypothesis in full. However, careful examination shows disagreements between the observed and simulated data. The simulated ellipticals tend to be too large and have too low central dispersions, especially at the faint end. These two discrepancies cannot be resolved simultaneously just by adjusting the stellar mass-to-light ratios of the simulated stars. Moreover, faint ellipticals show limited rotational support, unlike in ATLAS3D, and there is no apparent relation between rotational support and luminosity, while there is an excess of simulated slow rotators with large ellipticities.

The fundamental plane is fairly successfully reproduced, at least as long as one considers the stellar mass fundamental plane, ignoring contributions from variations in stellar populations. This is a rather major omission, though, since the $M_\star/L$ term may well be the most significant contributor to the tilt. Given that, the main conclusion of Chapter 4 is that multiple dry mergers can have a significant contribution to the tilt of the FP - nearly as large as the putative contribution from dissipation, as hypothesized by Robertson et al. (2006) and Hopkins

et al. (2008). However, neither those simulations nor our own have explained the origin of the dominant $M_\star/L$ term.

This is not to suggest that merger theory is in conflict with observations. There are plausible explanations for the origin of the stellar population term in the tilt. For example, it is generally the case that luminous spirals have older stellar populations and larger $M_\star/L$ than their less luminous siblings (e.g. Gallazzi et al., 2005), not unlike ellipticals. Mergers would likely preserve some of this trend. Furthermore, if low-mass ellipticals are formed in more gas-rich mergers than high-mass ellipticals (as Hopkins et al. (2008) suggest), then a larger fraction of their stars would be formed in a starburst, yielding a younger mean age. A similar argument applies for the stellar metallicity, as long as low-mass ellipticals form from mergers of low-mass, metal-poor spirals (both in the existing stars and in the star-forming gas, if any).

Nonetheless, it remains to be shown that realistic mergers actually do reproduce the same variations in stellar populations between different ellipticals as are observed (e.g. in Hyde & Bernardi, 2009b; Graves & Faber, 2010). In fact, Naab & Ostriker (2009) have suggested that it is difficult for major mergers (dissipational or otherwise) to reproduce the total metal content in massive ellipticals without including massive and metal-rich bulges in the progenitor spirals. Similarly, ellipticals have long been known to have colour (Peletier et al., 1990; Franx & Illingworth, 1990) and metallicity (Davies et al., 1993) gradients, such that stars near the centres of ellipticals are redder and more metal-rich than in the outskirts (the former trend possibly being due to the latter). In Fig. 3.1, we showed that the inner regions of ellipticals are dominated by former bulge stars, while the outskirts are formed primarily out of former disk stars. This is a consequence of the general trend for stars in a merger remnant to retain a "memory" of their original binding energies, which can preserve any radial gradients in the original galaxies (White, 1980). But it is is not clear if enough of these gradients are preserved, or indeed how strong these gradients are in high-redshift spirals. Dissipation may be required to form new metal-rich stars near the centres of merger remnants, but as Naab & Ostriker (2009) point out, the star-forming gas would need to be heavily enriched with metals first, and not just in the very centre of the merger.

More generally, some fraction of dissipation is an appealing solution to the problems posed by gas-free mergers. As Mihos & Hernquist (1994) showed (and later works confirmed), dissipational mergers tend to produce dense stellar "cores" (really cusps, in modern parlance) with large velocity dispersions. This was initially viewed as conflicting with observational data, but Kormendy et al. (2009) have argued that nearby ellipticals do in fact host such sharp, central stellar density peaks. Taken at face value, dissipation would precisely counteract the problem of the simulated ellipticals having too low dispersions and too large effective radii, since creating extra stars near the centre of the galaxy would shrink R_e and increase σ. As argued above, dissipation could also enhance trends in stellar populations, producing younger, metal-poor stars in low-mass ellipticals.

One alternative to dissipation is that mergers at higher redshift (z =1–2) may occur between

more compact spirals, with less extended disks than their $z = 0$ equivalents. Recent observations show that although the slope of the size-mass relation for both late-type (mainly spiral) and early-type galaxies does not change significantly to $z = 3$ (van der Wel et al., 2014), the intercepts become significantly lower. By $z = 2$, late-type galaxies have effective radii 1.5–2 times smaller than their local counterparts. This may temper the need for dissipation to shrink merger remnants, since denser merging galaxies produce denser remnants. Of course, z=1–2 spirals should still have higher (cold) gas fractions than their local counterparts, but Narayanan et al. (2012) suggest that these fractions may be a factor of 2 lower than commonly quoted (10–40% rather than 20–80%).

The greatest remaining uncertainty in this field is the potential variability in the stellar initial mass function (IMF) reported by van Dokkum (2008), Conroy & van Dokkum (2012) and Cappellari et al. (2012), amongst others. If the IMF is really variable and a strong function of luminosity in early-type galaxies, then this poses a significant challenge to theories of elliptical galaxy formation. It is not yet entirely understood why or how the IMF should vary between individual star forming regions in our own galaxy, so an ab initio prediction for IMF variations in high-redshift galaxies or starbursts would be largely speculative at this point. Indeed, it is still not entirely known whether the IMF is universal within individual galaxies. For example, in a sample of five strong-lensing spirals, Dutton et al. (2013) found that the disks are consistent with a Chabrier or Kroupa IMF, whereas the bulges favour a Salpeter-like IMF, much as for massive ellipticals. Whether the IMF really is universal or not, robust theoretical predictions are practically nonexistent at the moment and will likely remain elusive until our understanding of star formation on smaller scales improves.

Regardless of how the remaining discrepancies are resolved, we are left with the following broad conclusions. Multiple, mostly minor and dry mergers of spirals galaxies in groups are a plausible formation mechanism for elliptical galaxies. This is especially true for massive and luminous ellipticals. At the very least, mergers in groups can contribute significantly to the tilt of the fundamental plane, as well as the size and mass evolution of elliptical galaxies. The preceding chapters also presented one of the first robust predictions for the structural properties and scaling relations of realistic multiple merger remnants. The combination of a large sample of well-resolved simulations (over a hundred simulations with 100pc resolution), along with systematic and fair comparisons to observational data, are unique in the literature and represent significant progress in our understanding of the formation and evolution of elliptical galaxies. To conclude, we will examine how improvements to this methodology could further progress this field.

5.2 Alternative Methods

Both dissipation and hierarchical merging clearly play an important role in the formation of ellipticals. Why, then, is there an apparent shortage of simulations incorporating both of mech-

anisms? In fact, Hopkins et al. (2008) did include re-mergers of ellipticals in their simulations, but not hierarchical mergers or mixed-morphology mergers of spirals with ellipticals. Cosmological simulations do, by their nature, include hierarchical merging. Such simulations have argued for the importance of hierarchical, mainly merging in building early-type/elliptical galaxies (e.g. Naab et al., 2009). However, Naab et al. (2009) presented just a single, well-resolved galaxy. Their extended sample of cosmological halos (Oser et al., 2010) had roughly 100,000 stellar particles and a 600 pc spatial resolution, considerably lower than our own simulations. As a rule of thumb, the inner 2-3 softening lengths (about 1.6 kpc for those simulations) are considered unreliable and subject to numerical artefacts. Only the most massive galaxies in these simulations would have been adequately resolved, while their high-redshift progenitors would certainly be under-resolved. In fact, the resolution used in our group simulations (about 1 million star particles, 3 million dark matter particles, with a 100 pc softening length) could be considered a minimum to accurately recover density profiles within 1–2kpc - see Appendix D.1 for details.

Perhaps because of these limitations, the authors of studies using cosmological simulations have shied away from making precise measurements of the fundamental plane scaling relation. Oser et al. (2012) did present predictions for the evolution of 2D scaling relations, while Naab et al. (2013) analysed the kinematic structure of the merger remnants in even greater detail than this work (see also Bois et al. (2011) for more standard binary merger simulations). As far as we are aware, no other papers incorporating mergers (cosmological and controlled) have published values for the FP coefficients since Robertson et al. (2006) and Hopkins et al. (2008). Ruszkowski & Springel (2009) did report creating brightest cluster galaxies (BCGs) through dry mergers in clusters, noting a modest tilt in their FP; however, BCGs are very rare and considered distinct from (though related to) ellipticals. Oñorbe et al. (2006) is a notable exception as well, having measured many quantities similar to those presented in this thesis from elliptical-like merger remnants in cosmological, hydrodynamical simulations. They reported a tilted FP as measured from 3D stellar half-masses and radii. However, the resolution was quite limited (2.3 kpc spatial, and only 262,144 gas particles in a 10 Mpc-side box), and best-fit FP coefficients were omitted in favour of Bender et al. (1992) κ-space style measurements.

A new generation of cosmological, hydrodynamic simulations promise to achieve much higher resolution for larger samples of galaxies, along with more realistic prescriptions for star formation, stellar and black hole feedback. The MassiveBlack-II simulation (Khandai et al., 2014), with 5.7 billion gas particles in a 143 Mpc box and 2.6 kpc resolution, is one such example. Illustris-1 (Vogelsberger et al., 2014), with the equivalent of 6 billion particles in a 106 Mpc box and 0.71 kpc spatial resolution for the stars, may be sufficiently well-resolved to characterize $L*$ ellipticals, though likely not less luminous galaxies. As yet, neither of these simulations have released catalogues of galaxy properties, but these should be forthcoming. If smaller fractions of these simulations were to be re-simulated at higher resolution - say, 1/8 of the volume of Illustris-1 with eight times higher resolution - these would certainly be comparable to data from

ATLAS3D.

Since cosmological simulations are making significant progress and could soon adequately resolve ellipticals below $L*$, it is reasonable to ask what controlled merger simulations could hope to add to our understanding of elliptical formation. At the least, controlled simulations can always achieve still higher resolution. They may one day be able to marginally resolve the formation of individual stars. Given that our Milky Way contains several tens of billions of stars, it is not a stretch to imagine that a decade from now, controlled simulations could model each one with a single particle. The current record-holder for an isolated galaxy simulation, to our knowledge, is a billion-particle realization of a Small Magellanic Cloud-like galaxy (Hopkins et al., 2012), though it was not run for very many time steps. The interstellar medium of a massive galaxy would, of course, require considerably more resolution elements, but either way, such simulations would be much more realistic portrayals of massive galaxies than approximations with a million resolution elements or fewer.

The isolated galaxies simulated by Hopkins et al. (2012) use significantly more sophisticated codes and prescriptions for stellar feedback than full cosmological simulations like Illustris, though they are not necessarily more correct. This is one major advantage that higher resolution offers - the ability to use more physical, and hopefully more realistic, models for the interstellar medium and feedback. These models have also been applied to merger simulations (Hopkins et al., 2013b), and most recently to cosmological zoom re-simulations as well (Hopkins et al., 2013a). But this latter paper demonstrates that high resolutions can be achieved in cosmological simulations too, as long as the volume is shrunk to a few cubic Mpc - so again, why run controlled simulations?

The short answers to this question are that controlled simulations can be more realistic than cosmological simulations, more efficient (allowing for larger samples to be generated), and permit the testing of various prescriptions for star formation and feedback. These points will be elaborated upon in the next section.

5.3 Future Directions

We have now examined alternative simulation methods for studying the evolution and formation of elliptical galaxies, but these were mainly fully cosmological simulations, beginning from a a nearly uniform gas and dark matter distribution at high redshift. Can improvements be made to merger simulations, starting from the framework of the group mergers described in Chapter 2? After all, now that the results from controlled initial conditions are well-understood, some of the control could be relinquished in favour of realism.

The first readily apparent target for improvement is the merger histories of the simulations. We set up the groups to resemble high-redshift groups while sampling a broad range of possible merger histories. Now that high-resolution cosmological simulations are widely available and not computationally costly (relatively speaking), why not sample a realistic range of merger

histories?

In fact, some merger simulations have used cosmological merger trees, rather than mocked-up galaxy orbits. The first complete example of this kind of methodology is Martig et al. (2009, see also references therein for earlier attempts). Martig et al. (2009) began with a dark-matter only simulation at $z = 2$, replacing massive halos with model spiral galaxies. Subhalos merging with the central halo at $z < 2$ were also replaced with model galaxies, while diffuse accretion of individual, unbound particles was included by tracing such particles from the original cosmological simulation. More recently, Moster et al. (2014) added explicit treatment of a hot gas halo to this formalism, as well as defining the properties of input galaxies based on predictions from semi-analytical models.

Both of these works are examples of what will be deemed hybrid merger simulations, since they combine cosmological merger trees with controlled initial conditions for individual galaxies within halos. The latter feature distinguishes hybrid simulations from ab initio cosmological simulations; generally speaking, hybrid simulations also begin at lower redshift ($z \approx 2$) than cosmological simulations ($z > 5$). Existing examples of hybrid simulations have focused on simulating isolated galaxies, but there is no reason why this methodology couldn't be used for merger histories of ellipticals too, addressing the need for a realistic and possibly unbiased sample of merger histories in groups. We will now outline four avenues of development which would allow for group merger simulations using a hybrid technique.

5.3.1 Cosmological Merger Trees

Accurate cosmological merger trees from an unbiased sample of galaxy groups are needed to probe the impact of environment and merger history on elliptical structure. At a minimum, the masses and orbital velocities of merging halos are required, while some algorithm must be chosen to determine the structure of the galaxies within each halo. The former requirement can be met by extracting merger trees from cosmological simulations, while the latter should be motivated by observations.

As previously mentioned, a new generation of cosmological simulations - including Illustris-1 and MassiveBlack-II - are more than adequate for the extraction of merger trees. Within a volume of 100Mpc cubed, one can expect to find hundreds of galaxy groups, if not close to a thousand (depending on the mass cut and definition of a group). Modern halo-finding and merger tree-compiling codes are fairly robust, and many of the newer codes like ROCKSTAR (Behroozi et al., 2013) make full use of the six-dimensional phase space information (including velocities) to identify and measure the properties of halos. While there are systematic differences between such codes, these have largely been quantified by the recent comparison projects for halo-finding (Knebe et al., 2011), subhalo-finding (Onions et al., 2012) and merger tree-generating (Srisawat et al., 2013) codes. This is not to suggest that halo-finding is a completely solved problem, but there are many available solutions and one can make an informed choice as to which is ideal for this particular problem.

Once individual halos are identified, the more difficult step is determining what the properties of the galaxy (or galaxies) within the halo should be. Ab initio cosmological simulations make self-consistent predictions for these properties, but for hybrid simulations, the more important consideration is whether the properties are consistent with those of observed, high-redshift galaxies. Self-consistency of the predictions is an added bonus but not necessary. If one derives merger trees from hydrodynamic cosmological simulations, then the gross properties of the original galaxies (stellar mass, star formation rate, etc.) can be used as a first guess. These properties can be adjusted to match observation, first by lowering stellar mass, since stars tend to be overproduced in cosmological simulations even with strong feedback. The finer details of structure and morphology such as the bulge fraction and profile can be altered entirely as desired.

Other methods can be used to populate halos with galaxies, too. Moster et al. (2014) drew galaxy properties from semi-analytical model predictions. Even simpler, empirical predictions for the stellar mass-halo mass relation are available (e.g. Moster et al., 2010). Intermediate solutions like abundance matching (e.g. Behroozi et al., 2010; Moster et al., 2013) are, like semi-analytical models, tailored to reproduce observed stellar mass or luminosity functions exactly. Abundance matching algorithms simply match observed galaxies with simulated halos by, for example, preserving rank order in mass, rather than by using complex models with dozens of free parameters, as for semi-analytic models.

Ultimately, there is no shortage of solutions to the problem of assigning galaxies to halos, even if they all have significant systematic uncertainties - most notably in the observed z=1–2 galaxy stellar mass function, which most models are designed to match. Still, if one bases hybrid simulations off of cosmological, hydrodynamic simulations, then any well-designed modifications should make the initial conditions more realistic. This is assuming that one has suitable models for high-redshift galaxies available, which is the next major requirement for hybrid simulations.

5.3.2 Realistic Galaxy Models

By construction, the group simulations used a single re-scaled galaxy model, varying only the Sersic index of the bulge and marginalizing over all other possible variations in bulge properties. Other controlled simulations of spiral galaxies also model a limited number of galaxies - exactly five in the representative case of Hopkins et al. (2012). While the model used herein is a realistic facsimile of M31, it is not necessarily appropriate as a low-mass spiral. Less massive spirals are generally less bulge-dominated than their massive counterparts, as shown in §3.2.3 using SDSS data.

Unfortunately, SDSS is not a deep enough survey to simultaneously constrain the bulge and disc properties of spiral galaxies. For example, it is not clear what the distribution of bulge Sersic indices is, and whether they are correlated with bulge luminosity, size, or properties of the disk. Near-infrared data from the Hubble Space Telescope (HST) is better suited to this purpose, having roughly ten times better resolving power and being less sensitive to dust obscuration

than optical images. Balcells et al. (2003) took advantage of HST observations to find that spiral bulge indices are typically quite low ($n_s \approx 2$). In SDSS images of the same galaxies, unresolved nuclear emission biased the values of the bulge Sersic index significantly upward. Balcells et al. (2007) used the same sample to confirm that several bulge properties do correlate with disk parameters. Fisher & Drory (2010) performed similar analyses on infrared images from the Spitzer Space Telescope, suggesting that while some spiral galaxy bulges follow similar scaling relations to elliptical galaxies (classical bulges), most are so-called "pseudobulges", following entirely different scaling relations from classical bulges.

These results can certainly inform the construction of more lifelike model spiral galaxies, giving structural parameters for the bulge and disk. However, to completely specify each galaxy, kinematic parameters are necessary too. This includes not just the velocity dispersion of the bulge, but a full rotation curve to constrain halo properties. Spectroscopy from integral field spectrograph (IFS) galaxy surveys is ideal for this purpose, since IFSs provide spatially resolved stellar and ionized gas kinematics, along with stellar population parameters. Several existing IFS surveys including the DiskMass survey (Bershady et al., 2010) and the Calar Alto Legacy Integral Field Area survey (CALIFA, Sánchez et al., 2012) have provided data on approximately 40 and 150 nearby spirals, respectively. In-progress surveys from the Sydney Australian Astronomical Observatory Multi-object Integral Field Spectrograph (SAMI, Croom et al., 2012) and Mapping Nearby Galaxies at Apache Point Observatory (MaNGa, Law & MaNGA Team, 2014) promise to increase the quantity of available data by at least an order of magnitude, covering thousands of galaxies within the next few years. While there are limits to the spatial resolution and depth of MaNGa/SAMI, since they will target more distant galaxies than existing surveys, sample size and bias will not be an issue.

Complementary observations of neutral gas densities and kinematics are also useful for the purpose of modelling spiral galaxies, and are already an integral component of DiskMass. This includes radio observations of neutral, atomic hydrogen (from its 21cm line), as well as molecular hydrogen, typically traced indirectly by molecules like carbon monoxide (CO). Gas observations not only help to constrain the properties of the gaseous disk itself, but also trace the rotation curve beyond the extent of the stellar disk, since gas disks usually have larger scale radii and extend further than stellar disks (e.g. Rubin et al., 1978). Far-infrared observations of galaxy disks trace dust emission and hence also star formation (indirectly). Such observations are already available for the most nearby spirals from a variety of Nearby Galaxy Surveys (NGS) including the Heterodyne Receiver Array CO Line Extragalactic Survey (HERACLES Leroy et al., 2009), The HI NGS (THINGS Walter et al., 2008), and the Spitzer Infrared NGS (SINGS Kennicutt et al., 2003), amongst others. The gas observations would be used to constrain the initial conditions, while far-infrared star formation rates would serve as a consistency check once the model is run through a code with a star formation module.

High-redshift observations are needed to adapt the models for use at z=1–2, when many of the spirals would begin merging. Structural parameters and morphology are available from

various sources (e.g. Bruce et al., 2012; van der Wel et al., 2014), mainly using HST or ground-based adaptive optics imaging to achieve the necessary resolution. High-redshift IFS surveys exist for $z \approx 2$ galaxies (e.g. Wright et al., 2009). Grisms have also been used in the 3D-HST survey (Wuyts et al., 2013), sacrificing spatial resolution in one axis. In the next decade, the James Webb Space Telescope and thirty meter-class telescopes with adaptive optics should greatly expand this field. As it is, there is some data available on spiral galaxy scaling relations and kinematics at z=1–2, but the constraints are not as stringent as for nearby galaxies. For example, while Daddi et al. (2010) estimated very high gas fractions in $z \approx 1.5$ disks, Narayanan et al. (2012) claim that these fractions are overestimated by a factor of two, due to a mis-calibration of the conversion factor from CO to H2 abundances. Nonetheless, Daddi et al. (2010) suggest that these high-redshift, star-forming galaxies do have ordered rotation in their molecular gas, though the gas disks may be clumpier than at lower redshift; earlier near-infrared observations by Förster Schreiber et al. (2009) would seem to agree with this view. Higher-redshift objects appear to have larger dispersions (Law et al., 2009), and may be more likely to be mergers and/or irregular galaxies, possibly having vigorous active galactic nuclei (AGN) - see Förster Schreiber et al. (2014). For the purposes of hybrid simulations, more compact, gas-rich versions of z=0 spirals with higher dispersion gas disks would be reasonable facsimiles of z=1–1.5 spirals. If the simulations begin at $z = 2$, then the galaxies will have some time to evolve in isolation before the first major mergers occur. They would not need to match the properties of $z > 2$ spirals.

Finally, it is worth considering the possibility that some fraction of ellipticals were already compact, passively-evolving, dispersion-supported spheroids even at $z \approx 2$, as suggested by recent HST and adaptive optics observations (e.g. Longhetti et al., 2007; Trujillo et al., 2007). If this is the case, then some of the initial galaxies ought to be modelled not as spirals but as compact spheroids with large Sersic indices. Research into this field is ongoing - recent studies suggest that some of these passive galaxies are disk-dominated, while some of the bulge-dominated galaxies are not passive (Bruce et al., 2012), so exactly what fraction of $z \approx 2$ are compact, dispersion-supported spheroids is not well known. Whatever the case may be, implementing mixed-morphology mergers in hybrid simulations is a considerably less difficult task than constraining the initial conditions observationally in the first place.

5.3.3 Gas Dynamics and Star Formation

However the gas in spirals and the intergalactic medium is modelled, it is clear that future simulations must include gas dynamics, star formation and some level of feedback to more accurately predict the structure of ellipticals with early, gas-rich mergers. Numerous codes exist for this purpose, including smoothed particle hydrodynamics codes like GASOLINE (Wadsley et al., 2004) and GADGET (Springel et al., 2001; Springel, 2005), grid-based codes like RAMSES (Teyssier, 2002) and Enzo (Bryan et al., 2014), and most-recently, moving-mesh codes like Arepo (Springel, 2010). Even without the inclusion of star formation and feedback, there

are significant systematic differences between the output of these codes for the same initial conditions (Scannapieco et al., 2012). The differences between codes with complex prescriptions for star formation and feedback are set to be quantified in greater detail by the AGORA project (Kim et al., 2014). Even then, it may not be clear which code produces the most accurate results, since there are few test cases with known and/or analytic solutions in galaxy formation.

While there is not necessarily a single ideal code for simulating galaxy mergers, the importance of additional physical prescriptions beyond gravity should not be understated. AGN/black hole feedback is thought to be important for maintaining a hot interstellar medium in ellipticals (see Kim & Pellegrini, 2012, for a thorough review), preventing overcooling of gas and overproduction of stars in groups (e.g. McCarthy et al., 2010), in brightest cluster galaxies (e.g. Martizzi et al., 2012), and in very massive ellipticals (e.g. Dubois et al., 2013). The exact mechanism for feedback may be important too - Choi et al. (2014) argue that without mechanical feedback (in addition to the usual thermal feedback), AGN feedback overheats the halo gas, making simulated ellipticals orders of magnitude too luminous in x-rays.

Stellar feedback is thought to play a similarly important role in galaxy formation simulations, limiting the excessively rapid formation of stars in low-mass galaxies and during mergers (Springel, 2000; Springel et al., 2005a) and regulating the interstellar medium (e.g. Hopkins et al., 2011; Agertz et al., 2013). Again, there are a variety of formulations and implementations of stellar feedback, most including thermal feedback from supernovae and/or mechanical feedback driving winds.

Just as there is no single ideal code for galaxy simulations, there is no widely acknowledged optimal implementation of stellar or AGN feedback. This is both a problem and an opportunity. It is a problem in the sense that one may not be able to distinguish between discrepancies in the simulations caused by inaccurate initial conditions, an incorrect choice of IMF or an unrealistic implementation of star formation or feedback. At the same time, simulations of isolated model spiral galaxies could be calibrated against observations of the same galaxy they were based on, potentially constraining the parameters of the star formation and feedback models.

5.3.4 Sophisticated Mock Observations

The existing mock observation pipeline is already quite suitable for analysing dust-free elliptical galaxies. A simplifying assumption was made of a single, constant stellar mass-to-light ratio for the disk and bulge particles. If the age and metallicity of each individual stellar particle is specified instead, then the stellar-mass-to-light ratios would need to be drawn from model grids. This would be necessary both for existing stars, to match the observed ages and metallicities of the modelled spiral galaxy, and also for newly-formed stars in hydrodynamic simulations Again, while there is no shortage of codes for this purpose (Bruzual & Charlot, 2003; Maraston, 2005; Conroy et al., 2009; Conroy & Gunn, 2010), their predictions do differ systematically. These differences are typically dwarfed by uncertainties in the stellar IMF, so this is more or less a solved problem, notwithstanding some ongoing concerns over reproducing the red colours of

very old and metal-rich ellipticals (Maraston et al., 2009).

While most relaxed ellipticals do not contain especially large quantities of dust, it is nonetheless useful to model the absorption and scattering of starlight from dust. This would be more important during or shortly after a merger event. SUNRISE (Jonsson, 2006) is one commonly-used code for this purpose. SUNRISE is a radiative transfer code which models dust absorption and performs spectral synthesis via raytracing, effectively shooting millions of individual rays through the galaxy and predicting the output spectra. This approach is quite computationally intensive but fully self-consistent, and SUNRISE is already a mature code. The open-source software project yt (Turk et al., 2011) is a newer and more general framework for visualizing simulation data, and especially the gaseous component thereof. While it is not yet advanced enough to deem this a solved problem - after all, visualization is only one step towards full mock observations with a specific instrument - the rapid pace of progress in yt's development is encouraging.

Perhaps the most tantalizing prospect for hybrid simulations is the ability to produce high-quality mock survey data, not just idealized images of individual galaxies. It is no coincidence that a substantial portion of this thesis was dedicated to analysing the outputs of simulations with similar methodologies as for observational catalogues. Hybrid simulations could go one step further, using the information on halo positions and velocities within the cosmic web to generate as many mock surveys as desired, even mimicking observational selection effects and biases. One can imagine selecting any point within (or outside of) the original cosmological simulation as the origin of a mock survey, then imaging each galaxy with the appropriate orientation, redshift and instrumental parameters. If done correctly, the simulated catalogue would be virtually indistinguishable from an observational catalogue, finally bridging the gap between theory and observations. Such a sample of hybrid simulations would at last be able to answer the most pressing questions of how, where and when elliptical galaxies form.

Appendix A

Chapter 2 Appendices

A.1 Analysis Pipeline Testing

Several aspects of the simulation analysis pipeline merit further testing. First, we would like to determine if the pipeline can recover known or measurable quantities such as the total mass/luminosity and half-light radii in single galaxies. This is accomplished by analysing a sample of spherical, pure Sersic profile plus dark matter halo galaxies generated with GalactICS. This allows us to simultaneously test whether GalactICS can generate equilibrium Sersic profile models (which is how the bulges of progenitor spirals are initialized) and whether the analysis pipeline can successfully recover input parameters at arbitrary resolutions. We analyse these models before simulating them in any way. In Appendix A.2, we examine the results of simulating these simple models with PARTREE to test numerical convergence.

We can also use the group simulations themselves to test the analysis pipeline. Although we do not know the structural parameters of merger remnants a priori - indeed, they do not necessarily follow a single Sersic profile at all - the total luminosity is known in groups which have merged to a single remnant. Similarly, we can directly measure a half-light radius from mock images with no PSF or sky background in these cases and compare to observational estimates from the SDSS-equivalent mock images. This procedure allows us to determine whether single Sersic profile fits can simultaneously recover the total luminosity of a galaxy and its half-light radius.

In addition to Sersic fits from GALFIT, we fit de Vaucouleurs profiles with GALMORPH and measure non-parametric Petrosian radii to determine if these size measures can consistently recover the true half-light radius of a galaxy.

A.1.1 Sersic plus Halo Models

Our reference Sersic plus halo models consist of a single Sersic profile bulge and a dark halo with the same baryonic mass ratio as our fiducial M31 models. We produce $n_s = 2$ and $n_s = 4$ models to cover most of the range of typical elliptical surface brightness profiles. We create models with

R_e of 2, 4, 8 and 16 kpc, again covering ranges of typical elliptical galaxies and massive spiral bulges. The 2-kpc model is slightly larger than the 1.5-kpc bulge in our fiducial M31 model. All models are in virial equilibrium and follow a size-luminosity relation $\log(R_e) = 0.7\log(L_r)$, with one model exactly on this relation and an extra model either over- or under-luminous for its size. Each model is imaged at mock redshifts of 0.01, 0.025 and 0.1. These models will be used in the future to test recovery of scaling relations. However, for now we are mainly interested in whether the pipeline can recover the known values of n_s, R_e and L for each model and whether the systematics depend on any of those parameters.

In addition to varying the galaxy luminosity as a function of size, each set of Sersic plus halo models is simulated at three resolutions. The lowest resolution has 15,000 star and 40,000 dark matter particles, identical to the lowest resolution model used in the simulations. The resolution increases by a factor of 8 each step such that the highest resolution model has 7,680,000 star and 20,480,000 dark particles, or at least a factor of two more than the total particle counts of the most massive group simulations. In principle these models should be rescaled versions of each other; however, the nominal SDSS PSF and signal-to-noise ratio set a physical scale for mock images, while our fixed softening length sets another physical scale for the simulation.

A.1.2 Sersic Quantities

For $n_s = 2$ models imaged at z=0.025, GALFIT Sersic fits show excellent agreement with expectations, even at low numerical resolution. With just 15,000 star particles, sizes are recovered to within $1 \pm 0.5\%$ for 2 kpc radius, although larger galaxies have underestimated sizes to the level of $3 \pm 1\%$ at $R_e = 16$ kpc. However, n_s is underestimated by 10% for $R_e = 2$ kpc galaxies, which improves to $4 \pm 1\%$ at $R_e = 16$ kpc. Luminosities, in turn, are underestimated at fairly constant levels of 3%, with standard deviations increasing with size from 0.1 to 1%. Similar trends are found at medium resolution but with smaller amplitudes - the largest errors on n_s are just $1.4 \pm 0.3\%$ at 16 kpc, while errors on R_e are at most $3.5 \pm 0.5\%$ at 2 kpc and shrink to half of that value at 2 kpc.

Errors on parameters are reduced by about a factor of two by imaging at nearby redshifts (z=0.01) and increase by about the same factor by imaging at z=0.1. These errors are not eliminated by increasing the image size (and shrinking the PSF relative to R_e) but shrink dramatically at the highest numerical resolution, to well under 1% in n_s and L and about 1% in R_e. This suggests that these parameters are in principle completely recoverable with SDSS-equivalent imaging and good sky subtraction.

We have also fit $n_s = 4$ de Vaucouleurs profiles using GALMORPH, as in Hyde & Bernardi (2009a). GALMORPH fits to the $n_s = 2$ models show expectedly poor results. Sizes are overestimated by factors from 1.6 (at 2kpc) to 2.4 (at 16kpc) while luminosities are overestimated by $30 - 60\%$. These results are not entirely unexpected – $n_s = 4$ models have shallower outer profiles and hence more light at large radii compared to profiles with lower $n_s = 2$. However, they do demonstrate that other free parameters such as the effective radius and mean surface

brightness cannot adjust to compensate for an incorrect profile choice, and so pure de Vaucouleurs profiles are not a good choice to fit ellipticals if their underlying surface brightness profiles are truly Sersic profile with n_s significantly lower than 4.

For $n_s = 4$ models, GALFIT free-n_s fits show curiously constant fractional errors on sizes, consistently underestimating R_e by $8 - 9 \pm 1\%$. Underestimates of n_s vary from a substantial $14 \pm 1\%$ at 2 kpc to $4 \pm 0.6\%$ at 16 kpc. Luminosity underestimates shrink from $5 \pm 0.6\%$ to $1.5 \pm 0.3\%$. These errors are not improved by imaging at lower redshift and so are unrelated to the relative size of the PSF. Instead, they are reduced substantially by increasing numerical resolution. At the highest resolution, size estimates shrink to $5 - 6 \pm 1\%$ at all sizes, while n_s underestimates now scale from $8 - 2\%$.

Since typical resolutions for central group galaxies are at the medium level or slightly higher, we expect that n_s is underestimated by 7% on average for a pure de Vaucouleurs fit, with better performance at smaller n_s. Size estimates are a minimum of 2% lower for large galaxies and up to 10% off for $R_e = 2$kpc.

By contrast, the GALMORPH fits with fixed $n_s = 4$ accurately recover sizes and luminosities to better than 2% even at the smallest sizes and at medium resolution. We conclude that even in ideal situations, free-n_s fits will systematically underestimate sizes and luminosities at the 5% level, whereas fixed-n_s fits only perform better if the exact value of n_s is known. In Appendix A.2 we detail how these results change after 2 Gyr of simulation with PARTREE using a fixed 100 pc softening length, as in the simulations.

A.1.3 Group Simulation Results

As Fig. A.1 shows, Sersic models generally do an acceptable job recovering central galaxy luminosities. For the $n_s = 1$ sample, model luminosities are typically 85-90% of the total in groups with no satellites with relatively small scatter. The Sersic luminosities of $n_s = 4$ central galaxies appear to have little or no systematic deviations from the true luminosities, although the scatter appears somewhat larger than in the $n_s = 1$ case. The largest discrepancies are found for groups with many mergers, particularly equal mass mergers, in which case the models can overestimate the central galaxy's luminosity by at least 20-30%, largely due to runaway growth of the effective radius and Sersic index. However, in most cases Sersic profiles appear to be appropriate fits to the galaxies. The underestimation of $n_s = 1$ merger luminosities appears to be a systematic effect. The underestimation of luminosities in groups with satellite galaxies is difficult to quantify, as the total luminosity in satellites is not easily separable from that of the central galaxy.

Testing whether half-light radii are recovered is also complicated by the presence of satellite galaxies. Nonetheless, we attempt to measure how closely R_e matches the estimated 'true' half-light radius R_{50} of the central galaxy in Fig. A.2. We estimate R_{50} as the radius enclosing half of the group luminosity in a given sky- and satellite-subtracted image, using the same best-fit ellipse as the Sersic model. The ratio should be unity if there are no satellite galaxies in the

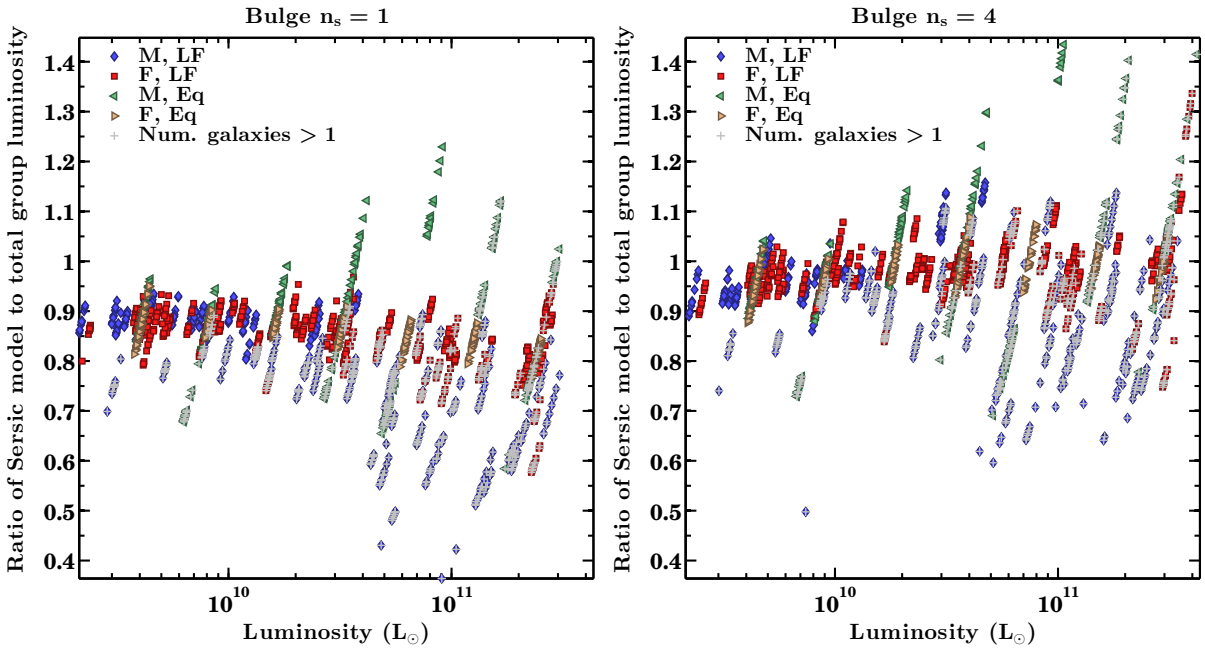

Figure A.1: Ratio of Sersic model luminosities to total group luminosity. Groups with multiple galaxies are highlighted, since the fraction contained in the satellites is not well-constrained. Mergers of equal-mass spirals ("Eq") tend to show the largest deviations from unity.

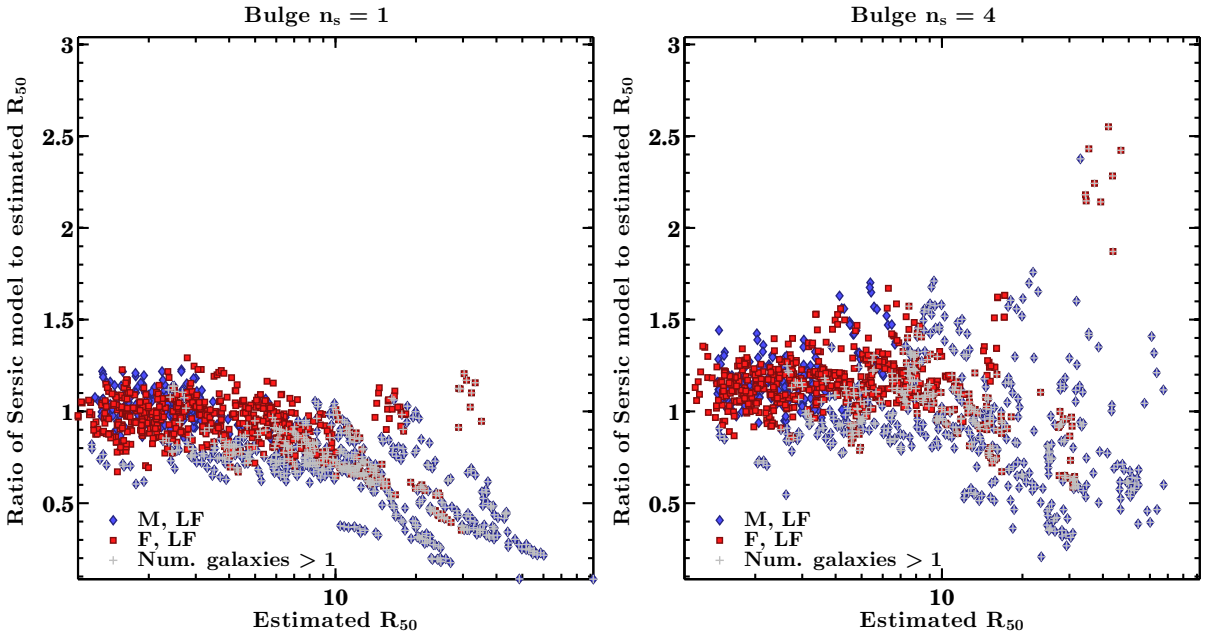

Figure A.2: Ratio of Sersic model effective radii to estimated half-light radii. Half-light radii are estimated by measuring the radius at which the enclosed light in a sky- and satellite-subtracted image equals half of the total group luminosity, and so are strictly larger than a true half-light radius if there are satellite galaxies. Regardless, Sersic half-light radii show considerably larger scatter relative to the estimated 'true' half-light radius than do Sersic model luminosities to the total group luminosity (Fig. A.1).

group and less than unity if there are. As Fig. A.2 shows, half-light radii are more difficult to measure than total galaxy luminosities - or rather, errors on half-light radii from Sersic fits are considerably larger than for luminosities, which likely contributes to the significant scatter in the Sersic size-luminosity relation compared to the Faber-Jackson relation.

At first glance, the large scatter in the ratio of Sersic model to 'true' half-light radius might suggest that much of the error in the Sersic size-luminosity relation is due to systematics rather than any intrinsic scatter. However, the size-luminosity relation using total group luminosity and 'true' half-light radius still shows significant scatter (0.08 dex) even when limited to galaxies with no satellites. A much larger sample of higher-resolution simulations would be required to determine if this scatter is due to numerical effects or genuinely intrinsic.

A.1.4 Petrosian Radii

As in SDSS, the Petrosian radius R_P is given by the radius at which the mean surface brightness in the ring bounded by $0.8R_P < r < 1.25R_P$ is 0.2 times the mean surface brightness within R_P. As a non-parametric size measure, it requires no fitting to measure, unlike the Sersic R_e. Since the Sersic profile is an analytical solution, one can compute R_P uniquely for any given n_s. For $n_s = 3$ to 6, R_P/R_e ranges from 1.5 to 2. The Petrosian magnitude of a galaxy is often estimated as the flux contained within a radius of a factor N_P larger than this Petrosian radius; SDSS uses $N_P = 2$. Petrosian magnitudes effectively measure half-light radii within $3 - 4R_e$ rather than the nominal $8R_e$ bounding box for the FITS images used to derive SDSS-equivalent magnitudes. We measure Petrosian radii using both circular apertures and elliptical apertures, using the best-fit ellipse from Sersic model fits in the latter case.

Unfortunately, as shown in Fig. A.3, Petrosian luminosities appear to underestimate the true galaxy luminosity by a similar amount to the analytical relation for purely circular profiles (see Graham & Driver (2005) for a reference to various Sersic quantities). Sizes are also underestimated to a similar degree as predicted for a pure circular Sersic profile, which suggests that most galaxies do not deviate greatly from a pure Sersic profile. The slight excess could be due to a number of factors, including the Sersic models underestimating the true half-light radii and/or Sersic indices, radial variations in the ellipticity or shape of the isophotes, or deviations of the underlying profile from a pure Sersic model, all of which are plausible. In principle, one can correct for this 'missing' flux using fitting formulae valid for a wide range of Sersic or other profiles (Graham et al., 2005), but this seems unnecessary given that the Sersic fits appear sufficient and are available for all of the simulations and observational catalogs alike.

A.2 Numerical Convergence

We test the numerical convergence of the spherical Sersic plus halo models by simulating every galaxy for 2 Gyr at 3 different resolutions (differing in particle number by a factor of 8 in each step). We also test a subset of the group simulations at similar resolutions. All measurements

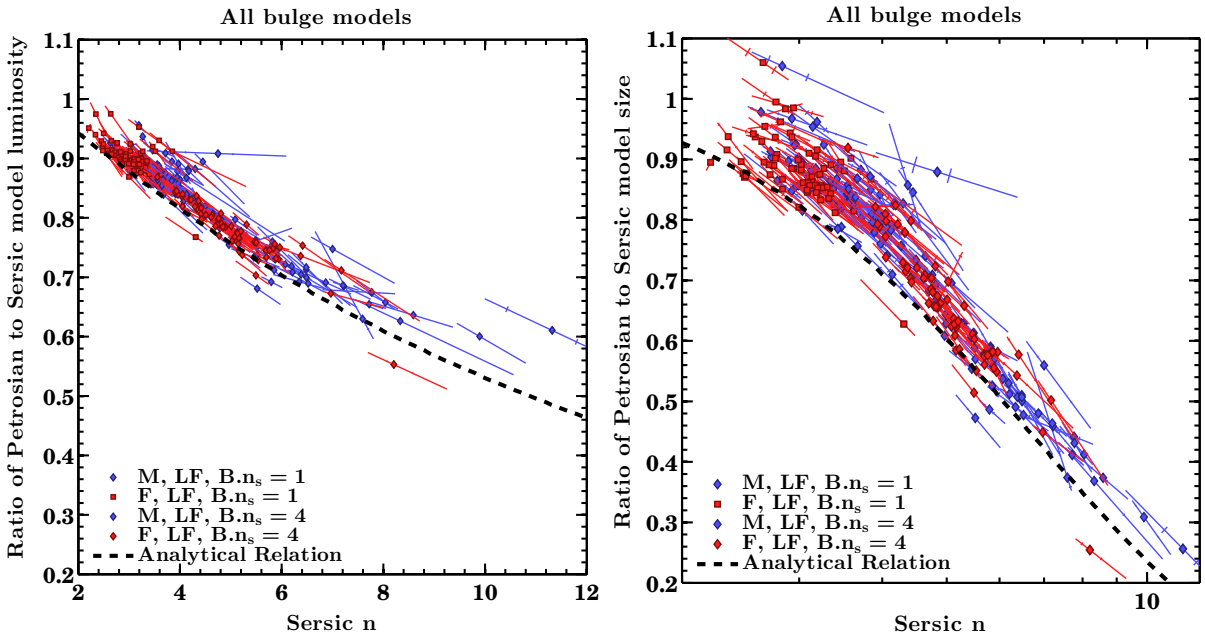

Figure A.3: Ratio of Petrosian model to Sersic model luminosities and sizes. Petrosian luminosities are derived from the elliptical Petrosian half-light radii measured within twice the Petrosian radius. Petrosian sizes and luminosities generally follow the analytical relation for a pure Sersic profile, underestimating sizes and luminosities by larger fractions for large Sersic indices.

are made using the same analysis pipeline as the results above; the images also have the same nominal redshift of $z = 0.025$.

Convergence is generally quite good. With a 0.2 Myr timestep, total energy is conserved to better than one part in 10^5. With the initial conditions re-centered to the barycenter, linear momentum remains small. The net angular momentum vector is the least well conserved quantity in Sersic plus halo models; each orthogonal component can vary by up to 5% of the net rotation. However, the total angular momentum is usually dominated by a small number of dark matter halo particles at large distances from the galaxy center. Angular momentum conservation for baryons in isolated galaxies is considerably better, and deviations of 1 to 2% are typical for groups where the bulk of the angular momentum is initially in galaxy orbits.

Having tested input parameter (Sersic index and effective radius) recovery with the analysis pipeline, we now turn to examining how these same parameters evolve in a 100 pc softened potential with a fixed, 0.2 Myr timestep, as in the group simulations. While idealized, these simulations are comparable to both the central ellipticals (which are slowly rotating and close to Sersic profiles, albeit somewhat flattened) and the bulges of the input spirals (which are smaller than the Sersic models and also slightly flattened by the presence of the disk) and will give estimates for how galaxy structure is affected by numerical resolution.

A.2.1 Sersic plus Halo Model Convergence

For a typical model (R_e=8 kpc) at very high resolution (7.68 million star particle), convergence of all parameters is achieved at the 1 to 2% level, with sizes, Sersic indices and dispersions shrinking slightly over 2 Gyr. Convergence is considerably worse for the $n_s = 4$ model and is strongly resolution dependent. A factor eight drop to high resolution (0.96 million star particles) approximately double errors in all parameters to 2-4%. For medium resolution (120,000 star particle), $n_s = 4$ models, parameters can shrink by over 10% - typical values being 5 to 15% for n_s (4 to 3.4), 15% for sizes (8 kpc to 6.8 kpc) and 5% for dispersions. Thus, for larger ellipticals to be suitably resolved, a million or more stellar particles are required, especially if the profiles are as or more centrally concentrated than an $n_s = 4$ model. Less centrally concentrated models such as $n_s = 2$ are much less sensitive to numerical resolution and can be resolved by 100,000 stellar particles with at most 3 to 4% level drops in sizes and Sersic index. Only 4 simulations in the sample have fewer than 720,000 stellar particles, so central remnants are largely unaffected by numerical relaxation after formation regardless of their central concentration.

Unfortunately, the results are not as encouraging for smaller models. For the smallest R_e=2 kpc model at low (15,000 star particle) resolution, Sersic indices shrink up to 50% (from 2 to 1.5, or 4 to 2.3). Sizes typically drop by less than 10%, but dispersions also shrink up to 20%. At high resolution, Sersic indices converge at the 5 to 15% level (from 2 to 1.9 and 4 to 3.4). Sizes remain constant for $n_s = 2$ and drop at most 5% for $n_s = 4$, with dispersions also shrinking by 3 to 5%. Typical remnants are resolved at close to this high resolution, so the greatest effect would be on the Sersic indices of small, high n_s ellipticals.

The greater concern with these results is the relaxation that occurs in the bulges of progenitor spirals. The effective radius of the M31 model is 1.5 kpc, but most galaxies are scaled to smaller sizes than this, with 0.5 to 1 kpc bulge R_e. Moreover, in groups with larger numbers of galaxies, total particle counts are larger, but individual spirals can have as few as 60,000 stellar particles, of which only 20,000 are in the bulge. The bulge is partially stabilized (and flattened) by the disk, but the disk forms a core near the center of the galaxy, and so one might expect the behaviour of these compact, marginally resolved bulges to be similar to the Sersic plus halo models. We will now test this hypothesis with convergence studies of group mergers.

A.2.2 Group Simulation Convergence

We test numerical convergence in the groups by running a selected sample with a factor of eight higher and lower resolution and comparing parameters after the usual elapsed times (5.0, 7.7 and 10.3 Gyr). As all of the groups are resolved with an average of over a million stellar particles, numerical convergence is expected to be good once groups have merged. However, as detailed above, the least massive spirals in more massive groups are not as well resolved, so not all groups are expected to be converged at our standard resolution.

Parameter Recovery

Fig. A.4 shows convergence for several identical groups on the size-luminosity and size-σ relations after 10.3 Gyr. Central remnant luminosities are fairly constant across all resolutions, but low resolutions can have slightly lower values. Sizes and dispersions are larger at low resolutions. Both trends continue from fiducial/medium to high resolution, although it is not as extreme - sizes are usually not more than 10 percent smaller between medium and high resolution.

Sersic indices are systematically lower at low resolution by a factor of 1 to 2 (Fig. A.5). The trend persists at high resolution, although n_s typically increases by a smaller factor of 0.2 to 0.3 between mid to high resolutions. Of the four parameters tested, then, luminosity appears to be the most robust, while the Sersic index is most sensitive to resolution effects. The effects on sizes are too small to fully reconcile the mismatch between sizes of faint simulated galaxies compared to observed ellipticals (Fig. 3.7). Dispersions generally decrease with increasing resolution, and so numerical effects also cannot explain the lower intercept of the simulated Faber-Jackson relation compared to that of observed ellipticals (Fig. 3.9).

In general, increasing resolution by a factor of eight produces similar trends in the group simulations as in isolated Sersic plus halo models - Sersic indices increase, while sizes and dispersions decrease. The effects are not very large going from our standard (medium) to high resolution but are considerable when stepping down to low resolution. We recommend that a minimum of a million stellar particles be used to adequately resolve spheroidal galaxies. While luminosities and masses remain converged at low resolution, sizes and dispersions are overestimated. Sersic indices are especially untrustworthy, being systematically offset lower by one or two from higher resolutions.

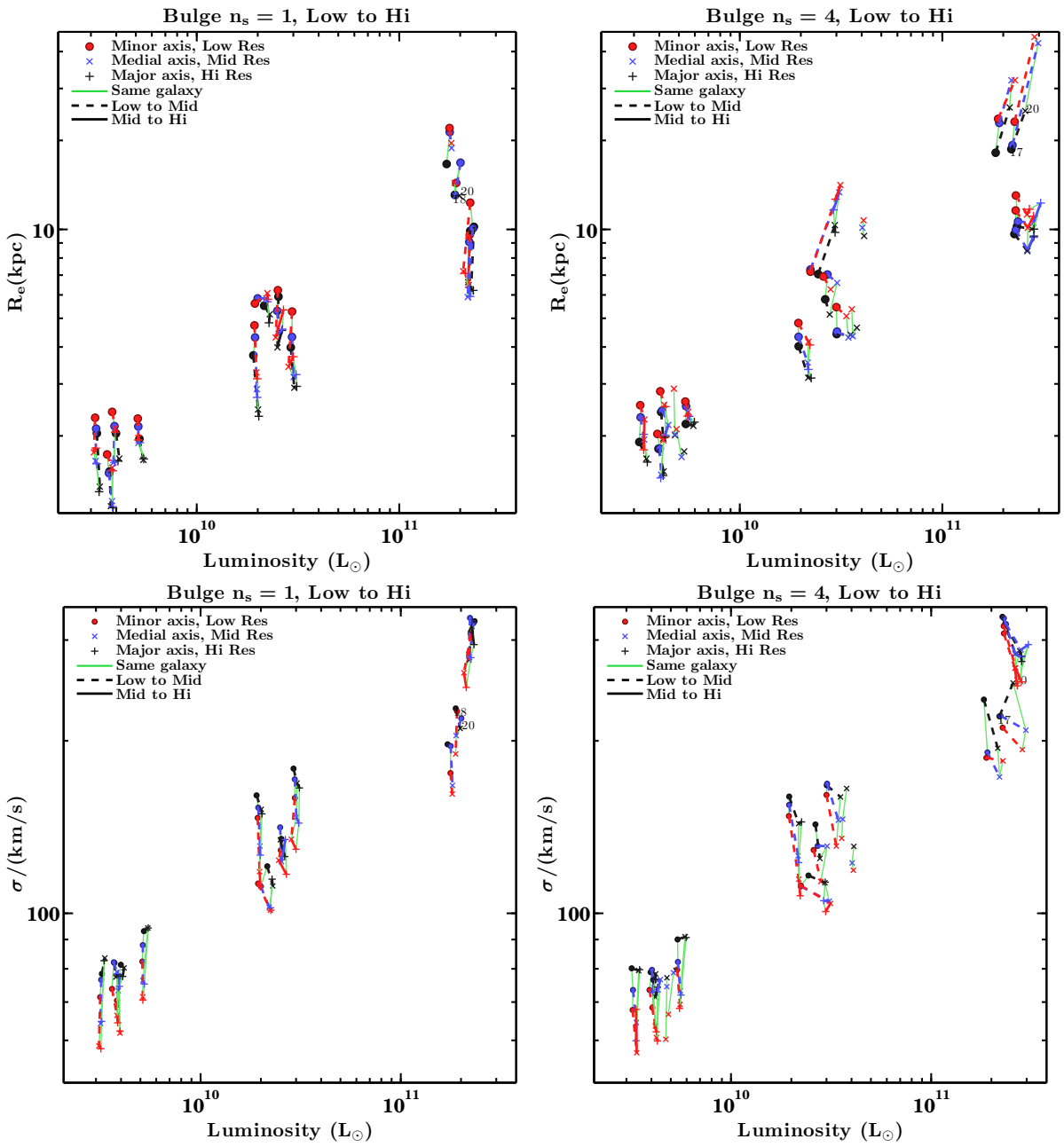

Figure A.4: Numerical convergence about size-luminosity and size-σ relations for principal axis projections of selected groups after 10.3 Gyr. At low resolutions, galaxies generally have larger sizes and dispersions than at higher resolution.

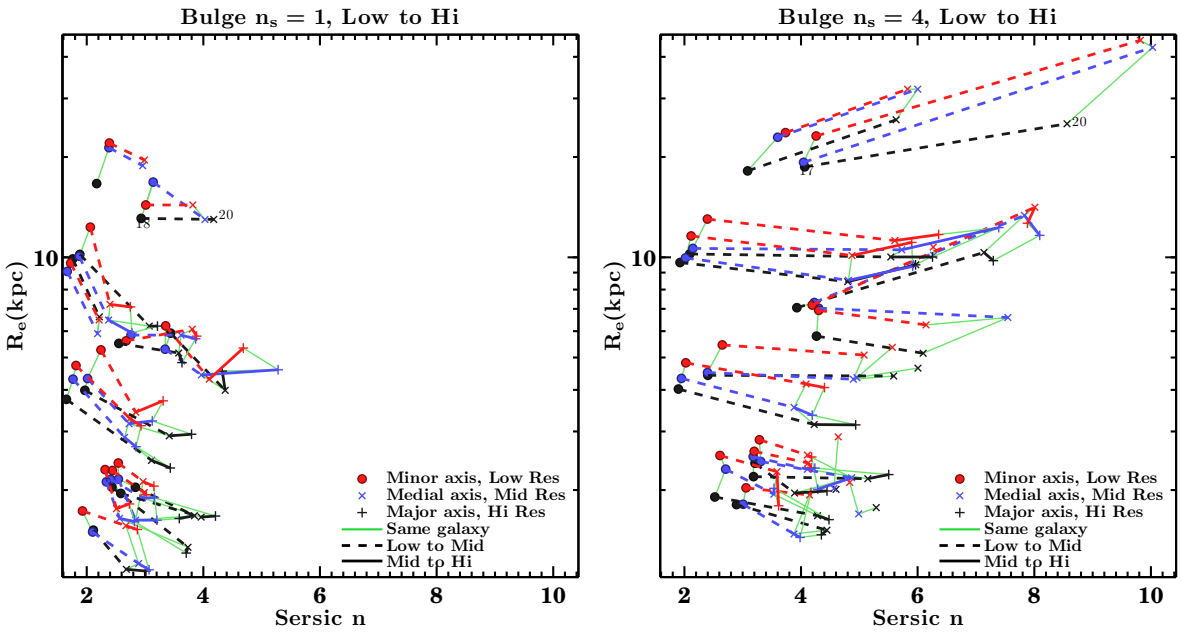

Figure A.5: Numerical convergence about the size-n_s relation for principal axis projections of selected groups. At low resolutions, galaxies have lower n_s by a factor of 1-2 than at medium or high resolution.

Appendix B

Chapter 3 Appendices

B.1 Scaling Relations at Different Times

The scaling relations presented in §3.1.2 are nominally for a zero-redshift galaxy population, assuming evolution from z=2. We can instead consider scaling relations at younger ages, assuming a fixed formation time for all groups. This is equivalent to assuming evolution from z=1 or z=0.5, since the only initial redshift-dependent parameter in the initial conditions is the group size. One might also consider combining groups from different snapshots into a single sample to simulate a sample with galaxies of different ages; however, this is best left to purely cosmological initial conditions with known merger trees and formation times.

With these caveats in mind, we now present predictions for the evolution of the slope and scatter of selected scaling relations assuming a fixed formation time for all groups. The best-fit relations measured in Tab. B.1 show slight evolution with time in the slopes (increasing) and intercepts (decreasing) and limited evolution in scatter. The steepening of the slope and lowering of the intercept would seem to suggest that brighter ellipticals grow off the relation at later times while fainter ellipticals grow slowly, if it all - in our case largely by construction, since the Few-merger sample does not have any late-time mergers. This interpretation is complicated by the fact that some of the largest groups do not have a relaxed, early-type central remnant formed in the earlier time steps and so are not included in the sample at earlier times but are included later on. Thus, as in most observational catalogs, not all of the descendants can necessarily be clearly identified with a previous early-type ancestor.

The best-fit Faber-Jackson relations measured in Tab. B.1 also show slight evolution of the slope, but in the opposite sense (decreasing/flattening), with a corresponding increase in the intercept. However, the scatter remains largely unchanged at 0.04 dex.

Table B.1: Sersic model size-luminosity relations at different times
Simulations, Sersic model L and R_e, Unweighted

B.n_s	Time	Sample	Slope	Intercept	R.M.S.
All	5.0	All	0.51 ± 0.01	-4.73 ± 0.06	0.11
All	7.7	All	0.53 ± 0.01	-4.88 ± 0.05	0.11
All	10.3	All	0.58 ± 0.01	-5.32 ± 0.06	0.12
All	5.0	Many	0.57 ± 0.01	-5.29 ± 0.10	0.11
All	7.7	Many	0.58 ± 0.01	-5.30 ± 0.06	0.10
All	10.3	Many	0.62 ± 0.01	-5.69 ± 0.06	0.10
All	5.0	Few	0.47 ± 0.01	-4.36 ± 0.06	0.10
All	7.7	Few	0.50 ± 0.01	-4.61 ± 0.06	0.10
All	10.3	Few	0.54 ± 0.01	-4.96 ± 0.08	0.12

Sersic model size-luminosity relations of simulations after different times have elapsed (in Gyr) or, equivalently, assuming different formation redshifts (0.5, 1.0 and 2.0). Data are for ten equally-spaced, randomly oriented projections of each galaxy.

Table B.2: Sersic model Faber-Jackson relations of simulations after different times
Simulations, Sersic model L, Unweighted

B.n_s	Time	Sample	Slope	Intercept	R.M.S.
All	5.0	All	0.31 ± 0.00	-1.08 ± 0.02	0.05
All	7.7	All	0.30 ± 0.00	-0.99 ± 0.02	0.04
All	10.3	All	0.28 ± 0.00	-0.86 ± 0.02	0.04
All	5.0	Many	0.29 ± 0.00	-0.89 ± 0.03	0.05
All	7.7	Many	0.28 ± 0.00	-0.83 ± 0.02	0.04
All	10.3	Many	0.27 ± 0.00	-0.72 ± 0.02	0.04
All	5.0	Few	0.32 ± 0.00	-1.21 ± 0.02	0.04
All	7.7	Few	0.31 ± 0.00	-1.09 ± 0.02	0.04
All	10.3	Few	0.30 ± 0.00	-0.98 ± 0.03	0.04

Sersic model Faber-Jackson relations of simulations after different times have elapsed. Format as in Tab. B.1. The slopes generally flatten slightly while intercepts increase and scatter remains constant at 0.04 dex.

Appendix C

Chapter 4 Appendices

C.1 Virial Ratios as a Function of Radius

This appendix demonstrates that the virial ratio within a given radius of a collisionless, multi-component system are not necessarily unity. The total potential and kinetic energy (cumulative) is measured within a sphere of radius r, as a function of r. The full potential of the galaxy is used in these calculations, including the contribution from mass outside r.

The left panel of Fig. C.1 shows these cumulative virial ratios for a number of galaxies. Included are idealized spherical Sersic models with and without halos, as well as a comparable merger remnant, all chosen to have $R_e \simeq 4$kpc. In each case, the virial ratio grows from a smaller value to converge to unity. The convergence is much slower for galaxies with a massive halo, occurring at around $10R_e$ rather than R_e for systems without halos. The only exception is if a surface pressure term is added to $2T$ (Carlberg et al., 1996; Shaw et al., 2006).

The surface pressure is calculated as $3PV = 4\pi\rho(r)v_r^2r^3$, summing over particles in a thin shell from $0.95r$ and $1.05r$ in practice. The surface pressure increases the virial ratio, but q remains below unity within R_e and overshoots to $q = 1.2$ at $10R_e$, so the surface pressure does not keep $q = 1$ at all r. This may be because the surface pressure term is meant to account for continuous, cosmological mass accretion, which does not occur in our simulations. On the other hand, Shaw et al. (2006) found that the surface pressure correction did yield values of $q = 1$ in two relaxed, simulated galaxy clusters; surprisingly, though, the surface pressure dominated at small radii ($r < 0.2R_{vir}$), where one might not expect accretion to be so important at z=0. Whatever the case, the surface pressure term is clearly not sufficient to yield $q = 1$ for galaxies.

Galaxies are multi-component systems, so it is worth considering whether the stellar component is virialized while embedded within a dark halo. The right panel of Fig. C.1 shows *stellar* virial ratios $q_\star$ for selected galaxies with halos. In practice, $q_\star$ is calculated identically to q, but only summing over stellar particles. In general, $q_\star$ is below unity, because the stellar dispersion is lower than the halo dispersion and stars are deeper in the potential well than most of the halo. $q_\star$ can exceed unity if a surface pressure term of the form is included is included, but not if it is weighted by the stellar mass fraction; in neither case is $q_\star$ exactly unity at all radii.

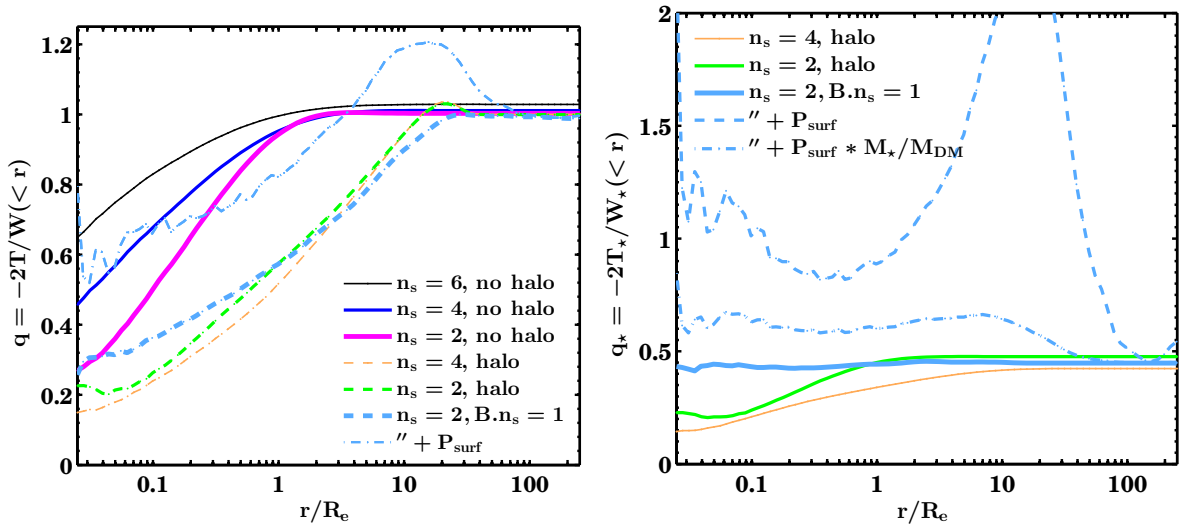

Figure C.1: Left panel: The virial ratio within a range of R/R_e for a number of model galaxies (plus one merger remnant) with effective radii of approximately 4kpc. Right panel: Stellar virial ratios $q_\star$ for galaxies with halos.

However, the stellar virial ratio for the simulated galaxy is remarkably flat, at a nearly constant value of 0.45 - the only such measure to remain constant over nearly 5 orders of magnitude in radial distance. If this ratio is universal in real galaxies, then the scalar virial theorem should be usable for any size measure and regardless of systematics; however, that is a substantial "if". Fig. 4.7 already showed that $q_\star$ for the entire galaxy (effectively at $r = \infty$) has some scatter, but it is unclear if the more substantial deviations from $q_\star = 0.45$ are just due to contamination from surviving satellites.

C.2 Sensitivity of the Fundamental Plane to Initial Conditions

The initial conditions in the first two subsamples were correlated, in the sense that groups of similar mass had similar positions of satellite galaxies, but randomized orbits (§2.1.2). A third subsample had entirely randomized positions and orbits for each galaxy. This was designed to test how sensitive the tilt is to orbital configurations in each group.

Tab. C.1 lists the tilt for all three subsamples. Subsample 3 with completely random orbits shows the largest tilt of the three, whereas subsamples 1 and 2 are largely consistent with one another. This suggests that the tilt is somewhat sensitive to both the placement of galaxies within the group and their initial velocities/orbits. Moreover, the difference between $\mathrm{B.n_s} = 1$ and $\mathrm{B.n_s} = 4$ is much smaller in subsample 3, so there is some uncertainty in the relative importance of initial galaxy structure to the tilt.

Table C.1: Sersic model Fundamental Plane fits for different simulation subsamples
Simulations: Ten equally-spaced projections, randomly oriented

$B.n_s$	Subsample	a	b	Intercept	R.M.S.
1	1	1.77	0.34	-10.04 ± 0.10	0.02
1	2	1.82	0.34	-10.19 ± 0.10	0.02
1	3	1.69	0.30	-9.01 ± 0.09	0.03
4	1	1.65	0.29	-8.77 ± 0.06	0.02
4	2	1.68	0.29	-8.89 ± 0.07	0.02
4	3	1.61	0.28	-8.41 ± 0.05	0.02

Fundamental plane fits to subsamples with less (1,2) and more (3) randomized initial conditions; other table definition as in Tab. 4.1. All fits are unweighted. Fully random orbits (subsample 3) produce slightly larger tilts, especially for $B.n_s = 1$. Errors on a are uniformly 0.01 and errors on b are smaller than 0.005.

Appendix D

Chapter 5 Appendices

D.1 Numerical Convergence of Density Profiles

In Appendix A.2, we showed detailed results for the resolution sensitivity of observed quantities like σ, R_e, L, μ and n_s. Using this same sample of resolution-testing simulations, we can also test for the effects of numerical resolution on the internal structure of galaxies. As an example, we will choose one of the groups in the highest mass bin, initially consisting of three spirals, each with a de Vaucouleurs bulge. This group was run at a standard resolution of 720,000 stellar particles and 1,920,000 dark matter particles, with a 100 pc softening length, as well as at eight times higher and lower particle numbers, keeping the softening length fixed.

Fig. D.1 shows the density profile of the galaxy at the three resolutions, both in the dark matter and stars. For reference, a number of fits using analytic functions are also shown, fitting over the range from 0.45–225kpc ($R_e/20$ to $25R_e$, for the galaxy's mean R_e of 9kpc). These are the Hernquist (Hernquist, 1990), NFW (Navarro et al., 1997) and Einasto (Einasto, 1965) profiles. The Hernquist profile, $\rho = \rho_0 r^{-1}(a+r)^{-b}$, with $b = 3$, was designed to approximate a de Vaucouleurs profile in projection. The NFW profile follows the same form, but with $b = 2$; it has been found to be a good fit to the density profiles of dark halos of a wide range of scales in cosmological simulations. The Einasto profile, $\rho = \rho_0 \exp((r/a)^n)$, is much like the Sersic function: an exponential with a tunable power-law index n, and hence an additional free parameter over Hernquist or NFW profiles.

The Hernquist profile is a fair approximation to both the stellar and dark matter density profiles of the galaxy, but does not entirely match the shape of the stellar profile. What is evident is that the fit changes from the standard to the higher resolution. In fact, there is a small "core" (a flattening of the density profile) in the stellar density profile at standard resolution, which is even more extreme at lower resolution. There is also a dark matter "cusp" (an sharp steepening of the density profile) at both standard and low resolution, which is absent at the highest resolution. While the dark matter cusps and stellar core are quite strong within 1–2kpc, the profiles beyond this radius are generally similar and largely indistinguishable at the effective radius of 9 kpc.

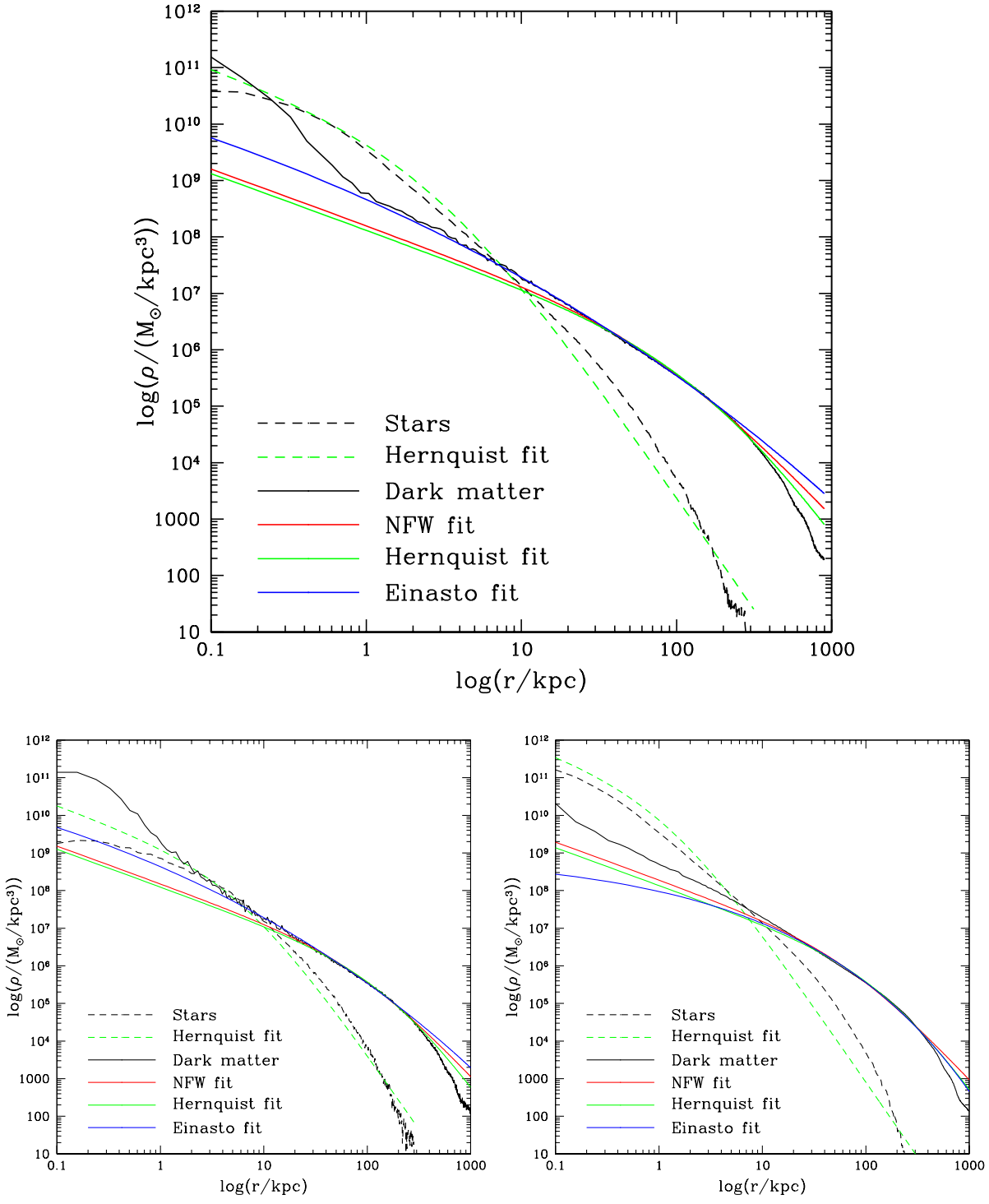

Figure D.1: Numerical convergence of the stellar and dark matter density profiles of a simulated elliptical. The top panel shows the profiles at standard resolution, while the bottom left was run with eight times fewer particles, and the bottom right with eight times as many. In addition, a number of fits from commonly-used analytic profiles are shown (see text for details).

These results are fairly representative of the tested groups, although neither the stellar nor the dark matter profiles are universal. There are certainly non-negligible numerical effects from limited particle numbers. More specifically, two-body relaxation of the more massive dark matter particles has evacuated less massive stellar particles, creating a dark matter cusp and a stellar core. Increasing the softening length can inhibit the formation of cores through numerical relaxation, but only by simultaneously softening the potential and flattening both the inner dark matter and stellar density profiles.

At standard resolution, these cusps and cores are still considerably smaller than R_e, but they are also somewhat larger than the softening length of 100pc. At the lowest resolution, the stellar profile changes significantly within 2–3kpc, and so too does the Hernquist profile fit. This is precisely why observables like n_s are sensitive to resolution. In principle, R_e should remain fairly robust as long as the profile remains unchanged beyond R_e, but if R_e is obtained via a parametric fit including a region affected by limited resolution, then it could be biased. Any other quantity measured within R_e would change as well, such as dark matter fractions - especially if the dark matter cusp extends beyond R_e, which may be the case in smaller galaxies with lower resolution.

Ultimately, one should view the standard resolution of the group simulations - approximately 1–2 million stellar particles, and 3 times that number of dark matter particles - as a minimum to reliably resolve merger remnants. This is also only considering collisionless dynamics, not hydrodynamics or star formation. Indeed, this should serve as a cautionary note for theorists running cosmological simulations with 4–8 times fewer particles and larger softening lengths. At the minimum, if the predictions from such simulations are to be compared with observations, then any profile fitting and derived quantities should exclude the inner 4–5 softening lengths, which in some simulations would be larger than R_e itself.

Bibliography

Abazajian K., Adelman-McCarthy J. K., Agüeros M. A., Allam S. S., Anderson K., Anderson S. F., Annis J., Bahcall N. A., Baldry I. K., Bastian S., Berlind A., Bernardi M., Blanton M. R., Bochanski Jr. J. J., Boroski W. N., Briggs J. W., Brinkmann J., Brunner R. J., Budavári T., Carey L. N., Carliles S., Castander F. J., Connolly A. J., Csabai I., Doi M., Dong F., Eisenstein D. J., Evans M. L., Fan X., Finkbeiner D. P., Friedman S. D., Frieman J. A., Fukugita M., Gal R. R., Gillespie B., Glazebrook K., Gray J., Grebel E. K., Gunn J. E., Gurbani V. K., Hall P. B., Hamabe M., Harris F. H., Harris H. C., Harvanek M., Heckman T. M., Hendry J. S., Hennessy G. S., Hindsley R. B., Hogan C. J., Hogg D. W., Holmgren D. J., Ichikawa S.-i., Ichikawa T., Ivezić Ž., Jester S., Johnston D. E., Jorgensen A. M., Kent S. M., Kleinman S. J., Knapp G. R., Kniazev A. Y., Kron R. G., Krzesinski J., Kunszt P. Z., Kuropatkin N., Lamb D. Q., Lampeitl H., Lee B. C., Leger R. F., Li N., Lin H., Loh Y.-S., Long D. C., Loveday J., Lupton R. H., Malik T., Margon B., Matsubara T., McGehee P. M., McKay T. A., Meiksin A., Munn J. A., Nakajima R., Nash T., Neilsen Jr. E. H., Newberg H. J., Newman P. R., Nichol R. C., Nicinski T., Nieto-Santisteban M., Nitta A., Okamura S., O'Mullane W., Ostriker J. P., Owen R., Padmanabhan N., Peoples J., Pier J. R., Pope A. C., Quinn T. R., Richards G. T., Richmond M. W., Rix H.-W., Rockosi C. M., Schlegel D. J., Schneider D. P., Scranton R., Sekiguchi M., Seljak U., Sergey G., Sesar B., Sheldon E., Shimasaku K., Siegmund W. A., Silvestri N. M., Smith J. A., Smolčić V., Snedden S. A., Stebbins A., Stoughton C., Strauss M. A., SubbaRao M., Szalay A. S., Szapudi I., Szkody P., Szokoly G. P., Tegmark M., Teodoro L., Thakar A. R., Tremonti C., Tucker D. L., Uomoto A., Vanden Berk D. E., Vandenberg J., Vogeley M. S., Voges W., Vogt N. P., Walkowicz L. M., Wang S.-i., Weinberg D. H., West A. A., White S. D. M., Wilhite B. C., Xu Y., Yanny B., Yasuda N., Yip C.-W., Yocum D. R., York D. G., Zehavi I., Zibetti S., Zucker D. B., 2004, AJ, 128, 502

Abazajian K. N., Adelman-McCarthy J. K., Agüeros M. A., Allam S. S., Allende Prieto C., An D., Anderson K. S. J., Anderson S. F., Annis J., Bahcall N. A., et al., 2009, ApJS, 182, 543

Aceves H., Velázquez H., 2005, MNRAS, 360, L50

Agertz O., Kravtsov A. V., Leitner S. N., Gnedin N. Y., 2013, ApJ, 770, 25

Aihara H., Allende Prieto C., An D., Anderson S. F., Aubourg É., Balbinot E., Beers T. C., Berlind A. A., Bickerton S. J., Bizyaev D., Blanton M. R., Bochanski J. J., Bolton A. S., Bovy J., Brandt W. N., Brinkmann J., Brown P. J., Brownstein J. R., Busca N. G., Campbell H., Carr M. A., Chen Y., Chiappini C., Comparat J., Connolly N., Cortes M., Croft R. A. C., Cuesta A. J., da Costa L. N., Davenport J. R. A., Dawson K., Dhital S., Ealet A., Ebelke G. L., Edmondson E. M., Eisenstein D. J., Escoffier S., Esposito M., Evans M. L., Fan X., Femenía Castellá B., Font-Ribera A., Frinchaboy P. M., Ge J., Gillespie B. A., Gilmore G., González Hernández J. I., Gott J. R., Gould A., Grebel E. K., Gunn J. E., Hamilton J.-C., Harding P., Harris D. W., Hawley S. L., Hearty F. R., Ho S., Hogg D. W., Holtzman J. A., Honscheid K., Inada N., Ivans I. I., Jiang L., Johnson J. A., Jordan C., Jordan W. P., Kazin E. A., Kirkby D., Klaene M. A., Knapp G. R., Kneib J.-P., Kochanek C. S., Koesterke L., Kollmeier J. A., Kron R. G., Lampeitl H., Lang D., Le Goff J.-M., Lee Y. S., Lin Y.-T., Long D. C., Loomis C. P., Lucatello S., Lundgren B., Lupton R. H., Ma Z., MacDonald N., Mahadevan S., Maia M. A. G., Makler M., Malanushenko E., Malanushenko V., Mandelbaum R., Maraston C., Margala D., Masters K. L., McBride C. K., McGehee P. M., McGreer I. D., Ménard B., Miralda-Escudé J., Morrison H. L., Mullally F., Muna D., Munn J. A., Murayama H., Myers A. D., Naugle T., Neto A. F., Nguyen D. C., Nichol R. C., O'Connell R. W., Ogando R. L. C., Olmstead M. D., Oravetz D. J., Padmanabhan N., Palanque-Delabrouille N., Pan K., Pandey P., Pâris I., Percival W. J., Petitjean P., Pfaffenberger R., Pforr J., Phleps S., Pichon C., Pieri M. M., Prada F., Price-Whelan A. M., Raddick M. J., Ramos B. H. F., Reylé C., Rich J., Richards G. T., Rix H.-W., Robin A. C., Rocha-Pinto H. J., Rockosi C. M., Roe N. A., Rollinde E., Ross A. J., Ross N. P., Rossetto B. M., Sánchez A. G., Sayres C., Schlegel D. J., Schlesinger K. J., Schmidt S. J., Schneider D. P., Sheldon E., Shu Y., Simmerer J., Simmons A. E., Sivarani T., Snedden S. A., Sobeck J. S., Steinmetz M., Strauss M. A., Szalay A. S., Tanaka M., Thakar A. R., Thomas D., Tinker J. L., Tofflemire B. M., Tojeiro R., Tremonti C. A., Vandenberg J., Vargas Magaña M., Verde L., Vogt N. P., Wake D. A., Wang J., Weaver B. A., Weinberg D. H., White M., White S. D. M., Yanny B., Yasuda N., Yeche C., Zehavi I., 2011, ApJS, 193, 29

Allanson S. P., Hudson M. J., Smith R. J., Lucey J. R., 2009, ApJ, 702, 1275

Auger M. W., Treu T., Bolton A. S., Gavazzi R., Koopmans L. V. E., Marshall P. J., Moustakas L. A., Burles S., 2010, ApJ, 724, 511

Balcells M., Graham A. W., Domínguez-Palmero L., Peletier R. F., 2003, ApJ, 582, L79

Balcells M., Graham A. W., Peletier R. F., 2007, ApJ, 665, 1104

Barnabè M., Czoske O., Koopmans L. V. E., Treu T., Bolton A. S., 2011, MNRAS, 415, 2215

Barnes J., 1985, MNRAS, 215, 517

Barnes J., Hut P., 1986, Nature, 324, 446

Barnes J. E., 1989, Nature, 338, 123

Behroozi P. S., Conroy C., Wechsler R. H., 2010, ApJ, 717, 379

Behroozi P. S., Wechsler R. H., Wu H.-Y., 2013, ApJ, 762, 109

Bekki K., 1998, ApJ, 496, 713

—, 2001, ApJ, 546, 189

Bender R., Burstein D., Faber S. M., 1992, ApJ, 399, 462

—, 1993, ApJ, 411, 153

Bernardi M., Meert A., Sheth R. K., Vikram V., Huertas-Company M., Mei S., Shankar F., 2013, MNRAS, 436, 697

Bernardi M., Sheth R. K., Annis J., Burles S., Eisenstein D. J., Finkbeiner D. P., Hogg D. W., Lupton R. H., Schlegel D. J., SubbaRao M., Bahcall N. A., Blakeslee J. P., Brinkmann J., Castander F. J., Connolly A. J., Csabai I., Doi M., Fukugita M., Frieman J., Heckman T., Hennessy G. S., Ivezić Ž., Knapp G. R., Lamb D. Q., McKay T., Munn J. A., Nichol R., Okamura S., Schneider D. P., Thakar A. R., York D. G., 2003, AJ, 125, 1866

Bershady M. A., Verheijen M. A. W., Swaters R. A., Andersen D. R., Westfall K. B., Martinsson T., 2010, ApJ, 716, 198

Blanton M. R., Schlegel D. J., Strauss M. A., Brinkmann J., Finkbeiner D., Fukugita M., Gunn J. E., Hogg D. W., Ivezić Ž., Knapp G. R., Lupton R. H., Munn J. A., Schneider D. P., Tegmark M., Zehavi I., 2005, AJ, 129, 2562

Bois M., Emsellem E., Bournaud F., Alatalo K., Blitz L., Bureau M., Cappellari M., Davies R. L., Davis T. A., de Zeeuw P. T., Duc P.-A., Khochfar S., Krajnović D., Kuntschner H., Lablanche P.-Y., McDermid R. M., Morganti R., Naab T., Oosterloo T., Sarzi M., Scott N., Serra P., Weijmans A.-M., Young L. M., 2011, MNRAS, 416, 1654

Bolton A. S., Treu T., Koopmans L. V. E., Gavazzi R., Moustakas L. A., Burles S., Schlegel D. J., Wayth R., 2008, ApJ, 684, 248

Borriello A., Salucci P., Danese L., 2003, MNRAS, 341, 1109

Bournaud F., Jog C. J., Combes F., 2007, A&A, 476, 1179

Bower R. G., Lucey J. R., Ellis R. S., 1992, MNRAS, 254, 601

Boylan-Kolchin M., Ma C.-P., Quataert E., 2005, MNRAS, 362, 184

—, 2006, MNRAS, 369, 1081

Bruce V. A., Dunlop J. S., Cirasuolo M., McLure R. J., Targett T. A., Bell E. F., Croton D. J., Dekel A., Faber S. M., Ferguson H. C., Grogin N. A., Kocevski D. D., Koekemoer A. M., Koo D. C., Lai K., Lotz J. M., McGrath E. J., Newman J. A., van der Wel A., 2012, MNRAS, 427, 1666

Bruzual G., Charlot S., 2003, MNRAS, 344, 1000

Bryan G. L., Norman M. L., O'Shea B. W., Abel T., Wise J. H., Turk M. J., Reynolds D. R., Collins D. C., Wang P., Skillman S. W., Smith B., Harkness R. P., Bordner J., Kim J.-h., Kuhlen M., Xu H., Goldbaum N., Hummels C., Kritsuk A. G., Tasker E., Skory S., Simpson C. M., Hahn O., Oishi J. S., So G. C., Zhao F., Cen R., Li Y., The Enzo Collaboration , 2014, ApJS, 211, 19

Busarello G., Capaccioli M., Capozziello S., Longo G., Puddu E., 1997, A&A, 320, 415

Capelato H. V., de Carvalho R. R., Carlberg R. G., 1995, ApJ, 451, 525

Cappellari M., Bacon R., Bureau M., Damen M. C., Davies R. L., de Zeeuw P. T., Emsellem E., Falcón-Barroso J., Krajnović D., Kuntschner H., McDermid R. M., Peletier R. F., Sarzi M., van den Bosch R. C. E., van de Ven G., 2006, MNRAS, 366, 1126

Cappellari M., Emsellem E., Krajnović D., McDermid R. M., Scott N., Verdoes Kleijn G. A., Young L. M., Alatalo K., Bacon R., Blitz L., Bois M., Bournaud F., Bureau M., Davies R. L., Davis T. A., de Zeeuw P. T., Duc P.-A., Khochfar S., Kuntschner H., Lablanche P.-Y., Morganti R., Naab T., Oosterloo T., Sarzi M., Serra P., Weijmans A.-M., 2011, MNRAS, 413, 813

Cappellari M., McDermid R. M., Alatalo K., Blitz L., Bois M., Bournaud F., Bureau M., Crocker A. F., Davies R. L., Davis T. A., de Zeeuw P. T., Duc P.-A., Emsellem E., Khochfar S., Krajnović D., Kuntschner H., Lablanche P.-Y., Morganti R., Naab T., Oosterloo T., Sarzi M., Scott N., Serra P., Weijmans A.-M., Young L. M., 2012, Nature, 484, 485

Cappellari M., McDermid R. M., Alatalo K., Blitz L., Bois M., Bournaud F., Bureau M., Crocker A. F., Davies R. L., Davis T. A., de Zeeuw P. T., Duc P.-A., Emsellem E., Khochfar S., Krajnović D., Kuntschner H., Morganti R., Naab T., Oosterloo T., Sarzi M., Scott N., Serra P., Weijmans A.-M., Young L. M., 2013a, MNRAS, 432, 1862

Cappellari M., Scott N., Alatalo K., Blitz L., Bois M., Bournaud F., Bureau M., Crocker A. F., Davies R. L., Davis T. A., de Zeeuw P. T., Duc P.-A., Emsellem E., Khochfar S., Krajnović D., Kuntschner H., McDermid R. M., Morganti R., Naab T., Oosterloo T., Sarzi M., Serra P., Weijmans A.-M., Young L. M., 2013b, MNRAS, 432, 1709

Carlberg R. G., 1986, ApJ, 310, 593

Carlberg R. G., Yee H. K. C., Ellingson E., Abraham R., Gravel P., Morris S., Pritchet C. J., 1996, ApJ, 462, 32

Carnevali P., Cavaliere A., Santangelo P., 1981, ApJ, 249, 449

Chabrier G., 2003, PASP, 115, 763

Chiosi C., Carraro G., 2002, MNRAS, 335, 335

Choi E., Ostriker J. P., Naab T., Oser L., Moster B. P., 2014, ArXiv e-prints

Ciotti L., 1991, A&A, 249, 99

Ciotti L., Lanzoni B., Volonteri M., 2007, ApJ, 658, 65

Conroy C., Gunn J. E., 2010, ApJ, 712, 833

Conroy C., Gunn J. E., White M., 2009, ApJ, 699, 486

Conroy C., van Dokkum P. G., 2012, ApJ, 760, 71

Cooper M. C., Newman J. A., Coil A. L., Croton D. J., Gerke B. F., Yan R., Davis M., Faber S. M., Guhathakurta P., Koo D. C., Weiner B. J., Willmer C. N. A., 2007, MNRAS, 376, 1445

Courteau S., Dutton A. A., van den Bosch F. C., MacArthur L. A., Dekel A., McIntosh D. H., Dale D. A., 2007, ApJ, 671, 203

Courteau S., Widrow L. M., McDonald M., Guhathakurta P., Gilbert K. M., Zhu Y., Beaton R. L., Majewski S. R., 2011, ApJ, 739, 20

Cox T. J., Dutta S. N., Di Matteo T., Hernquist L., Hopkins P. F., Robertson B., Springel V., 2006, ApJ, 650, 791

Croom S. M., Lawrence J. S., Bland-Hawthorn J., Bryant J. J., Fogarty L., Richards S., Goodwin M., Farrell T., Miziarski S., Heald R., Jones D. H., Lee S., Colless M., Brough S., Hopkins A. M., Bauer A. E., Birchall M. N., Ellis S., Horton A., Leon-Saval S., Lewis G., López-Sánchez Á. R., Min S.-S., Trinh C., Trowland H., 2012, MNRAS, 421, 872

Croton D. J., Farrar G. R., Norberg P., Colless M., Peacock J. A., Baldry I. K., Baugh C. M., Bland-Hawthorn J., Bridges T., Cannon R., Cole S., Collins C., Couch W., Dalton G., De Propris R., Driver S. P., Efstathiou G., Ellis R. S., Frenk C. S., Glazebrook K., Jackson C., Lahav O., Lewis I., Lumsden S., Maddox S., Madgwick D., Peterson B. A., Sutherland W., Taylor K., 2005, MNRAS, 356, 1155

Daddi E., Bournaud F., Walter F., Dannerbauer H., Carilli C. L., Dickinson M., Elbaz D., Morrison G. E., Riechers D., Onodera M., Salmi F., Krips M., Stern D., 2010, ApJ, 713, 686

Davies R. L., Sadler E. M., Peletier R. F., 1993, MNRAS, 262, 650

de Lapparent V., Arnouts S., Galaz G., Bardelli S., 2004, A&A, 422, 841

de Vaucouleurs G., 1948, Annales d'Astrophysique, 11, 247

—, 1959, Handbuch der Physik, 53, 275

de Zeeuw P. T., Bureau M., Emsellem E., Bacon R., Carollo C. M., Copin Y., Davies R. L., Kuntschner H., Miller B. W., Monnet G., Peletier R. F., Verolme E. K., 2002, MNRAS, 329, 513

Djorgovski S., Davis M., 1987, ApJ, 313, 59

Dressler A., 1980, ApJ, 236, 351

Dressler A., Lynden-Bell D., Burstein D., Davies R. L., Faber S. M., Terlevich R., Wegner G., 1987, ApJ, 313, 42

Dubinski J., 1996, New Astronomy, 1, 133

—, 1998, ApJ, 502, 141

Dubois Y., Gavazzi R., Peirani S., Silk J., 2013, MNRAS, 433, 3297

Dutton A. A., Conroy C., van den Bosch F. C., Simard L., Mendel J. T., Courteau S., Dekel A., More S., Prada F., 2011, MNRAS, 416, 322

Dutton A. A., Treu T., Brewer B. J., Marshall P. J., Auger M. W., Barnabè M., Koo D. C., Bolton A. S., Koopmans L. V. E., 2013, MNRAS, 428, 3183

Eggen O. J., Lynden-Bell D., Sandage A. R., 1962, ApJ, 136, 748

Einasto J., 1965, Trudy Astrofizicheskogo Instituta Alma-Ata, 5, 87

Emsellem E., Cappellari M., Krajnović D., Alatalo K., Blitz L., Bois M., Bournaud F., Bureau M., Davies R. L., Davis T. A., de Zeeuw P. T., Khochfar S., Kuntschner H., Lablanche P.-Y., McDermid R. M., Morganti R., Naab T., Oosterloo T., Sarzi M., Scott N., Serra P., van de Ven G., Weijmans A.-M., Young L. M., 2011, MNRAS, 414, 888

Emsellem E., Cappellari M., Krajnović D., van de Ven G., Bacon R., Bureau M., Davies R. L., de Zeeuw P. T., Falcón-Barroso J., Kuntschner H., McDermid R., Peletier R. F., Sarzi M., 2007, MNRAS, 379, 401

Faber S. M., Gallagher J. S., 1976, ApJ, 204, 365

Faber S. M., Jackson R. E., 1976, ApJ, 204, 668

Fakhouri O., Ma C.-P., Boylan-Kolchin M., 2010, MNRAS, 406, 2267

Feldmann R., Carollo C. M., Mayer L., 2011, ApJ, 736, 88

Fisher D. B., Drory N., 2010, ApJ, 716, 942

Förster Schreiber N. M., Genzel R., Bouché N., Cresci G., Davies R., Buschkamp P., Shapiro K., Tacconi L. J., Hicks E. K. S., Genel S., Shapley A. E., Erb D. K., Steidel C. C., Lutz D., Eisenhauer F., Gillessen S., Sternberg A., Renzini A., Cimatti A., Daddi E., Kurk J., Lilly S., Kong X., Lehnert M. D., Nesvadba N., Verma A., McCracken H., Arimoto N., Mignoli M., Onodera M., 2009, ApJ, 706, 1364

Förster Schreiber N. M., Genzel R., Newman S. F., Kurk J. D., Lutz D., Tacconi L. J., Wuyts S., Bandara K., Burkert A., Buschkamp P., Carollo C. M., Cresci G., Daddi E., Davies R., Eisenhauer F., Hicks E. K. S., Lang P., Lilly S. J., Mainieri V., Mancini C., Naab T., Peng Y., Renzini A., Rosario D., Shapiro Griffin K., Shapley A. E., Sternberg A., Tacchella S., Vergani D., Wisnioski E., Wuyts E., Zamorani G., 2014, ApJ, 787, 38

Franx M., Illingworth G., 1990, ApJ, 359, L41

Gallazzi A., Charlot S., Brinchmann J., White S. D. M., Tremonti C. A., 2005, MNRAS, 362, 41

Geller M. J., Huchra J. P., 1983, ApJS, 52, 61

Gerhard O., Kronawitter A., Saglia R. P., Bender R., 2001, AJ, 121, 1936

Graham A. W., 2013, Elliptical and Disk Galaxy Structure and Modern Scaling Laws, Oswalt T. D., Keel W. C., eds., p. 91

Graham A. W., Driver S. P., 2005, PASA, 22, 118

Graham A. W., Driver S. P., Petrosian V., Conselice C. J., Bershady M. A., Crawford S. M., Goto T., 2005, AJ, 130, 1535

Graham A. W., Erwin P., Trujillo I., Asensio Ramos A., 2003, AJ, 125, 2951

Graves G. J., Faber S. M., 2010, ApJ, 717, 803

Guzman R., Lucey J. R., Bower R. G., 1993, MNRAS, 265, 731

Hernquist L., 1990, ApJ, 356, 359

—, 1992, ApJ, 400, 460

—, 1993, ApJ, 409, 548

Hernquist L., Spergel D. N., Heyl J. S., 1993, ApJ, 416, 415

Hilz M., Naab T., Ostriker J. P., 2013, MNRAS, 429, 2924

Holmberg E., 1941, ApJ, 94, 385

Hopkins P. F., Cox T. J., Hernquist L., 2008, ApJ, 689, 17

Hopkins P. F., Croton D., Bundy K., Khochfar S., van den Bosch F., Somerville R. S., Wetzel A., Keres D., Hernquist L., Stewart K., Younger J. D., Genel S., Ma C.-P., 2010, ApJ, 724, 915

Hopkins P. F., Hernquist L., Cox T. J., Keres D., Wuyts S., 2009, ApJ, 691, 1424

Hopkins P. F., Keres D., Onorbe J., Faucher-Giguere C.-A., Quataert E., Murray N., Bullock J. S., 2013a, ArXiv e-prints

Hopkins P. F., Kereš D., Murray N., Hernquist L., Narayanan D., Hayward C. C., 2013b, MNRAS, 433, 78

Hopkins P. F., Quataert E., Murray N., 2011, MNRAS, 417, 950

—, 2012, MNRAS, 421, 3488

Huang S., Ho L. C., Peng C. Y., Li Z.-Y., Barth A. J., 2013, ApJ, 766, 47

Hubble E. P., 1936, Realm of the Nebulae

Hyde J. B., Bernardi M., 2009a, MNRAS, 394, 1978

—, 2009b, MNRAS, 396, 1171

Ishizawa T., Matsumoto R., Tajima T., Kageyama H., Sakai H., 1983, PASJ, 35, 61

Jonsson P., 2006, MNRAS, 372, 2

Kaviraj S., Ting Y.-S., Bureau M., Shabala S. S., Crockett R. M., Silk J., Lintott C., Smith A., Keel W. C., Masters K. L., Schawinski K., Bamford S. P., 2012, MNRAS, 423, 49

Kennicutt Jr. R. C., Armus L., Bendo G., Calzetti D., Dale D. A., Draine B. T., Engelbracht C. W., Gordon K. D., Grauer A. D., Helou G., Hollenbach D. J., Jarrett T. H., Kewley L. J., Leitherer C., Li A., Malhotra S., Regan M. W., Rieke G. H., Rieke M. J., Roussel H., Smith J.-D. T., Thornley M. D., Walter F., 2003, PASP, 115, 928

Khalatyan A., Cattaneo A., Schramm M., Gottlöber S., Steinmetz M., Wisotzki L., 2008, MNRAS, 387, 13

Khandai N., Di Matteo T., Croft R., Wilkins S. M., Feng Y., Tucker E., DeGraf C., Liu M.-S., 2014, ArXiv e-prints

Kim D.-W., Pellegrini S., eds., 2012, Astrophysics and Space Science Library, Vol. 378, Hot Interstellar Matter in Elliptical Galaxies

Kim J.-h., Abel T., Agertz O., Bryan G. L., Ceverino D., Christensen C., Conroy C., Dekel A., Gnedin N. Y., Goldbaum N. J., Guedes J., Hahn O., Hobbs A., Hopkins P. F., Hummels C. B., Iannuzzi F., Keres D., Klypin A., Kravtsov A. V., Krumholz M. R., Kuhlen M., Leitner S. N., Madau P., Mayer L., Moody C. E., Nagamine K., Norman M. L., Onorbe J., O'Shea B. W., Pillepich A., Primack J. R., Quinn T., Read J. I., Robertson B. E., Rocha M., Rudd D. H., Shen S., Smith B. D., Szalay A. S., Teyssier R., Thompson R., Todoroki K., Turk M. J., Wadsley J. W., Wise J. H., Zolotov A., AGORA Collaboration29 f. t., 2014, ApJS, 210, 14

King I. R., Minkowski R., 1972, in IAU Symposium, Vol. 44, External Galaxies and Quasi-Stellar Objects, Evans D. S., Wills D., Wills B. J., eds., p. 87

Knebe A., Knollmann S. R., Muldrew S. I., Pearce F. R., Aragon-Calvo M. A., Ascasibar Y., Behroozi P. S., Ceverino D., Colombi S., Diemand J., Dolag K., Falck B. L., Fasel P., Gardner J., Gottlöber S., Hsu C.-H., Iannuzzi F., Klypin A., Lukić Z., Maciejewski M., McBride C., Neyrinck M. C., Planelles S., Potter D., Quilis V., Rasera Y., Read J. I., Ricker P. M., Roy F., Springel V., Stadel J., Stinson G., Sutter P. M., Turchaninov V., Tweed D., Yepes G., Zemp M., 2011, MNRAS, 415, 2293

Kormendy J., 1977, ApJ, 218, 333

Kormendy J., Fisher D. B., Cornell M. E., Bender R., 2009, ApJS, 182, 216

Krajnović D., Alatalo K., Blitz L., Bois M., Bournaud F., Bureau M., Cappellari M., Davies R. L., Davis T. A., de Zeeuw P. T., Duc P.-A., Emsellem E., Khochfar S., Kuntschner H., McDermid R. M., Morganti R., Naab T., Oosterloo T., Sarzi M., Scott N., Serra P., Weijmans A.-M., Young L. M., 2012, MNRAS, 278

Kravtsov A., Vikhlinin A., Meshscheryakov A., 2014, ArXiv e-prints

Lablanche P.-Y., Cappellari M., Emsellem E., Bournaud F., Michel-Dansac L., Alatalo K., Blitz L., Bois M., Bureau M., Davies R. L., Davis T. A., de Zeeuw P. T., Duc P.-A., Khochfar S., Krajnović D., Kuntschner H., Morganti R., McDermid R. M., Naab T., Oosterloo T., Sarzi M., Scott N., Serra P., Weijmans A.-M., Young L. M., 2012, MNRAS, 424, 1495

Larson R. B., 1969, MNRAS, 145, 405

Law D. R., MaNGA Team, 2014, in American Astronomical Society Meeting Abstracts, Vol. 223, American Astronomical Society Meeting Abstracts #223, p. #254.31

Law D. R., Steidel C. C., Erb D. K., Larkin J. E., Pettini M., Shapley A. E., Wright S. A., 2009, ApJ, 697, 2057

Leroy A. K., Walter F., Bigiel F., Usero A., Weiss A., Brinks E., de Blok W. J. G., Kennicutt R. C., Schuster K.-F., Kramer C., Wiesemeyer H. W., Roussel H., 2009, AJ, 137, 4670

Li I. H., Yee H. K. C., Hsieh B. C., Gladders M., 2012, ApJ, 749, 150

Longhetti M., Saracco P., Severgnini P., Della Ceca R., Mannucci F., Bender R., Drory N., Feulner G., Hopp U., 2007, MNRAS, 374, 614

Madgwick D. S., Lahav O., Baldry I. K., Baugh C. M., Bland-Hawthorn J., Bridges T., Cannon R., Cole S., Colless M., Collins C., Couch W., Dalton G., De Propris R., Driver S. P., Efstathiou G., Ellis R. S., Frenk C. S., Glazebrook K., Jackson C., Lewis I., Lumsden S., Maddox S., Norberg P., Peacock J. A., Peterson B. A., Sutherland W., Taylor K., 2002, MNRAS, 333, 133

Magoulas C., Springob C. M., Colless M., Jones D. H., Campbell L. A., Lucey J. R., Mould J., Jarrett T., Merson A., Brough S., 2012, MNRAS, 427, 245

Maraston C., 2005, MNRAS, 362, 799

Maraston C., Strömbäck G., Thomas D., Wake D. A., Nichol R. C., 2009, MNRAS, 394, L107

Martig M., Bournaud F., Teyssier R., Dekel A., 2009, ApJ, 707, 250

Martizzi D., Teyssier R., Moore B., 2012, MNRAS, 420, 2859

McCarthy I. G., Schaye J., Ponman T. J., Bower R. G., Booth C. M., Dalla Vecchia C., Crain R. A., Springel V., Theuns T., Wiersma R. P. C., 2010, MNRAS, 406, 822

McGee S. L., Balogh M. L., Bower R. G., Font A. S., McCarthy I. G., 2009, MNRAS, 400, 937

Meert A., Vikram V., Bernardi M., 2013, MNRAS, 433, 1344

Mendel J. T., Simard L., Palmer M., Ellison S. L., Patton D. R., 2014, ApJS, 210, 3

Mihos J. C., Hernquist L., 1994, ApJ, 437, L47

Moster B. P., Macciò A. V., Somerville R. S., 2014, MNRAS, 437, 1027

Moster B. P., Naab T., White S. D. M., 2013, MNRAS, 428, 3121

Moster B. P., Somerville R. S., Maulbetsch C., van den Bosch F. C., Macciò A. V., Naab T., Oser L., 2010, ApJ, 710, 903

Naab T., Johansson P. H., Ostriker J. P., 2009, ApJ, 699, L178

Naab T., Oser L., Emsellem E., Cappellari M., Krajnovic D., McDermid R. M., Alatalo K., Bayet E., Blitz L., Bois M., Bournaud F., Bureau M., Crocker A., Davies R. L., Davis T. A., de Zeeuw P. T., Duc P.-A., Hirschmann M., Johansson P. H., Khochfar S., Kuntschner H.,

Morganti R., Oosterloo T., Sarzi M., Scott N., Serra P., van de Ven G., Weijmans A., Young L. M., 2013, ArXiv e-prints

Naab T., Ostriker J. P., 2009, ApJ, 690, 1452

Nair P., van den Bergh S., Abraham R. G., 2011, ApJ, 734, L31

Nair P. B., Abraham R. G., 2010, ApJS, 186, 427

Narayanan D., Bothwell M., Davé R., 2012, MNRAS, 426, 1178

Navarro J. F., Frenk C. S., White S. D. M., 1997, ApJ, 490, 493

Nipoti C., Londrillo P., Ciotti L., 2003, MNRAS, 342, 501

Nipoti C., Treu T., Auger M. W., Bolton A. S., 2009a, ApJ, 706, L86

Nipoti C., Treu T., Bolton A. S., 2009b, ApJ, 703, 1531

Oñorbe J., Domínguez-Tenreiro R., Sáiz A., Artal H., Serna A., 2006, MNRAS, 373, 503

Onions J., Knebe A., Pearce F. R., Muldrew S. I., Lux H., Knollmann S. R., Ascasibar Y., Behroozi P., Elahi P., Han J., Maciejewski M., Merchán M. E., Neyrinck M., Ruiz A. N., Sgró M. A., Springel V., Tweed D., 2012, MNRAS, 423, 1200

Oser L., Naab T., Ostriker J. P., Johansson P. H., 2012, ApJ, 744, 63

Oser L., Ostriker J. P., Naab T., Johansson P. H., Burkert A., 2010, ApJ, 725, 2312

Peletier R. F., Davies R. L., Illingworth G. D., Davis L. E., Cawson M., 1990, AJ, 100, 1091

Peng C. Y., Ho L. C., Impey C. D., Rix H.-W., 2002, AJ, 124, 266

—, 2010, AJ, 139, 2097

Petrosian V., 1976, ApJ, 209, L1

Prugniel P., Simien F., 1996, A&A, 309, 749

—, 1997, A&A, 321, 111

Riess A. G., Filippenko A. V., Challis P., Clocchiatti A., Diercks A., Garnavich P. M., Gilliland R. L., Hogan C. J., Jha S., Kirshner R. P., Leibundgut B., Phillips M. M., Reiss D., Schmidt B. P., Schommer R. A., Smith R. C., Spyromilio J., Stubbs C., Suntzeff N. B., Tonry J., 1998, AJ, 116, 1009

Rix H.-W., de Zeeuw P. T., Cretton N., van der Marel R. P., Carollo C. M., 1997, ApJ, 488, 702

Robertson B., Cox T. J., Hernquist L., Franx M., Hopkins P. F., Martini P., Springel V., 2006, ApJ, 641, 21

Robotham A., Phillipps S., de Propris R., 2010, MNRAS, 403, 1812

Rubin V. C., Thonnard N., Ford Jr. W. K., 1978, ApJ, 225, L107

Ruszkowski M., Springel V., 2009, ApJ, 696, 1094

Sadler E. M., Gerhard O. E., 1985, MNRAS, 214, 177

Salpeter E. E., 1955, ApJ, 121, 161

Sánchez S. F., Kennicutt R. C., Gil de Paz A., van de Ven G., Vílchez J. M., Wisotzki L., Walcher C. J., Mast D., Aguerri J. A. L., Albiol-Pérez S., Alonso-Herrero A., Alves J., Bakos J., Bartáková T., Bland-Hawthorn J., Boselli A., Bomans D. J., Castillo-Morales A., Cortijo-Ferrero C., de Lorenzo-Cáceres A., Del Olmo A., Dettmar R.-J., Díaz A., Ellis S., Falcón-Barroso J., Flores H., Gallazzi A., García-Lorenzo B., González Delgado R., Gruel N., Haines T., Hao C., Husemann B., Iglésias-Páramo J., Jahnke K., Johnson B., Jungwiert B., Kalinova V., Kehrig C., Kupko D., López-Sánchez Á. R., Lyubenova M., Marino R. A., Mármol-Queraltó E., Márquez I., Masegosa J., Meidt S., Mendez-Abreu J., Monreal-Ibero A., Montijo C., Mourão A. M., Palacios-Navarro G., Papaderos P., Pasquali A., Peletier R., Pérez E., Pérez I., Quirrenbach A., Relaño M., Rosales-Ortega F. F., Roth M. M., Ruiz-Lara T., Sánchez-Blázquez P., Sengupta C., Singh R., Stanishev V., Trager S. C., Vazdekis A., Viironen K., Wild V., Zibetti S., Ziegler B., 2012, A&A, 538, A8

Scannapieco C., Wadepuhl M., Parry O. H., Navarro J. F., Jenkins A., Springel V., Teyssier R., Carlson E., Couchman H. M. P., Crain R. A., Dalla Vecchia C., Frenk C. S., Kobayashi C., Monaco P., Murante G., Okamoto T., Quinn T., Schaye J., Stinson G. S., Theuns T., Wadsley J., White S. D. M., Woods R., 2012, MNRAS, 423, 1726

Schechter P., 1976, ApJ, 203, 297

Schmidt M., 1968, ApJ, 151, 393

Serra P., Oosterloo T. A., 2010, MNRAS, 401, L29

Sersic J. L., 1968, Atlas de galaxias australes

Shao Z., Xiao Q., Shen S., Mo H. J., Xia X., Deng Z., 2007, ApJ, 659, 1159

Shaw L. D., Weller J., Ostriker J. P., Bode P., 2006, ApJ, 646, 815

Shu Y., Bolton A. S., Brownstein J. R., Montero-Dorta A. D., Koopmans L. V. E., Treu T., Gavazzi R., Auger M. W., Czoske O., Marshall P. J., Moustakas L. A., 2014, ArXiv e-prints

Simard L., Clowe D., Desai V., Dalcanton J. J., von der Linden A., Poggianti B. M., White S. D. M., Aragón-Salamanca A., De Lucia G., Halliday C., Jablonka P., Milvang-Jensen B., Saglia R. P., Pelló R., Rudnick G. H., Zaritsky D., 2009, A&A, 508, 1141

Simard L., Mendel J. T., Patton D. R., Ellison S. L., McConnachie A. W., 2011, ApJS, 196, 11

Simard L., Willmer C. N. A., Vogt N. P., Sarajedini V. L., Phillips A. C., Weiner B. J., Koo D. C., Im M., Illingworth G. D., Faber S. M., 2002, ApJS, 142, 1

Spergel D. N., Verde L., Peiris H. V., Komatsu E., Nolta M. R., Bennett C. L., Halpern M., Hinshaw G., Jarosik N., Kogut A., Limon M., Meyer S. S., Page L., Tucker G. S., Weiland J. L., Wollack E., Wright E. L., 2003, ApJS, 148, 175

Springel V., 2000, MNRAS, 312, 859

—, 2005, MNRAS, 364, 1105

—, 2010, MNRAS, 401, 791

Springel V., Di Matteo T., Hernquist L., 2005a, MNRAS, 361, 776

Springel V., White S. D. M., Jenkins A., Frenk C. S., Yoshida N., Gao L., Navarro J., Thacker R., Croton D., Helly J., Peacock J. A., Cole S., Thomas P., Couchman H., Evrard A., Colberg J., Pearce F., 2005b, Nature, 435, 629

Springel V., Yoshida N., White S. D. M., 2001, New A, 6, 79

Srisawat C., Knebe A., Pearce F. R., Schneider A., Thomas P. A., Behroozi P., Dolag K., Elahi P. J., Han J., Helly J., Jing Y., Jung I., Lee J., Mao Y.-Y., Onions J., Rodriguez-Gomez V., Tweed D., Yi S. K., 2013, MNRAS, 436, 150

Stewart K. R., Bullock J. S., Wechsler R. H., Maller A. H., Zentner A. R., 2008, ApJ, 683, 597

Stoughton C., Lupton R. H., Bernardi M., Blanton M. R., Burles S., Castander F. J., Connolly A. J., Eisenstein D. J., Frieman J. A., Hennessy G. S., Hindsley R. B., Ivezić Ž., Kent S., Kunszt P. Z., Lee B. C., Meiksin A., Munn J. A., Newberg H. J., Nichol R. C., Nicinski T., Pier J. R., Richards G. T., Richmond M. W., Schlegel D. J., Smith J. A., Strauss M. A., SubbaRao M., Szalay A. S., Thakar A. R., Tucker D. L., Vanden Berk D. E., Yanny B., Adelman J. K., Anderson Jr. J. E., Anderson S. F., Annis J., Bahcall N. A., Bakken J. A., Bartelmann M., Bastian S., Bauer A., Berman E., Böhringer H., Boroski W. N., Bracker S., Briegel C., Briggs J. W., Brinkmann J., Brunner R., Carey L., Carr M. A., Chen B., Christian D., Colestock P. L., Crocker J. H., Csabai I., Czarapata P. C., Dalcanton J., Davidsen A. F., Davis J. E., Dehnen W., Dodelson S., Doi M., Dombeck T., Donahue M., Ellman N., Elms B. R., Evans M. L., Eyer L., Fan X., Federwitz G. R., Friedman S., Fukugita M., Gal R., Gillespie B., Glazebrook K., Gray J., Grebel E. K., Greenawalt B., Greene G., Gunn J. E.,

de Haas E., Haiman Z., Haldeman M., Hall P. B., Hamabe M., Hansen B., Harris F. H., Harris H., Harvanek M., Hawley S. L., Hayes J. J. E., Heckman T. M., Helmi A., Henden A., Hogan C. J., Hogg D. W., Holmgren D. J., Holtzman J., Huang C.-H., Hull C., Ichikawa S.-I., Ichikawa T., Johnston D. E., Kauffmann G., Kim R. S. J., Kimball T., Kinney E., Klaene M., Kleinman S. J., Klypin A., Knapp G. R., Korienek J., Krolik J., Kron R. G., Krzesiński J., Lamb D. Q., Leger R. F., Limmongkol S., Lindenmeyer C., Long D. C., Loomis C., Loveday J., MacKinnon B., Mannery E. J., Mantsch P. M., Margon B., McGehee P., McKay T. A., McLean B., Menou K., Merelli A., Mo H. J., Monet D. G., Nakamura O., Narayanan V. K., Nash T., Neilsen Jr. E. H., Newman P. R., Nitta A., Odenkirchen M., Okada N., Okamura S., Ostriker J. P., Owen R., Pauls A. G., Peoples J., Peterson R. S., Petravick D., Pope A., Pordes R., Postman M., Prosapio A., Quinn T. R., Rechenmacher R., Rivetta C. H., Rix H.-W., Rockosi C. M., Rosner R., Ruthmansdorfer K., Sandford D., Schneider D. P., Scranton R., Sekiguchi M., Sergey G., Sheth R., Shimasaku K., Smee S., Snedden S. A., Stebbins A., Stubbs C., Szapudi I., Szkody P., Szokoly G. P., Tabachnik S., Tsvetanov Z., Uomoto A., Vogeley M. S., Voges W., Waddell P., Walterbos R., Wang S.-i., Watanabe M., Weinberg D. H., White R. L., White S. D. M., Wilhite B., Wolfe D., Yasuda N., York D. G., Zehavi I., Zheng W., 2002, AJ, 123, 485

Struck C., 1999, Phys. Rep., 321, 1

—, 2006, Galaxy Collisions - Dawn of a New Era, Mason J. W., ed., p. 115

Taranu D. S., Dubinski J., Yee H. K. C., 2013, ApJ, 778, 61

—, 2014, ArXiv e-prints

Teyssier R., 2002, A&A, 385, 337

Toomre A., 1977, in Evolution of Galaxies and Stellar Populations, Tinsley B. M., Larson D. Campbell R. B. G., eds., p. 401

Toomre A., Toomre J., 1972, ApJ, 178, 623

Trager S. C., Faber S. M., Worthey G., González J. J., 2000, AJ, 119, 1645

Trujillo I., Burkert A., Bell E. F., 2004, ApJ, 600, L39

Trujillo I., Conselice C. J., Bundy K., Cooper M. C., Eisenhardt P., Ellis R. S., 2007, MNRAS, 382, 109

Trujillo I., Ferreras I., de La Rosa I. G., 2011, MNRAS, 415, 3903

Tully R. B., Fisher J. R., 1977, A&A, 54, 661

Turk M. J., Smith B. D., Oishi J. S., Skory S., Skillman S. W., Abel T., Norman M. L., 2011, ApJS, 192, 9

van der Kruit P. C., Freeman K. C., 2011, ARA&A, 49, 301

van der Wel A., Franx M., van Dokkum P. G., Skelton R. E., Momcheva I. G., Whitaker K. E., Brammer G. B., Bell E. F., Rix H.-W., Wuyts S., Ferguson H. C., Holden B. P., Barro G., Koekemoer A. M., Chang Y.-Y., McGrath E. J., Häussler B., Dekel A., Behroozi P., Fumagalli M., Leja J., Lundgren B. F., Maseda M. V., Nelson E. J., Wake D. A., Patel S. G., Labbé I., Faber S. M., Grogin N. A., Kocevski D. D., 2014, ApJ, 788, 28

van Dokkum P. G., 2008, ApJ, 674, 29

van Dokkum P. G., Franx M., 1995, AJ, 110, 2027

van Dokkum P. G., Whitaker K. E., Brammer G., Franx M., Kriek M., Labbé I., Marchesini D., Quadri R., Bezanson R., Illingworth G. D., Muzzin A., Rudnick G., Tal T., Wake D., 2010, ApJ, 709, 1018

Vogelsberger M., Genel S., Springel V., Torrey P., Sijacki D., Xu D., Snyder G. F., Nelson D., Hernquist L., 2014, ArXiv e-prints

Wadsley J. W., Stadel J., Quinn T., 2004, New A, 9, 137

Walter F., Brinks E., de Blok W. J. G., Bigiel F., Kennicutt Jr. R. C., Thornley M. D., Leroy A., 2008, AJ, 136, 2563

Watkins L. L., Evans N. W., An J. H., 2010, MNRAS, 406, 264

Weil M. L., 1995, PhD thesis, UNIVERSITY OF CALIFORNIA, SANTA CRUZ.

Weil M. L., Hernquist L., 1996, ApJ, 460, 101

Wetzel A. R., 2011, MNRAS, 412, 49

White S. D. M., 1980, MNRAS, 191, 1P

White S. D. M., Rees M. J., 1978, MNRAS, 183, 341

Widrow L. M., Dubinski J., 2005, ApJ, 631, 838

Widrow L. M., Pym B., Dubinski J., 2008, ApJ, 679, 1239

Wolf J., Martinez G. D., Bullock J. S., Kaplinghat M., Geha M., Muñoz R. R., Simon J. D., Avedo F. F., 2010, MNRAS, 406, 1220

Wright S. A., Larkin J. E., Law D. R., Steidel C. C., Shapley A. E., Erb D. K., 2009, ApJ, 699, 421

Wuyts S., Förster Schreiber N. M., Nelson E. J., van Dokkum P. G., Brammer G., Chang Y.-Y., Faber S. M., Ferguson H. C., Franx M., Fumagalli M., Genzel R., Grogin N. A., Kocevski D. D., Koekemoer A. M., Lundgren B., Lutz D., McGrath E. J., Momcheva I., Rosario D., Skelton R. E., Tacconi L. J., van der Wel A., Whitaker K. E., 2013, ApJ, 779, 135

Yip C. W., Connolly A. J., Szalay A. S., Budavári T., SubbaRao M., Frieman J. A., Nichol R. C., Hopkins A. M., York D. G., Okamura S., Brinkmann J., Csabai I., Thakar A. R., Fukugita M., Ivezić Ž., 2004, AJ, 128, 585